Synthesis and Characterisation of Multifunctional Bioresponsive Magnetic Resonance Imaging Probes

Dissertation

der Mathematisch-Naturwissenschaftlichen Fakultät

der Eberhard Karls Universität Tübingen

zur Erlangung des Grades eines

Doktors der Naturwissenschaften

(Dr. rer. nat.)

vorgelegt von

Liam Connah

Barnsley, Groβbritannien

Tübingen

2019

Gedruckt mit Genehmigung der Mathematisch-Naturwissenschaftlichen Fakultät der Eberhard Karls Universität Tübingen.

Tag der mündlichen Qualifikation:	16.07.2019
Dekan:	Prof. Dr. Wolfgang Rosenstiel
1. Berichterstatter:	Priv.-Doz. Dr. Goran Angelovski
2. Berichterstatter:	Prof. Dr. Martin E. Maier

Erklärung/Declaration

„Ich erkläre hiermit, dass ich die zur Promotion eingereichte Arbeit mit dem Titel: “Synthesis and Characterisation of Multifunctional Bioresponsive Magnetic Resonance Imaging Probes ” selbständig verfasst, nur die angegebenen Quellen und Hilfsmittel benutzt und wörtlich oder inhaltlich übernommene Stellen (alternativ: Zitate) als solche gekennzeichnet habe. Ich erkläre, dass die Richtlinien zur Sicherung guter wissenschaftlicher Praxis der Universität Tübingen (Beschluss des Senats vom 25.5.2000) beachtet wurden. Ich Amtliche Bekanntmachungen der Universität Tübingen 2015, Nr.5, S. 154 versichere an Eides statt, dass diese Angaben wahr sind und dass ich nichts verschwiegen habe. Mir ist bekannt, dass die falsche Abgabe einer Versicherung an Eides statt mit Freiheitsstrafe bis zu drei Jahren oder mit Geldstrafe bestraft wird.“

“I hereby declare that the thesis I submit for my doctorate with the title: „Synthesis and Characterisation of Multifunctional Bioresponsive Magnetic Resonance Imaging Probes“ is my own independent work, that I used only the sources and resources cited and have clearly indicated all content adopted either word-for-word or in substance. I declare that the University of Tübingen’s guidelines to ensure good academic practice (Senate decision of 25.5.2000) have been observed. I solemnly swear that this information is true and that I have not concealed any relevant information. I am aware that making a false declaration is punishable by a fine or by a prison term of up to three years.”

Tübingen, den

Datum/Date Unterschrift/Signature

Acknowledgements

The work described in this thesis would not have been possible without help of many people. Here, I would like to mention a few people have played a key role across my studies.

Firstly, I would like to say a major thank you to Priv.-Doz. Dr. Angelovski for allowing me to become part of his research group and conduct research with the freedom to express my own ideas. Furthermore, I would like to thank him for mentoring me over these last few years, providing encouragement and advice which has undoubtedly assisted in my development as a research scientist. Next, I would like also say a big thank you to Prof. Maier for agreeing to be my second supervisor and for the insights gained through his Wednesday group seminars.

The advice and scientific discussions with my colleagues and friends within the 'MR Neuroimaging agents' research group have also been important during this research and for that I would like to express my gratitude. I would like to say a specific thank you to Dr. Gambino, who I have worked with closely over the course of the PhD, for his advice and encouragement. The contributions from Dr. Savić regarding MR phantom measurements are also greatly appreciated. I also thank Dr. Correia for teaching me the technique of solid phase synthesis in Lisbon at the beginning of my PhD studies.

Next, I would like to acknowledge Dr. Truffault for his advice and assistance with NMR experiments. In addition, I would like to express thanks to Dr. Wistuba for performing all ESI-HRMS experiments.

The funding from the Max-Planck Society, German Research Foundation (DFG, grant AN 716/7-1) and COST TD1004 Action for the short term scientific mission are gratefully acknowledged.

Finally, I would like to express my most sincere appreciations to all my friends and family who have encouraged me throughout life and supported me during my studies.

Abstrakt

Die Entwicklung von bioresponsiven Kontrastmitteln (KM) zur spezifischen Überwachung von Ca^{2+}-Fluktuationen mittels Magnetresonanztomographie (MRT) sind von wachsendem Interesse, besonders für Studien der neuronalen Aktivität durch funktionelle MRT (fMRT). Solche Marker können Schlüsselinformationen bezüglich ihrer Mikroumgebung durch Veränderung des MR-Signals liefern. Diese Signalveränderungen lassen wiederum Rückschlüsse über die Funktion des Gewebes zu. Bisher wurden einige Ca^{2+}-empfindliche KM im Bereich von ‚kleinen' Molekularsystemen bis Nanoskala beschreiben. In dieser Arbeit wird die Erweiterung dieses wachsenden Feldes um die Entwicklung einer Bibliothek von mono- und multimerischen, sowie Ca^{2+}-responsiven intelligenten KM mit Nanogröße beschrieben.

Es werden eine Reihe von bioresponsiven dendrimerischen KM verschiedener Struktur und Ladungsverteilung für T_1-gewichtete MRT und r_2/r_1 ratiometric Bildgebungsmarkern entwickelt. Die Verwendung von Nanoplattformen ermöglicht stärker Gd^{3+}-Beschickung und langsamere Diffusionsraten. Beide sind wesentliche Charakteristiken für in vivo Anwendungen. Sowohl Veränderungen der Struktur als auch der Ladungsverteilung resultierten in signifikanten Änderungen der Leistungsfähigkeit der Marker als Ca^{2+}-responsiven MRT-Kontrastmittel. Der aktivste Marker wies gewöhnliche Veränderung von r_1 bei gleichzeitiger Zunahme des r_2/r_1-Verhältnisses auf, größer als dies bisher erreicht wurde. In weiteren Untersuchungen stellte sich heraus, dass nur durch synergistische Kombination von Ladungsanstieg einhergehend mit einer Größenänderung und Rigidität des Konjugats solche relaxometrischen Veränderungen erzielt werden können. Letztendlich lieferte dies signifikante Erkenntnisse über das Verhalten solcher dendrimerischen Systeme und eine Model anhand dessen zukünftige Probenvorbereitungen in der Entwicklung von Markern für T_1-gewichtete Bildgebung und r_2/r_1 ratiometric Markern zur dynamischen Visualisierung von Ca^{2+}-Fluktuationen basiert werden sollten.

Tiefergehende Studien der Struktur wurden in zwei momomerischen Systemen durchgeführt. Für jedes Derivat wurde ein Linker mit unterschiedlicher Länge zwischen dem MR-Reporter Teil und dem bioempfindlichen Element eingesetzt. Verschiedene Studien zeigten signifikante Unterschiede im relaxometrischen Verhalten im Vergleich der Marker. Charakterisierung mit vielartigen analytische Techniken zeigte die erwarteten Veränderungen in der komplexen Koordinationsumgebung zwischen ‚off' und ‚on' Zuständen. Auβerdem bleibt das diffusion Verhalten quasi konstant unabhängig von den Änderungen in die Ca^{2+}-Koordinationsumgebung. Die Ergebnisse dieser Studie zeigten, dass geringste Strukturveränderungen die Leistungsfähigkeit eines Kontrastmittels

signifikant beeinflussen können und helfen folglich dabei die Voraussetzungen für zukünftige Marker zu identifizieren.

Der letzte Abschnitt dieser Arbeit fokussiert sich auf die Anwendung von Festphasen-Synthesetechniken als Alternative zu gewöhnlicher Lösungsphasenchemie für die Bereitstellung ‚komplexerer' SCA Verbindungen. Im ersten Ansatz wurde ein funktionalisiertes bis-makrozyklisches Derivat in der Festphase durch den Gebrauch verschiedener Grundbausteine aufgebaut. Die Effizienz des Markers wurd mittels relaxometrischer Tritration bestätigt. In der zweiten Studie wurde ein selektiver multimerischer Marker, bestehend aus drei SCA Monomeren und eine RGD Proteinsequenz, synthetisiert. Das Multimer zeigte bei Zugabe von Ca^{2+} einen signifikanten Anstieg in der Relaxivität. Die Anwendung von Festphasen-Protokollen erlaubte in beiden Fällen die Herstellung von komplexeren SCA, die in Lösung kaum möglich sind. Des Weiteren erlaubt die Verwendung von Peptidgerüsten eine einfache spezifische Anpassung anhand derer sich multimerische oder multifunktionale Marker hervorbringen lassen. Somit steht Chemikern für die Entwicklung von bioresponsiven MR-Kontrastmitteln ein weiteres Synthesewerkzeug zur Verfügung.

Abstract

The development of bioresponsive magnetic resonance imaging (MRI) contrast agents (CAs) specific to monitoring Ca^{2+} fluctuations are of increasing interest for fMRI studies of neural activity. Such probes can provide key information regarding their microenvironment through changes in MR signal which in turn can lead to vital information concerning the functioning of tissue being extracted. Thus far, a number of CAs sensitive to Ca^{2+} have been developed ranging from 'small' molecular systems to larger nano-sized derivatives. Here, an extension to this ever growing field with the development of a range monomeric, multimeric and nano-sized Ca^{2+}-responsive smart contrast agents (SCAs) is described.

A range of bioresponsive dendrimeric CAs with different structures and charge distributions are described in the pursuit of probes for T_1-weighted imaging and r_2/r_1 ratiometric imaging probes. The use of nano-sized platforms enabled higher Gd^{3+} loading and slower diffusion rates, which are favoured characteristics for *in vivo* applications. The impact of structural and charge changes resulted in significant consequences for the performance of the probes as Ca^{2+}-responsive MRI CAs. The most active probe displayed common changes in r_1 while also exhibiting a remarkable increase in the r_2/r_1 ratio, greater than that previously achieved. Further investigation revealed that only through a synergistic combination of an increase in q with a change in size and rigidity of the conjugate could such relaxometric changes be realised. This ultimately provided significant insights into the behaviour of such dendrimeric systems and provided a model in which future preparations should be based in the development of T_1-weighted and r_2/r_1 ratiometric probes to visualise Ca^{2+} fluctuations dynamically.

Deeper structural studies were performed on two monomeric systems in which the linker length between the MR reporting moiety and the bioresponsive unit were extended. Various studies revealed significant differences in relaxometric behaviour between the probes. Characterisation with a range of techniques revealed structural changes in the complex coordination environment between the 'off' and 'on' states which is expected for such systems. Furthermore, the diffusive behaviour of each complex described systems which do not significantly change upon Ca^{2+} coordination. The results of this study revealed how subtle structural changes can significantly impact the performance of a SCA, thus helping to identify the requirements for future probes.

The final parts of this work focused on employing solid phase synthetic techniques as an alternative to standard solution phase chemistry in the preparation of more 'complex' SCA derivatives. In one approach, a functionalised bismacrocyclic derivative was assembled on solid phase through the use of multiple building blocks in a straightforward manner. The potency of this probe was confirmed by

relaxometric titrations. In a second study, a targeted multimeric probe consisting of three SCA monomers and the RGD peptide sequence was developed. This multimer showed significant increases in relaxivity upon Ca^{2+} addition. The use of solid phase protocols in both of these cases allowed for more complex SCAs to be developed, which would otherwise be extremely difficult following solution phase protocols. Furthermore, the use of peptide scaffolds allows for simple customisation in which multimeric or multifunctional probes can be developed, providing an additional synthetic tool for chemists attempting to develop bioresponsive MRI CAs.

Abbreviations

AAZTA	6-amino-6-methylperhydro-1,4-diazepinetetraacetic acid
BAPTA	1,2-bis(*o*-aminophenoxy)-ethane-*N*,*N*,*N''*,*N'*-tetraacetic acid
Boc	*tert*-Butyloxycarbonyl
BOLD	Blood-oxygen-level dependent
BPEN	*N*,*N*-bis(2-pyridyl-methyl) ethylene diamine
CA	Contrast agent
Cbz	Carboxybenzyl
CD	Cyclodextrin
CEST	Chemical exchange saturation transfer
COSY	Correlation spectroscopy
CT	Computed tomography
CuAAC	Copper-assisted azide-alkyne cycloaddition
DCA	Dendrimeric contrast agent
DCC	*N*,*N*'-Dicyclohexylcarbodiimide
DIC	*N,N'*-Diisopropylcarbodiimide
DIPEA	Diisopropylethylamine
DLS	Dynamic light scattering
DMAP	4-Dimethylaminopyridine
DMF	Dimethylformamide
DOSY	Diffusion ordered nuclear mangetic resonance spectroscopy
DOTA	1,4,7,10-Tetraazacyclodocecane-1,4,7,10-tetraacetic acid
DO3A	1,4,7,10-Tetraazacyclododecane-1,4,7-triacetic acid
DO3AP	1,4,7,10-Tetraazacyclododecane-1,4,7-triacetic acid methylenephosphonic acid
DO3A-PA	1,4,7,10-Tetraazacyclododecane-1,4,7-triacetic acid propyl amine
DSCA	Dendrimeric smart contrast agent
DTMA	1,4,7,10-Tetraazacyclodocecane-1,4,7,10-tetraacetic acid tetrakis(methylamide)

DTPA	Diethlyenetriaminepentaacetic acid
DTPA-BMA	Diethylenetriaminepentaacetic acid bis methylamide
DTTAP	diethylenetriamine-*N*,*N*,*N*′,*N*″-tetraacetic acid-N″-propionic acid
EDC	1-ethyl-3-(3-dimethylaminopropyl)carbodiimide
EDTA	Ethylenediaminetetraacetic acid
EGTA	Ethylene glycol tetraacetic acid
EMA	European Medicines Agency
ENDOR	^{1}H electron-nuclear double resonance spectroscopy
EPTPA	Ethylenepropylenetriaminepentaacetic acid
Eq	Equation
Equiv	Equivalent
ESI-MS	Electrospray ionization mass spectrometry
ESI-TOF-MS	Electrospray ionization/time of flight mass spectrometry
FDA	U.S. Food and Drug Administration
Fmoc	Fluoren-9-ylmethyloxycarbonyl
fMRI	Functional magnetic resonance imaging
G	Generation
GBCA	Gadolinium based contrast agent
Gly	Glycine
HATU	1-[Bis(dimethylamino)methylene]-1*H*-1,2,3-triazolo[4,5-*b*]pyridinium 3-oxid hexafluorophosphate
HBTU	*N,N,N′,N′*-Tetramethyl-*O*-(1*H*-benzotriazol-1-yl)uronium hexafluorophosphate
HEPES	4-(2-Hydroxyethyl)piperazine-1-ethanesulfonic acid
HOBt	Hydroxybenzotriazole
HOPO	Hydroxypyridinone
HPLC	High performance liquid chromatography
HRMS	High resolution mass spectrometry
HSA	Human serum albumin

HSQC	Heteronuclear single quantum correlation
IS	Inner sphere
ivDde	1-(4,4-dimethyl-2,6-dioxocyclohex-1-ylidene)-3-methylbutyl
J	Coupling constant
LC-MS	Liquid chromatography-mass spectrometry
Ln	Lanthanide
Lys	Lysine
m	Multiplet (NMR)
MALDI-TOF	Matrix-assisted laser desorption/ionization-time of flight
MPIO	Micron iron oxide particles
MR	Magnetic resonance
MRI	Magnetic resonance imaging
Mtt	4-Methyltrityl
NMR	Nuclear magnetic resonance
NSF	Nephrogenic systemic fibrosis
OS	Outer sphere
PAMAM	Polyamidoamine
PBS	Phosphate buffer saline
Pbf	2,2,4,6,7-Pentamethyldihydrobenzofuran-5-sulfonyl
PEG	Polyethylene glycol
PET	Positron emission tomography
PPI	Polypropylene imine
PyBOP	(Benzotriazol-1-yloxy)tripyrrolidinophosphonium hexafluorophosphate
RF	Radiofrequency
RGD	Arginine-glycine-aspartic acid
RIME	Receptor-induced magnetisation enhancement
RP-HPLC	Reverse phase high performance liquid chromatography

RT	Room temperature
s	Singlet (NMR)
SAP	Square antiprismatic
SBM	Solomon, Bloembergen and Morgan theory
SCA	Smart contrast agent
SPECT	Single-photon emission computed tomography
SPIO	Superparamagnetic iron oxide
SPPS	Solid phase peptide synthesis
TACN	1,4,7-Triazacyclononane
TAM	Terephthalamide
TFA	Trifluoroacetic acid
THF	Tetrahydrofuran
TIS	Triisopropylsilane
TSAP	Twisted square antiprismatic
T_1	Spin lattice relaxation time
T_2	Spin spin relaxation time
*t*Bu	*tert*-butyl
TLC	Thin layer chromatography
USPIO	Ultra small superparamagnetic iron oxide
δ	Chemical shift

Table of Contents

1. Introduction

1.1 Magnetic resonance imaging

MRI is an imaging modality that has rapidly increased in popularity over recent decades to become one of the essential techniques utilised in diagnostic medicine. Alongside CT, PET and SPECT, MRI is used to help study biological phenomena including the identification of regions of pathology, understanding biological phenomena and aiding investigations into disease mechanisms.[1, 2] Although each method brings various advantages and disadvantages, MRI has taken a leading role amongst the various imaging modalities as it can provide anatomical images with high spatial resolution in a non-invasive manner, whilst additionally avoiding the use of ionising radiation that is a key component in modalities such as PET and SPECT.[1-5] Furthermore, MRI provides excellent soft tissue contrast and versatility through the use of a variety of pulse sequences to highlight differences between tissues with dissimilar proton densities, different chemical shifts or differing rates of water diffusion.[3, 5] MR images are generated by mapping out the spatial distribution of the nuclei present in the imaged object which is influenced by a powerful external magnetic field.[2, 4] In a biological system, the MR image is typically that of water protons (^{1}H) distributed in tissue. The selection of the ^{1}H nuclei is mainly due to a high concentration (90 M) in tissues in addition to almost 100% natural abundance of the proton.[3, 5] Signal intensity in MRI mostly arises from the longitudinal ($1/T_1$) and transverse relaxation ($1/T_2$) rates of water protons, with signal increase achieved through an increase in the longitudinal relaxation rate and a decrease in the transverse relaxation rate.[6] Despite the exceptional capabilities of MRI, one major drawback is the low sensitivity of the technique.[3, 5] Although high resolution images can in some cases be obtained through the use of multiple imaging sequence techniques, additional contrast is often required. This additional contrast is provided by exogenous materials, namely contrast agents (CAs) that alter the MR signal of water molecules in the immediate vicinity of the substance. Generally, CAs are assigned as either T_1-weighted or T_2-weighted CAs depending on their effect on the bulk water protons and are composed of paramagnetic, superparamagnetic or ferromagnetic materials.

1.2 The basic concept and principles of MRI

MRI operates on the basic principles of NMR with nuclei that possess a nuclear spin quantum number, I, that is not equal to zero.[5, 7, 8] The most commonly studied magnetic nuclei (^{1}H, ^{19}F, ^{13}C and ^{31}P) are those which have I = ½. Nuclei with a spin angular momentum produce a magnetic field which is randomly distributed. Application of an external magnetic field causes the nuclear moments to orient themselves along the external magnetic field in discrete directions determined by I. The

magnetic quantum number, m_I, denotes the number of allowed orientations ($2I + 1$ possible orientations) which when applied to protons or other $I = ½$ nuclei gives two possible orientations where $m_I = +½$ or $-½$. This dictates that the spins of $I = ½$ systems will align with or against the applied external magnetic field. When placed in a static magnetic field the nuclei will precess around the field at a specific frequency (Larmor frequency, ω_0) which is dependent on a constant known as the gyromagnetic ratio, γ, and is linearly dependent on the applied magnetic field B_0, as shown in Eq 1.

$$\omega_0 = \gamma B_0 \tag{1}$$

Application of an appropriate resonant energy (ΔE), such as in the form of a RF pulse, can cause the spins to transition between the two allowed states. [2, 8]

$$\Delta E = h\nu = \frac{\gamma h B_0}{2\pi} \tag{2}$$

In Eq 2, h is Planck's constant and ν is the applied frequency. The required frequency needed to apply the appropriate resonant energy for a transition between the +½ and -½ spin states is directly dependent on the applied magnetic field and the gyromagnetic ratio.[5, 7, 8] The ratio of these populations ($N_{-1/2}/N_{+1/2}$) is defined by the Boltzmann equation, Eq 3:

$$\frac{N_{-\frac{1}{2}}}{N_{+\frac{1}{2}}} = e^{\left(-\frac{h\nu}{kT}\right)} \tag{3}$$

$$= 1 - \frac{h\nu}{kT} \qquad \text{since } h\nu << kT$$

Here kT is defined as thermal energy (k = Boltzmann constant, T = absolute temperature). With the quantum spin energy being significantly lower than thermal energy, the population of excess spins aligning parallel with the magnetic field as opposed to against the magnetic field, the 'spin excess', is also considerably small (Eq 4, $\hbar \equiv \mathrm{h}/2\pi$).[5, 8]

$$spin\ excess\ \simeq N\frac{\hbar\omega_0}{2kT} \tag{4}$$

This low excess of spins means that only 0.001% of hydrogen is detected in NMR and is the fundamental reason for the low sensitivity of the technique.[5, 8] As frequency is directly proportional to sensitivity, the use of nuclei with high γ (e.g. ^{1}H) at high applied magnetic fields would result in the greatest sensitivity increase. This is the typical reason for the selection of water to be imaged, as it is the most abundant hydrogen containing molecule. Fluorine, which also has a high γ, has also been successfully imaged. An additional method to increase the sensitivity of NMR can also arise from decreasing the thermal temperature (kT), which is possible with certain nuclei (^{13}C, ^{129}Xe, ^{3}He) that

can be polarised at low temperatures and then maintain this polarisation upon returning to room temperature.[5]

1.2.1 Relaxation rates

After placing nuclei in a magnetic field and applying a RF pulse, the spins will absorb energy and undergo transitions between the +½ and -½ spin states. Once the RF pulse has been switched off, the spins will return to their equilibrium state via a process termed as relaxation. The time taken for regrowth parallel to the external magnetic field is called the longitudinal relaxation time (T_1), which is also referred to as spin-lattice decay or relaxation due to the interaction between the spins and their environment, Eq 5.

$$M_z = M_0(1 - e^{-t/T_1}) \quad (5)$$

Additionally, after a RF excitation, the magnetisation present perpendicular to the external magnetic field will decay towards zero in a time referred to as the transverse relaxation time, or spin-spin relaxation time, Eq 6.

$$M_{xy} = M_0(1 - e^{T_R/T_1})e^{-t/T_2} \quad (6)$$

M_0 represents the equilibrium magnetisation at the applied external magnetic field, e^{-t/T_2} is the spin-spin decay factor that is characterised by the time constant T_2, and T_R is the interval time between successive RF pulses. The spin-spin decay factor characterises the loss of coherence between spins, often referred to as the dephasing of spins, and is due to variations in local precessional frequencies. The cause of transverse relaxation can be dedicated to two factors, firstly, the magnetic interactions between neighbouring molecules and secondly the effects of inhomogeneity in the external magnetic field. Relaxation exclusively due to molecular interactions is described as T_2 whereas a combination of these two effects is represented by the term T_2*.

1.3 Contrast agents (CAs)

As previously mentioned, one of the major drawbacks of MRI is the inherently low sensitivity of the technique. The main approach to address this issue involved increasing the specificity of the technique through the development and application of CAs. These substances alter the relaxation rates of the surrounding water molecules, affecting the produced MR signal. Multiple types of CAs exist and are generally classified depending on (a) whether they predominantly affect T_1 or T_2, (b) their magnetic properties, (c) their biodistribution, (d) their effect on the image or (e) their chemical structure.[4] Here I will briefly discuss the main classifications of MR CAs.

1.3.1 Paramagnetic CAs

Paramagnetic metal ions possess a permanent magnetic moment due to having one or more unpaired electrons.[4] CAs containing paramagnetic metal ions have been extensively studied as efficient materials to suitably shorten T_1 and T_2 proton relaxation times through dipolar magnetic interactions between the electronic magnetic moment of the paramagnetic ion and the magnetic moment of the surrounding protons. Although they will affect both T_1 and T_2, generally CAs based on paramagnetic ions are known as T_1 contrast agents, providing a positive contrast (brightening of the image). Gadolinium (Gd^{3+}) and manganese (Mn^{2+}) are examples of paramagnetic ions used in positive CAs for T_1-weighted MRI. Both Gd^{3+} and Mn^{2+} possess a high number of unpaired electrons (Gd^{3+} - seven, Mn^{2+} - five) with symmetrical S ground states giving a slow electronic relaxation rate.[4, 6] Other paramagnetic metals such as dysprosium (Dy^{3+}) have larger magnetic moments than Gd^{3+} but with more rapid electronic relaxation rates. This makes them inferior to Gd^{3+} in standard T_1- or T_2-weighted imaging but useful as other types of MRI CAs such as susceptibility agents or as liposomal and paramagnetic chemical exchange saturation transfer (lipoCEST and paraCEST) agents.[4, 9-11] Gd^{3+} is much more widely used than Mn^{2+} due to its higher paramagnetism with many GBCAs being approved for clinical use (Figure 1).

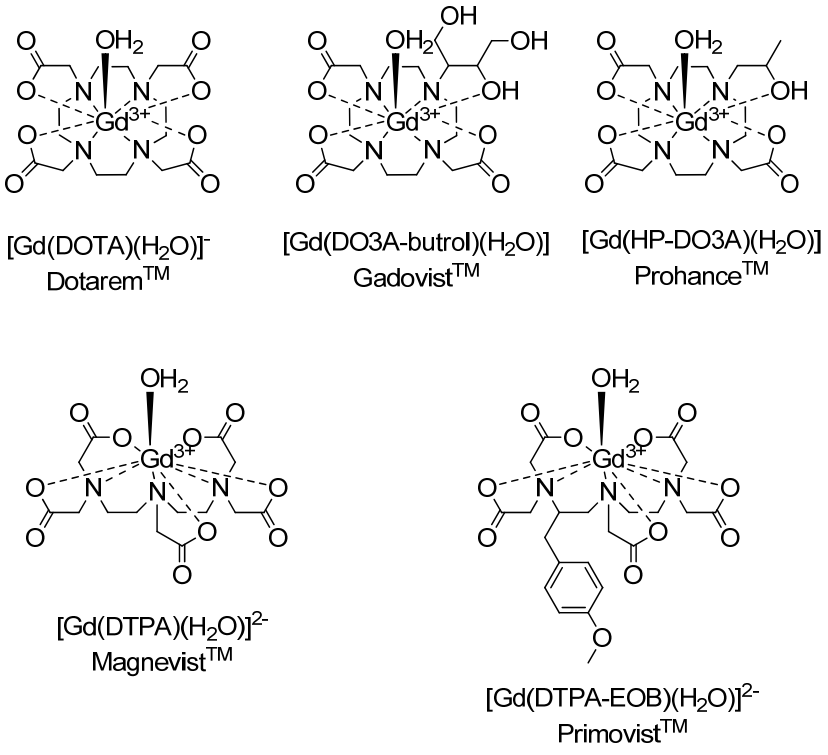

Figure 1. Clinically approved GBCAs.

Additionally, Mn^{2+}-based CAs have been reported to have low stability as coordination complexes and as Mn^{2+} is an essential metal ion, its stability to biological scavengers is also low. One Mn^{2+}-based CA that has been used clinically is a hepatotropic agent which releases Mn^{2+} to macromolecules resulting in an enhancement in proton relaxation (Figure 2).[11, 12]

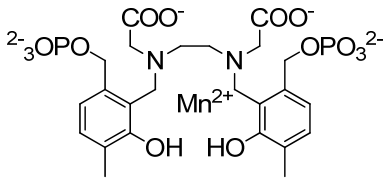

Mn-DPDP
TESLASCAN®

Figure 2. A manganese-based MRI CA.

Gd^{3+} is known to have a high toxicity as a free metal ion in biological systems arising from its similar ionic radius to Ca^{2+}.[13, 14] This allows Gd^{3+} to compete with Ca^{2+} and adversely affect biological processes that require Ca^{2+} for proper function. In order to avoid this scenario, Gd^{3+} is encapsulated by a multidentate organic ligand know as a chelating agent. The purpose of this chelating agent is to bind the free Gd^{3+} ion, thus preventing its release and its interaction with biological systems until it can be excreted. Gd^{3+} has a coordination number of 8-9 as the hydrated aqua ion.[14] Once chelated, these water molecules are displaced by donor atoms from the ligand, which are typically carboxylates and amides, usually leaving one water molecule binding site for the purpose of MRI. Both linear and macrocyclic ligand structures have been synthesised for Gd^{3+} chelation and both types of ligand structure have been used to design clinically approved MRI CAs, with the first CA being based on the linear ligand, DTPA (Figure 1).[7]

As some of the main requirements of MRI CAs include excellent *in vivo* stability, excretability and general lack of toxicity (as well as high relaxivity and specific *in vivo* biodistribution), the thermodynamic stability and kinetic inertness are important factors that must be considered.[14, 15] Generally, macrocyclic ligands are more thermodynamically stable than linear ligands (higher log*K*).[14] Additionally, the kinetics of association and subsequently dissociation of the Gd^{3+} ion is generally faster for linear ligand structures, leading to a more rapid release of lanthanide compared to macrocyclic ligands. Although historically GBCAs have been considered safe when used at the correct dosage, a number of reports have related the use of GBCAs with the development of NSF in patients with severe renal impairment.[13, 16] Furthermore, observations of Gd^{3+} accumulation in tissues such as brain, bone and kidneys of patients with normal renal function has led to investigations by the FDA and the EMA which has resulted in the EMA restricting the use of certain

linear GBCAs from clinical application. With these safety issues in mind, GBCAs should be designed which are kinetically inert and thermodynamically stable, e.g. using macrocyclic ligand structures such as DOTA. Moreover, further exploration of alternative non-GBCAs remains an attractive proposition.[17] Of these Mn^{2+} seems the most appropriate alternative to Gd^{3+} as a T_1-contrast agent, although complex stability is a major challenge that needs to be addressed through thoughtful ligand design.[18] In addition, probes designed for alternative MR mechanisms such as CEST remain promising although drawbacks surrounding sensitivity are still to be resolved.[18, 19] Hyperpolarized methods are an additional alternative to standard T_1-weighted imaging although these require additional expensive hardware. Finally, the use of paramagnetic transition metals gives rise to alternative MRI CAs which are currently being evaluated.[20]

1.3.2 Superparamagnetic CAs

SPIO nanoparticles are a class of contrast agents composed of iron oxide crystals such as magnetite (Fe_3O_4) and maghemite (Fe_2O_3) coated with dextran or carboxydextran to facilitate solubility in biological media and prevent any destabilisation or agglomeration that may occur.[21-23] There are two main considerations that must be taken into account when synthesising SPIOs: a) defining a process to obtain monodisperse particles and b) having a reproducible process that can be replicated in industry without requiring any complicated purification.[24] There are many methods to synthesise magnetic nanoparticles reported including coprecipitation, the use of microemulsions, sonochemical reactions, sol-gel syntheses, flow injection syntheses, hydrothermal reactions, electrospray syntheses, and the hydrolysis and thermolysis of precursors.[24-35] Of these methods, coprecipitation is the most commonly used and can produce sufficiently large amount of nanoparticles, with the only drawback of the method being the limited control of size distribution. According to the size of the particle, separate subclasses can be also be distinguished.[21-23] SPIO particles have mean diameters of more than 50 nm, USPIO nanoparticles have a mean diameter of less than 50 nm and MPIO have a mean diameter of about 1000nm. Each of these particles is composed of small crystallites (1-10 nm) which contain thousands of magnetic ions displaying superparamagnetic behaviour.[4] Unlike ferromagnetic materials, superparamagnetic substances possess no magnetic properties in the absence of an external magnetic field.[4, 5, 23, 36]

Upon application of an external magnetic field, the superparamagnetic crystals display a large magnetic moment, which is considerably greater than that of any single Gd^{3+} chelate.[4, 23, 24, 37-39] In terms of MRI, SPIO nanoparticles are primarily used in T_2- or T_2*-weighted imaging (negative contrast) although they can also have useful effects on T_1 relaxation times.[4, 23, 40, 41] Contributions to the relaxation of superparamagnetic particles can be described by models derived from outer-

sphere relaxation theory where water molecules diffuse close to the local magnetic field generated by the particle.[4, 5, 21, 24, 42-44] The ratio of relaxivities, r_2/r_1, is sensitive to the particle size with larger sizes leading to a greater ratio.[4, 37, 45] This has led to the development of USPIOs with superior properties for T_1-weighted imaging.[37, 46-50] SPIOs have been utilised in research for a variety of functions including, macrophage imaging, liver imaging, stem cell labelling, as blood pool agents and in molecular imaging when functionalised with a targeting moiety.[4, 21-23, 36, 51] Although many functions have been explored, only a limited number have received FDA approval for clinical use with Feridex I.V. being one of a few iron oxide nanoparticle based MRI contrast agents that have been approved for liver imaging, but was discontinued by the manufacturer.[52, 53] Currently, there are no functionalised SPIOs that are being used in humans.

1.4 Relaxivity

Characterisation of contrast agents is primarily based on their relaxivity (r_1 or r_2), which is defined as the change in longitudinal or transverse relaxation rates ($1/T_1$ or $1/T_2$) of the surrounding solvent water protons normalised to the concentration of contrast agent applied, Eq 7.[2, 5, 54]

$$r_i = \frac{\Delta\left(\frac{1}{T_i}\right)}{[CA]}; i = 1,2 \tag{7}$$

1.4.1 Longitudinal relaxivity

The observed longitudinal relaxation rate (R_1^{obs}) of the water protons in an aqueous solution containing a paramagnetic CA is traditionally described with a model that considers the contributions from inner sphere (IS) and outer sphere (OS) mechanisms.[2, 5, 11, 54] There are three main contributions within this model (Eq 8.); (i) the exchange of the inner sphere water molecules from the paramagnetic ion with the bulk water (R^{is}_{1p}); (ii) the contribution from the water molecules that diffuse in the outer sphere of the CA (R^{OS}_{1p}) and (iii) the diamagnetic contributions, the relaxation rate in the absence of paramagnetic CA (R^0_1).[5, 11, 55] An additional fourth parameter is sometimes taken into account arising from mobile protons in the second coordination sphere of the CA.[56]

$$R_1^{\mathrm{obs}} = R_1^0 + R_{1p}^{\mathrm{is}} + R_{1p}^{\mathrm{OS}} \tag{8}$$

The contributions from the inner sphere are considered to be the most important in determining the longitudinal relaxation rate of a paramagnetic CA and have led to decades of investigations into the optimisation of these parameters initially highlighted by SBM theory.[2, 6, 57-59] The contributions arising from the inner sphere are directly proportional to the concentration of the paramagnetic ion and the number of water molecules (q) coordinated to the metal centre. Inner sphere relaxivity is

also inversely proportional to the sum of the relaxation time of the water protons (T_{1m}) and their mean residence lifetime (τ_m), Eq 9.[11]

$$R_{1p}^{is} = \frac{q[CA]}{55.5(T_{1m}+\tau_m)} \quad (9)$$

Outer-sphere contributions, described by Freed,[60] additionally need to be taken into account when determining relaxivity. Here, parameters affecting the outer-sphere longitudinal relaxivity are identical to that affecting the inner-sphere; however the residency time of the protons plays a more dominant role.[61]

Paramagnetic relaxation depends on a number of factors including the magnetogyric ratio (γ_H), Bohr magneton (μ_B), spin quantum number, electronic g factor (g_e = 2 for Gd^{3+}), the distance between the metal and hydrogen (r_{M-H}), the proton (ω_H) and electron (ω_S) Larmor frequencies and a correlation time τ_c, Eq 10.[5]

$$\frac{1}{T_{1m}} = \frac{2}{15}\left(\frac{\mu_0}{4\pi}^2\right)\frac{\gamma_H^2 g_e^2 \mu_B^2 S(S+1)}{r_{M-H}^6}\left(\frac{7\tau_C}{1+\omega_S^2\tau_C^2}+\frac{3\tau_C}{1+\omega_H^2\tau_C^2}\right) \quad (10)$$

The relaxation time of the water protons is directly proportional to the distance between the paramagnetic metal centre and the coordinated water protons to the sixth power. It is also influenced by the average rate constant for fluctuating magnetic dipoles (τ_C), which can cause spin relaxation. τ_C is affected by processes such as the magnetic field strength, the electronic relaxation ($1/T_{1e}$) of the Gd^{3+}, the molecular reorientational time ($1/\tau_R$) of the paramagnetic complex and the water exchange ($1/\tau_m$) between the inner and outer coordination spheres (Eq 11).[5, 11, 57]

$$\frac{1}{\tau_C} = \frac{1}{\tau_R} + \frac{1}{T_{1e}} + \frac{1}{\tau_m} \quad (11)$$

The efficiency of the relaxation is determined by how similar τ_C is to the Larmor frequency with higher efficiency arising from more closely matched rates.[5] The design of CAs with higher relaxivities is a primary goal in the field of Gd-based contrast enhanced MRI to enable the use of lower doses of CAs, or in the case of molecular imaging, enable the detection of targets that exist in lower concentrations.

Currently, the relaxivities of commercially available GBCAs are generally around 3-5 $mM^{-1}\,s^{-1}$ (1.5-3 T, q = 1, τ_m = 150-1000 ns, τ_R in the picosecond range for small molecules) which is lower than that what can be theoretically achieved.[6, 57, 62] With optimisation of the parameters previously discussed a relaxivity of 300 $mM^{-1}\,s^{-1}$ can be achieved (20 MHz, q = 3, τ_m = 1-30 ns, τ_R in the nanosecond range). Although obtaining these optimal relaxivities is desirable, it must not come at the expense of

complex stability which is an ongoing challenge that chemists must overcome. Fine tuning of parameters such as the hydration number, the rotational correlation time of the complex and the residence lifetime of the coordinated water protons has been pursued to try and achieve optimal relaxivities and will be discussed in the following sections (Figure 3).

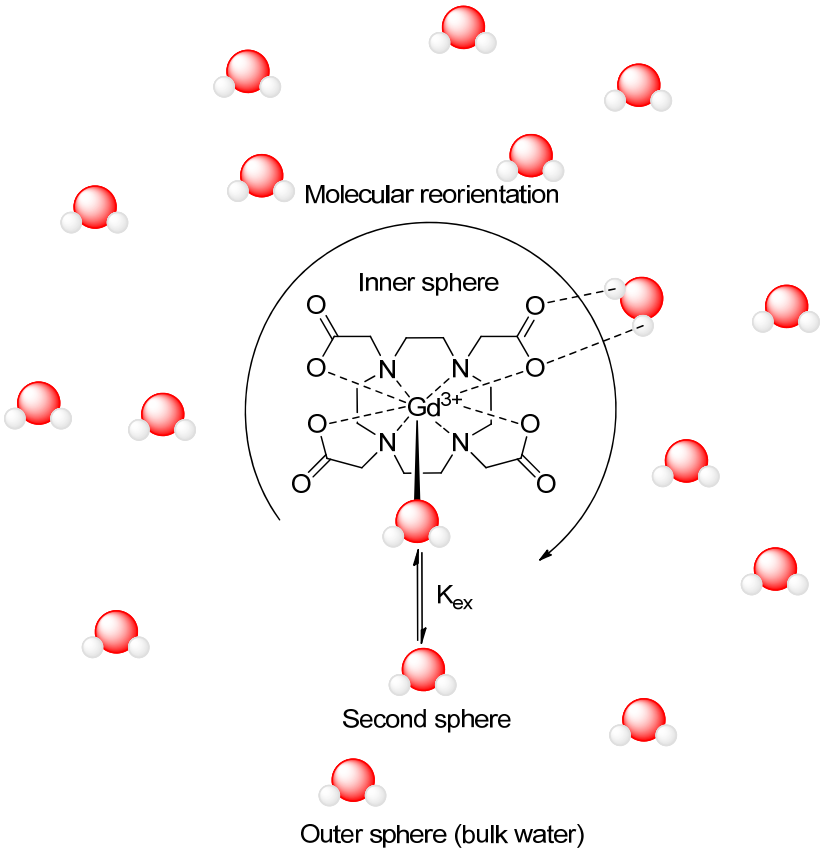

Figure 3. Schematic showing the parameters governing relaxivity.

1.4.2 Transverse relaxivity

Similar to longitudinal relaxivity, transverse relaxivity is composed of both inner- and outer-sphere components, Eq 12.

$$R_2^{\text{obs}} = R_2^0 + R_{2p}^{\text{is}} + R_{2p}^{\text{OS}} \tag{12}$$

The inner-sphere contribution to transverse relaxivity can be described by Eq. 13. The T_{2m} and $\Delta\omega_m$ terms refers to the T_2 and the chemical shift of the coordinated water, respectively.[54, 61, 63]

$$R_{2p}^{is} = \frac{q[CA]}{55.5}\frac{1}{\tau_m}\left(\frac{T_{2m}^{-1}\left(\tau_m^{-1}+T_{2m}^{-1}\right)+\Delta\omega_m^2}{\left(T_{2m}^{-1}+\tau_m^{-1}\right)^2+\Delta\omega_m^2}\right) \tag{13}$$

T_{2m} is expressed in terms of the Solomon-Bloembergen-Morgan theory, Eq 14.

$$\frac{1}{T_{2m}} = \frac{1}{15}\left(\frac{\mu_0}{4\pi}^2\right)\frac{\gamma_H^2 g_e^2 \mu_B^2 S(S+1)}{r_{M-H}^6}\left(4\tau_C + \frac{13\tau_C}{1+\omega_S^2\tau_C^2} + \frac{3\tau_C}{1+\omega_H^2\tau_C^2}\right) + \frac{S(S+1)}{3}\left(\frac{A}{\hbar}\right)^2 \tau_C \quad (14)$$

T_2 has contributions from dipolar (as described for longitudinal relaxation), scalar and Curie spin interactions.[42, 54, 58, 61, 64] The scalar portion is independent of rotation and refers to contact through bonds rather than through space and shows a greater contribution for metals such as Mn(II) and Fe(III) over Gd(III). The correlation time τ_{SC} and the hyperfine coupling constant between a proton and the metal ion influence the scalar term, Eq 15.

$$\frac{1}{\tau_{sc}} = \frac{1}{\tau_m} + \frac{1}{T_{1e}} \quad (15)$$

As the magnetic field strength increases towards high fields, differences occur in the behaviour of r_1 and r_2 relaxation. Specifically, r_1 tends to decrease differently to r_2. The impact of Curie spin relaxation results in an r_2 which is increased at high magnetic fields under the conditions that the ion has a large magnetic moment.[61, 65] Additionally, the Curie spin relaxation correlation time is dependent on the water exchange rate and the rotation correlation time, and thus independent of the electronic relaxation time Eq 16.[54]

$$\frac{1}{\tau_{cs}} = \frac{1}{\tau_m} + \frac{1}{\tau_R} \quad (16)$$

As previously mentioned in Chapter 1.3.2, superparamagnetic particles are generally classified as T_2 CAs. The effectiveness of such CAs is highly dependent on the saturation magnetisation (*Ms*) and effective radius according the T_2 outer sphere relaxation theory, Eq 17.[61, 65]

$$\frac{1}{T_2^{OS}} = \left(\frac{256\pi^2\gamma^2}{405}\right) \times \frac{\kappa M_s^2 r^2}{D\left(1+\frac{l}{r}\right)} \quad (17)$$

Here, κ is the volume fraction (V^*) divided by the total concentration (C) of iron ($\kappa = V^*/C$), D is the diffusivity of the water molecules and l is the impermeable surface coating thickness.

1.4.3 Hydration number (q)

The hydration number of a complex is an important parameter in determining the inner sphere relaxivity and is independent of the magnetic field applied.[3, 11, 54, 57] Ideally, an increased hydration number ($q > 1$) would improve the efficiency of the GBCA. Utilisation of ligand structures with 6 or 7 coordinating groups, as opposed to the 8 coordinate ligands currently used, would result in a q number of 3 or 2 respectively. Although this may seem advantageous, there is generally a trade-off between the hydration number of the complex and the overall thermodynamic stability that the complex possesses. Higher hydration numbers could lead to lower complex stabilities and thus a

leakage of free Gd^{3+} inducing an increase in toxicity. Additionally as the number of water coordination sites increase, coordination from endogenous anions such as phosphate and bicarbonate as well as interactions from proteins are more likely to occur, resulting in quenching of the relaxivity through water displacement.[3, 11, 66, 67] This is demonstrated in the case of [GdDO3A(H_2O)$_2$] (Figure 4), which exists as a *q* = 2 complex that suffers from the quenching effect of endogenous ions previously described.[3, 67, 68]

Despite these concerns, there have been reports of *q* = 2 Gd-based systems that are themodynamically stable and exhibit increased relaxivities. The HOPO systems developed by Raymond and co-workers are one example of this (Figure 4).[69-73]

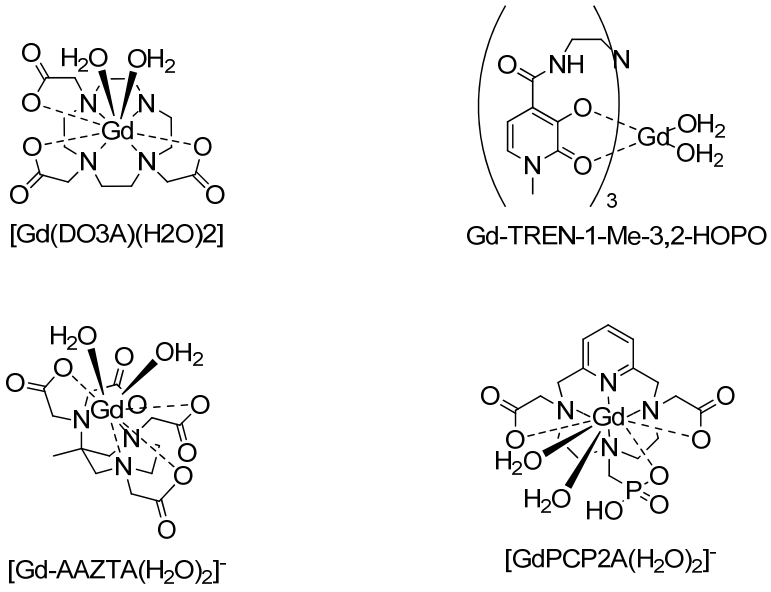

Figure 4. Examples of *q* = 2 GBCAs.

Based on 4-carboxyamido-3,2-hydroxypyridinone ligand structures, this class of CA exist as stable Gd^{3+}complexes with two free coordination sites for water. Optimisation of the water exchange rates additionally contributed to enhanced relaxivities in the range of 7-13 mM^{-1} s^{-1} (20 MHz). With improved relaxometric properties, later designs focused on improving the aqueous solubility of the parent compound,[69, 74, 75] through the replacement of one HOPO component with a TAM chelator which also allowed further derivatisation with targeting groups.[57, 74, 76, 77] The susceptibility of the HOPO compound series to the quenching effect described earlier was not observed due to the coordination geometry of the HOPO ligands which prevents the easy replacement of the two inner sphere water molecules with other anions or coordinating groups.[11]

Another example of a stable q = 2 system is that based on a DOTA derivative containing a pyridine moiety with one methylenephosphonic and two acetic arms, otherwise known as the PCP2A (Figure 4).[11, 54, 78, 79] The relaxivity of this system is reported to be around double that of commercially available CAs, with the increase attributed to a combination of contributions from the two inner sphere water molecules and the interactions of the additional protons present on the methylenephosphonic arm.

In addition, AAZTA is a macrocyclic ligand reported by Aime and co-workers whose Gd^{3+} complex exhibits high relaxivities (7.1 mM^{-1} s^{-1}, 20 MHz, 298 K) (Figure 4).[11, 80] The complexes formed are again thermodynamically stable q = 2 systems which are inert to quenching from endogenous ions and a possess a reasonably fast water exchange rate. These properties make this class of macrocyclic system an interesting alternative to the DOTA-based systems previously reported with further derivatives being developed for further investigation.[81]

Estimation of the hydration states of such complexes has previously been attempted through a variety of methods. X-ray crystallography is one example; however, this method does not fully represent the true coordination of the complex in aqueous solutions and is not useful when attempting to determine the q number of a protein bound complex.[3] Another method is based on measuring the luminescence lifetimes of Eu^{3+} or Tb^{3+} analogues in H_2O and D_2O from which the q number can be determined.[82, 83] This technique is appropriate to use for protein bound complexes and can be performed with µM concentrations of complex. Alternatively, the Dy^{3+} induced shift of $H_2{}^{17}O$ NMR was a method reported by Peters and co-workers which uses the directly proportional relationship between the Dy^{3+} shift and the q number.[84] This technique requires samples with high concentration (≥ 10 mM) and the need to synthesise a Dy^{3+} derivative (in addition to the Gd^{3+} complex) which can be considered as a significant drawback. One procedure that does not require the use of a surrogate complex is ^1H ENDOR spectroscopy.[85] In ENDOR, q is determined through measurements in both D_2O and H_2O and comparing the difference in intensities, and is applicable to protein bound complexes.[86]

1.4.4 Water/proton residence times (τ_m)

The residence time of inner-sphere water molecules and the rate at which they exchange with the bulk solvent ($K_{ex} = 1/\tau_m$) are extremely important parameters affecting relaxivity and are determined from high field measurements of variable temperature ^{17}O NMR transverse relaxation rates.[3, 6, 86-88] Although it has been argued as the most important parameter, it is often overlooked in the design of CAs with the modulation of the hydration number and complex rotational correlation times being

favoured.[87] This is possibly due to the fact that these parameters are easier to measure and predict compared to water exchange. In order to achieve the maximum possible relaxivity for a specific MRI CA, the coordinated water must be rapidly exchanging with the bulk water to efficiently relax the water protons, although this exchange rate must be in an appropriate range when other parameters are optimised.[3, 15, 87] If the residence time is too short (< 1 ns), the relaxivity is limited due to the coordinated water molecule dissociating from the paramagnetic centre too quickly to become fully relaxed. On the other hand, CAs with water residence times which are too long (> 1 μs) suffer limitations in relaxivity because fewer water molecules from the bulk solvent are able to reach the inner-sphere and become relaxed.

The first generation of GBCAs were found to have slower than expected water exchange rates that followed a dissociative mechanism.[89-92] The effects of the slower water exchange rates become more pronounced upon the coupling of low molecular weight gadolinium complexes to macromolecules with slower rotational correlation times.[3, 87] Additionally, the molecular design of each complex can significantly alter the exchange rates, for example by replacing acetate arms with amides such as in the case of DTPA and DTPA-BMA, the water residence times differ significantly (300 ns and 2222 ns respectively). The effects of this difference are emphasised when conjugated to macromolecules, where the inner-sphere r_1 limit of DTPA and DTPA-BMA would be ~45 mM^{-1} s^{-1} and ~8 mM^{-1} s^{-1} respectively. Furthermore, replacing acetate arms with phosphonates results in an increase in the water exchange rate due to an increase in the steric bulk of the complex (valid for complexes with dissociative water exchange mechanisms).[3, 93]

Generally ligands based on polyazapolycarboxylate scaffolds such as DOTA display suboptimal water exchange rates.[87] Systems based on HOPO, PCP2A and AAZTA provide water exchange rates which are closer to optimal values, which in addition to higher q, gives higher r_1 values.[70, 71, 78, 80, 94-97] Furthermore, prototropic exchange between the protons of the bound inner-sphere water molecule and the bulk is an additional phenomenon which can lead to increases in r_1 in acidic or basic media.[6, 92] Aime et al investigated two systems, $[Gd(DTMA)(H_2O)]^{3+}$ and $[Gd(DTPA)(H_2O)]$ in which they observed this effect and found that at low or high pH values, the relaxivity increased without a change in the overall water exchange rate.[98, 99] The observation was attributed to an acid catalysed ion-pair dissociation leading to water proton exchange in strong acidic conditions, and a base catalysed mechanism of proton exchange in basic media. Furthermore it is important to note that the trend of negatively charged complexes with ligands such as DTPA and DOTA display faster water exchange rates than neutral or positively charged derivatives.[98]

1.4.5 Rotational correlation times (τ_R)

The modulation of the rotational correlation times of GBCAs is a commonly explored method to increase longitudinal relaxivity at clinically relevant fields (0.5-1.5 T).[11, 92, 100] At these magnetic field strengths, an increase in τ_R leads to an increase in relaxivity, which is further realised if the water residence times are optimised to the range of 10-50 ns. Upon moving to higher magnetic fields (2.3-9.4 T), the requirements for the rotational correlation time and water residence times change to more intermediate and shorter values respectively, demonstrating that the magnetic field applied has to be taken into account in the design of GBCAs.[100] Slowing down the rotational motion of GBCAs is achieved through a variety of methods involving the covalent or noncovalent attachment of small Gd^{3+} complexes to larger macromolecules.[15] Some examples of macromolecules used as scaffolds include dendrimers, polymers, micelles, liposomes, proteins and silica.[2, 101-106]

In terms of molecular design, numerous approaches have been investigated including; 1) the use of linear oligomers or macromolecules such as dendrimers; 2) the positioning of Gd^{3+} at the barycentre of a molecule; 3) exploiting self-assembly systems and, 4) through the use of targeting groups to anchor GBCAs to macromolecules.[3, 100]

The relaxivities of the linear oligomer systems were reported to be lower than expected because of anisotropic rotation due to fast rotation along the short axis of the molecule. A modified dextran polymer with GdDO3A-monoamide complexes is one example of a linear oligomer investigated.[3, 100, 107] Despite achieving a high MW (52 kDa), the relaxivity of this macromolecule was reported to be lower than expected, 10.6 $mM^{-1}s^{-1}$ measured at 37 °C and 20 MHz. Additional examples of linear oligomer systems display similar relaxivities, all of which are significantly lower than expected due to internal flexibility.[3, 6, 108-112]

The use of dendrimeric scaffolds for the attachment of GBCAs gave higher relaxivities than the related linear oligomers. This is due to a more isotropic rotation in the dendrimeric species which emphasises the effect of increased molecular weight. Conjugating the same GdDO3A-monoamide chelate to a lysine-based dendrimeric system revealed higher relaxivities under similar conditions (16.5 mM^{-1} s^{-1}, 40 °C, 0.47 T).[3, 62, 100, 113] Although the relaxivity achieved in this system was higher than that of the corresponding linear analogue, this was also lower than theoretically predicted. Further investigations into several PAMAM dendrimeric systems with GBCAs; DTTAP, EPTPA, DO3AP, DO3A-monoamide and DO3Apy exhibited similarly lower relaxivities than anticipated according to simulated values.[100, 101, 114-116] Although many of these dendrimeric systems varied structurally, and in terms of charges and water exchange rates; the limited relaxivities are derived from the high flexibility and internal motion of the Gd^{3+} complex or the PAMAM backbone (for neutrally charged

conjugates).[100] In order to realise the full potential of these systems, careful attention to optimising the rigidity of the complex and the dendrimer as well as fine tuning the water exchange rates of the system are neccessary.

Alternatively, optimisation of τ_R was explored through the use of self-assembly systems. Metal templates based on transition metal ions as the scaffold were investigated as self-assembly platforms for q = 1 and q = 2 systems, affording rigid heteropolymetallic assemblies with longer correlation times.[117-119] Specifically, Livramento and co-workers developed a system in which they applied this principle through a bipyridyl ligand functionalised with two Gd^{3+} complexes.[120] By introducing Fe^{2+}, three bipyridyl ligands were able to coordinate to the Fe^{2+} centre forming an octahedral geometry which resulted in a higher relaxivity of 33.6 mM^{-1} s^{-1}. This type of approach has also been followed for HOPO ligands, leading to increases in relaxivity.[121]

Particle-based self-assemblies using GBCAs with long alkyl chains to form macromolecular structures such as perfluorocarbon emulsions and liposomes provided platforms with slower rotational correlation times, high molecular weights, larger sizes, a vast number of Gd^{3+} ions per particle and a platform for further functionalisation with moieties for targeted imaging.[3, 122, 123] Despite these advantages, the size of these constructs limits their applicability to vascular targets.[3] A similar approach capable of providing a reduction in internal motion in addition to a high Gd^{3+} payload was investigated through the use of Gd^{3+} complexes in a multimeric system. [3, 124] A discrete number of bound complexes were anchored to a target protein through the use of a targeting vector. Any limitations in relaxivity from fast internal motion could be mitigated by introducing a second targeting group, thus providing increased rigidity and subsequently providing a higher relaxivity.[3, 125]

All of the previously described approaches to modulating the rotational correlation time of a given GBCA have involved the formation of a species with multiple Gd^{3+} centres. Optimisation of the rotational correlation times of GBCAs with only one Gd^{3+} centre have also been examined via placing Gd^{3+} at the barycentre of the molecule.[3, 126] This is demonstrated in gadomelitol (or Vistarem), which consists of a GdDOTA scaffold with four large hydrophilic moieties attached to each α-carbon of the acetate arms. The control in rotational correlation and subsequent high r_1 relaxivity (39.0 mM^{-1} s^{-1}, 37 °C, 0.47 T) is attributed to the lack of independent rotation of the Gd-H_{water} vector. In this case, the rotational correlation times can be further influenced by altering the size of the bulky hydrophilic substituents around the macrocycle.[3, 100, 127]

In order to achieve greater selectivity, methods such as RIME have been employed.[128, 129] Selective target signal enhancement relative to the background is achieved through the accumulation of

GBCAs at a specific site through the use of a targeting moiety, resulting in an increase in relaxivity. For non-covalent interactions, GBCAs capable of reversibly interacting with HSA and supramolecular species such as CDs have been developed.[3, 6, 100, 108-110, 130-134] Monomeric units containing hydrophobic substituents with a high affinity for larger macromolecular species are suitable for this type of approach. MS-325 (Vasovist®) and MultiHance® are two examples of commercially available GBCAs with hydrophobic moieties (Figure 5). Prior to HSA addition the relaxivity of MS-325 is 5 mM^{-1} s^{-1}, this increases to 40 mM^{-1} s^{-1} upon HSA binding (20 MHz, 37 °C).[105, 135] Another instance of a HSA-binding GBCA with high relaxivity is a C_{17} derivative of GdAAZTA which exists as a q = 2 complex with a short water exchange rate. At concentrations below the critical micellar concentration this compound displays high affinity for HSA ($K_a = 2.4 \times 10^4$ M^{-1}) giving a relaxivity of 84 mM^{-1} s^{-1}.[100, 136] For CDs, the hydrophobic moieties of the GBCA enter the CD which largely reduces the molecular tumbling leading to increases in relaxivity.

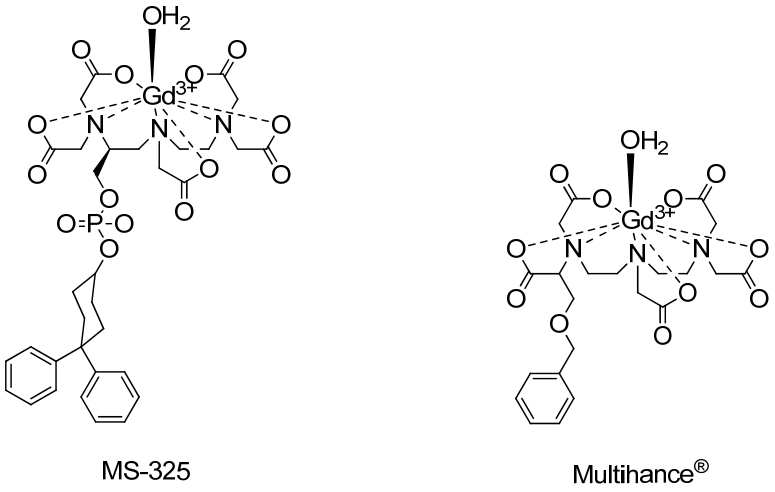

Figure 5. Commerically available GBCAs with hydrophobic moieties.

1.5 Smart contrast agents (SCAs)

Molecular imaging is a research field aimed at monitoring and characterising processes that occur on a molecular or cellular level.[137, 138] In a move away from conventional diagnostic imaging using nonspecific GBCAs, there was great interest and desire in developing fundamental understandings of biological and pathological events rather than their final effects. While the major application of molecular imaging is to understand the underlying abnormalities in diseased states, additional applications exist, such as being employed as a replacement to invasive research procedures such as histology.[138] As MRI is a particularly attractive imaging modality, much effort has been invested into designing CAs capable of changing their MR properties upon a specific change in their

microenvironment.[137, 139, 140] These changes will arise due to specific biological or molecular events, therefore enabling the reporting and monitoring of particular events in functional experiments. To date, a large variety of SCAs have been developed capable of responding to a wide range of stimuli.[2, 65, 139, 141-146] While the main focuses have been on monitoring pH changes, enzyme activity and changes in cation concentration; probes responsive to small biomolecules,[144, 147-149] temperature fluctuations,[150-152] glucose concentrations, oxygen partial pressure,[153, 154] singlet oxygen,[155] hypoxic conditions[156] and light[157, 158] have also been developed.[2, 139, 142] The GBCAs utilised as SCAs are usually based on the same macrocyclic polyazapolycarboxylate based organic scaffolds that were previously described for conventional nonspecific GBCAs, although transition metal complexes and supramolecular assemblies are also of interest. As previously mentioned, in order to be considered as a SCA, the complexes must be responsive to stimuli which induce a change in their MR properties. The change in properties inducing this alteration are dependent on the specific contrast mechanism in which the SCA operates, namely either T_1, T_2, hyperpolarised, fluorinated or paraCEST mechanisms.[137, 159] Here, I will briefly describe the requirements for T_1 and T_2 SCAs.

Both T_1 and T_2 SCAs are affected by parameters which were described in the previous sections. When designing a T_1-weighted SCA, there must be a change in one of: a) hydration number; b) rotational correlation time; c) water exchange rate; or d) the electron spin relaxation times. For most SCAs, changes in the reorientational correlation times and hydration numbers are the mechanisms of MR signal alteration.[138] At low magnetic fields, changes in the rotational correlation times of the complex were the most dominant, however this is strongly dependent on the magnetic field. With the development of high and ultra-high field MR scanners (4.7 – 14.1 T), the effects of rotational correlation time on T_1 diminish and the modulation of q and the water exchange rate become more relevant.[137, 138] As alterations in the water exchange rate are difficult to predict, the predominant mechanism responsible for changes in relaxivity for SCAs at high magnetic fields is the change in hydration state of the complex. For T_2-weighted SCAs, size change is the main factor related to an increase in r_2, which is additionally proportional to an increase in magnetic field. The general design of q-based SCAs requires three key components, namely, the MR reporting unit, a bioresponsive moiety and a linker which combines the two (Figure 6).[139, 160] Prior to activation, the bioresponsive moiety is usually positioned in a way to block water access to the Gd^{3+} centre. This is usually through the weak binding of a functional group from the bioresponsive unit to the metal centre giving a $q = 0$ state. Upon bioactivation, the coordination environment of the Gd^{3+} chelate will change due to the dissociation of the bioresponsive unit from the Gd^{3+} centre, consequently allowing water access to the inner sphere of Gd^{3+} ion, which subsequently increases the inner-sphere relaxivity.

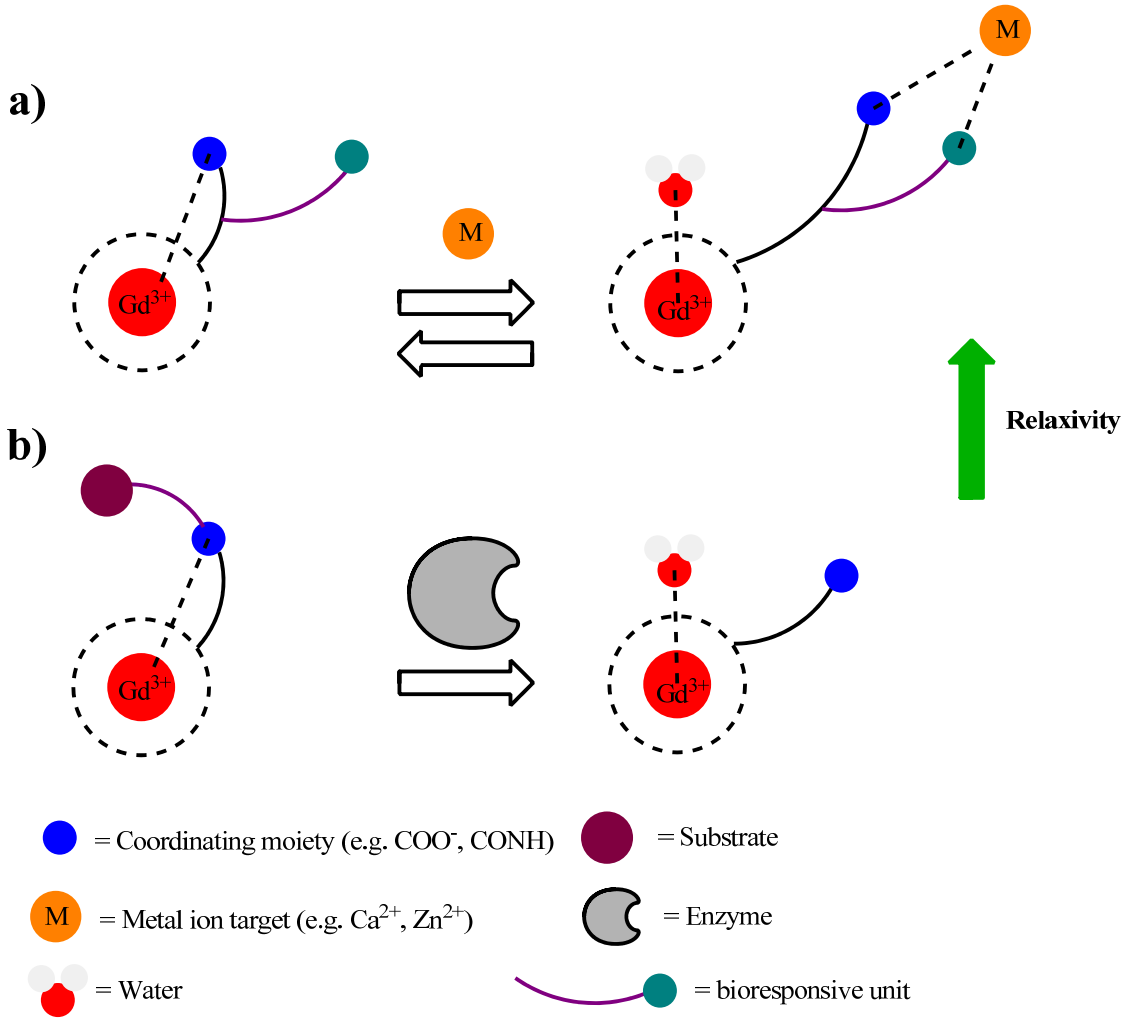

Figure 6. Mechanism of action of *q*-based SCAs. (a) Reversible (metal ion responsive) and (b) irreversible (enzyme responsive) variations.

In cation-responsive probes, the bioresponsive domain will have a high affinity for the target analyte which facilitates this structural rearrangement. At lower magnetic fields, SCAs have been developed which are responsive through the modulation of their rotational correlation times. In this approach these SCAs experience an increase in molecular weight upon activation leading to an increase in the overall rotational correlation time and consequently an increase in relaxivity.[139, 160] This increase in τ_R can be achieved following two different methods: 1) through self-assembly or 2) through binding to large molecules such as proteins (Figure 7a and b respectively).

Additional mechanisms involving, for example, paraCEST CAs have also been utilised in the development of bioresponsive CAs, although they will not be discussed further here. Ultimately, in order to achieve higher sensitivities for *q*- and τ_R-based bioresponsive MR CAs the difference in their relaxivities prior to and after bioactivation should be maximised.

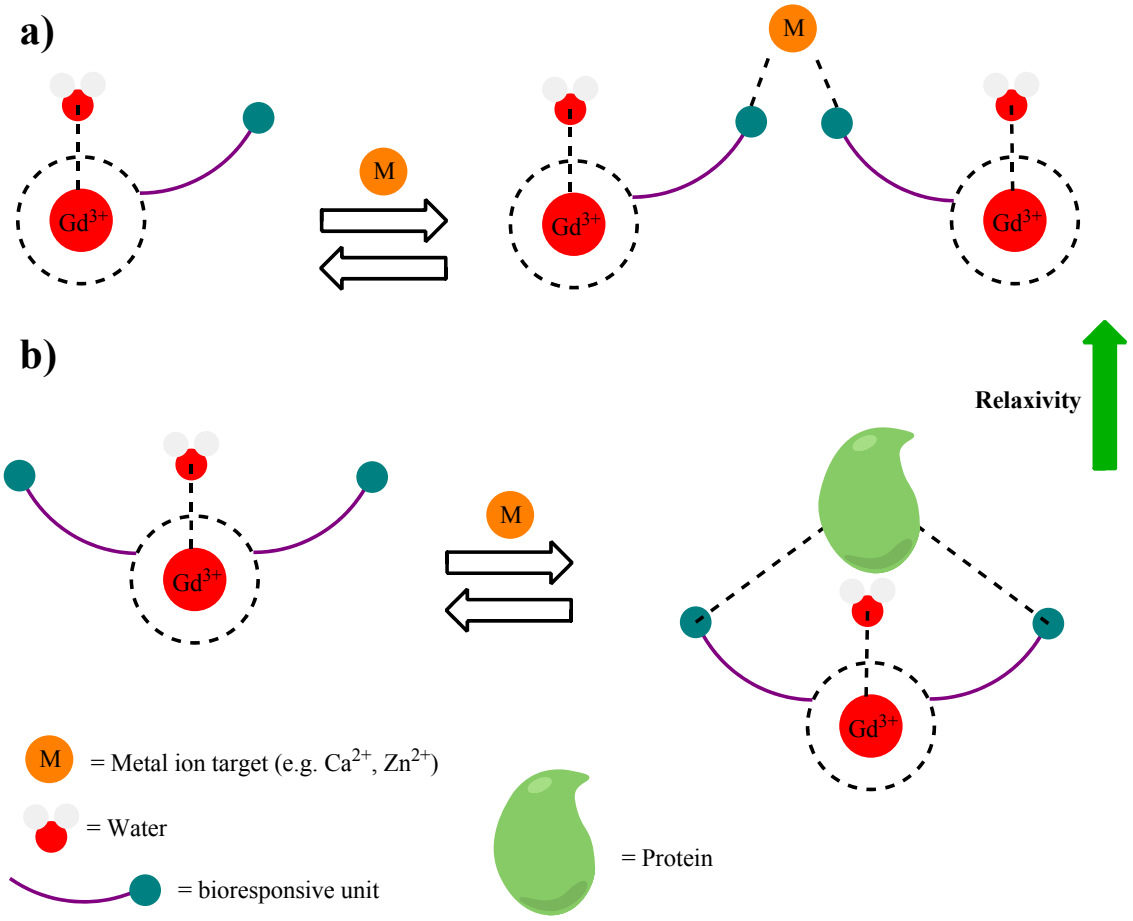

Figure 7. Mechanism of τ_R-based SCAs. (a) dimer formation. (b) Protein binding.

1.5.1 Cation-responsive SCAs

Cations such as Ca^{2+}, Zn^{2+}, Fe^{2+} and Cu^{2+} are biologically relevant species involved in numerous essential processes in living organisms.[161] Proper regulation of these ions is vital for healthy function with irregularities leading to certain disorders such as Alzheimer's and Parkinson's diseases.[160] Therefore the ability to monitor cation concentration changes would be extremely beneficial. One major requirement in the development of SCAs is the inclusion of a chelate capable of selectively binding the metal ion of interest.[141] This aspect is crucial due to the high concentrations of certain ions such as Mg^{2+} and Na^{+} which could bind and deliver inaccurate results. A number of cation-responsive SCAs have been developed and will be described in the following section.[141, 143, 146]

1.5.1.1 Ca-responsive SCAs

Ca^{2+} has received a lot of attention due to its critical involvement in almost all cellular processes, for example in maintaining membrane potentials through concentration fluctuations.[137, 145, 162, 163]

Irregular fluctuations in both intra- and extracellular Ca^{2+} can lead to a number of pathologies such as hypoglycemia, seizures and ischemia.[138, 164] Furthermore, Ca^{2+} plays a role in neurological disorders such as Parkinson disease,[165] Huntington disease[166] and schizophrenia.[138, 167, 168] Given its biological significance, various methods have been employed to monitor Ca^{2+} changes, namely, optical imaging with Ca^{2+}-sensitive fluorescent dyes,[169, 170] and the use of Mn^{2+}.[138, 171, 172] Collectively, these methodologies have provided significant insights into Ca^{2+} fluctuations and neural activity, however they also carry a series of drawbacks. Regarding optical methods, limitations arise due to the insufficient depth penetration caused by light scattering and tissue absorption.[138, 173] Mn^{2+} has been utilised as a mimic of Ca^{2+}, relying on the accumulation of paramagnetic Mn^{2+} which provides an increase in signal intensity.[138, 171, 172] Drawbacks associated with this technique arise from the requirement of a significantly high concentration of Mn^{2+} to produce signal in the detectable range, which can lead to toxic effects. When discussing in terms of neural activity, BOLD fMRI is the mainstay in neuroimaging. However, this does not directly measure Ca^{2+} changes and instead measures brain activity indirectly with signal changes arising from a combination of factors such as blood volume, cerebral blood flow and oxygenation.[174, 175] In addition, the vascular origin of the BOLD signal provides physiological limitations.[176] Taking this into account, MRI with Ca^{2+}-responsive SCAs is an alternative method for direct Ca^{2+} visualisation which provides all the advantages of the MRI technique and specificity through the use of SCAs which selectively target Ca^{2+} (Figure 8).[139]

The first Ca^{2+}-responsive MRI SCA, DOPTA-Gd (**Ca-1**), was developed by Meade and co-workers.[177, 178] This was a bismacrocyclic construct composed of a modified BAPTA bound to two DO3A macrocyclic chelates. The initial relaxivity was 3.26 mM^{-1} s^{-1} and increased by 80 % to 5.76 mM^{-1} s^{-1} upon the addition of Ca^{2+}. Mechanistically, this is achieved via an increase in hydration number upon dissociation of the iminodiacetate arms of the BAPTA moiety from the Gd^{3+} centre to preferentially coordinate Ca^{2+}. The binding of the modified BAPTA unit displayed selectivity for Ca^{2+} over Mg^{2+} in the micromolar range (K_d = 0.96 µM) making it suitable for monitoring intracellular Ca^{2+} fluctuations. An ethyl ester derivative of Gd-DOPTA was prepared where cell internalisation was achieved *in vitro*, enabling intracellular Ca^{2+} monitoring.[173] Retention of the ethyl esters increased the lipophilicity and cell permeability of the CA. Upon internalisation, the esterases in the cell cleaved the ethyl esters and allowed Ca^{2+} binding, therefore leading to increases in relaxivity. Cell internalisation in the off-state allowed for discrimination of intracellular Ca^{2+} over extracellular Ca^{2+}.

More recently, Barandov *et al.*, reported a manganese-based MRI contrast agent suitable for monitoring intracellular calcium.[179] Through the combination of a cell-permeable phenylenediamido Mn^{3+} complex and a BAPTA-based Ca^{2+} chelator (**Ca-2**), a probe was developed which could monitor

intracellular Ca^{2+} changes *in vivo*. Although the initial work concerning monitoring intracellular Ca^{2+} was ground-breaking, and approaches to this area are still being investigated, the issue of monitoring intracellular Ca^{2+} remains problematic.[137, 138] The low sensitivity of MRI along with the need to deliver the SCA across a cell membrane poses major challenges in the future development of intracellular probes.

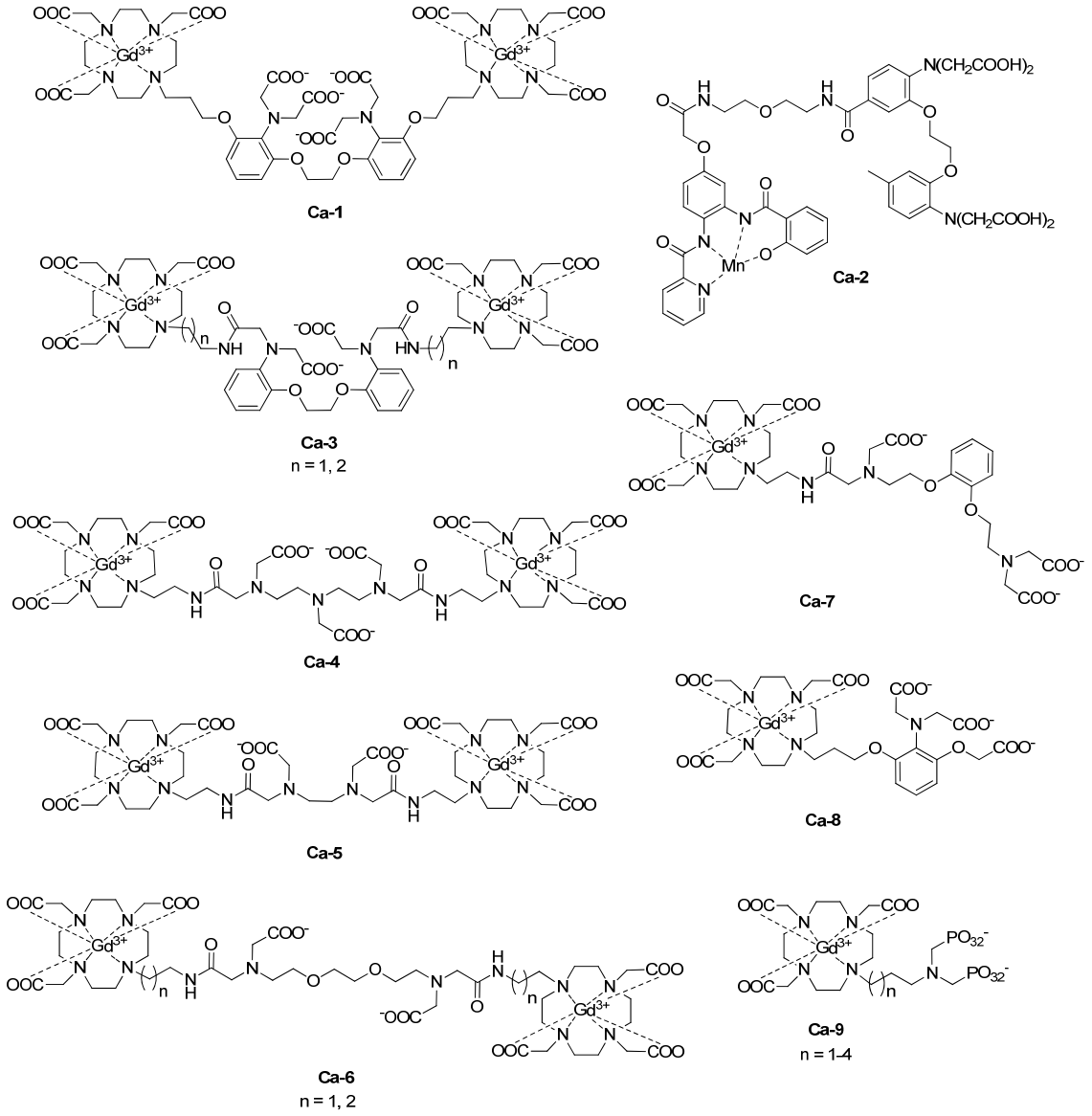

Figure 8. Examples of Ca^{2+} responsive SCAs.

With these limitations in mind, the monitoring of extracellular Ca^{2+} presented as a more ideal target. Upon intense stimulation, significant fluctuations of extracellular Ca^{2+} in the order of 30-35 % are observed (1.2-0.8 mM). This concentration is in a more reasonable range for MR applications. When targeting extracellular Ca^{2+}, the metal-ion binding moiety must have a lower affinity than that for

intracellular applications and be suitable for the concentrations of Ca^{2+} present in the extracellular space.[141] The development of mono- and bismacrocyclic systems with a variety of Ca^{2+} chelating units such as BAPTA-bisamide,[180] DTPA, EDTA, and EGTA (**Ca-3-8**) have all been reported.[141, 181-183] Each system exhibited a lower affinity for Ca^{2+}, although the relaxivity enhancements were modest (10 – 32 % for the BAPTA-bisamide, EDTA and DTPA derivatives). Additionally, variations in ligand design altered the coordination environment and therefore the selectivity for Ca^{2+} over Mg^{2+}. This was demonstrated when DTPA (**Ca-4**) was employed as the bioresponsive moiety (three carboxylates vs two carboxylates for EDTA (**Ca-5**), EGTA (**Ca-6**), BAPTA-bisamide (**Ca-3**)). EGTA-derivatives (**Ca-6**) developed in our group were found to give the largest changes in relaxivity.[137]

Two bismacrocyclic SCAs composed of two DO3A units bound to an EGTA derivative via either an ethylene or propylene linker exhibited increases in relaxivity of 69 % and 83 % per Gd^{3+} respectively in a buffered medium.[184] The presence of two Gd^{3+} ions results in a doubling of signal amplification relative to the monomacrocyclic analogues. Further investigations were carried out to determine the suitability of these SCAs to monitor Ca^{2+} fluctuations in biologically relevant media. For this, the responsivity of the SCA in a more complex DMEM-F-12 medium with a GIBCO N-2 supplement was evaluated. This system was chosen as a close approximation to the brain extracellular medium. Relaxometric responses of approximately 50 % were observed for both SCAs while maintaining similar binding affinities for Ca^{2+} (25-50 μM) making them relevant candidates for further investigations. Finally, phosphonate derivatives have also been examined as Ca-responsive SCAs.[183] In this case, Ca^{2+} coordination led to aggregation resulting in larger species which displayed a drop in relaxivity due to a decrease in *q*. In terms of tracking Ca^{2+} fluctuations *in vivo*, these compounds were envisaged to be useful as their r_1 relaxivity would increase upon a decrease in $[Ca^{2+}]$, which occurs during neuronal activation. However, during initial *in vivo* studies, the anticipated functional signal was not detected.[185] This was postulated to be due to an insufficient change in r_1 of the complex during stimulation, or its interaction with brain tissue impeding the responsive mechanism.

1.5.1.2 Nano-sized Ca-responsive SCAs

Ideally for *in vivo* experiments, large changes in relaxivity and slow diffusion properties are desired.[137] For monomeric probes the issue of a fast diffusion time limits their capabilities in functional MRI experiments.[185, 186] With this in mind, the research direction of our group turned to developing multimeric or nano-sized SCAs based on similar DO3A-EGTA derived systems previously described. Through this combination, robust changes in relaxivity of the 'small-molecule' species can be retained while also displaying favourable slow *in vivo* diffusion properties. Additionally, the conjugation of multiple monomeric units to each nanoparticle increases the local Gd^{3+}

concentration, amplifying the local signal. Furthermore in many cases, the ability to functionalise these nanosystems with molecules such as fluorescent dyes or targeting moieties provides added versatility.[137, 187] Thus far dendrimers, liposomes and polysiloxane-based nanoparticles have all been exploited as nanoscaffolds for Ca^{2+}-responsive SCAs (Figure 9).[188-191]

Incorporating a modified amphiphilic DO3A-EGTA monomer into liposomes revealed an astonishing increase in relaxivity of 400 % (0.5 T).[190] The slow rotational correlation time of this large molecule is increasingly relevant at low magnetic fields enabling such a colossal change in relaxivity. Further contributions can also be attributed to the increased rigidity of the EGTA component upon binding of Ca^{2+}. Grafting of a DO3A-EGTA isothiocyanate derivative onto polysiloxane-based nanoparticles led to the development of the first MRI probes capable of detecting Ca^{2+} changes *in vivo*.[189] Dendrimeric systems have also been exploited by our group as a biomaterial for developing nanosized MRI probes. Specifically, a G1 PAMAM DSCA provided slower diffusion than the monomeric analogue while maintaining its high relaxivity.[188] Moving towards larger G4 PAMAM dendrimers, dramatic changes in r_2 compared to r_1 were observed, leading to the development of a ratiometric imaging method which enabled rapid image acquisition accompanied by a contrast-to-noise gain which was three times greater than standard imaging sequences. [191] The work conducted in this ratiometric study provided a basis for the project discussed in Chapter 3.

Systems based on SPIO nanoparticles have also been explored as a platform to develop Ca^{2+}-responsive SCAs.[192] Specifically, Atanasijevic *et al* developed a series of Ca^{2+} sensors based on SPIO nanoparticles conjugated to the protein calmodulin. These systems produced variations in the T_2-weighted signal due to particle aggregation at sub micromolar levels.[193] Moreover, due to their high relaxivity, low concentrations (1 nM) of the nanoparticles are required, enabling easier delivery of the CA and significantly less disruption to the calcium dynamics of the system. Slow Ca^{2+} response times were the major limiting factor of the nanoparticle systems developed in this study, preventing the monitoring of fast dynamic Ca^{2+} fluctuations *in vivo*.[194] To this end, further modifications to the design of these systems improved the kinetics to achieve responses on the second scale.[195] Most recently, Okada *et al* utilised a mixture of lipid-coated iron oxide nanoparticles and synaptotagmin proteins to develop a Ca^{2+} sensor that targets extracellular Ca^{2+}.[196] Significant increases in r_2 were observed after Ca^{2+} additions which were reversible through the use of EDTA. Importantly, the response time of the probe was in the order of seconds. The application of these nanoparticles was demonstrated *in vivo* giving the first demonstration of the use of a Ca^{2+} responsive SCA in a living brain.[197] Future generations of these types of sensors should aim to possess improved response kinetics and an optimised method of delivery to the brain.

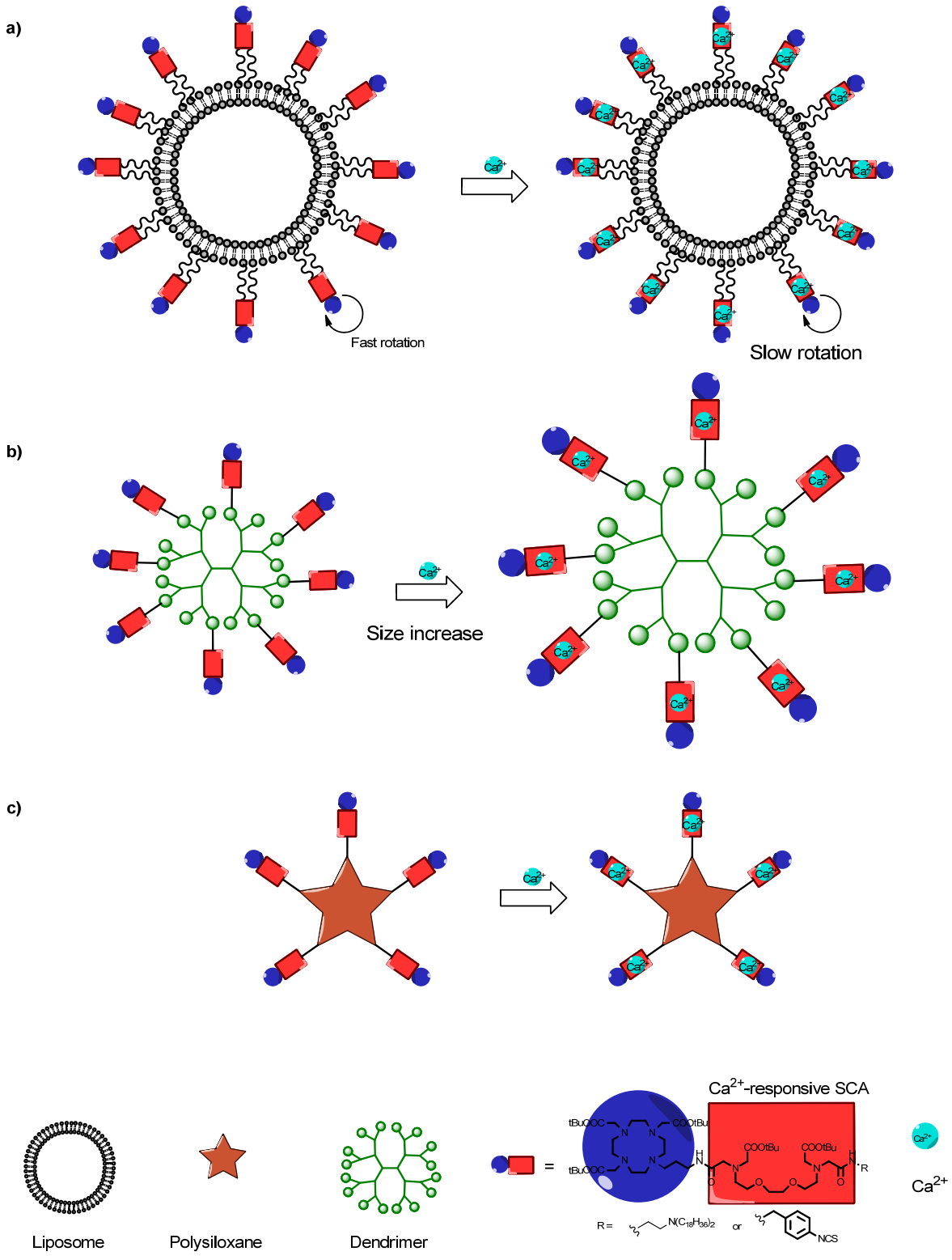

Figure 9. Representations of nanosized Ca^{2+}-responsive SCAs based on a) liposomes, b) dendrimers and c) polysiloxane nanoparticles.

1.5.1.3 Zn-responsive SCAs

Zinc is an important metal ion involved in critical processes in the body.[198] It can be found either in a bound form as part of metalloproteins or as free mobile Zn^{2+}. Static Zn^{2+} accounts for more than 90% of the total Zn^{2+} found in the body playing essential physiological roles in transcription factors, proteins and enzymes.[138] In the brain, Zn^{2+} has a primary role in neuronal transmission with free Zn^{2+} concentrations amounting to about 150 nM in the extracellular brain tissue and up to 1 mM within synaptic nerves.[142, 199] Conditions such as stroke cause 200-300 μM of Zn^{2+} to be released from the synaptic nerve. These irregular fluctuations of mobile Zn^{2+} can have devastating consequences, leading to neuronal cell death and later being linked to neurodegenerative disorders such as Alzheimer's or Parkinson's disease.

The sensing of Zn^{2+} has been pursued with SCAs through *q* modulation, τ_R modulation and the use of paraCEST CAs (Figure 10).[141] Nagano and co-workers designed the first MRI Zn^{2+} sensors, composed of a Gd-DTPA scaffold.[200, 201] The first SCA possessed two dipicolylamine units (**Zn-1**) for Zn^{2+} binding while the second replaced two picolylamines with carboxylates (**Zn-2**). In both cases a decrease in r_1 was observed due to a restriction of water access to the Gd^{3+} centre upon Zn^{2+} binding, giving a turn-off effect. Meade and co-workers developed the Gd-daa-n series, a group of turn-on sensors which operate following the same *q* modulation mechanism described for the Ca^{2+}-responsive Gd-DOPTA series.[202, 203] The iminodiacetate units (**Zn-3**) showed selectivity for Zn^{2+} over Ca^{2+} and Mg^{2+}, although some response to Cu^{2+} was observed. Significant relaxivity changes of 122% were observed for this SCA (r_1 = 2.3 to 5.1 mM^{-1} s^{-1}). Structural studies revealed a dependence of the relaxivity on the linker length between Zn^{2+} binding moiety and the Gd^{3+} centre, with intermediate lengths (4 or 5 carbons) giving the greatest changes in relaxivity.[204] Replacing one acetate with a pyridine moiety gave rise to another selective Zn^{2+} sensor (**Zn-4**) with relaxivity changes of around 100% (r_1 = 3.4 to 6.9 mM^{-1} s^{-1}) upon Zn^{2+} binding.[141, 203]

Our group recently investigated a Zn^{2+} responsive system composed of a DO3A MR reporting unit with a TACN Zn^{2+} recognition moiety (**Zn-5**).[205] Increases in r_1 of 150% (7 T, 25 °C) upon Zn^{2+} addition were observed with excellent selectivity over other biologically relevant ions. Gd-DOTA-diBPEN SCAs (**Zn-6/7**) have been utilised by Sherry *et al*. as τ_R modulated probes.[206] In the absence of Zn^{2+} the SCA has no affinity for HSA. However, upon Zn^{2+} addition, the dipicolylamine groups coordinate Zn^{2+} in a 2:1 (Zn:SCA) ratio which results in a high affinity for HSA, thus increasing the overall rotational correlation time of the complex and the relaxivity (6.6 mM^{-1} s^{-1} to 17.4 mM^{-1} s^{-1}). Analogues with two bis-(3-pyrazolyl) units providing tighter HSA binding have also been reported.[207] paraCEST and

alternate scaffolds such as porphyrins (**Zn-8**) have also been investigated as systems to track Zn^{2+} changes.[208, 209]

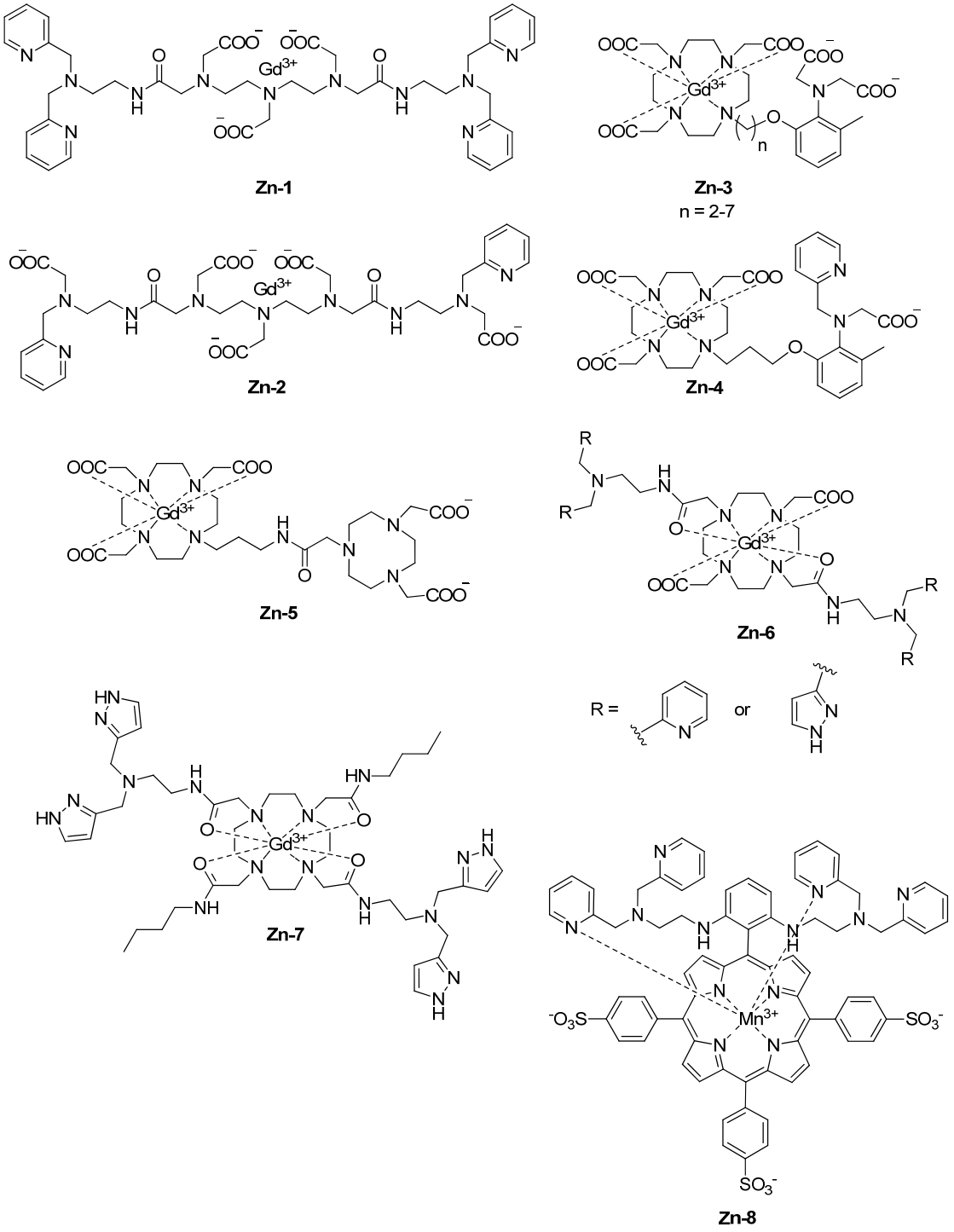

Figure 10. Examples of zinc-responsive SCAs.

1.5.1.4 Cu/Fe-responsive SCAs

A range of bioresponsive probes have been developed to monitor Cu^{+}/Cu^{2+} and Fe^{2+}/Fe^{3+} changes (Figures 11 + 12).[141, 160] In both cases, the different oxidation states of each cation require specific probes for their detection. In the case of Cu^{+}/Cu^{2+}, softer ligands (thioethers) will be more selective for Cu^{+}, while harder ligands (carboxylates) will favour Cu^{2+}. All Cu-based SCAs are *q*-modulated systems. For Cu^{+}, large increases in r_1 are achievable upon Cu^{+} coordination due to the system progressing from a q = 1 state to q = 2. In contrast, Cu^{2+} SCAs are q = 0 complexes in the off state, allowing the interaction of water with the paramagnetic centre upon activation of the probe.

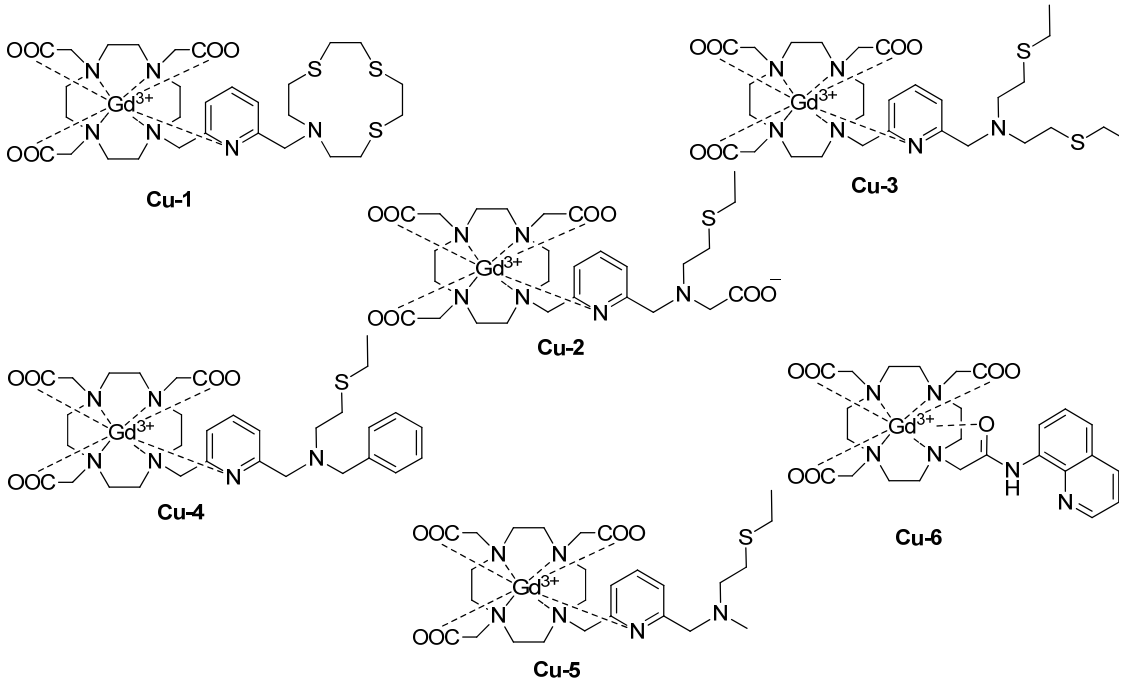

Figure 11. Examples of copper-responsive SCAs.

With regards to the detection of Fe^{2+}/Fe^{3+}, several Gd-Fe heterobimetallic complexes have been reported previously. Although initially intended as CAs for high magnetic field imaging, these systems also act as iron responsive SCAs (Figure 12).[141] Upon the addition of Fe^{2+}/Fe^{3+} the systems will form supramolecular structures with an increased rotational correlation time and therefore an enhanced relaxivity. As is the case for Cu^{+}/Cu^{2+}, the selectivity of Fe^{2+} or Fe^{3+} is determined by the choice of recognition moiety. For Fe^{2+}, chelation with 2,2'-bipyridine (**Fe-1**),[120] phenanthroline (**Fe-2**),[117, 210] or terpyridine (**Fe-3**)[211] ligands have been examined. For Fe^{3+}, salicylic acid (**Fe-4**) and catechol (**Fe-5**) chelators have been utilised.[212, 213]

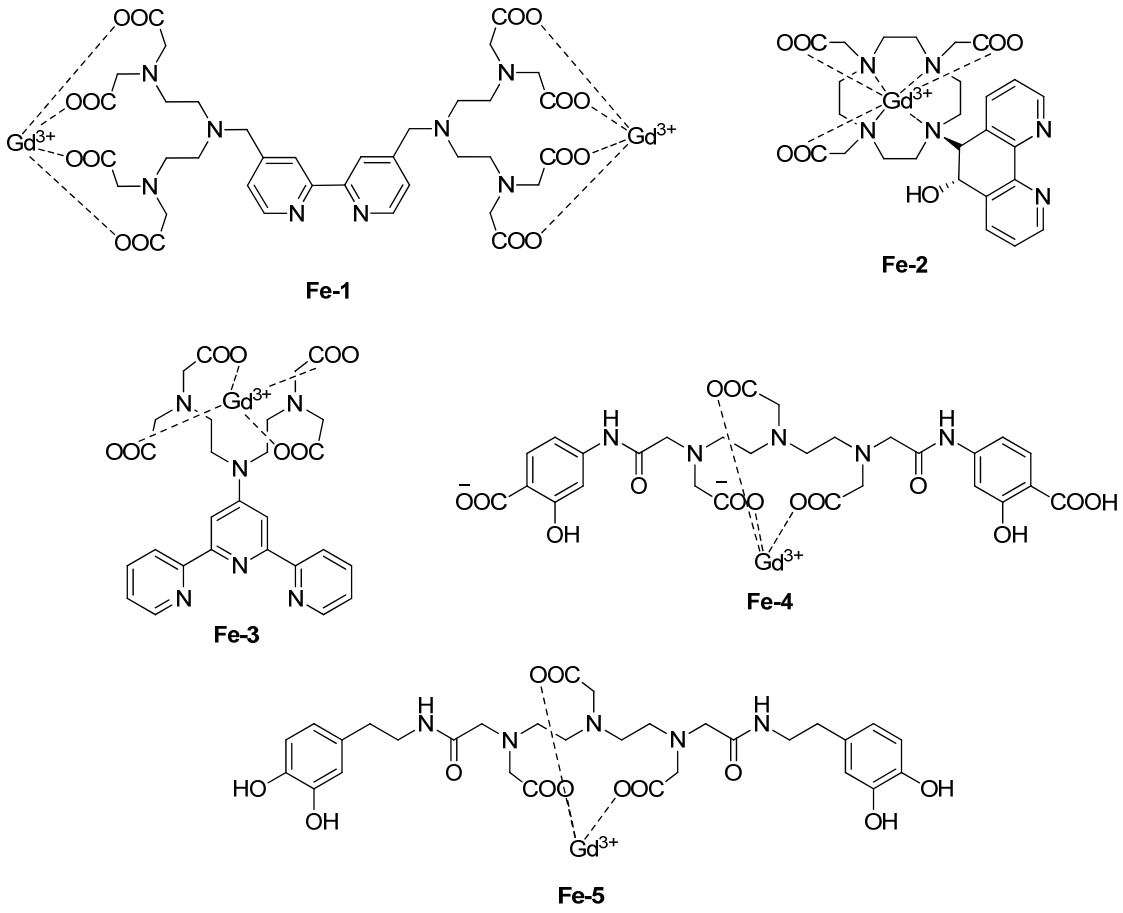

Figure 12. Examples of Iron-responsive SCAs.

1.6 Dendrimers

Dendrimers are nano-sized, monodisperse, spherical, hyperbranched molecules with a well-defined three dimensional structure.[214-216] First discovered by Vogtle et al, this class of compounds were originally coined as 'cascade molecules'.[217] Pioneering research by Denkewalter,[218] Tomalia,[219] and Newkome further explored the synthesis of these complex molecules, which are now described by the term 'dendrimer'.[220] The name is derived from the Greek words *dendron* and *meros* meaning 'tree' and 'part' respectively, describing the structural organisation of the molecule.[216] The arrangement of a dendrimer can be split into three components (Figure 13): a) the core, b) the interior layers (also known as generations) and c) an outer surface composed of many functional groups (amine, carboxyl and alcohol groups). The central core is made up of a group of atoms which are connected to branching units. The number of layers of branching units is described as the number of generations, e.g. a core with two layers of branching units is referred to as a generation two dendrimer or G2. The number of generations influences the number of external surface functional groups on the dendrimer; G1 has 8 surface groups, G2 – 16, G3 – 32, G4 – 64 etc. With an

increase in generation, comes an increase in both the molecular weight and also the particle diameter.

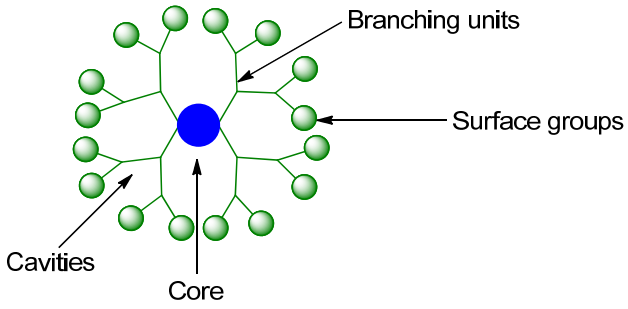

Figure 13. Graphical representation of a dendrimer.

The synthesis of dendrimers has been explored using multiple strategies (Figure 14).[214-216] Namely; 1) divergent growth method,[221] 2) convergent growth method,[222] 3) hypercores and branched monomer growth,[223-225] 4) double exponential growth,[226] 5) lego chemistry,[227, 228] and 6) click chemistry.[229]

In the divergent synthesis, the dendrimer is built from the core outwards with each reaction providing an additional generation.[221] Although seemingly relatively simple, this process is associated with two major problems. Firstly, due to the outwards approach, each generation will have an increasing number of functional groups which are further functionalised. This requires effective conversion of each surface group to circumvent possible errors in the dendrimeric structure.[215, 216]

Additionally, as the number reaction positions increases, the kinetics of the reaction decreases leading to defects in dendrimers of a higher generation.[230] Consequently, the formation of defects, otherwise known as deletion products, increases the difficulty of purification of the mixture. Operating with the reverse methodology, convergent synthesis builds the dendrimer from the outer surface towards the core moiety.[215, 231] By utilising this approach, the potential for defects is circumvented while also increasing the reaction rates. The convergent approach is the method of choice for the synthesis of low generation dendrimers. For higher generations the divergent method is preferred due to a significant decrease in yields reported with convergent synthesis. The hypercores and branched technique is a form of convergent synthesis, with the oligomeric components assembled prior to building the dendrimer, thus enabling higher yields in fewer reaction steps. With double exponential growth, monomers are used in either divergent or convergent synthesis through a trimer species. Rapid synthesis and flexibility in the choice of convergent or divergent approaches are the main advantages of this technique. The lego chemistry strategy allows for the preparation of phosphorus dendrimers with additional functional groups.[215, 216, 227, 228]

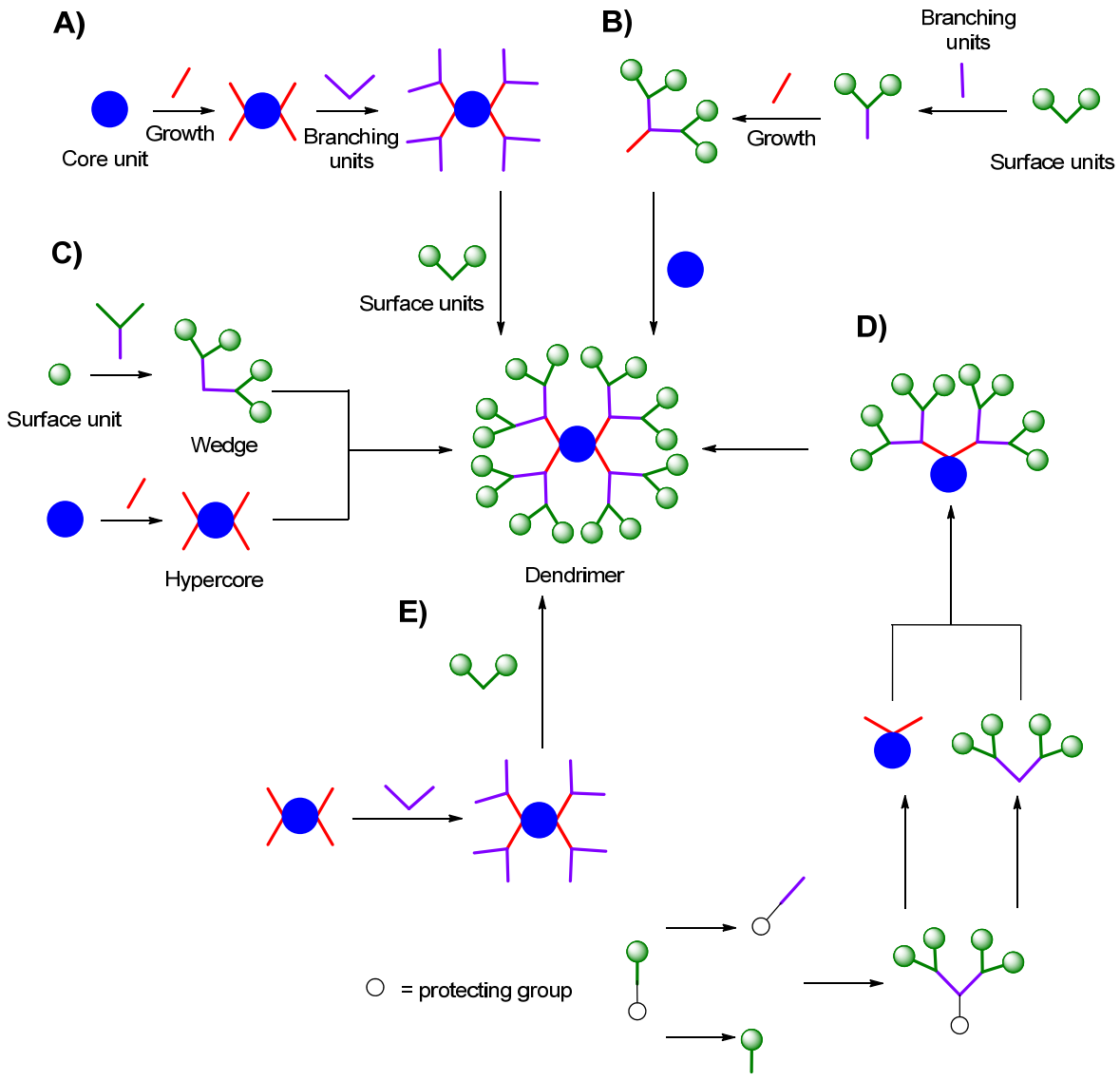

Figure 14. Schematic representation of different dendrimer synthetic methods. A) Divergent growth method, B) Convergent growth method, C) Hypercores and Branched monomers' growth, D) 'Double exponential' growth and E) Lego chemistry.

In this procedure the number of surface functional groups can be expanded from 48 to 250 in one step. Key advantages to this approach are minimal solvent usage, simple purification and the production of environmentally friendly waste products. Finally, click chemistry is an alternate approach applied in the synthesis of dendrimers.[215] High yields with excellent purity are achievable under these conditions, with various types of click chemistry being utilised including; CuAAC, thiol-ene and thiol-yne click reactions.[215]

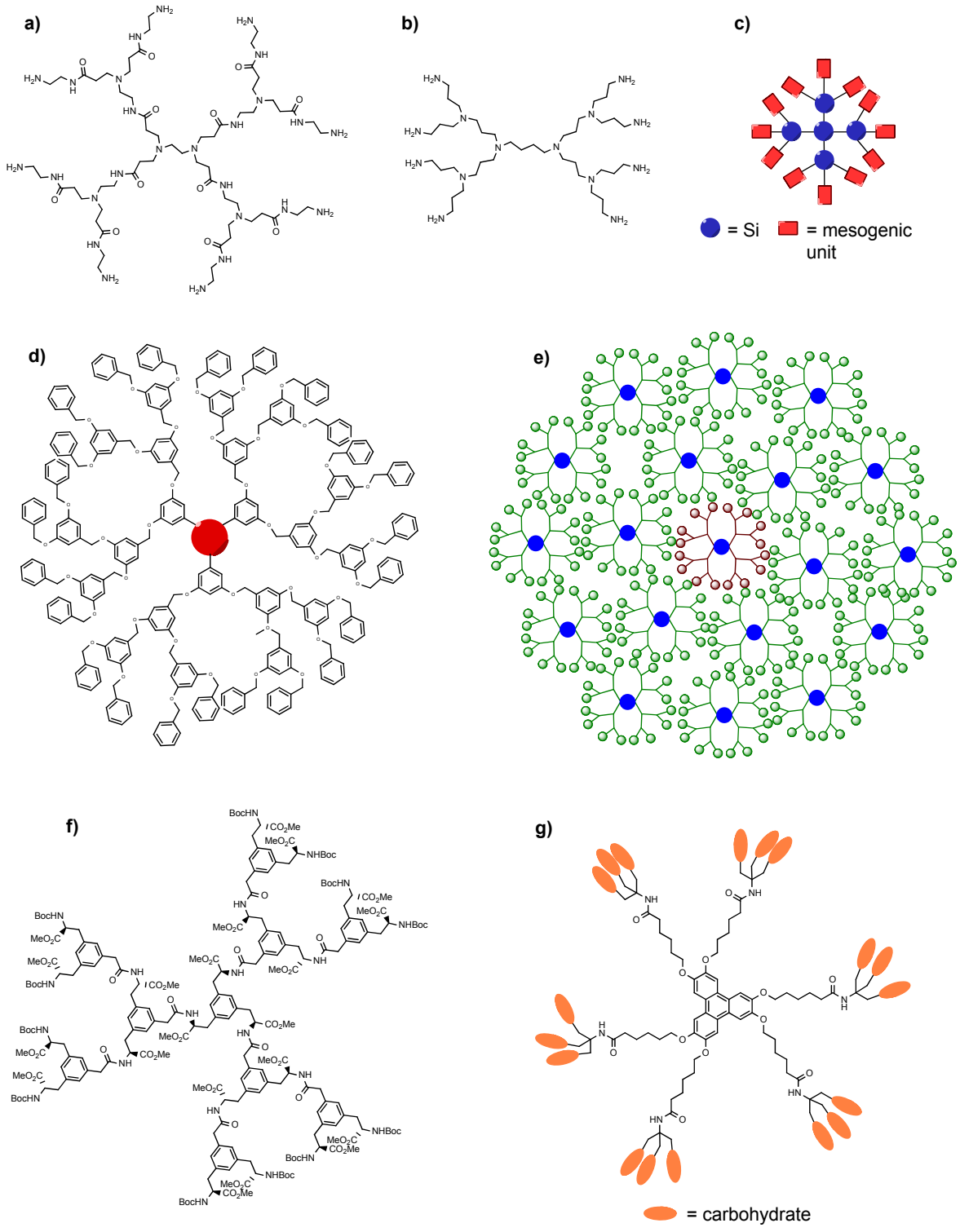

Figure 15. A selection of different dendrimer types discussed in this section. a) PAMAM, b) PPI, c) liquid crystalline, d) Frechet-type, e) tecto, f) chiral and g) glycodendrimers.

Dendrimers became attractive nanomaterials for functional applications due to their unique properties such as monodispersity, a well-defined three dimensional structure, biocompatibility and a highly functionalised surface.[214-216, 230, 232] Various types of dendrimers have been developed for multiple applications (Figure 15). Namely, liquid crystalline,[233-236] PPI,[217] Frechet-type,[237, 238] tecto,[239] chiral,[240] multiple antigen peptide,[241] polyester,[242] poly(amidoamine-organosilicon),[243] hybrid,[244, 245] peptide,[246, 247] glyco,[248] and PAMAM dendrimers.[219] This highly diverse family of compounds has found uses across many applications including; 1) cancer therapy,[249] 2) drug delivery and targeting,[250] 3) antimicrobial applications,[251, 252] 4) therapy (photodynamic and boron neutron capture),[253, 254] 5) as protein mimics,[255] 6) as gene, protein and enzyme delivery agents,[256] and finally 7) in diagnostic and molecular imaging applications.[257, 258] For MRI, PAMAM or PPI dendrimers are generally the most used, although the application of alternative cores such as those based on triazines have also been exploited.[259]

1.6.1 Dendrimeric MRI CAs

Low molecular weight MRI CAs possess limitations in their application due to their fast clearance from vascular circulation.[257] By attaching these to macromolecular scaffolds, such as dendrimers, the rate of diffusion is slowed down due to the size of the system, allowing for time-dependent imaging. Additionally, with the incorporation of many Gd^{3+} chelators to the dendrimeric surface, the overall payload of Gd^{3+} is increased.

At low magnetic fields the relaxivity of dendrimeric systems follows that of other macromolecular systems with a great increase in relaxivity observed due to a slower rotational correlation time.[260] This effect dissipates at higher magnetic fields, although the overall relaxivity per molecule is greater than that of low molecular weight GBCAs due to the higher number of Gd^{3+} chelators attached to the dendrimeric surface.[261] Attaining higher relaxivities is desirable as it allows for the use of lower Gd^{3+} doses which are of particular concern for patients with compromised renal function.

The first example of a dendrimeric CA investigated *in vivo* was carried out by Lauterbur and co-workers, establishing the capabilities of these macromolecular platforms for vascular imaging.[262] Dendrimers functionalised with a Gd^{3+}-DTPA derivative were also developed showing that when at G5 or larger, a 6-8 fold increase in relaxivity could be achieved relative to the monomeric unit at 20-64 MHz and 25 °C.[257] Further investigations with more stable macrocyclic chelators conjugated to the nanoparticle surface were also pursued.[263] One example of a bifunctional DOTA chelator was conjugated to the surface of a range of dendrimers of higher generation.[260] The resulting longitudinal relaxivity per dendrimeric molecule ranged from 30 mM^{-1} s^{-1} to 36 mM^{-1} s^{-1} in the case of

the G = 5 and G = 10 dendrimers. Relating this to the number of conjugated Gd^{3+} chelates, the overall molecular longitudinal relaxivity was found to be 2880 mM^{-1} s^{-1} for the G = 5 dendrimer increasing to a remarkable 66,960 mM^{-1} s^{-1} for the G = 10 dendrimer. In order to achieve sufficiently high relaxivities it is also important that the Gd^{3+} chelates are exposed to the outer surface.[261] This was demonstrated with the comparison of lysine-dendri-grafts and PAMAM dendrimers.[261, 264] In the case of PAMAM dendrimers, all the Gd^{3+} chelates are exposed on the outer surface of the scaffold and therefore interact with water. However, in the case of lysine-dendri-grafts lower relaxivities were observed due to some of the Gd^{3+} units being located internally and therefore not being fully exposed to water. Increasing the temperature resulted in an increase in relaxivity due a change in the flexibility of the molecule and an increased exposure of the Gd^{3+} chelates to water.

One distinct advantage with using dendrimeric systems is the ability to easily alter the properties of the macromolecule for specific applications. Modification of the core, the internal branching units, the external functional groups and the overall size of the macromolecule allow for increased specificity.[265] The size of the dendrimeric species has been shown to have a significant impact on *in vivo* behaviour due to changes in the pharmacokinetics, excretion route, recognition by the reticuloendothelial system and permeability across the vascular wall.[265, 266]

Kobayashi et al synthesised a library of dendrimeric MRI CAs in which they varied the core moiety, dendrimer type, generation number and further surface properties to yield systems with molecular weights ranging from 29 to 3850 kDa and sizes from 3 to 15 nm.[267] The smaller dendrimers (G2-4) showed fast excretion with larger generations being excreted at lower rates. Larger dendrimeric species (G6 and larger) showed minimal leakage from tumour vasculature in comparison to smaller dendrimers which passed more easily into the surrounding tissue. Although larger dendrimers generally show slower clearance rates, by further increasing the size of the dendrimers to that of G9/10 this no longer holds true. Due to the significant size of these molecules they are easily recognised by the reticuloendothelial system which results in rapid clearance. Hydrophilicity is an additional factor that can be easily tuned with the introduction of PEG chains onto the outer surface or through core modifications. The highly tuneable nature of these types of macromolecules allows for molecules to be designed for a vast array of applications such as blood pool, liver, renal function, lymphatic and tumour specific MRI CAs.[268] Furthermore, environmental conditions such as pH and solvent/buffer have been shown to be particularly influential on the hydrodynamic radius depending on the surface functionality, thus further demonstrating the unique variable characteristics of this family of macromolecules.[269, 270] Over recent years, there has been a significant rise in the popularity of dendrimers as a scaffold for application in MRI with paramagnetic T_1 and T_2, superparamagnetic,

CEST (diaCEST and paraCEST) and fluorinated dendrimers being developed.[258] Our group has also readily exploited this method for the development of new Ca^{2+}-responsive SCAs as previously discussed.[137]

1.7 Solid phase synthesis

The solid phase synthetic technique emerged in the early 1960's as a result of pioneering work by Bruce Merrifield, eventually earning him the Nobel Prize in Chemistry in 1984.[271, 272] This technique focused on building a peptide through a series of peptide bond formations on an insoluble resin support.[273-276] The development of this method had great impacts across many fields, enabling the synthesis of more complex peptides/proteins. When compared to standard solution phase chemistry, the solid phase technique boasts a series of unique advantages including; i) the ability to separate compounds in solution from those attached to the solid support by means of washing, ii) the utilisation of excess reagents to drive the reaction, which can then be subsequently washed away, iii) physical losses are minimised, iv) the synthesis of unsymmetrical molecules can be achieved in a more straightforward manner, and v) the process can be automated. However, there are some limitations with the technique. Specifically, any byproducts as a result of incomplete reactions, side reactions or arising from impure reagents can contaminate the final product leading to difficulties in the final purification steps. Additionally, the analytical techniques usually employed for reaction monitoring in solution are not applicable. Instead, a set of qualitative colourimetric tests can be used to assess the completeness of a reaction;[277] or a process in which a small amount of the resin is cleaved and evaluated can be followed.

Commencing from an insoluble support, standard SPPS follows a general process (Figure 16). The first amino acid is coupled through its C-terminal to the N-terminal of the solid support linker. Any side chains of the amino acid are masked by protecting groups which are orthogonal to the protecting groups along the peptide backbone. Then through a series of N-terminal deprotections followed by peptide couplings, the desired peptide sequence is synthesised. At this point, the peptide is cleaved from the solid support and can be purified by methods such as HPLC. The most widely utilised synthetic methods in SPPS are the Fmoc and Boc strategies (Figure 17).

The Boc strategy involves peptides with Boc amino protecting groups which are cleaved with strong acids such as TFA. Resin cleavage protocols also employ harsh conditions such as the use of hydrogen fluoride (HF). Also known as Merrifield SPPS, the Boc strategy was the first form of SPPS utilised and has been efficient in the synthesis of large peptides and proteins. However, due to the

requirement to use HF, which is highly toxic, the popularity of this method has decreased and been replaced by a much milder protocol known as the Fmoc strategy.

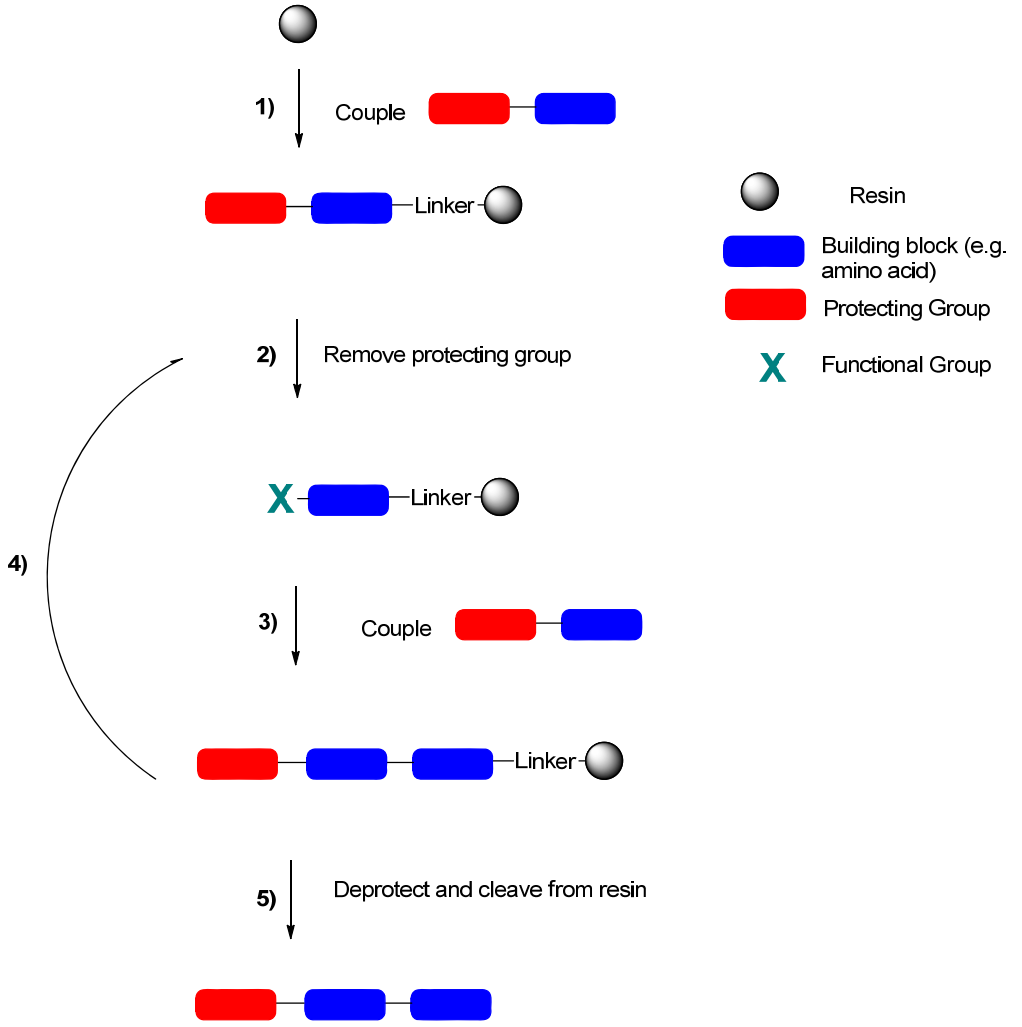

Figure 16. General synthetic process for solid-phase protocols. 1) Coupling of a protected amino acid to the resin. 2) Removal of the amino acid protecting group to reveal the terminal functional group. 3) Coupling of a protected amino acid. 4) Repeat steps 2 and 3 until the desired peptide is synthesised. 5) Deprotection of the peptide unit from the resin.

In the Fmoc method, amines are protected with the Fmoc group which can be deprotected under mild basic conditions (e.g. 20% piperidine in DMF). Before commencing any synthesis, the appropriate resin with linker must be chosen. There have been many resins and linkers developed for SPPS to cater for the vast array of compounds that can be synthesised using this method. Typically polystyrene based resins are used containing 1-2 % divinylbenzene as a cross-linking agent. These are insoluble in all common solvents and usually have sizes between 35-150 microns. One of

the most important factors to consider in SPPS is resin swelling which is highly linked to synthetic efficiency.

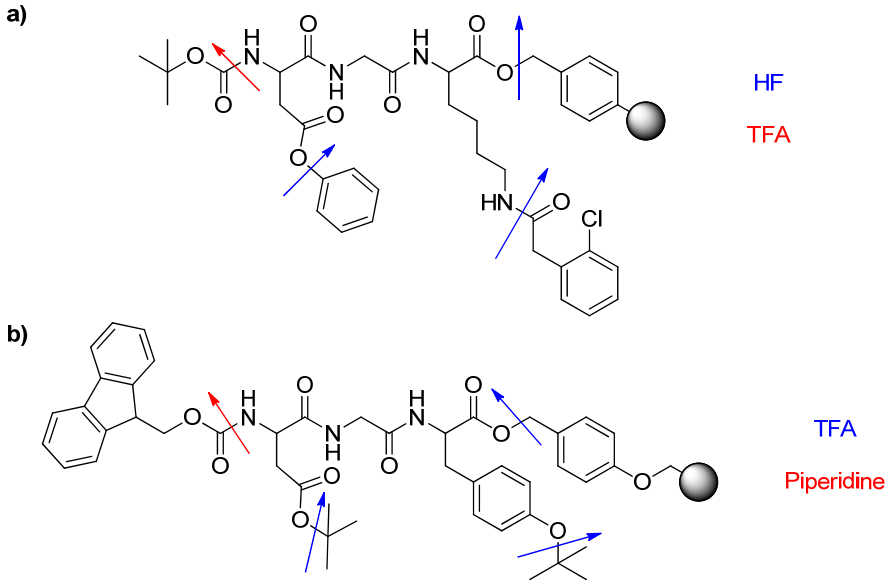

Figure 17. Deprotection conditions for resins and common protecting groups in a) the Boc and b) the Fmoc strategies.

Prior to synthetic procedures, the resin beads must be swollen in an appropriate solvent in order to allow full access of the reagents to the surface functional groups. For typical polystyrene based resins, this swelling is usually most efficient in solvents such as THF or dichloromethane. More recently, resins with PEG chains have been developed for the synthesis of polar compounds in solvents such as water. In order to attach the desired peptide sequence to the PS beads a chemical linker is used. A wide variety of linkers exist and are an important component in SPPS as they determine the cleavage conditions of the peptide from the resin and the C-terminal functional group. In each coupling step, activating agents are used to form more reactive species through activation of the C-terminal. The choice of coupling agents is vast, ranging from those based on carbodiimides such as diisopropylcarbodiimide to aminium/uranium and phosphonium salt based coupling agents. In addition to standard SPPS, which operates in the C to N direction, inverse SPPS (N to C) has also been explored as a method of generating peptides modified at the C-terminal, further expanding the scope of SPPS methodologies.[278, 279]

1.7.1 Solid phase synthesis of MRI CAs

SPPS has been widely utilised in the synthesis of many peptides and small proteins for a variety of applications. In the field of MRI CA development, SPPS has emerged as an alternative technique to

develop peptide-based targeted MRI CAs offering greater specificity and more favourable pharmacokinetic properties.[280] Below are some examples of where SPPS has been exploited so far in the field of MR probe development, ranging from purely synthetic outlooks to molecule screening and development of highly specific imaging probes (Figure 18).

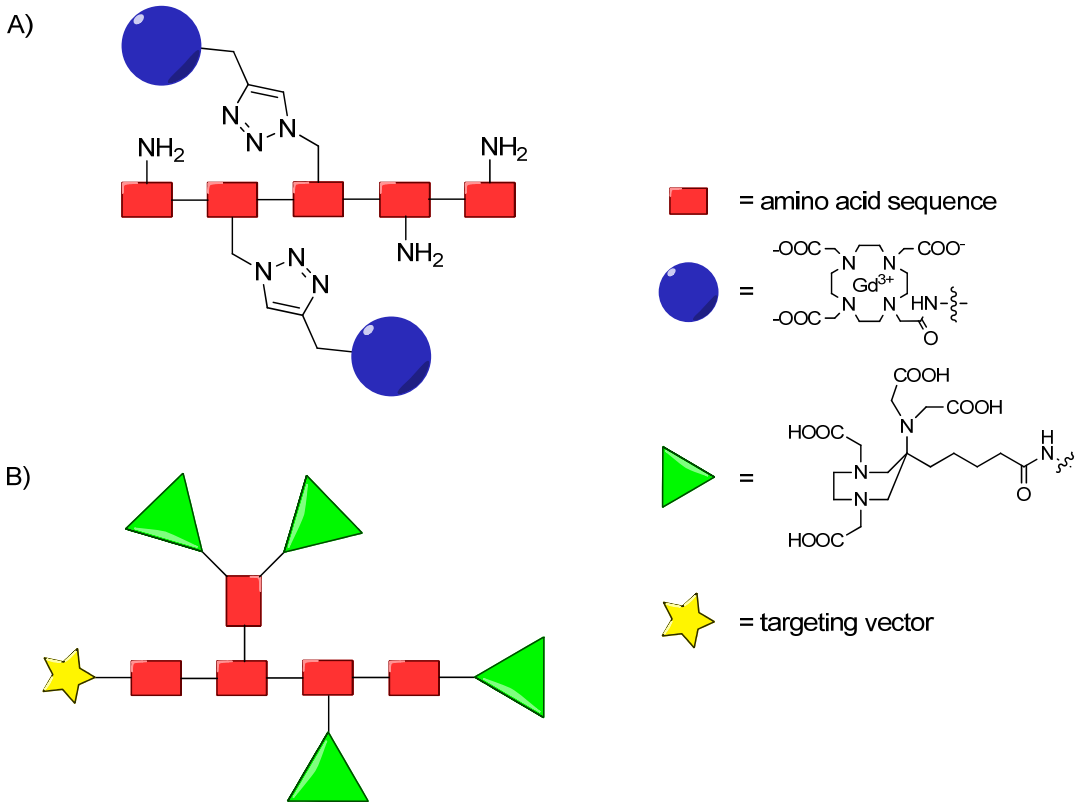

Figure 18. Examples of two MRI CAs built using SPPS techniques. A) Multimeric CA built utilising copper catalysed click chemistry. B) AAZTA tetramer with targeting moiety.[81, 281]

Yoo *et al* synthesised an amine-derivatised DOTA peptide conjugate as a paraCEST MRI CA with high yield and purity.[282, 283] In this set of studies, the DOTA component was coupled via one of the carboxylic acid pendant arms onto the resin using standard Fmoc SPPS conditions. In the first attempt, a Cbz protecting group was utilised for the α-amino group.[282] The Cbz group could be removed under harsh conditions which also resulted in cleavage of the DOTA derivative from the resin. In an attempt to circumvent the reduced final yield, an Fmoc derivative was synthesised allowing for much milder deprotection conditions.[283] Sherry and co-workers developed two DOTA derivatives linked to lysine or phenylalanine using standard solution chemistry.[284] Then through SPPS they synthesised DOTA analogues of the peptide binding sequence for Gal-80 demonstrating that the position of the DOTA moiety strongly influences the binding in peptide-protein systems. This type of screening could have a significant impact in identifying new targeted MRI diagnostic systems.

Probes designed to image mRNA transcription have also been pursued through a peptide system composed of a Gd^{3+}-DOTA complex linked to a peptide nucleic acid and a cell-penetrating peptide through continuous SPPS.[285] The synthesis of libraries of compounds is also possible through combinatorial chemistry. This has been exploited to develop and assess a library of DOTA-tetraamide compounds to determine optimal probe characteristics which increase CEST sensitivity.[286, 287] Here the efficient synthesis of several compounds simultaneously enabled the key properties of efficient CEST agents to be identified in a timely manner.

A recently published article from Tripepi *et al* demonstrated the use of SPPS to build Gd^{3+}-AAZTA tetramers which were used for bioconjugation to targeting vectors.[81] As a proof of concept, a fibrin-binding peptide was targeted and an increase in relaxivity per Gd^{3+} was observed, from 7.1 mM^{-1} s^{-1} (monomer) to 16.4 ± 0.2 mM^{-1} s^{-1} (tetramer) which increased further to 18.5 ± 0.3 mM^{-1} s^{-1} upon conjugation to the fibrin-binding peptide (0.5 T, 25 °C). The application of SPPS in the development of MRI molecular imaging probes has also been demonstrated through the synthesis of a polyadenylic acid targeted multimeric CA.[281] Here a peptide sequence containing azide units was synthesised via standard Fmoc SPPS and a series of GdDOTA complexes with alkyne moieties were attached via CuAAC. The resulting conjugate displayed enhanced relaxivities at 20 MHz and 25 °C compared to the monomeric chelate.

In a very recent article, the development of ^{129}Xe biosensors for HyperCEST was reported using SPPS.[288] The authors report that the use of such a synthetic strategy enables the development of highly sensitive probes capable of labelling and visualising a variety of biological targets which would otherwise be MR-inaccessible *in vivo*.

The development of the solid phase synthetic technique as an alternative to standard solution phase methods has paved the way for the development of a large variety of novel MRI CAs with more favourable pharmacokinetics and specificity. The technique can be used as a platform to build multimeric species through the use of specific building blocks. Also with the use of combinatorial chemistry, large libraries of compounds can be synthesised simultaneously and screened for favourable properties. All of these clear advantages make SPPS a viable alternative synthetic tool in the future development of MRI CAs with ever increasing specificity.

2 Aims of the project

The development of CAs has contributed significantly to the promotion of MRI to be one of the main diagnostic tools utilised in clinics. Further to this, the desire to perform functional imaging has been facilitated through the emergence of SCAs capable of visualising biological processes in a dynamic manner. Previous investigations of parameters modulating relaxivity such as q, τ_R and τ_m have enabled the careful design of such probes which can evaluate a vast array of targets. Aiming towards *in vivo* studies with such compounds, more emphasis is given to improving properties such as diffusion, relaxometric enhancement and specificity to achieve the desired end goals. Specifically, the introduction of targeting moieties can provide improved specificity while the use of nano-sized platforms such as dendrimers can enable higher Gd^{3+} loading and enhanced pharmacokinetic behaviours. Improvements in relaxometric behaviours allow for the detection of targets in lower concentrations or the use of lower doses of CA, which is beneficial regarding the current safety concerns of some GBCAs. The manipulation of such compounds, which are already complex in nature, can be synthetically challenging. Therefore the use of alternate sophisticated methodologies, such as solid phase synthesis has provided a different outlook to what can be synthetically achievable using standard solution phase techniques.

The aim of this work was to combine some of the previously employed strategies utilised in MRI CA development to generate a range of compounds which are undergo significant relaxometric alterations in responsive to fluctuations in $[Ca^{2+}]$ and would thus be applicable for the monitoring of Ca^{2+} *in vivo*. To achieve this, an understanding of the influence of specific structural properties is of paramount importance to provide blueprints for future SCA design. Furthermore, the synthetic difficulties encountered in the production of such compounds should be minimised. Here, a set of studies were performed focusing on these particular aspects. Specifically, a series of dendrimeric and monomeric systems were examined to identify which particular parameters contribute to high relaxometric changes upon Ca^{2+} addition and provide blueprints for future SCA design. As the field moves towards desiring probes of increased specificity and functionality, SPPS was explored as a viable synthetic technique in the pursuit of highly diverse Ca-responsive SCAs to be applied in fMRI investigations.

Previously, a study involving the use of dendrimeric platforms as excellent nanoscaffolds for the grafting of Ca-responsive monomeric units was reported, resulting in the development of an r_2/r_1 ratiometric imaging method. This gave a higher contrast to noise ratio than typical T_1- or T_2-weighted pulse sequences with faster acquisition times. With the desire to further explore the behaviour of these nanosized systems as potential bioresponsive probes, a detailed study was conducted in which

a series of dendrimeric conjugates with varying monomeric units were developed. The synthesised conjugates were then examined as potential T_1 and r_2/r_1 ratiometric bioresponsive MRI probes. Investigating the effects of multiple parameters, such as the type of macrocyclic unit or charge, on the relaxometric behaviours of the conjugates would enable the key structural requirements to be determined. Furthermore, with the significant parameters identified, a blueprint for the future design of Ca-responsive DCAs could be developed, thus aiding in the future development of highly responsive DCAs for *in vivo* functional MR studies (Chapter 3).

The results from the DCA study additionally indicated that the monomeric SCAs attached to the most responsive DCAs were also sensitive to Ca^{2+}. Understanding the relationship between changes in the structure of monomeric SCAs and their relaxometric properties is also of critical importance when aiming to develop future probes either as monomeric SCAs or to evaluate candidates for coupling to nano-scaffolds. Therefore, a deeper structural evaluation of these monomeric SCAs was performed to identify how the linker length between the macrocyclic and bioresponsive moieties impacts the behaviour of the system. With the aid of a series of characterisation techniques, such differences could be assessed and therefore give further insights into how such structural changes would impact on the relaxometric properties of the systems. In addition, insights into the mechanism of action and coordination chemistry of the complex could potentially be further consolidated and aid in the future development of DO3A-EGTA based SCAs for Ca^{2+} tracking *in vivo* (Chapter 4).

Following the previous characterisation studies, focus was turned towards the production of such SCAs with increased diversity, in a more straightforward fashion. Increasing the scope of SCA application, such as in fMRI experiments, requires probes with increased functionality and specificity. Currently, the pathway to such molecules with standard solution phase chemistry is often riddled with difficult and time consuming synthetic and purification procedures. The emergence of solid phase synthesis presented an alternative which has been subsequently exploited in the development of peptide-based MRI CAs as described previously (section 1.7.1). However, reports of SCAs synthesised using the same methods are not common. The use of SPPS as a viable synthetic tool in which to develop Ca-responsive SCAs was therefore examined following a building block style approach. The development of such a methodology would allow for more complex designs to be synthesised and result in probes with increased functionality, which are currently desired to increase the scope of SCA use in functional studies. Initially, the advantage of SPPS to circumvent the arduous synthetic and purification techniques currently employed with these types of compounds was explored. Consequently, the development of such a methodology provided opportunities to develop several highly diverse multifunctional probes (Chapter 5).

After successfully implementing a SPPS method for Ca-responsive SCA production, the attention turned towards developing a targeted Ca-responsive multimeric SCA derivative. Switching from the building block approach, the design of the new molecule was based on a peptide sequence with a specific RGD targeting moiety. The incorporation of 'pre-made' Ca-responsive SCA units resulted in a targeted multimeric probe. The design of this molecule further validates SPPS as a viable synthetic methodology in the realms of Ca-responsive SCA production and opens a new chapter in terms of SCA development. In terms of application, this specific SCA targeted here should demonstrate binding to integrins found on the surface of cells, and thus possess advantageous properties of slower diffusion thus allowing for longer *in vivo* studies. Furthermore, with the flexibility that the SPPS platform offers, this design can be manipulated further in a relatively simple manner and help to simply the access to such elaborate derivatives (Chapter 6).

3 Development of Bioresponsive Dendrimeric MRI Probes

3.1 Introduction

Calcium is an essential metal ion involved in numerous physiological processes in biological systems.[163] The tracking of fluctuations of this ion could prove instrumental in the understanding of various pathological states. With the emergence of fMRI, many biological processes can be dynamically visualised in an unprecedented fashion. Various Ca^{2+}-responsive SCAs have been developed as 'off-on' sensors ranging from 'small-molecule' responsive probes to larger macromolecular systems.[137] The usage of nanosystems aims to increase the Gd^{3+} payload and improve the pharmacokinetics of the SCA. Additionally by utilising a larger scaffold, the diffusion rates will decrease, allowing for fundamental time-dependent studies.

Previous investigations explored the coupling a previously reported Ca^{2+}-responsive monomeric SCA to a G1 and G4 PAMAM dendrimer.[188, 191] In the case of the G4 derivative, a significant change in T_2 compared to T_1 was observed upon the addition of Ca^{2+} along with a significant increase in size. Although surprising, the diameter change could possibly be explained due to the size dependency of dendrimers on their environmental conditions and electrostatic charge.[269, 270] The led to the development of a ratiometric imaging method which provided rapid image acquisition with a high contrast-to-noise ratio by exploiting the T_2/T_1 ratio change of the SCA as a function of $[Ca^{2+}]$.[191] Furthermore, this approach has provided significant insights into the development of an fMRI method that can image dynamic events with exceptionally high temporal resolution.

Following initial study, we were interested in conducting a more detailed investigation into this particular class of DCAs to try and determine the favourable characteristics required to develop a nano-system that can be applied in dynamic fMRI studies. Therefore, we developed a novel series of DCAs each with an identical EGTA-derived Ca^{2+} chelator conjugated to a G4 PAMAM dendrimer.[289] Variation comes through altering the design of the macrocyclic MR reporter motif, which enabled evaluations of a series of molecular characteristics such as charge, type of macrocyclic reporter and linker distance between the MR reporter and Ca^{2+} chelator. Specifically, we wanted to identify which of these characteristics influences the size changing abilities previously observed upon Ca^{2+} chelation, thus potentially determining how to maximise the T_2/T_1 ratio changes.

3.2 Design of DCAs

The design of the novel DCAs in this study was based upon a previously reported dendrimeric system.[188, 191] Specifically, this system was composed of a DO3A MR reporting unit and an EGTA-

derived linker attached to a G4 PAMAM dendrimer. Here we developed five new derivatives which can be split into two distinct groups depending on their MR reporter (Figure 19).

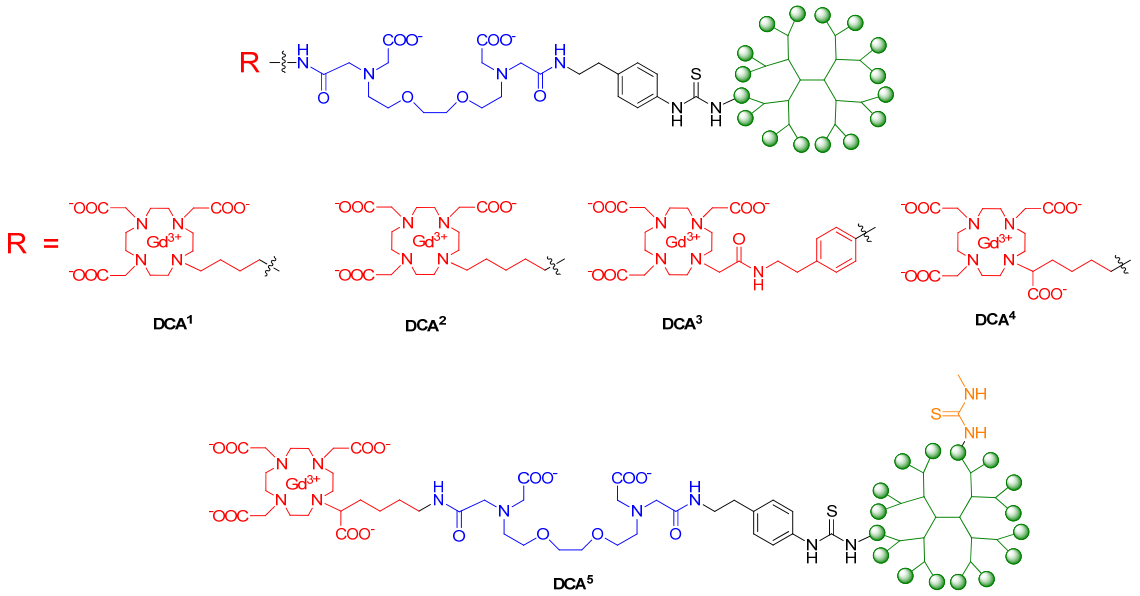

Figure 19. Chemical structures of the synthesised DO3A-, DO3A-monoamide and DOTA-based DCAs. Reproduced with permission from Ref 289. Copyright 2018 American Chemical Society.

The first set possessed a DO3A macrocyclic unit, similar to that of the initially investigated DSCA.[188, 191] The novelty of these conjugates arises from an expansion of the linker units (butyl and pentyl) between the MR reporting macrocycle and the bioresponsive EGTA-derived unit (**DCA**^{1} and **DCA**^{2} respectively). In the second group, the macrocyclic component consists of an organic scaffold with 8 coordination bonds available to envelop Gd^{3+} as opposed to 7 in DO3A units. Specifically, a DO3A-monoamide (**DCA**^{3}) and DOTA type (**DCA**$^{4\text{-}5}$) macrocycle was used. **DCAs**$^{4\text{-}5}$ were composed of the same monomeric units attached to the G4 PAMAM dendrimer. Differentiation was achieved through modifications on the dendrimeric surface itself in the form of a capping procedure of **DCA**^{4} with methyl-thiourea units to yield **DCA**^{5}.

This selection of DCAs allowed for a comprehensive study into the effects of the MR reporter and dendrimer surface functionalisation on the overall behaviour of the system in terms of size changing capabilities and relaxometric behaviour. The use of DO3A MR reporting units gave systems with a neutrally charged macrocycle, a positively charged dendrimeric core and an EGTA unit which is likely to possess a negative charge.[290] Through expanding the linker distance a direct comparison could be made between the performance of each DCA and determine if such a change significantly effects the behaviour of the nano-system. The macrocyclic component of **DCA**^{3} is also neutral in charge; here the difference lies in the coordination geometry of the macrocycle and the effective communication

between the EGTA and MR reporting moieties. With a high coordination number, the Gd^{3+} centre in **DCA^{3}** is fully saturated and therefore undergoes no change in *q* upon Ca^{2+} coordination. **DCA^{4}** and **DCA^{5}** have DOTA-type macrocycles which have an identical coordination number to **DCA^{3}**, except due to the replacement of one amide unit with an acetic arm, the overall charge of the macrocycle is negative. Charge variation is also achieved in the case of **DCA^{5}** with the capping of the positively charged dendrimer surface. It should also be noted that in all systems, the EGTA-derived chelator was anticipated to experience a change in charge upon Ca^{2+} coordination from negative to neutral, thus altering the charge distribution across the molecule (Figure 20).

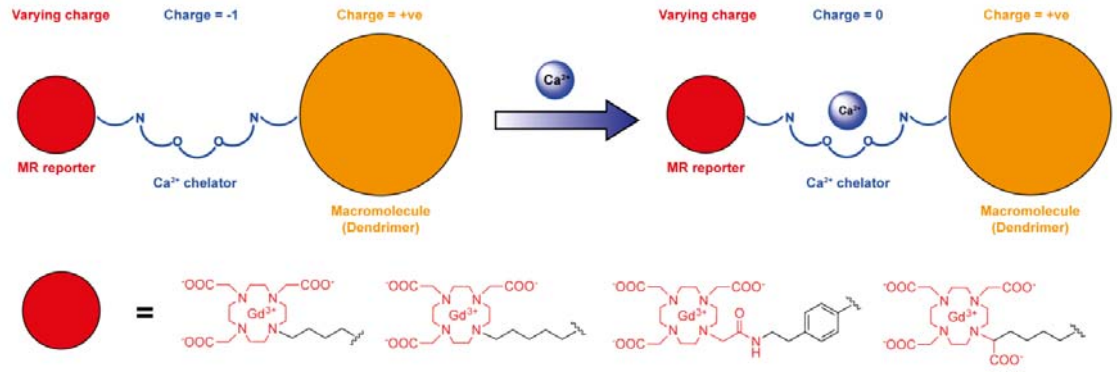

Figure 20. The anticipated Ca^{2+} response mechanism for DCAs$^{1-5}$ with the associated changes in electrostatic charge across the system. Reproduced with permission from Ref 289. Copyright 2018 American Chemical Society.

The importance and effect of differing charge distributions across the whole macromolecular structure on the properties of the system could then be assessed.

3.3 Results and discussion

3.3.1 Synthesis of L^{1} and L^{2}

The synthesis of the monomeric Ca^{2+}-responsive units for **DCA^{1}** and **DCA^{2}** began from *t*Bu-DO3A which was alkylated with bromide **1** or **2** giving Cbz protected amines **3** or **4** respectively (Scheme 1).[291-293] Removal of Cbz was performed with catalytic hydrogenation using 10 wt% $Pd(OH)_2/C$ in ethanol to yield amines **5** or **6**. Macrocyclic bromides **7** or **8** were synthesised via coupling of **5** or **6** with bromoacetic acid using DCC as the coupling agent. The EGTA-derived unit **11** was prepared via the monoalkylation of amine **9** with bromide **10** which was then subject to exhaustive alkylation with macrocyclic bromides **7** or **8** to yield monomeric nitro **12** or **13**. Reduction of the nitro moieties of **12**

and **13** followed by conversion of the resulting aromatic amines (**14** and **15**) to isothiocyanates gave the final monomeric ligands **L**^{1} and **L**^{2}.

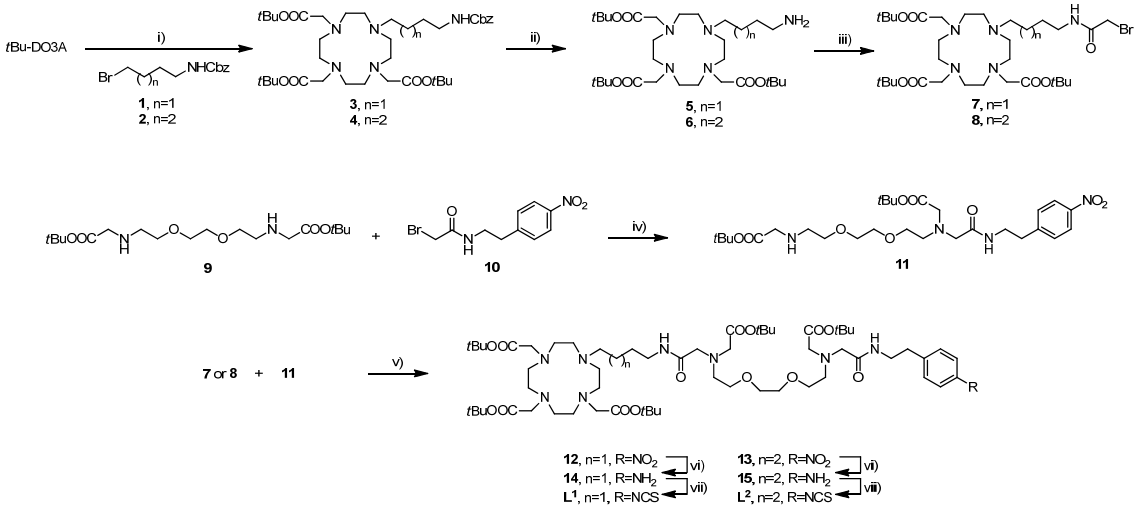

Scheme 1. Synthesis of DO3A-based SCA monomers (**L**^{1}, **L**^{2}). Reagents and conditions: (i) **1** or **2**, K_2CO_3, CH_3CN, 70 °C. **3** = 94% , **4** = 84%. (ii) H_2, $Pd(OH)_2$/C, NH_3/MeOH, EtOH, RT. **5** = 97%, **6** = 99%. (iii) $BrCH_2COOH$, DCC, CH_2Cl_2, RT. **7** = 53%, **8** = 69%. (iv) **9**, **10**, K_2CO_3, CH_3CN, RT, 34%. (v) **7** or **8**, **11**, K_2CO_3, CH_3CN, 70 °C. **12** = 58%, **13** = 44%. (vi) H_2, Pd/C, EtOH, RT. **14** = 99%, **15** = 93%. (vii) $CSCl_2$, $NaHCO_3$ (sat), CH_2Cl_2, RT. **L**^{1} = 41%, **L**^{2} = 42%. Reproduced with permission from Ref 289. Copyright 2018 American Chemical Society.

3.3.2 Synthesis of L^{3}

The DO3A-monoamide monomer **L**^{3} was synthesised commencing from *t*Bu-DO3A (Scheme 2). Alkylation of the free remaining secondary amine with bromide **10** yielded **16**. Reduction of the nitro functional group was achieved by catalytic hydrogenation with Pd/C in ethanol to give macrocyclic amine **17**. Coupling with bromoacetic acid was performed under the same conditions as in the preparation of **7** and **8** yielding macrocyclic bromide **18**. N-alkylation of **11** was performed in acetonitrile with K_2CO_3 at reflux to afford nitro **19**. Conversion of aromatic nitro to amine **20** was achieved with catalytic hydrogenation with Pd/C which was subsequently converted to isothiocyanate **L**^{4} with thiophosgene in a biphasic system.

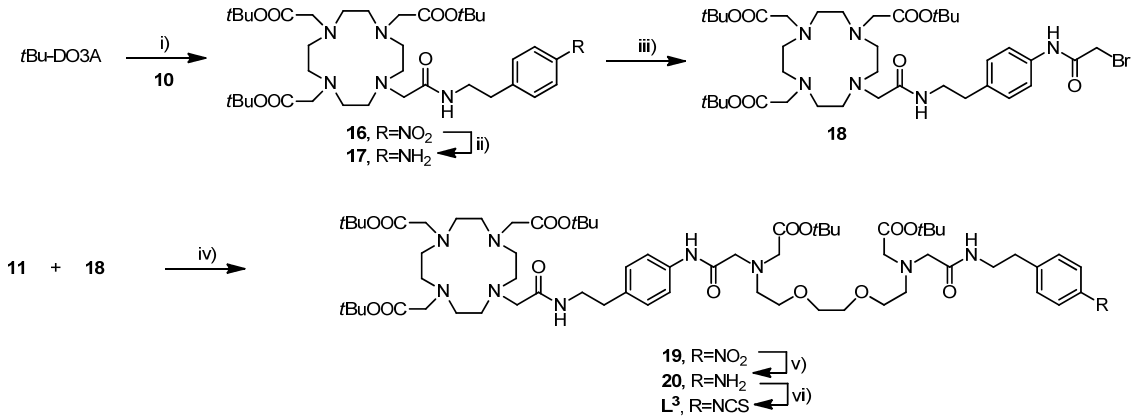

Scheme 2. Synthesis of the DO3A-monoamide based SCA monomer (**L**[3]). Reagents and conditions: (i) **10**, K_2CO_3, DMF, RT, 67%. (ii) H_2, Pd/C, EtOH, RT, 90%. (iii) $BrCH_2COOH$, DCC, CH_2Cl_2, RT, 51%. (iv) **11**, **18**, K_2CO_3, CH_3CN, 70 °C, 59%. (v) H_2, Pd/C, EtOH, RT, 76%. (vi) $CSCl_2$, $NaHCO_3$ (sat), CH_2Cl_2, RT, 55%. Reproduced with permission from Ref 289. Copyright 2018 American Chemical Society.

3.3.3 Synthesis of L[4]

The DOTA-based protected ligand, **L**[4], was developed following procedures previously described for **L**[1-3] (Scheme 3).

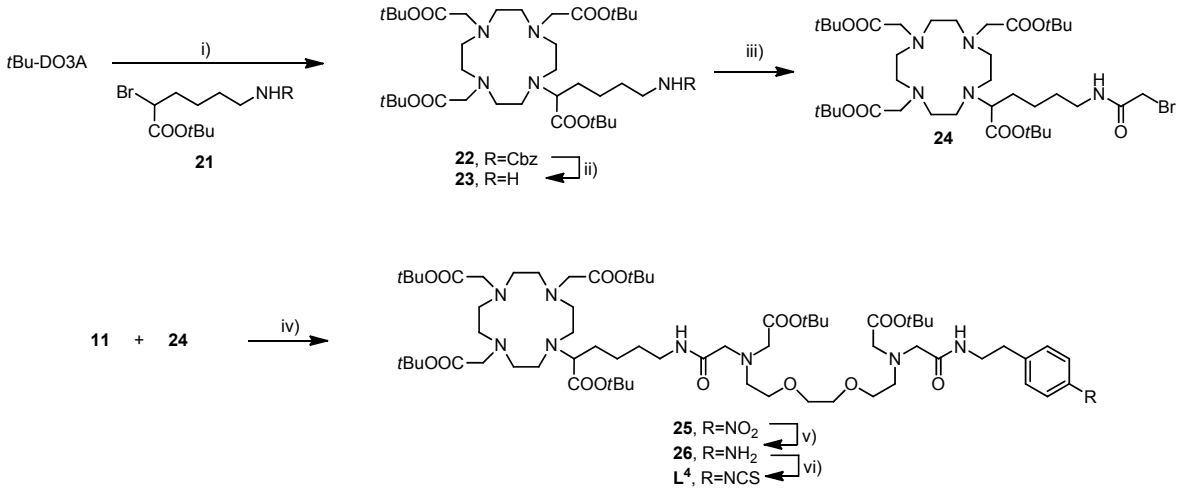

Scheme 3. Synthesis of the DOTA-based SCA monomer (**L**[4]). Reagents and conditions: (i) **21**, K_2CO_3, DMF, 45 °C, 79%. (ii) H_2, $Pd(OH)_2/C$, EtOH, RT, 99%. (iii) $BrCH_2COOH$, DCC, CH_2Cl_2, RT, 51%. (iv) **11**, **24**, K_2CO_3, CH_3CN, 70 °C, 76%. (v) H_2, Pd/C, EtOH, RT, 100%. (vi) $CSCl_2$, $NaHCO_3$ (sat), CH_2Cl_2, RT, 42%. Reproduced with permission from Ref 289. Copyright 2018 American Chemical Society.

Diazotization followed by bromination and esterification of H-Lys(Cbz)-OH gave aliphatic bromide **21**.[294] Alkylation of *t*Bu-DO3A with **21** yielded macrocycle **22**. Hydrogenation with $Pd(OH)_2/C$ in

ethanol gave amine **23**. Carbodiimide activated coupling with DCC afforded macrocyclic bromide **24** in moderate yields. Monomeric nitro **25** was synthesised by N-alkylation of **11** with **24**. Conversion of the nitro moiety to amine **26** and isothiocyanate $\mathbf{L^4}$ was achieved using the same conditions described previously.

The synthetic procedures described for $\mathbf{L^{1\text{-}4}}$ all follow the same methodology. Alternate synthetic routes were initially investigated for the DO3A-monoamide and DOTA-based monomers $\mathbf{L^{3\text{-}4}}$, leading to synthetic difficulties and subsequently development of the synthetic route described above.

Initially a synthetic procedure with a modified EGTA-derived Ca^{2+}-chelator was developed (Scheme 4).

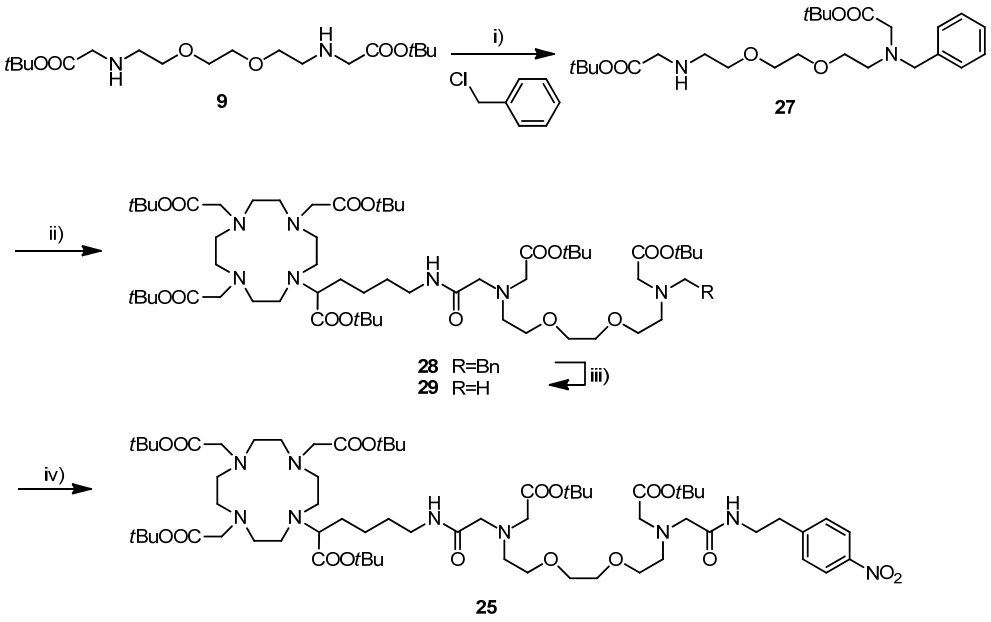

Scheme 4. Attempted alternative synthesis of the DOTA based SCA monomer ($\mathbf{L^3}$). Reagents and conditions: (i) Na_2CO_3, MeCN, RT, 44%. (ii) **11**, K_2CO_3, DMF, 60 °C, 42%. (iii) H_2, $Pd(OH)_2/C$, EtOH, RT, 94%. (iv) **10**, K_2CO_3, KI, DMF, 50 °C, 56%.

In this method, identical synthesis towards macrocyclic bromide **24** was performed. Instead of **11**, a monobenzylated derivative (**27**)[188] was synthesised and monoalkylation with **24** was achieved in DMF with K_2CO_3 as the base to give **28**. Following this, debenzylation was carried out by catalytic hydrogenation in ethanol with Pd/C to yield amine **29**. The benefit to this general procedure lies in the development of the EGTA component; starting from **9**, the process of monobenzylation yields both mono- and bis-benzylated products which can either be used further (mono derivative) or be recycled (bis-product) by catalytic hydrogenation to yield **9**. Problems arise in the final step, where

alkylation with **10** gave a moderate yield of 56% which was difficult to purify and problematic to reproduce.

Alternatively, coupling of **17** with an EGTA-derivative bearing a free carboxylic acid and the nitro phenyl moiety was attempted (Scheme 5). Trials with HATU, DCC and EDC coupling agents with DIPEA as the base in DMF yielded negative results and hence were not pursued any further.

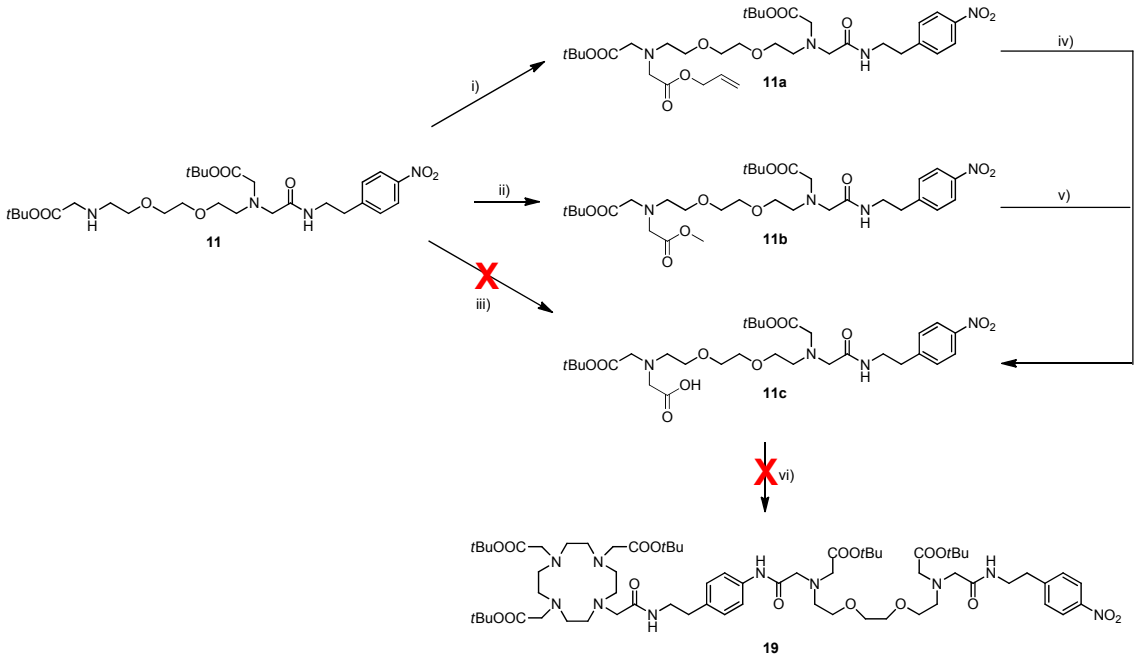

Scheme 5. Attempted alternative synthesis of the DO3A-monoamide based SCA monomer (**L**[3]). Reagents and conditions: (i) $ClCH_2COOCH_2CH{=}CH_2$, K_2CO_3, MeCN, 70 °C, 46%. (ii) $BrCH_2COOMe$, K_2CO_3, MeCN, 70 °C, 46%. (iii) $BrCH_2COOH$, K_2CO_3, MeCN, 70 °C. (iv) morpholine, $Pd(PPh_3)_4$, THF, RT. (v) LiOH, THF/H_2O/MeOH (1.5:0.5:1), RT. (vi) 1) HATU, DIPEA, DMF, RT. 2) EDC, HOBt, CH_2Cl_2, RT. 3) DCC, CH_2Cl_2, RT.

3.3.4 Synthesis of DCAs[1-5]

Step wise addition of SCAs **L**[1-4] to the surface amines of G4 PAMAM dendrimers in DMF afforded the protected dendrimers **D**[1a-4a] (Scheme 6). Removal of the *tert*-butyl esters was then performed in formic acid at 60 °C yielding **D**[1b-4b]. The final **DCAs**[1-4] were then synthesised after complexation of **D**[1b-4b] with Gd^{3+} at pH 7. **DCA**[5] was developed via an additional capping step with methyl isothiocyanate on the remaining surface amines of **D**[4a] to give **D**[5a]. Subsequent deprotection and complexation with Gd^{3+} following the same conditions previously described afforded **DCA**[5]. Characterisation of the number of monomeric units attached to the dendrimeric surface was carried out with ^{1}H NMR on the protected (**D**[1a-4a]) and deprotected (**D**[1b-4b]) dendrimers. Average loadings of the monomeric units were calculated using ^{1}H NMR for both the protected (**D**[1a-4a]) and deprotected (**D**[1b-4b]) derivatives and

found to be in the range of 52-77 %. These loading values are consistent with that previously reported for dendrimeric preparations involving a DO3A-based Ca-responsive SCA and a DOTA macrocyclic scaffold.[191, 295] MALDI-TOF (**D^{1b-5b}** and **DCA$^{1-5}$**) and elemental analysis (**DCA$^{1-5}$**) was also carried out, however only qualitative trends were extracted from the MALDI-TOF results and no conclusions could be drawn from the elemental analysis, possibly due to the high complexity of the system.

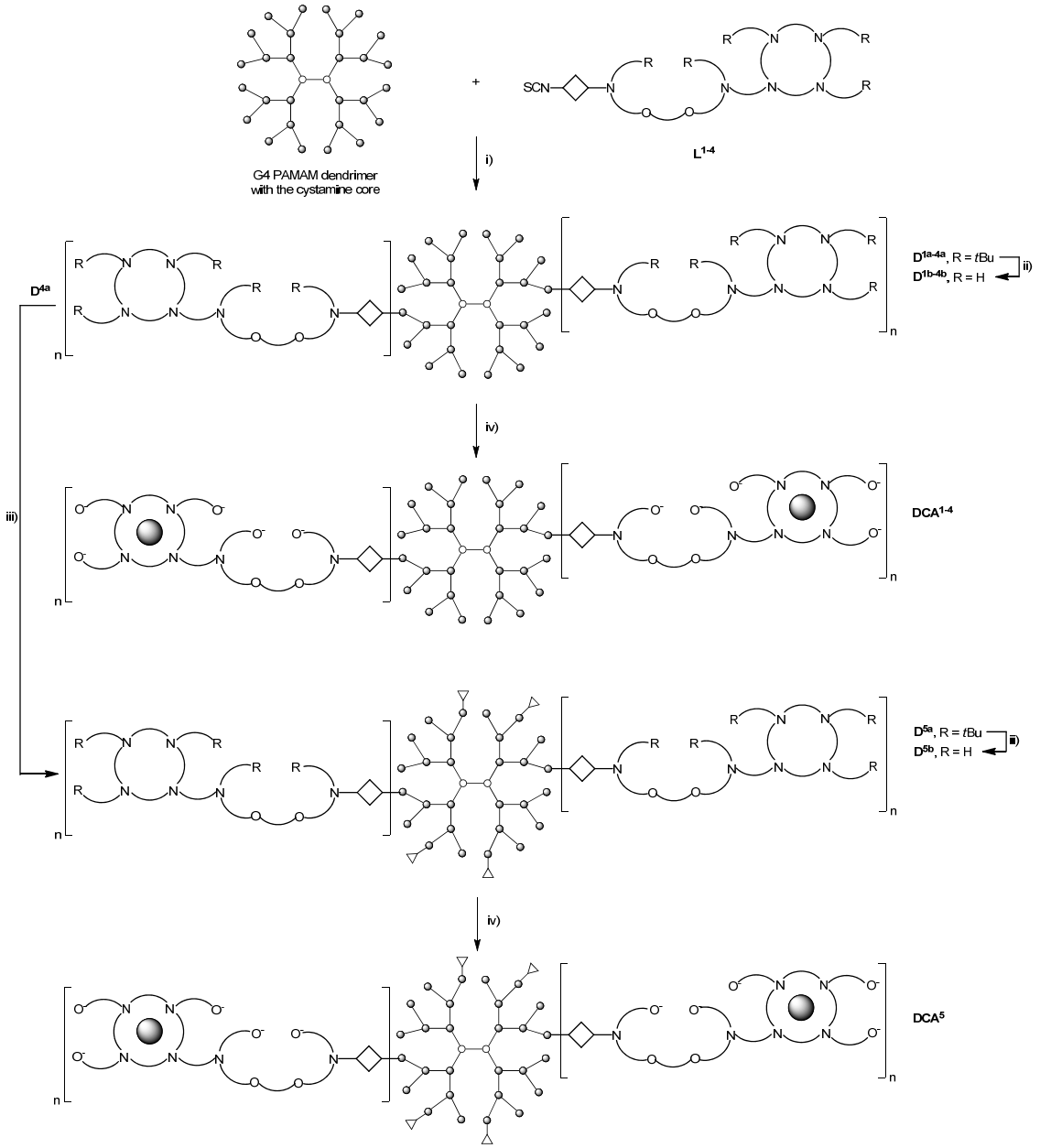

Scheme 6. Synthesis of **DCA$^{1-5}$**. Reagents and conditions: (i) **L$^{1-4}$**, Et_3N, DMF, 45 °C. (ii) HCO_2H, 60 °C. (iii) MeNCS, Et_3N, DMF, 45 °C. (iv) $GdCl_3.6H_2O$, H_2O, pH 7, RT, followed by EDTA.2Na.2H_2O, H_2O, pH 7, RT. Reproduced with permission from Ref 289. Copyright 2018 American Chemical Society.

3.3.5 Relaxometric characterisation

Relaxometric characterisation of **DCAs**[1-5] was carried out by proton longitudinal and transverse relaxometric titrations. All measurements were conducted at 7 T and 25 °C using equal initial concentrations of Gd^{3+} (2.5 mM). Both T_1 and T_2 relaxation times were determined before and after each addition of Ca^{2+}, with relaxivities r_1 and r_2 then being calculated and plotted as a function of [Ca^{2+}]. Broadly, the relaxometric behaviours of the investigated systems can be split into two divisions, the DO3A and the DOTA-like systems. The responsivity of the DO3A-type systems, **DCA**[1] and **DCA**[2], exhibited remarkable increases in relaxivity upon the addition of Ca^{2+} with changes in the range of 76-84 % for r_1 and 280-365 % for r_2 being observed (Figure 21).

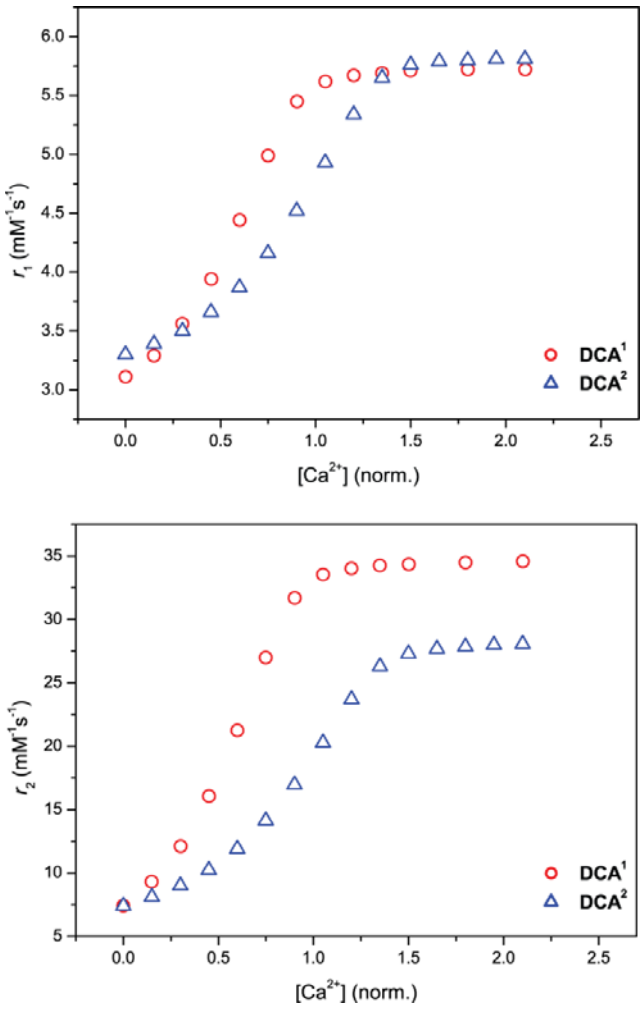

Figure 19. Relaxometric titration curves for **DCA**[1] and **DCA**[2]. Upper graph: Longitudinal (r_1) relaxometric curves for **DCA**[1-2]. Lower graph: Transverse (r_2) relaxometric curves for **DCA**[1-2]. [Gd^{3+}] = 2.5 mM, pH 7.4 (50 mM HEPES), 25 °C, 7 T. Reproduced with permission from Ref 289. Copyright 2018 American Chemical Society.

Comparing both derivatives shows that **DCA^{1}** displayed the greatest changes in relaxivity. Specifically, r_1 increased from 3.11 $mM^{-1} s^{-1}$ to 5.72 $mM^{-1} s^{-1}$ and r_2 from 7.44 $mM^{-1} s^{-1}$ to 34.57 $mM^{-1} s^{-1}$. For **DCA^{2}**, r_1 increased from 3.30 $mM^{-1} s^{-1}$ to 5.80 $mM^{-1} s^{-1}$ and r_2 rose from 7.39 $mM^{-1} s^{-1}$ to 28.05 $mM^{-1} s^{-1}$. When comparing both **DCA^{1}** and **DCA^{2}** from this study with that which was previously investigated,[188] the differences in the designed systems was the linker length between the macrocyclic MR reporter and the EGTA-derived Ca^{2+} sensitive moiety. Increasing from propyl to butyl (**DCA^{1}**) resulted in a higher relaxivity. Increasing the distance further to a pentyl (**DCA^{2}**) linker caused a decrease in relaxivity which required additional Ca^{2+} to fully saturate. The observations from the relaxometric titrations indicated that the optimal distance between the two chelating moieties is four methylene units.

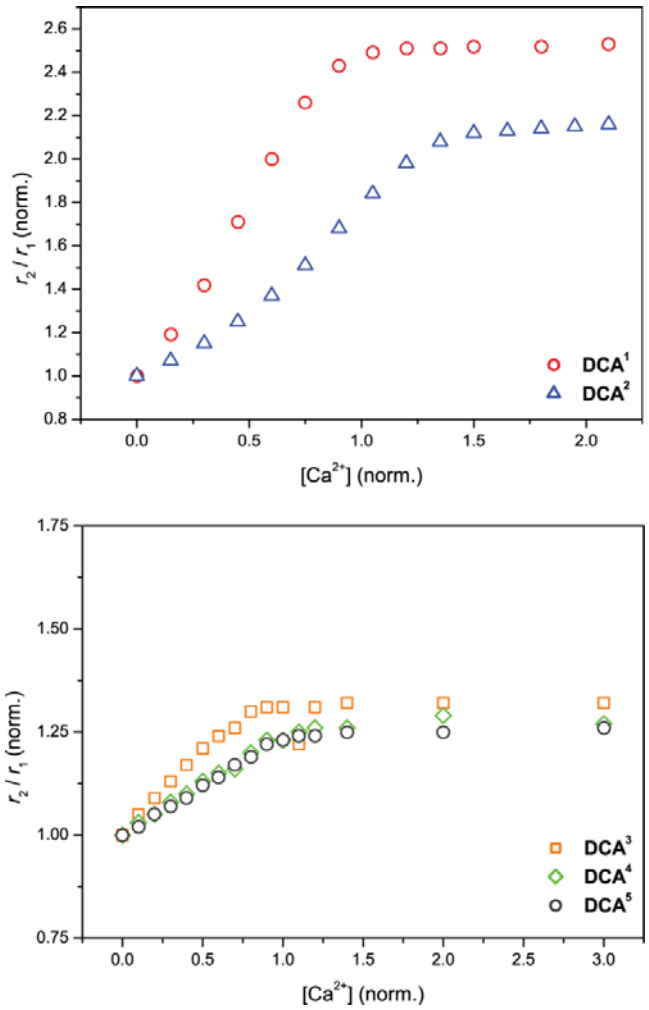

Figure 20. Relaxometric titration curves showing the r_2/r_1 ratio change of **DCAs$^{1-2}$** (top) and **DCAs$^{3-5}$** (bottom). Reproduced with permission from Ref 289. Copyright 2018 American Chemical Society.

Moreover, the dissimilar changes in r_1 and r_2 for these macromolecular systems make them eligible for use with the ratiometric imaging method previously exploited. Plotting of the r_2/r_1 ratio for both **DCA**[1] and **DCA**[2] gave factors of 2.52 and 2.14 respectively (Figure 22, Table 1). Furthermore, as **DCA**[1] revealed superior relaxometric behaviour, both in terms of r_2 changes and the r_2/r_1 ratio, this dendrimeric derivative can be explored further for the possibility of *in vivo* use.

Table 1. r_2/r_1 ratios of **DCAs**[1-5] at Ca^{2+} saturation. Reproduced with permission from Ref 289. Copyright 2018 American Chemical Society.

DCA	**1**	**2**	**3**	**4**	**5**
r_2/r_1	2.52	2.14	1.32	1.26	1.25

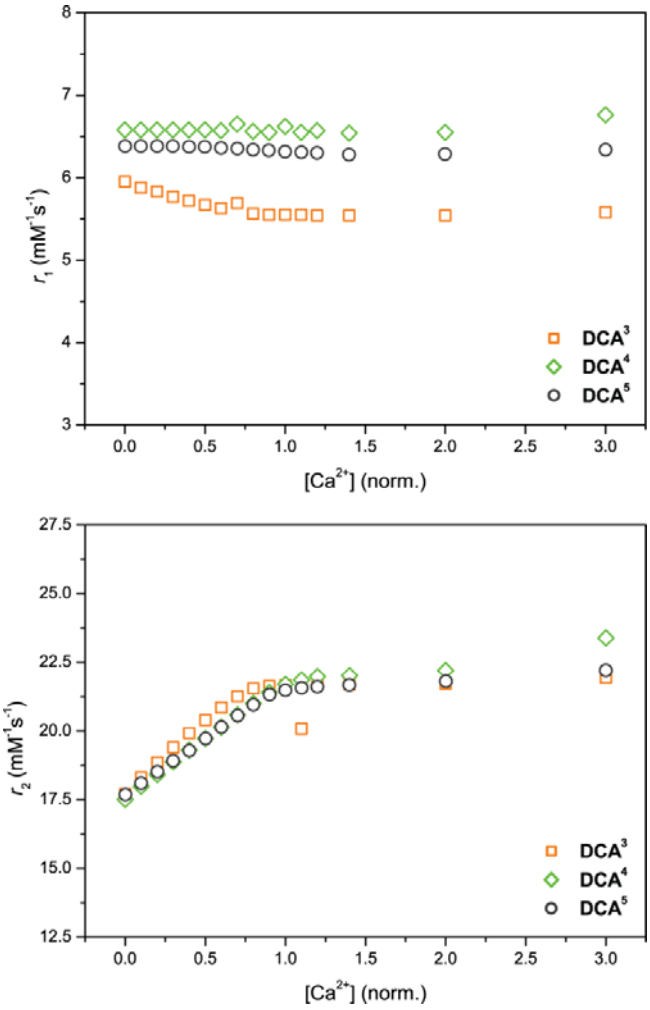

Figure 21. Relaxometric titration curves for **DCAs**[3-5]. Upper graph: Longitudinal (r_1) relaxometric curves for **DCA**[3-5]. Lower graph: Transverse (r_2) relaxometric curves for **DCA**[3-5]. [Gd^{3+}] = 2.5 mM, pH 7.4 (50 mM HEPES), 25 °C, 7 T. Reproduced with permission from Ref 289. Copyright 2018 American Chemical Society.

With the aim of maximising the r_2/r_1 ratio, an alternate strategy was devised. The incorporation of DO3A-monoamide or DOTA MR reporters was envisaged to result in a system which did not experience a variation in q upon Ca^{2+} coordination and therefore would result in no change in r_1.

However the transverse relaxivity, r_2, would increase due to a greater rigidity of the monomeric units and an expansion in the diameter of the whole dendrimeric system as observed previously. Experimentally determined relaxometric titrations revealed the expected r_1 behaviour of DOTA-type dendrimeric systems,[296] with values for **DCAs$^{3-5}$** remaining constant between 5.50 mM^{-1} s^{-1} and 6.50 mM^{-1} s^{-1} for each variant, indicating their insensitivity towards Ca^{2+} (Figure 23). Discrepancies from the anticipated behaviour were experienced for r_2 (Figure 23).

With increasing [Ca^{2+}], the significant r_2 increase displayed in the DO3A-type systems was not observed for **DCAs$^{3-5}$**. Specifically, r_2 increased by 25 % from 17.50 mM^{-1} s^{-1} to 22.50 mM^{-1} s^{-1} in each system. Evidently, through achieving absolute control of r_1, the enhancement of r_2 was severely affected leading to suppression in the overall r_2/r_1 ratio compared to the DO3A-type derivatives thus revealing their unsuitability towards the desired ratiometric imaging application (Figure 22, Table 1). Interestingly these results seem to indicate that these nanosystems rely on a synergistic combination of multiple properties such as hydration change, diameter increase and an enhanced rigidity of the monomeric units to attain the high relaxivities reported for the DO3A-type systems.

3.3.6 Dynamic light scattering (DLS)

Given the interesting relaxometric behaviours of **DCAs$^{1-5}$**, further insights into the overall structural behaviour were pursued. Dynamic light scattering is a method used to measure the hydrodynamic diameter of particles such as liposomes and dendrimers. When the light interacts with the nanoparticle, it scatters in all directions with the intensity of scattering recorded by a detector and the hydrodynamic size distribution determined. An increase in hydrodynamic diameter was reported for the previously examined DO3A-propyl derivative upon the addition of Ca^{2+}, which was an unexpected for a G4 PAMAM dendrimeric system.[191, 263] This could be explained through changes in charge of the EGTA-derived unit upon Ca^{2+} coordination and through an increased rigidity of the system. Analysis of **DCA^{1}** and **DCA^{2}** revealed a similar behaviour to that of the propyl analogue, with **DCA^{2}** giving the greatest size variation from 5.6 ± 0.9 nm to 10.2 ± 0.9 nm upon Ca^{2+} addition (Table 2, Figure S19). Changes in particle diameter distribution were more modest for **DCA^{1}** from 7.1 ± 1.2 nm in the 'off-state' to 8.5 ± 0.7 nm in the 'on-state' (Table 2). Additionally, size variations for the 'non-responsive' **DCAs$^{3-5}$** were also observed upon Ca^{2+} coordination.

Table 2. Particle hydrodynamic diameter determined using the DLS method before and after the addition of Ca^{2+} (2 equiv.). Conditions: 0.3 mM [Gd^{3+}], pH 7.4 (25 mM HEPES). Reproduced with permission from Ref 289. Copyright 2018 American Chemical Society.

DCA	1	2	3	4 [a)]	5 [a)]
No Ca^{2+}	7.1 ± 1.2	5.6 ± 0.9	7.4 ± 0.4	–	8.9 ± 1.4
+ Ca^{2+} (2 equiv.)	8.5 ± 0.7	10.2 ± 0.9	8.9 ± 0.6	–	–

a) Values for hydrodynamic diameters not provided for polydisperse samples.

Aggregation and high polydispersity was observed in **DCA[4]** and Ca-**DCA[5]** which prevented the exact size distributions being determined. Environmental properties such as electrostatic interactions and solvent/buffer composition have previously been reported to significantly affect the sizes of dendrimeric conjugates. **DCA[3]** contains a neutrally charged macrocycle whereas **DCAs[4-5]** have a net macrocyclic charge of -1. The effect of this charge discrepancy and the structural nature of the linker units between the MR reporter and EGTA-derived chelator influenced the size behaviour of the conjugates in solution. Furthermore, by capping the amino surface of the PAMAM dendrimer as is the case for **DCA[5]**, aggregation in the 'off-state' of **DCA[4]** seems to be prevented although polydispersity increases upon Ca^{2+} addition. Significantly, these findings signify how minor changes to the monomeric structure can have huge impacts on the behaviour of the dendrimeric conjugate, further highlighting the sensitivity of this class of compounds to their environment. Moreover, with a change in size displayed for each DCA, the relaxometric behaviours displayed by each DCA is clearly a product of a combination of multiple factors. For example **DCA[1]** and **DCA[3]** display similar particle size distributions prior to and after the addition of Ca^{2+}, which is a key component in r_2 change; however the responsiveness of each DCA is markedly different, indicating that hydration change amplifies the response demonstrated in **DCA[1]**. Further manipulations with acidic and basic buffered media (pH 5.5 and pH 8.5) revealed behaviours that deviated significantly from that observed at neutral pH. Most notably, by placing the DCAs in acidic or basic environments, the expansive capabilities as well as the polydispersities of the samples were considerably altered. For example in the case of **DCA[2]**, at physiological pH the system doubles in size from 5.6 ± 0.9 nm to 10.2 ± 0.9 nm upon Ca^{2+} addition. Exposing **DCA[2]** to a basic environment resulted in a smaller particle size distribution change from 6.8 ± 0.5 nm to 7.8 ± 1.1 nm upon Ca^{2+} coordination, demonstrating the delicate nature of dendrimeric conjugates.

3.3.7 Zeta potential studies

Characterisation by means of zeta potential measurements is routinely carried out in nanosystems such as dendrimers, colloidal gold or liposomes,[297] and in this case it was of interest to determine the organisation of the molecules in solution and their surface charge both in the 'off' and 'on' states. The term zeta potential refers to the electrical potential at an interface of the electric double layer of a nanoparticle and the surrounding bulk medium and is related to the overall surface charge of the particle.[297-299] It was found that initially each DCA had a negative zeta potential, which decreased upon Ca^{2+} binding (Table 3).

Table 3. The zeta potential change of each **DCA** upon Ca^{2+} addition. Conditions: 0.3 mM [Gd^{3+}], pH 7.4 (25 mM HEPES). Reproduced with permission from Ref 289. Copyright 2018 American Chemical Society.

DCA	**1**	**2**	**3**	**4**	**5**
No Ca^{2+}	-20.4 ± 1.3	-18.8 ± 1.0	-20.2 ± 2.0	-15.2 ± 1.4	-13.2 ± 1.8
+ Ca^{2+} (2 equiv.)	-5.2 ± 0.4	-3.8 ± 1.3	-0.6 ± 1.0	-3.9 ± 0.3	-6.0 ± 1.2

These observations can be explained due to the binding of the positively charged Ca^{2+} ions in all DCAs, which consequently leads to a discharging of the EGTA-derived Ca^{2+} chelator. Furthermore, the initial negative zeta potential indicates that the arrangement of the dendrimeric system exposes the SCA monomeric units to the outer surface of the nanosystem. Moreover, although the addition of Ca^{2+} leads towards a net neutral surface charge, DLS measurements show that except for in the cases of **DCA^4** and **DCA^5** + Ca, there was no observation of poor solubility or suspension formation in the studied systems.

3.4 Conclusion

Here a novel series of DCAs have been developed and characterised by means of ^{1}H longitudinal and transverse relaxometric titrations, DLS and zeta potential measurements. The results of this study have established the significance of the macrocyclic structure and the environmental conditions in the size changing capabilities of DCAs. In order to maximise the desired increase in r_2/r_1 ratio, a combination of changes in size, hydration number and the overall rigidity of the system are required. Modification of one parameter alone does not lead to a rise in r_2 values, which can only be achieved through their synergistic combination. The results of this systematic study have aided in determining the ideal characteristics required in the design of highly responsive DCA systems and provided a blueprint which can be used for the development of such probes for ratiometric imaging.

Furthermore, the system with the butyl linker provided an improved r_2/r_1 ratio along with an enhanced r_1 response relative to those previously published.[191] The superior properties of this probe, along with its anticipated slow diffusion in tissue, support its use in conventional T_1-weighted and rapid r_2/r_1 ratiometric imaging in dynamic fMRI studies and future investigations *in vivo*.

4 Investigation into the Effects of Subtle Structural Modifications on the Relaxometric Behaviour of DO3A-based Monomeric Bioresponsive Systems.

4.1 Introduction

In the pursuit of developing MRI SCAs with desirable properties, such as maximal changes in relaxivity between the 'off' and 'on' states, fundamental understandings of the internal behaviour of the probe is required. With this information, further derivatives of such probes can be designed and applied for specific functions. Many cation-responsive SCAs reported both in our group and across the literature are based on cyclen scaffolds with paramagnetic ions, such as Gd^{3+}.[2, 137, 139, 146, 300] The importance of understanding the relationship between the molecular structure and performance as an effective SCA is fundamentally important in the future development of bioresponsive probes and has brought about various structural and mechanistic studies.[182, 301, 302]

Cyclen-based lanthanide chelates are known to be present as two isomers, namely, the SAP and TSAP geometries which interconvert through ring flipping or by pendant arm rotation.[303-308] The impact of such configurations in Ca^{2+}-responsive SCAs were previously investigated showing that only the SAP configuration is capable of contributing to the relaxometric enhancement observed.[301] The TSAP isomer is present as a q = 1 species and therefore does not partake in the responsive process. Furthermore, the influence of the distance between the cyclen-based scaffold and the bioresponsive moiety has been previously investigated in the bismacrocyclic Ca^{2+}-responsive probes developed in our group, as well as a selection of model compounds reported recently.[182, 302] In the case of the bismacrocyclic SCAs, a thorough study compared the effect of a propyl and ethyl linker between the chelating groups. Here the propyl derivative showed an increased relaxometric enhancement.[182] Additionally, discrepancies were observed in the starting relaxivities prior to Ca^{2+} addition; and the hydration states of each derivative. In a recent advanced coordination study of model Ca^{2+}-responsive SCAs, it was again demonstrated that the effects of linker distance bear significant consequences on the overall behaviour of the probes.[302] Here, it was concluded that the ethyl linker was likely to be too short, bringing a protonated amine of the pendant arm too close to the paramagnetic metal centre leading to electrostatic repulsion, and therefore hindering the interaction of the carboxylate with the Gd^{3+} centre.

In chapter 3, a range of dendrimeric bioresponsive probes with differing monomeric units were developed. Of these, two new DO3A-based monomeric units were attached to G4 PAMAM dendrimers with increased linker lengths, **DCA^{1}** and **DCA^{2}**.[289] Significant differences in the properties

of the nano-sized probes were observed, prompting a thorough structural and coordination study of the two monomeric derivatives.[309] Initially, a range of diamagnetic and paramagnetic complexes were prepared and a variety of techniques such as 1D and 2D NMR, luminescence lifetime measurements, DOSY and proton relaxometric titrations were utilised to understand the behaviour of the butyl and pentyl monomeric systems and compare this to the propyl derivative, which is frequently employed in the development of various other SCAs.[137]

4.2 Results and discussion

4.2.1 Synthesis of LnL^5 and LnL^6

The synthesis of the protected nitro monomeric SCAs, **12** and **13**, were reported in section 2.3.1. Acid hydrolysis of the *tert*-butyl esters was achieved by heating in formic acid at 60 °C overnight. The resulting deprotected ligands (**L^5**, **L^6**) were used for the complexation reactions without further purification. In total, four complexes of each system were synthesised containing different lanthanide ions (Gd^{3+}, Eu^{3+}, Yb^{3+} and Y^{3+}, Scheme 7).

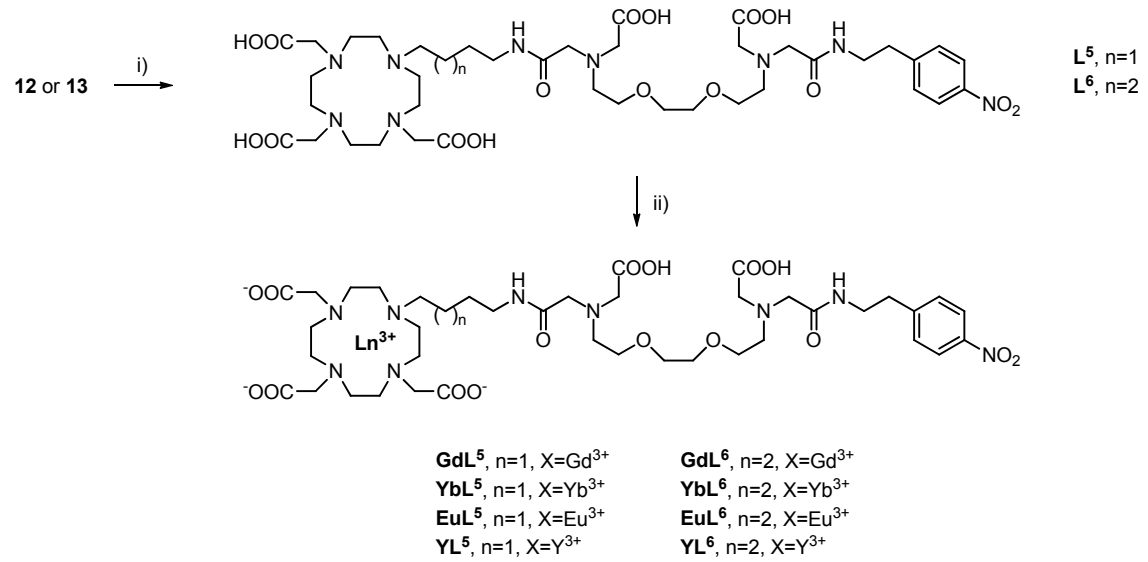

Scheme 7. Synthesis of **LnL^5** and **LnL^6**. Reagents and conditions: (i) **12** or **13**, HCO_2H, 60 °C. (ii) $LnCl_3.6H_2O$ (or $YCl_3.xH_2O$), H_2O, pH 7, RT followed by Chelex®. Reproduced with permission from Ref 309. Copyright 2019.

For relaxometric characterisation, the complexes with Gd^{3+} were used. Eu^{3+} derivatives were utilised for *q* determination, diffusion measurements and high resolution NMR; while the Yb^{3+} and Y^{3+} complexes were only used for high resolution NMR measurements. The synthesis of each complex was carried out in an identical way. Specifically, **L^5** and **L^6** were dissolved in water and the pH was adjusted to 7 through the addition of a 0.1 M NaOH solution. An excess of lanthanide hydrate was

added while maintaining the pH at 7 and stirred overnight. The excess lanthanide was then removed by repeated treatments with Chelex®, filtered and lyophilised to afford the final complexes, **LnL^5** and **LnL^6**.

4.2.2 Relaxometric titrations

Proton longitudinal and transverse relaxometric titrations with Ca^{2+} were carried out for **GdL^5** and **GdL^6**. Each measurement was performed with identical initial Gd^{3+} concentrations (2.5 mM) at 25 °C and 7 T. The T_1 and T_2 relaxation times were recorded and the relaxivities calculated as a function of [Ca^{2+}]. For the butyl derivative, **GdL^5**, the longitudinal relaxivity increased by 99 % from 2.49 to 4.96 mM^{-1} s^{-1} upon the addition of Ca^{2+}, saturating after the addition of 1.6 equivalents of Ca^{2+} (Figure 24). The initial relaxivity value is smaller than that observed for the previously reported propyl derivative.[137, 191] The transverse relaxivity increased by 107 % from 3.19 to 6.62 mM^{-1} s^{-1} over the same [Ca^{2+}] range, in line with that expected of a monomeric compound (Figure 25).

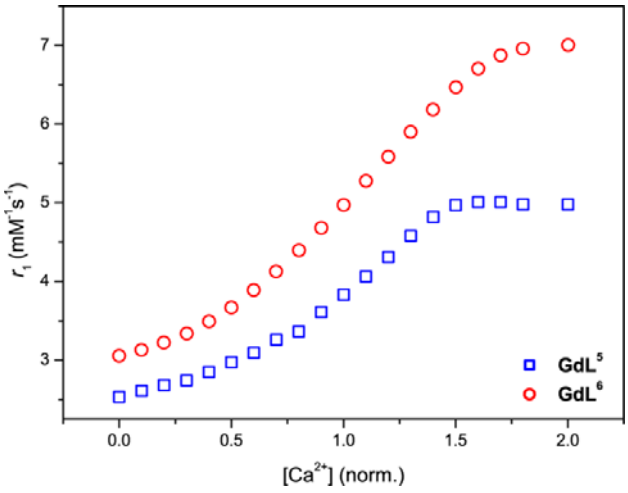

Figure 24. Longitudinal (r_1) relaxometric titration curves for **GdL^5** and **GdL^6** ([Gd^{3+}] = 2.5 mM, pH = 7.4 (50 mM HEPES), 25 °C, 7 T). Reproduced with permission from Ref 309. Copyright 2019.

For the pentyl derivative, **GdL^6**, an initial r_1 relaxivity of 3.01 mM^{-1} s^{-1} was observed, in line with that previously observed with monomeric SCAs (Figure 24).[137, 191] With the addition of Ca^{2+}, the relaxivity increased by 131 % to 6.97 mM^{-1} s^{-1}. Two equivalents of Ca^{2+} were required to reach full saturation of the probe, revealing a trend across the series of increasing saturation point with increasing linker length. The transverse relaxivity increased by 138 % from 3.92 to 9.31 mM^{-1} s^{-1} (Figure 25). Examining the behaviours across the series, it can be clearly seen that subtle changes in the linker lengths between the MR reporting unit and the EGTA-derived moiety impacts the relaxometric behaviour of the SCA.

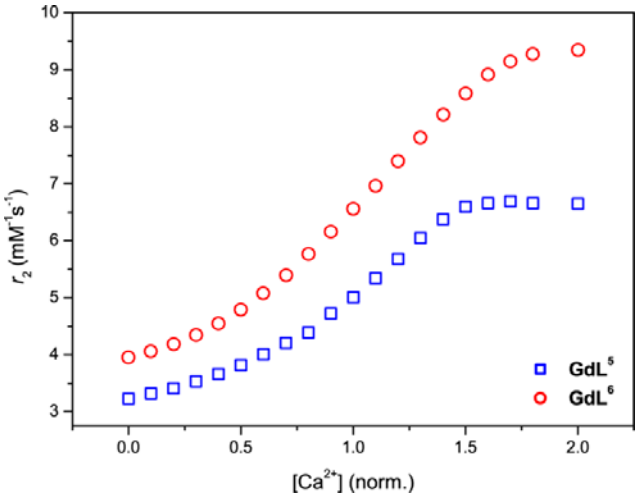

Figure 25. Transverse (r_2) relaxometric titration curves for **GdL^5** and **GdL^6** ([Gd^{3+}] = 2.5 mM, pH = 7.4 (50 mM HEPES), 25 °C, 7 T). Reproduced with permission from Ref 309. Copyright 2019.

As the linker length is increased, the amount of Ca^{2+} required to saturate each SCA increased. This difference suggests a decrease in affinity for Ca^{2+}. Surprisingly, when examining the trends of changes in relaxivity, it was found that the butyl derivative, **GdL^5**, showed deviant behaviour. Specifically, the overall change in r_1 and r_2 relaxivity is smaller than that of the longer variant, **GdL^6**, and the shorter propyl derivative (which are similar to each other, ~130 % increase in r_1).[191] Furthermore, the starting relaxivity value for **GdL^5** is lower than that of the other complexes, indicating a lower initial hydration state of the lanthanide complex possibly due to a change in coordination capabilities of the carboxylate of the EGTA-derived chelator. Interestingly, conjugating these monomeric SCAs onto G4 PAMAM dendrimers (Chapter 3) produces a different trend in behaviour, with the butyl derivative producing the greatest r_1 enhancement compared to the propyl and pentyl derivatives. This deviation in behaviour could be a consequence of the specific environmental arrangement of the butyl derivative when conjugated to the nanosystem.

4.2.3 NMR studies

Attempts to understand the impact of Ca^{2+} addition to each of the derivatives was conducted through a range of high resolution 1D and 2D NMR experiments (^{1}H, COSY, HSQC) at 800 MHz with a variety of complexes. Specifically, a series of complexes ranging from highly paramagnetic to diamagnetic (Yb^{3+}, Eu^{3+} and Y^{3+}) were prepared and studied at 20 mM and pD 7.0. The peaks which displayed changes in different conditions (pre- and post Ca^{2+}) were assigned. These were the methylene units in the linker between the DO3A macrocycle and the EGTA-derived moiety. Subsequently the analysis of each NMR spectra was concentrated on that structural region. The

methylene unit closest to the amine of the EGTA-derived moiety was not observed and therefore could not be followed, possibly due to exchange processes occurring due to the protonation state of the amine at pD 7.0.[301] The HSQC spectra of the diamagnetic yttrium derivatives, **YL^5** and **YL^6**, illustrated the differences between the pre- and post-Ca^{2+} states. Specifically, for the butyl derivative, **YL^5**, the methylene units closest (**A_1**) to and furthest (**D_1**) from the macrocycle showed minor shifts upon Ca^{2+} addition (Figure 26).

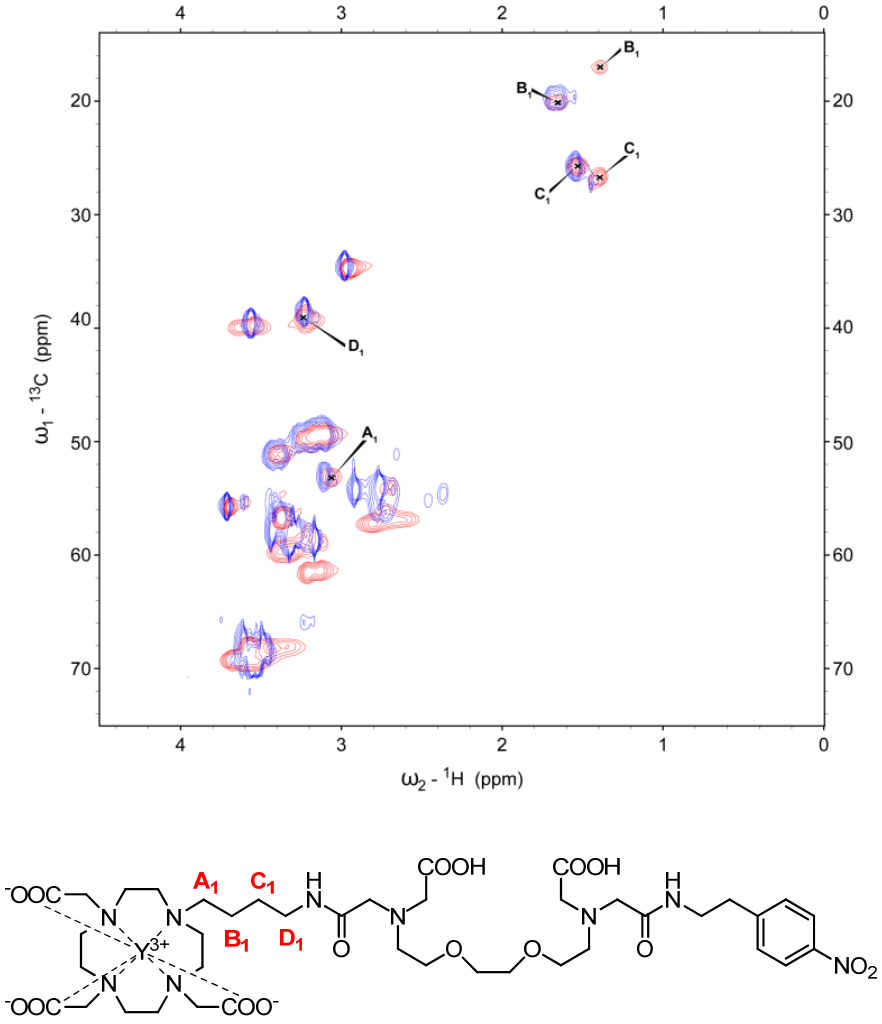

Figure 26. HSQC spectrum of **YL^5** with the signals of interest assigned pre-(blue) and post-Ca^{2+} (red) addition (Top). Chemical structure of **YL^5** with the carbon units of interest labelled (Bottom). Reproduced with permission from Ref 309. Copyright 2019.

On the contrary, the methylene units situated in the centre of the linker (**B_1** and **C_1**) displayed significant changes upon Ca^{2+} binding. In the unsaturated state, both of these methylene units present as a single major signal which splits to form two clear signals with equal intensity upon Ca^{2+}

coordination. Paramagnetic derivatives, **EuL**[5] and **YbL**[5], showed similar trends to that of **YL**[5] with the exception that the signal from the $\mathbf{A_1}$ methylene unit is lost upon Ca^{2+} coordination (Figure S20).

In a similar manner, the methylene units in **YL**[6] which are closest ($\mathbf{A_2}$) to and furthest ($\mathbf{E_2}$) from the DO3A-based macrocycle showed minor shifts upon Ca^{2+} coordination (Figure 27). Moving towards the inner methylene units, $\mathbf{B_2}$ is observed as a single signal which then splits to form a new additional signal with lower intensity after Ca^{2+} binding. The central methylene unit, $\mathbf{C_2}$, undergoes similar splitting after the addition of Ca^{2+}; however, the resulting signals are present with similar intensities. Finally, the methylene unit, $\mathbf{D_2}$, experiences the opposite trend as it is initially displayed as two spots which converge towards one signal in the presence of Ca^{2+}.

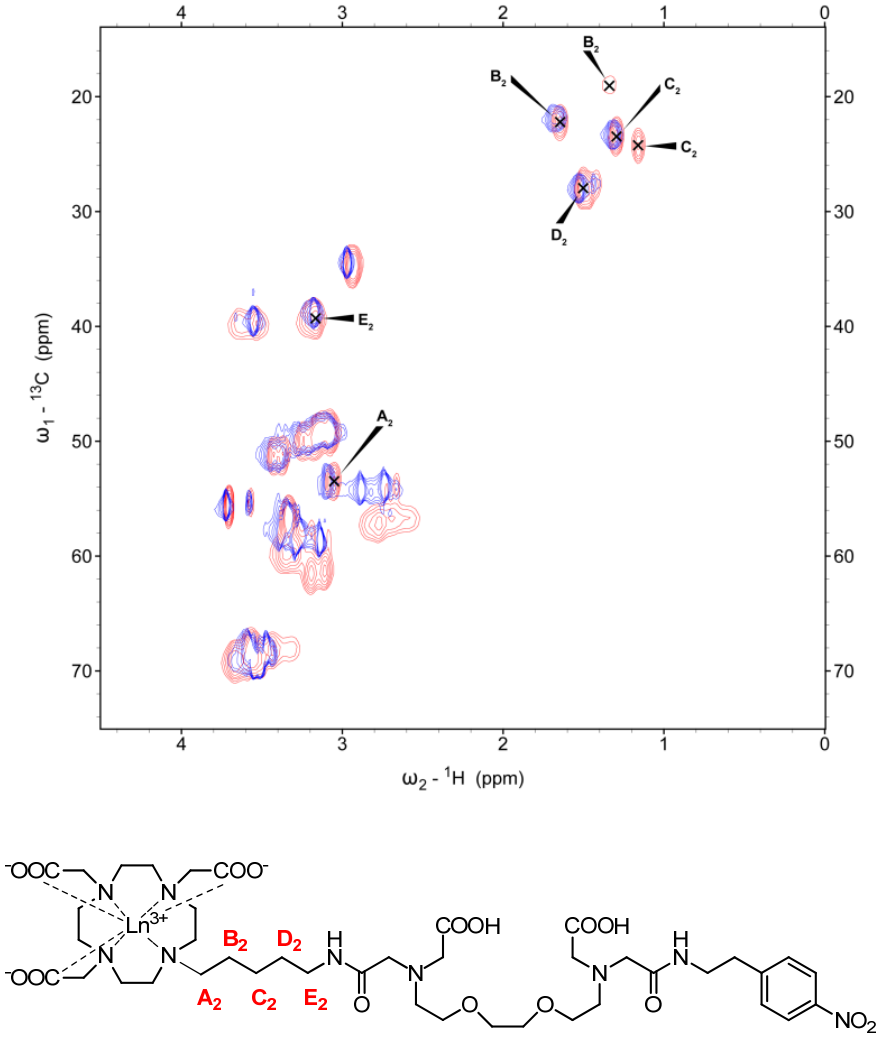

Figure 27. HSQC spectrum of **YL**[6] with the signals of interest assigned pre-(blue) and post-Ca^{2+} (red) addition (Top). Chemical structure of **LnL**[6] with the carbon units of interest labelled (Bottom). Reproduced with permission from Ref 309. Copyright 2019.

Analysis of the corresponding paramagnetic derivatives, **EuL^{6}** and **YbL^{6}**, again displayed similar trends to the diamagnetic derivative. Additionally, the signal for the closest methylene unit, **A_2**, disappeared upon Ca^{2+} as was similarly observed for the paramagnetic butyl derivatives.

The loss of signal for **A_1/A_2** after Ca^{2+} addition in the spectra for **EuL$^{5\text{-}6}$** and **YbL$^{5\text{-}6}$** can be explained by the paramagnetic effects of the lanthanide ion. Specifically, the impact of T_1 and T_2 shortening due to the paramagnetic relaxation effect is felt by the closest methylene unit due to its proximity to the lanthanide ion. Additionally, the impact of Ca^{2+} binding leads to increased conformational exchange. Together, both of these effects lead to signal loss, thus making them undetectable in the NMR spectra.

Substantial signal splitting and shifting is observed for the methylene groups **$B_{1,2}$**, **$C_{1,2}$**, and **D_2**, suggesting a significant change in their environment between the pre- and post-Ca^{2+} states. Considering that the methylene units in the linker between the MR reporting and EGTA-derived bioresponsive moiety should not be involved in the binding of Ca^{2+}, the change in these signals is indicative of a change to the coordination behaviour and environment of lanthanide complex. In the process of Ca^{2+} binding, only the EGTA-derived chelator will be involved with the major structural change arising from the flipping of EGTA carboxylate from the lanthanide of the DO3A scaffold to preferentially bind Ca^{2+} over Gd^{3+} and thus allow an increase in hydration of the complex, as was previously described for similar systems.[178, 203, 301] In such a system, it can be envisaged that in the 'off' state, when Ca^{2+} is not present, the coordination of the EGTA-derived carboxylate to the lanthanide gives a ring-like structure which is broken upon Ca^{2+} addition. Such a major conformational change is indicated through the splitting and shifting of signals and therefore provides additional evidence that these SCAs respond via the mechanism described for similar *q*-based systems.[177, 203] Furthermore, the presence of multiple signals upon Ca^{2+} addition could be related to the presence of two geometric isomers, SAP and TSAP. With the luminescence lifetime measurements describing equilibrium between non- and mono-hydrated species (see below), the binding of the carbonyl group of the amide is envisaged to coordinate with the lanthanide in both the presence and absence of Ca^{2+}. Although this group could not be observed during the NMR experiments, the hydration states of the complex along with the absence of NMR signals is suggestive of such a scenario.

4.2.4 NMR diffusion measurements

The diffusive behaviour of the europium analogues (**EuL$^{5\text{-}6}$**) was assessed in DOSY experiments at three different concentrations (20, 10 and 5 mM) in the presence and absence of Ca^{2+}. The

assessment of diffusion is a useful tool that can aid in describing the behaviour of the molecules in solution and determine if any aggregation takes place. The diffusion coefficients measured for all samples was found to be in agreement with that previously observed for similar monomeric compounds previously developed (Table 4).[183, 191]

Table 4. Diffusion coefficients calculated for **EuL$^{5\text{-}6}$** with and without Ca^{2+} (2 equiv). Reproduced with permission from Ref 309. Copyright 2019.

	Diffusion coefficient (10^{-10} m^2 s^{-1})					
	No Ca^{2+}			+ Ca^{2+}		
	20 mM	10 mM	5 mM	20 mM	10 mM	5 mM
EuL^5	1.76 ± 0.06	1.97 ± 0.01	1.99 ± 0.04	1.89 ± 0.02	2.01 ± 0.04	2.05 ± 0.06
EuL^6	1.76 ± 0.02	1.90 ± 0.04	1.95 ±0.04	1.71 ± 0.01	1.91 ± 0.01	1.96 ± 0.02

As a general trend, the diffusion coefficient slightly increases upon moving to lower complex concentrations as expected. Additionally, the diffusion of **EuL^6** was slightly slower than **EuL^5** as expected for a minor increase in size. The addition of Ca^{2+} also causes a slight increase in diffusion coefficient, indicating a change in conformation of the species which occurs upon Ca^{2+} binding. Furthermore, the reported diffusion coefficients and the observed changes upon Ca^{2+} addition are indicative of systems that likely do not undergo aggregation and in fact lead to systems that provide faster diffusion upon Ca^{2+} addition.

4.2.5 Luminescence experiments

Luminescence emission lifetime measurements were performed to assess the hydration of the systems in the absence and presence of Ca^{2+} to further understand the coordination environment of the DO3A-based lanthanide ion. All measurements were carried out with the europium analogues, **EuL$^{5\text{-}6}$**, which closely resemble the coordination environment of the Gd^{3+} derivatives. Samples were prepared with **EuL$^{5\text{-}6}$** (5 mM) in both H_2O and D_2O and the luminescence emission lifetime was measured. Following this the *q* for each complex was calculated following a previous reported method (Table 5).[310] Expectedly, the hydration numbers for **EuL$^{5\text{-}6}$** increase upon Ca^{2+} binding as anticipated for *q*-based SCAs and as previously observed across this class of SCA as well as in other DO3A-based Ca^{2+}-responsive SCAs.[178, 182, 203, 301] This increase in hydration is a result of decoordination of the EGTA carboxylate which 'flips' from the lanthanide ion to preferentially coordinate the added Ca^{2+}, which subsequently allowed water to access the inner sphere of the lanthanide.

Table 5. *q* values calculated for **EuL$^{5\text{-}6}$** with and without Ca^{2+} (2 equiv). Reproduced with permission from Ref 309. Copyright 2019.

	No Ca^{2+}			+ Ca^{2+} (2 equiv)		
	τ_{H_2O} (ms)	τ_{D_2O} (ms)	*q*	τ_{H_2O} (ms)	τ_{D_2O} (ms)	*q*
EuL^5	0.726	1.142	0.30	0.584	1.159	0.72
EuL^6	0.652	1.140	0.49	0.539	0.982	0.70

Differences in linker length led to differences in the initial hydration state of the complex. For **EuL^5** with the shorter butyl linker, a *q* value of 0.3 was calculated, which was lower than that of **EuL^6** (*q* = 0.49). Furthermore, these values are complimentary to the initial r_1 relaxivities previously described and aid in describing the coordination behaviour of the complex in the 'off' state. Specifically, for **EuL^6**, the greater initial value of *q* could indicate a decreased interaction between the EGTA-derived carboxylate and the lanthanide complex compared to **EuL^5**. By increasing the linker length, it can be envisaged that the distance between the two moieties impacts the interaction between the positively charged lanthanide and the negatively charged carboxylate, thus altering the conformational arrangements of the molecules in solution. Additionally, a change in the SAP and TSAP ratios could provide possible explanations for this behaviour.

4.3 Conclusion

A new pair of Ca^{2+}-responsive SCAs were developed based on previously reported DO3A-based probes but with increased linker lengths between the MR reporting and bioresponsive moieties. The coordination behaviour was analysed through relaxometric, NMR, DOSY and luminescence lifetime studies. Throughout, the impact of such structural changes is apparent. As the linker length increased, the initial hydration state of the complexes increased, resulting in a higher starting r_1 relaxivity. The overall observed relaxivity change upon Ca^{2+} additon was strongly dependant on the linker length. The r_1 and r_2 relaxivities increased by 99 and 107 % respectively for **GdL^5**. Increasing the linker size resulted in an enhanced change in r_1 and r_2 relaxivity of 131 and 138 % respectively. The diffusive behaviour of the europium analogues, **EuL$^{5\text{-}6}$**, was assessed with DOSY experiments. The resulting diffusion coefficients describe systems that show minimal/negligible changes between the Ca^{2+} unsaturated and saturated states. High resolution NMR studies with various complexes revealed further insights into the behaviour of the linker unit upon Ca^{2+} binding. The linker itself undergoes significant structural changes upon Ca^{2+} addition which is consistent with the internal rearrangement mechanism of action previously described for these types of Ca^{2+}-responsive probes.

Overall, the coordination properties of the two novel DO3A-based Ca^{2+}-responsive systems were assessed and compared to the frequently employed propyl derivative to assess their suitability in the future development of Ca^{2+}-responsive bioresponsive probes. Importantly, this study has provided important insights into how subtle structural changes in these systems can fundamentally alter their behaviour and thus provides an important basis in the pursuit of more effective Ca^{2+}-responsive probes. Finally, both investigated systems revealed good relaxometric properties in response to Ca^{2+} and can be considered as candidates for further utilisation in the preparation of multifunctional SCAs for fMRI.

5 Solid Phase Assisted Approach for the Preparation of Multifunctional Bioresponsive Probes.

5.1 Introduction

Increasing the diversity and specificity of MR probes is of paramount importance in order to monitor particular and unique environments and conditions. Often the desire for such probes can lead to 'complex' molecular designs which require significantly challenging synthetic and purification procedures, resulting in inefficient reaction pathways and unsatisfactory yields. Throughout molecular imaging, bifunctional probes based on polyazamacrocycles are frequently employed with the macrocycle responsible for metal chelation and the second functionality involved in conjugation to biomolecules, utilised for synthetic modifications or applied for the detection of specific analytes or targets.[311] Although theoretically seemingly simple to handle, often functionalization of such constructs can be difficult, time consuming and require the use of large amounts of starting material to compensate for lower reaction yields. This is especially prevalent in the case of more complicated 'unsymmetrical' derivatives, limiting their broader application. Furthermore, the highly polar nature of these molecules can further complicate purification procedures additionally contributing to the difficulties experienced.

Aside from standard solution phase protocols, SPPS has been widely exploited in peptide synthesis as a suitable alternative synthetic technique.[271-273] Operating on the principles described in the introduction, the method operates on a protection/deprotection scheme similar to that defined for solution phase chemistry, with the exception that the first step features the attachment of the first component to a solid support ensuring a number of advantages. Although, SPPS as a synthetic methodology has been widely explored across multiple fields, its use in the field of MRI CAs has not been fully exploited, especially in the synthesis of bioresponsive derivatives. The bifunctional nature of SCAs positions them as prime candidates for synthesis by SPPS. Furthermore, the development of such a methodology would enable an expansion in scope of the utilisation of such probes through the inclusion addition of a targeting vector or a suitable probe for additional another imaging modality.

With the desire to develop bioresponsive probes with increased diversity, we embarked on utilising Fmoc SPPS protocols to produce Ca^{2+}-responsive SCAs, circumventing the typically tedious and demanding synthetic procedures required for such MRI chelates. Initially, SPPS was explored as a methodology to synthesise a more 'complex' derivative of a previously reported potent bismacrocyclic Ca^{2+}-responsive SCA,[312] which has shown a strong relaxometric response in the

presence of Ca^{2+}.[182, 184] In a further study (Chapter 6), we employed the simplicity of peptide synthesis with SPPS to develop a multimeric Ca^{2+}-responsive probe with an additional targeting vector.

5.2 Synthetic design

The design of the modified bismacrocycle consisted of a small peptide unit conjugated to the bismacrocycle. The peptide unit had two functions, firstly to act as a spacer between the resin and the bismacrocycle and most importantly to provide a position which could be further functionalised with a functional group. Lysine was selected as an amino acid in the peptidyl spacer as it contains a ω-NH_2 function which can be utilised to anchor the functional molecule. The simplistic stepwise approach consisted of five stages (Figure 28); 1) the synthesis of the peptide unit, 2-4) the assembly of the bismacrocycle through the use of two macrocyclic and one EGTA-derived building block and 5) the incorporation of biotin as the functional molecule.

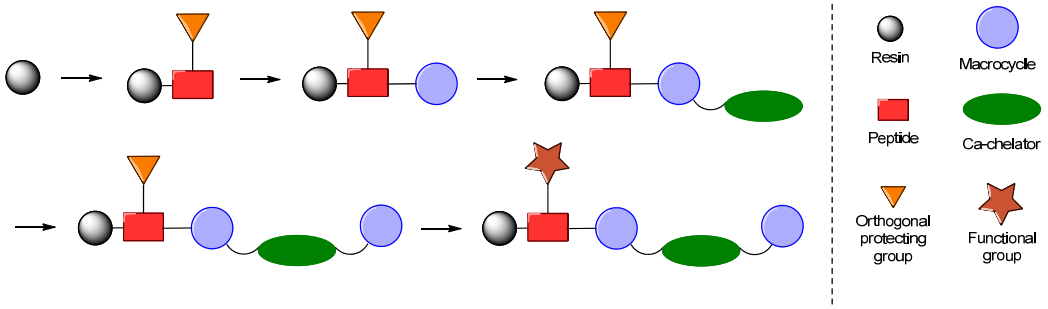

Figure 28. Schematic representation of the synthetic approach followed in this study. Reproduced with permission from Ref 312. Copyright 2019 American Chemical Society.

This approach reduced the number of steps that are required in solution and subsequently the number of tedious purification steps. Furthermore, the flexibility of this synthetic protocol will allow for the production of a large variety of SCAs based on peptides by simply electing different SCA building blocks. Additionally the peptide can be easily modified to enable total flexibility in SCA design. In order to fully take advantage of this method, the building blocks used must contain orthogonal protecting groups that are suitable for use in SPPS and which can be selectively deprotected in the presence during the synthetic procedure.

In this study various building blocks were explored for their applicability in SPPS with building blocks (**BB1-BB3**, Figure 29) being selected as the most suitable.

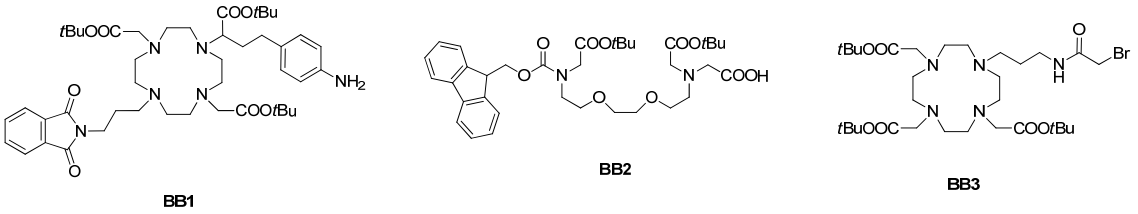

Figure 29. Chemical structures of the building blocks used. Reproduced with permission from Ref 312. Copyright 2019 American Chemical Society.

Here **BB1** possesses a free amino group to couple to the peptide unit while also containing an additional amino group which can be selectively revealed through the removal of the pthalimide function for coupling to **BB2**. Through the use of **BB2** with the extremely labile Fmoc protecting group, the strategy of alkylation with **BB3** could be employed, further demonstrating the flexibility and applicability of various reaction types with SPPS.

The design of **BB1** was based on DO2A-derived building block. This differed from that previously described for the synthesis of a bismacrocyclic Ca^{2+}-responsive SCA, which was based on two DO3A components.[182] Diversification of the first cyclen-based macrocycle was necessary to facilitate its attachment to a peptide unit. As the aromatic amine function is initially masked as a nitro moiety and with the presence of acid labile *tert*-butyl esters, a relevant protecting group which could be selectively removed was required. The requirements of this were that it must be stable to the conditions for reduction of the nitro function prior to coupling to the peptide, and should not impact other functional groups upon removal. Commonly, Cbz is employed as an amine protecting group for these DO3A-alkyl amine functionalities. However, deprotection usually consists of heterogeneous catalysis with Pd/C in a hydrogen atmosphere limiting is applicability for solid phase. Alternatively, Cbz has been explored for solid phase applications by Yoo *et al*. Here, they employed harsh conditions consisting of diethylaluminium chloride/thioanisole at -78 °C which resulted in some of the product being cleaved from the resin.[282] As a result, in subsequent studies, the Cbz group was deemed inappropriate and replaced with Fmoc.[283] The phthalimide group meets the requirements previously outlined. The conditions to unmask this group reported in the literature typically use hydrazine.[313] Considering future potential applications, the use of hydrazine could potentially limit the use of certain commercially available amino acids with sensitive protecting groups such as ivDde. As a less harsh alternative, ethylene diamine has been employed in the deprotection of phthalimide offering increased reactivity and safer conditions, and is performed in butanol or isopropanol at reflux.[314, 315] Phthalimide was therefore selected as a suitable protecting group for **BB1**.

The EGTA-derived building block, **BB2**, differed from the 'standard' derivatives frequently employed in the development of Ca-responsive SCAs. The use of benzyl esters as orthogonal protecting groups

is commonly used which are again incompatible with SPS due to the need for deprotection with heterogeneous catalysts.[190] The derivative developed here contains an Fmoc protecting group which is routinely removed in SPS.

The final macrocyclic building block, **BB3**, is one which is routinely used in the synthesis of Ca^{2+}-responsive SCAs.

5.3 Results and discussion

5.3.1 Synthesis of BB1

The synthesis of **BB1** was carried out in accordance with previously reported procedures (Scheme 8).

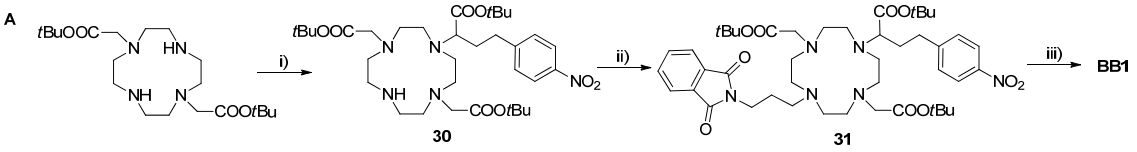

Scheme 8. Synthetic route towards **BB1**. Reagents and conditions: (i) *tert*-butyl 2-bromo-4-(4-nitrophenyl)butanoate, $NaHCO_3$, MeCN, RT, 65 % (ii) *N*-(3-bromopropyl)phthalamide, K_2CO_3, MeCN, 70 °C, 66 %. (iii) H_2, Pd/C, EtOH, 35 psi, RT, 78 %. Reproduced with permission from Ref 312. Copyright 2019 American Chemical Society.

Starting from DO2A (synthesised from a previously reported procedure),[316] monoalkylation with *tert*-butyl 2-bromo-4-(4-nitrophenyl)butanoate in acetonitrile with sodium bicarbonate as the base yielded amine **30**. N-alkylation of the secondary amine was performed at reflux with N-(3-bromopropyl)phthalamide to give nitro **31**. Reduction of the aromatic nitro was carried out by catalytic hydrogenation with Pd/C in ethanol to give the final building block (**BB1**).

5.3.2 Synthesis of BB2

For the EGTA-derived building block (**BB2**), a number of designs were explored and a series of derivatives were synthesised (Figure 30). The final building block used further in this study (**BB2**) was synthesised via a series of synthetic steps commencing from **9** (Scheme 9).

The use of a phenyl isopropanol ester and Fmoc successfully provided a system in which both groups could be selectively deprotected and used further in the solid phase assembly process. Synthesis of the alkylating agent bearing the phenyl isopropanol ester was performed using a previously reported method (Scheme 9).[317]

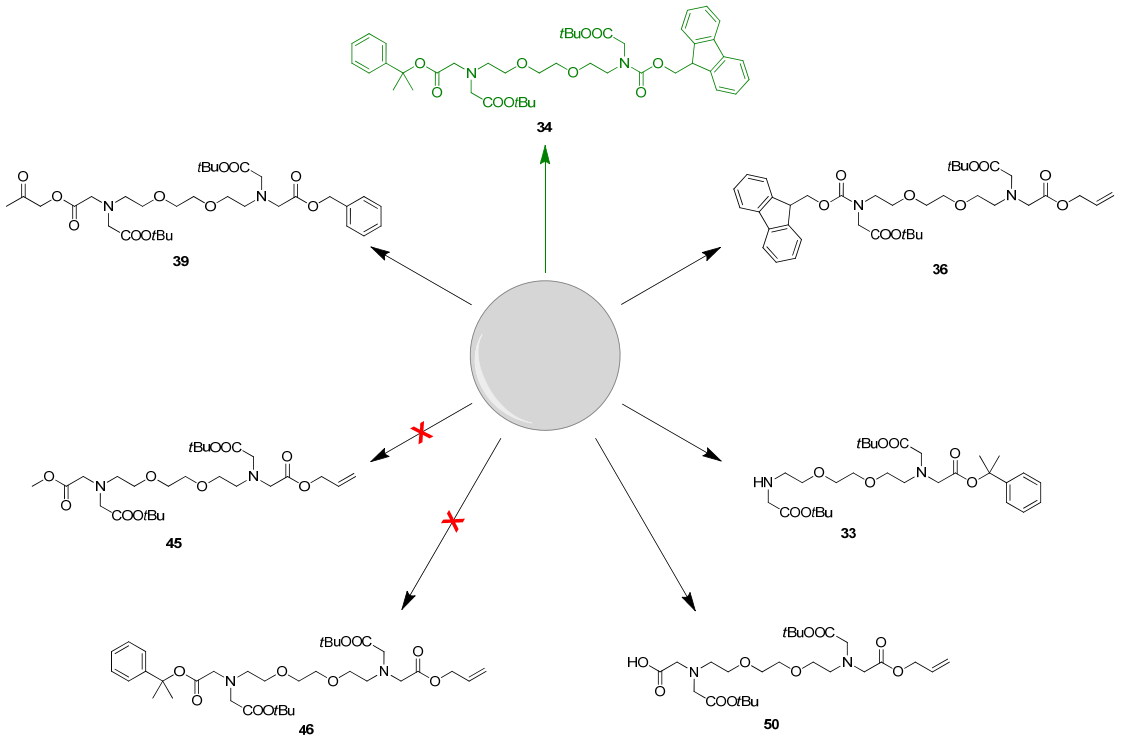

Figure 30. Structures explored in the development of **BB2**.

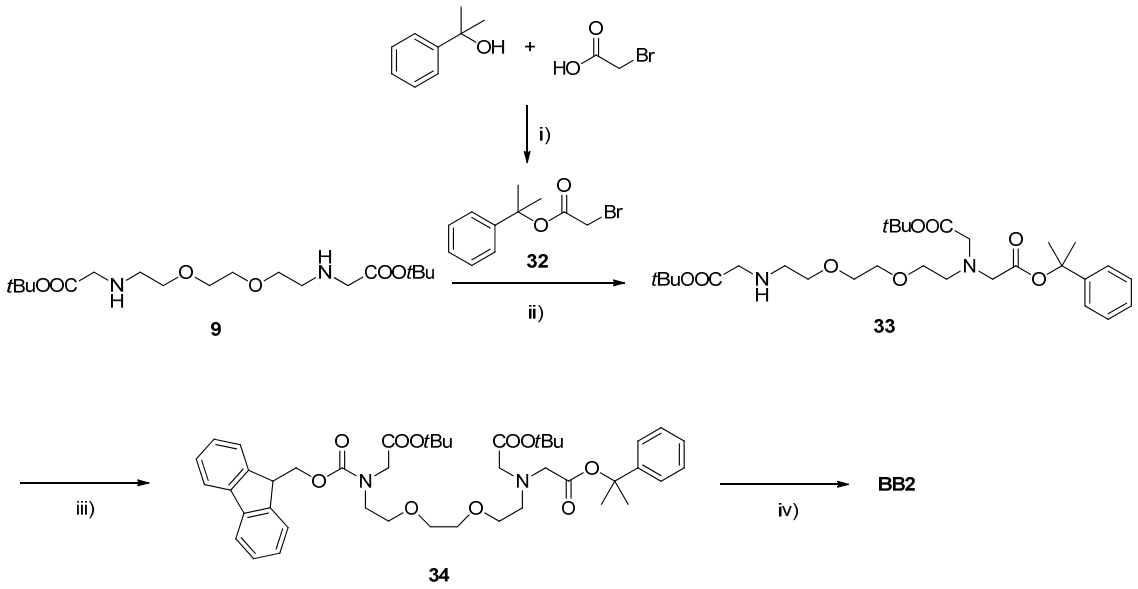

Scheme 9. Synthetic route towards **BB2**. Reagents and conditions: (i) DCC, DMAP, CH_2Cl_2, 0 °C to RT, 49 %. (ii) K_2CO_3, MeCN, RT, 44 %. (iii) Fmoc-Cl, Na_2CO_3, H_2O/dioxane, 0 °C to RT, 70 %. (iv) 3 % TFA/ CH_2Cl_2, RT.

Specifically, Steglich esterification of bromoacetic acid was achieved with 2-phenyl-2-isopropanol, DCC and DMAP in dichloromethane giving **32**. Monoalkylation of **9** with **32** in acetonitrile with potassium carbonate as the base yielded amine **33**. Acylation of **33** with Fmoc-Cl was achieved with

sodium carbonate in a dioxane/water (1:1) mixture to afford **34**.[284] Finally, **BB2** was prepared via the cleavage of the phenyl isopropanol ester of **34** in a solution of 3% TFA in dichloromethane. **BB2** was used in subsequent reactions without further purification. Although **BB2** was the EGTA-derived unit used to successfully synthesise the bismacrocyclic probe in this study, a series of alternate derivatives were initially explored for their suitability. **BB2** was initially developed through a synthetic route closely resembling that described previously with an allyl ester in place of the phenyl isopropanol ester (Scheme 10).

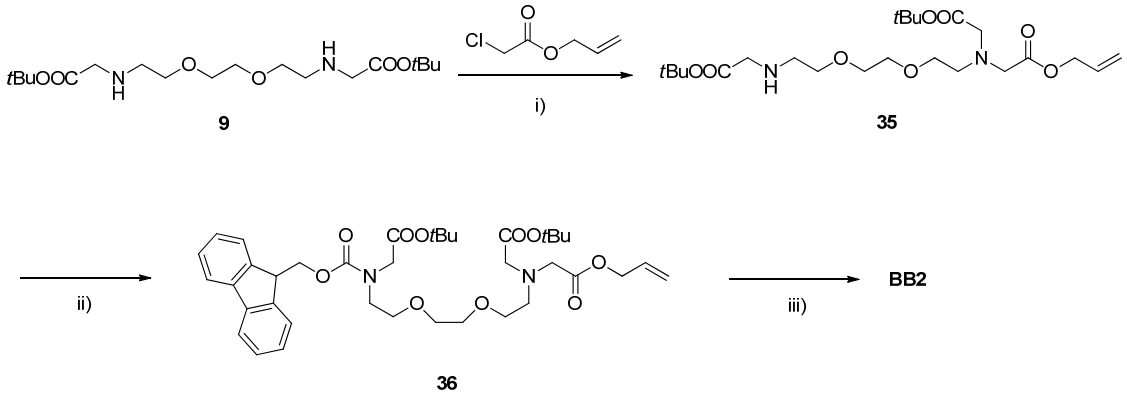

Scheme 10. Alternative synthetic route towards **BB2**. Reagents and conditions: (i) K_2CO_3, MeCN, RT, 35 %. (ii) Fmoc-Cl, Na_2CO_3, H_2O/dioxane, 0 °C to RT, 63 %. (iii) $Pd(PPh_3)_4$, $C_6H_5SiH_3$, CH_2Cl_2, RT.

Proceeding in the same fashion as previously described, monoalkylation of **9** with allyl chloroacetate in acetonitrile with potassium carbonate as the base gave amine **35**. Treatment with Fmoc using the same procedure previously described gave **36**.[284] The carboxylic acid was revealed by deprotection of the allyl ester with tetrakis(triphenylphopshine)palladium(0) catalyst and a phenylsilane scavenger in dichloromethane. Although this resulted in the same product, the route via the phenyl isopropanol ester derivative was selected for a variety of reasons. Specifically, the initial monoalkylation reaction gave significantly higher yields in a shorter reaction time, resulting in a derivative that could be purified by column chromatography more easily. In the case of **33**, the reaction proceeded for two days after which it could be easily purified with a total yield of 44%. In contrast, the allyl derivative **35** was synthesised with a reaction time in the region of four days with a yield of 34% after several days of tedious purification and the use of copious amounts of solvent. Therefore, the method described in Scheme 9 was selected as the synthetic route towards **BB2**.

In addition, derivatives with two orthogonal ester functions (**39, 45, 46,** Figure 30) were designed. Successful synthesis of such derivatives would enable the use of more commonly performed coupling procedures to be explored.

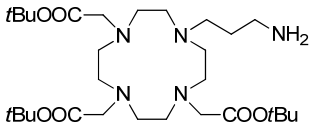

Figure 31. Chemical structure of DO3A-propyl amine.

Specifically, selective deprotection of one ester and subsequent coupling to **BB1**, followed by removal of the remaining ester function and coupling to an amine derivative of **BB3** as the concluding step of the bismacrocycle assembly (Figure 31). EGTA derivative **40** with a benzyl and acetol ester function was synthesised across a series of steps (Scheme 11). Monoalkylation of **9** with benzyl bromoacetate following a modified literature procedure yielded **37**.[190] Bromide **38** bearing an acetol ester function was then synthesised following a previously reported method involving bromoacetyl bromide and hydroxypropan-2-one and subsequently used for the alkylation of **37** affording protected EGTA-derivative **39**.[318] Deprotection of the benzyl ester by catalytic hydrogenation with Pd/C catalyst in ethanol, revealed the final derivative **40**.

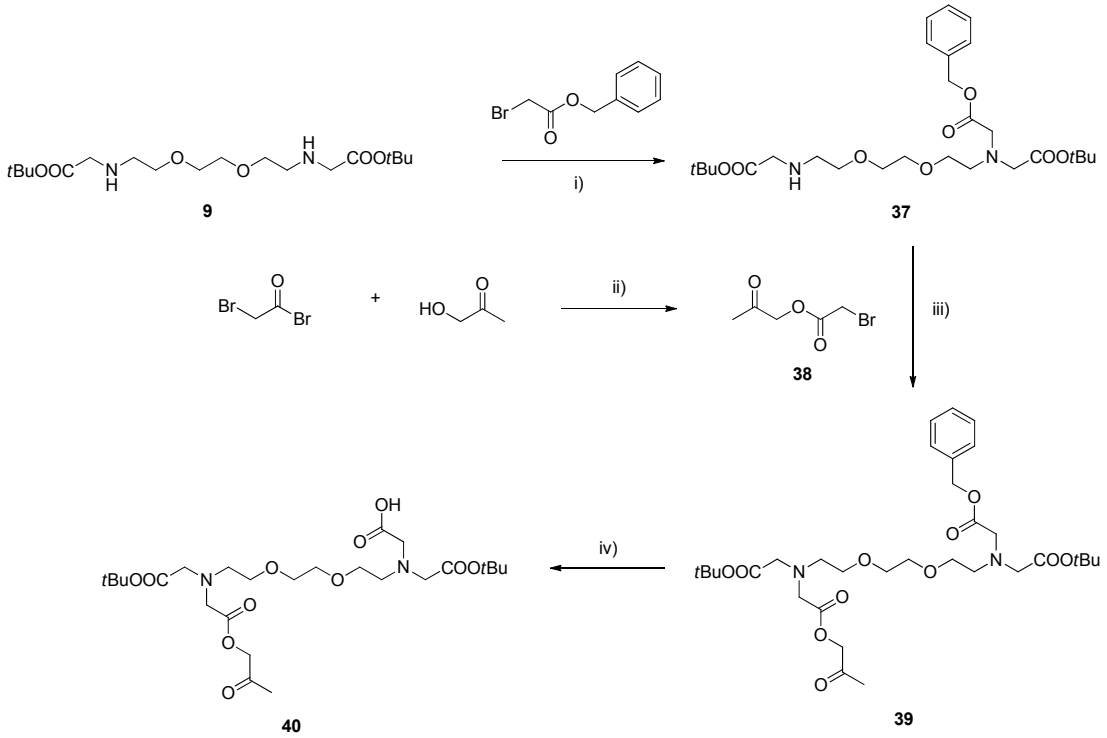

Scheme 11. Synthetic route towards **40**. Reagents and conditions: (i) K_2CO_3, MeCN, RT, 42 %. (ii) K_2CO_3, CH_2Cl_2, 0 °C, 47 %. (iii) K_2CO_3, MeCN, 70 °C, 36 %. (iv) H_2, Pd/C, EtOH, 3 Bar, RT, 88 %.

In order to test the viability of such a compound for use with the SPPS method, a simple model peptide consisting of three amino acids (Lys(Mtt)-Gly-Gly-NH_2, **41**) was synthesised on resin using standard peptide coupling conditions (Scheme 12). EGTA derivative **40** was then coupled to the

terminal amine of the peptide. The reaction was assessed by the Kaiser test, which indicates the presence or absence of free primary amines, and by LC-MS revealing the success of the coupling to give peptide **42**. The terminal acetol ester of **42** was then subject to deprotection conditions to reveal the free carboxylic acid (**43**) (Scheme 12) which was confirmed by LC-MS and a resin test which utilises a malachite green solution for the rapid and sensitive detection of free COOH on resin.[319, 320]

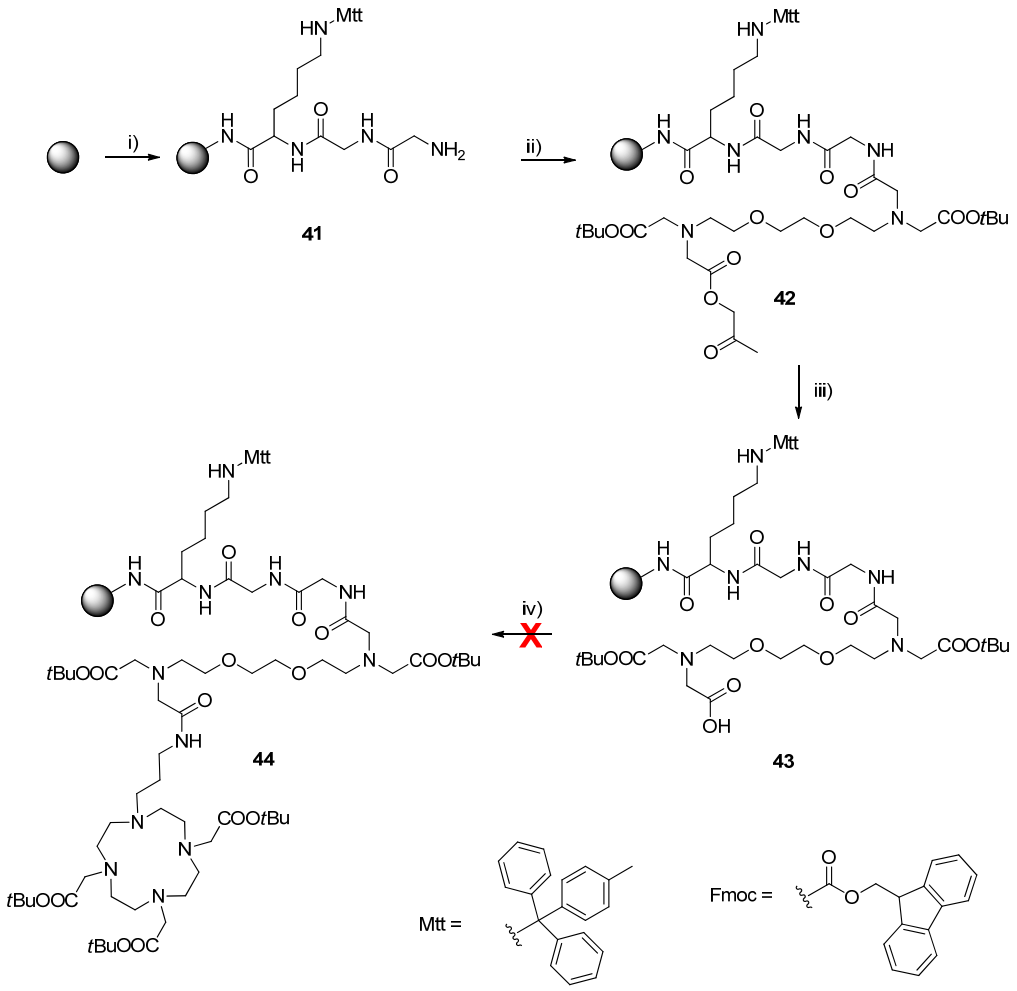

Scheme 12. Assessment of **40** as a suitable EGTA-derived building block. Reagents and conditions: (i) Fmoc-SPPS. (ii) 40, HATU, DIPEA, DMF, RT. (iii) TBAF.3H_2O, THF, RT. (iv) DO3A-PA, RT, see Table 6.

With the successful deprotection of the acetol ester, trials for the coupling of DO3A-propyl amine (Figure 31) were carried out (Scheme 12). A number of coupling conditions were attempted (Table 6) all of which resulted in no product formation (**44**) according to LC-MS analysis. It was speculated that the conditions for acetol ester deprotection could possibly affect the following coupling reaction. Alternatively, the availability of the carboxylic acid for coupling could be limited or not sufficiently

activated by the coupling agents employed therefore hindering the reaction. With this in mind, compound **40** was deemed unsuitable and alternative building blocks were explored.

Table 6. Coupling conditions tested in the coupling of DO3A-PA and **42**.

Coupling conditions	Observations/result
HATU, DIPEA, DMF	No product
EDC, HOBt, 4-methylmorpholine, DMF	No product
DIC, HOBt, DIPEA, DMF	No product
PyBOP, HOBt, DIPEA, DMF	No product
Via an activated succinimide ester intermediate	No product

In the case of **46**, a methyl and allyl ester variant was selected as a possible alternative to **40**. Unfortunately, synthetic issues were encountered preventing **46** from being examined further (Scheme 13).

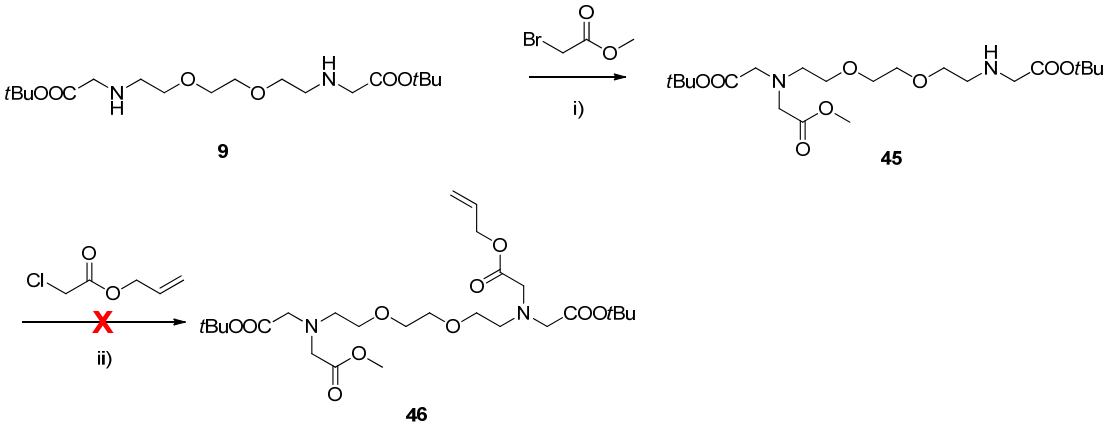

Scheme 13. Attempted synthesis of EGTA building block precursor **46**. Reagents and conditions: (i) K_2CO_3, MeCN, RT, 33 %. (ii) K_2CO_3, MeCN, 70 °C.

Monoalkylation of **9** with methyl bromoacetate in acetonitrile with K_2CO_3 as the base yielded **45** which was then subject to exhaustive alkylation with allyl chloroacetate. Despite indications that the reaction had proceeded, attempts to purify the crude material proved unsuccessful with the product (**46**) not being isolated. Further synthetic modifications were pursued through the use of a phenyl isopropanol ester as an alternative to the methyl ester previously attempted. Amine **33** was subject to alkylation with allyl chloroacetate in acetonitrile with potassium carbonate base at reflux (Scheme

14). However, despite being left to react for several days and the addition of further alkylating agent, the reaction did not proceed. As the allyl ester is an ideal and widely utilised orthogonal protecting group with very specific, SPPS friendly removal conditions, further attempts to incorporate such a moiety were pursued.

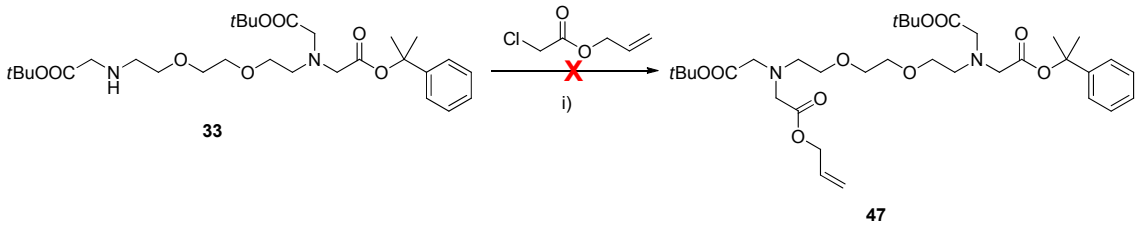

Scheme 14. Attempted synthesis of EGTA building block precursor **47**. Reagents and conditions: (i) K_2CO_3, MeCN, 70 °C.

Carboxylic acid **50** was designed and synthesised in which the allyl ester functionality was successfully installed. Alkylation of the monobenzyl derivative **27** with benzyl bromoacetate yielded **48** (Scheme 15).

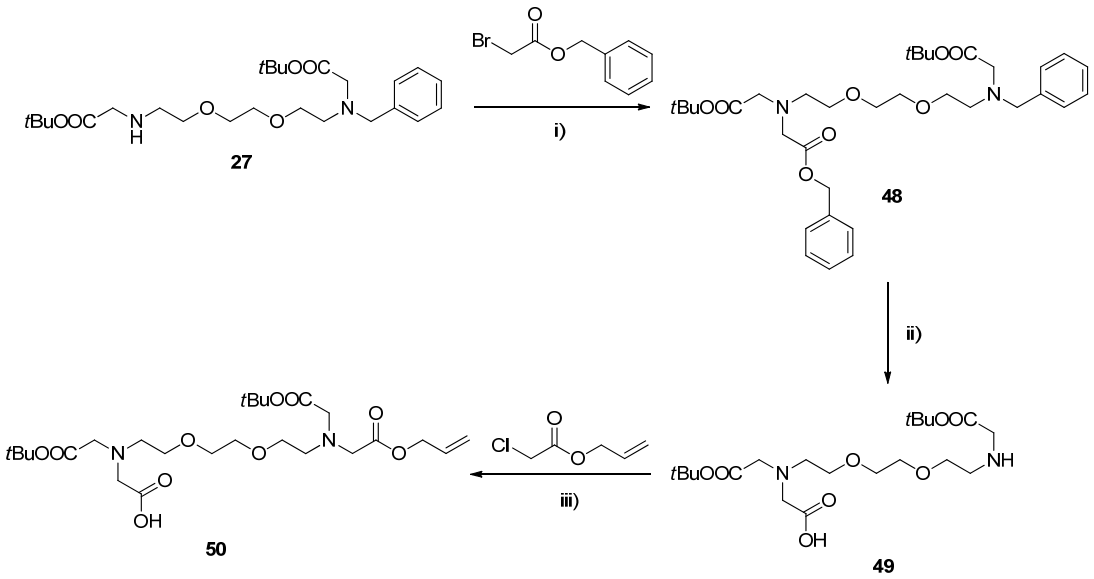

Scheme 15. Attempted synthesis of EGTA building block **50**. Reagents and conditions: (i) K_2CO_3, MeCN, 70 °C, 53 %. (ii) H_2, Pd/C, EtOH, 3 bar, RT, 96 %. (iii) K_2CO_3, KI, DMF, RT.

Both benzyl protections on the amine and carboxylic acid were then removed via catalytic hydrogenation with Pd/C in ethanol to afford **49**. Exhaustive alkylation with allyl chloroacetate yielded the final EGTA-derivative **50**. This was used further for coupling to **BB1** attached to the resin (see later, Scheme 18)**,** however attempts to remove the allyl ester on solid phase proved to be problematic preventing further progress. N-alkylation was explored as one alternative method to

anchor the EGTA-derived building block to the peptidyl resin. This approach has previously been used for the functionalization of various azamacrocycles.[321] The design requirements for such a derivative involved using a mono functionalised scaffold in which the remaining free amine could be used as the point of attachment. Two compounds were tested with this method, one with an allyl ester (**35**) and the other with a phenyl isopropanol ester (**33**) previously described. As a test, a model peptide consisting of three glycine units was synthesised with the final free amine coupled to bromoacetic acid with DIC as the coupling agent (**51**, Scheme 16).

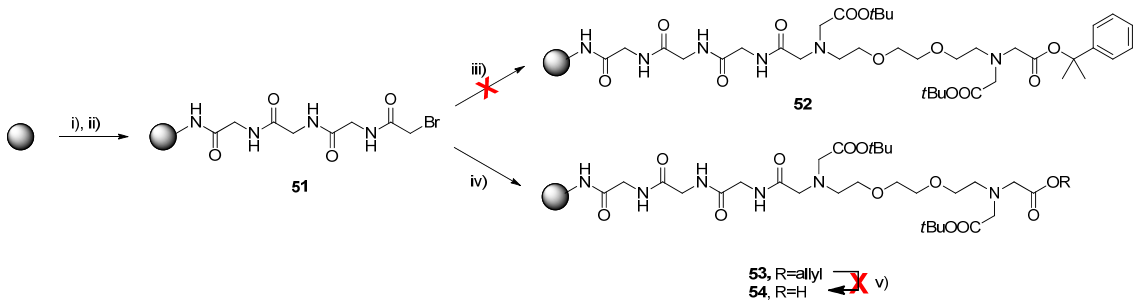

Scheme 16. N-alkylation coupling tests with **33** and **35**. Reagents and conditions: (i) Fmoc-SPPS. (ii) $BrCH_2COOH$, DIC, RT. (iii) **33**, DMF, RT. (iv) **35**, DMF, RT. (v) $Pd(PPh_3)_4$, $PhSiH_3$, CH_2Cl_2, RT.

N-alkylation was successful with the allyl ester derivative (**35**), however further attempts to remove the allyl ester protection on the solid support were unsuccessful and thus could not be used further in this reaction scheme. Utilising the alternative phenyl isopropanol analogue (**33**) proved unsuccessful in the alkylation step, halting the progress of this alternative approach.

5.3.3 Synthesis of BB3

The DO3A-derived building block (**BB3**) was synthesised according to previously published procedures (Scheme 17).[180, 182]

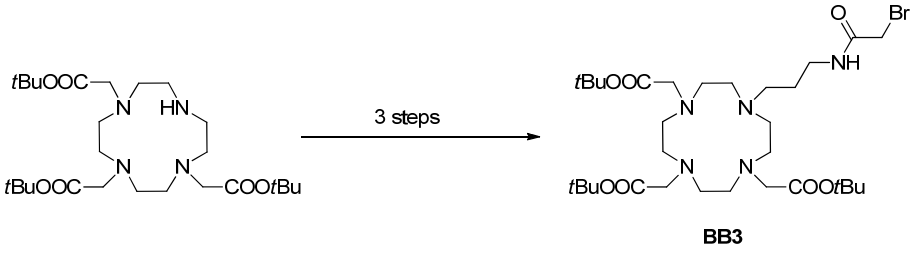

Scheme 17. Synthetic route to **BB3** previously reported.[182]

Specifically, DO3A was subjected to exhaustive alkylation with benzyl (3-bromopropyl)carbamate to yield the protected amine. Unmasking of amine was achieved by catalytic hydrogenation with a Pd/C catalyst in ethanol, which was subsequently coupled to bromoacetic acid with DCC as the coupling agent to give the final building block (**BB3**). With the building blocks prepared, assembly of the SCA was performed utilising solid phase synthetic techniques.

5.3.4 Synthesis of Gd_2L^7

A rink amide resin was selected as the solid support in which the SCA could be built upon. Cleavage conditions for this resin (95 % TFA, 2.5 % H_2O, 2.5 % TIS) were compatible with the synthetic procedures used throughout the synthesis. Additionally, after cleavage of the resin, a terminal amide would occupy the C-terminus of the peptidyl SCA. The peptide scaffold (Lys(Mtt)-Gly-Gly-NHFmoc) in which both the bismacrocyclic SCA and functional molecule could be conjugated was synthesised following standard Fmoc-SPPS techniques (coupling – HBTU, DIPEA, DMF; Fmoc deprotection – 20% piperidine/DMF).[276] In each of these coupling procedures, three equivalents of the relevant Fmoc protected amino acid was determined to be sufficient in providing complete conversion with a reaction time in the range of two to three hours. The coupling and subsequent Fmoc deprotection efficiencies were in each case assessed by the Kaiser test. In the event of an inefficient coupling reaction, the peptidyl resin was treated further with half of the initial amount of amino acid, coupling agent and base used to provide full conversion. It should also be noted that after the coupling of the first amino acid in the sequence, a capping step was carried out with a solution of acetic anhydride in pyridine. The importance of this procedure was to ensure all of the initial sites available for conjugation were occupied, thus aiding in reducing the amount of potential incorrect or deletion sequences, and subsequently avoiding further complications during the final purification steps. With the initial peptide sequence synthesised, a spacer unit was introduced to provide further distance from the resin to the bulky SCA components (Scheme 18).

Furthermore, the spacing unit enabled the functional group at the N-terminus to be exchanged from a primary amine to a carboxylic acid to allow for the coupling of **BB1**. Succinic anhydride was selected to be the spacer moiety and was easily reacted with the N-terminus of the peptide through ring opening of the anhydride to provide the final peptidyl unit (**55**). Attachment of **BB1** to the carboxylic acid terminus of the peptidyl unit was carried out through the unmasked aromatic amine with the more active HATU coupling agent and DIPEA as the base in DMF to give phthalimide **56**. In total, 2 equivalents of **BB1** were required to complete the coupling over a period of 18 hours. This is particularly significant, as common amino acids can be considered expendable and are used in ratios approximately five times that of the resin in typical SPPS procedures. However, the solution

synthesis of **BB1** is complex and time-consuming, so preservation of compound is desired. Removal of the phthalimide protecting group was easily achieved through the treatment of the peptidyl resin with an excess of ethylene diamine in isopropanol, affording amine **57**. The use of ethylene diamine enabled efficient deprotection in less harsh than those previously reported.[314, 315] It should be noted that exchanging the solvent for ethanol had detrimental effects on the efficiency of the reaction, due to the formation of clusters of the resin which most likely reduced access to all of the reaction sites. Next, the coupling of the EGTA-derived component was explored in which both **50** and **BB2** were examined (Scheme 18 + 19, respectively).

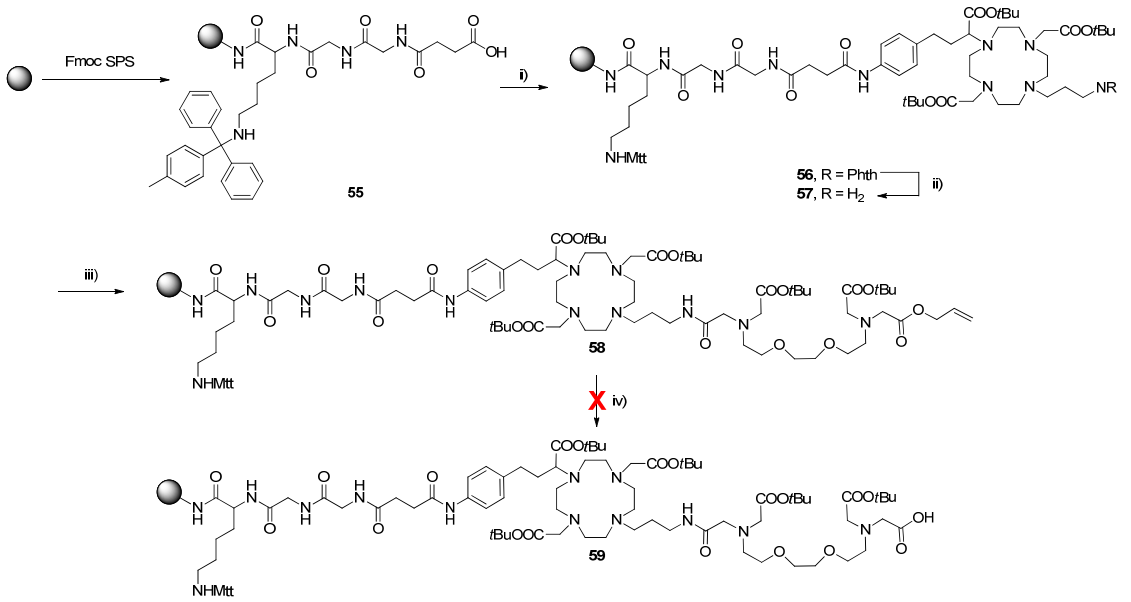

Scheme 18. Attempted synthesis of the final SCA using **50** as the EGTA scaffold. Reagents and conditions: (i) **BB1**, HATU, DIPEA, DMF, RT. (ii) $NH_2CH_2CH_2NH_2$, *i*PrOH, RT. (iii) **50**, HATU, DIPEA, DMF, RT. (iv) $Pd(PPh_3)_4$, C_4H_9NO or $PhSiH_3$, DMF, RT.

For allyl **50**, coupling to amine **57** was achieved using identical conditions as those employed for the conjugation of **BB1**. Removal the terminal allyl ester proved unsuccessful under standard deprotection conditions frequently employed in the unmasking of both allyl esters and Alloc carbamates, similar to that described previously. The inability to reveal the carboxylic acid prevented the preparation of the bismacrocyclic SCA being pursued via this route.[322] Alternatively, the coupling of **BB2** to amine **57** was achieved with conditions described previously to give Fmoc protected derivative **60** (Scheme 19). Again, only two equivalents of **BB2** were required to complete the reaction over a period of one day. Fmoc deprotection was achieved with repeated applications of a 40 % piperidine in DMF solution to reveal the secondary amine. The final macrocyclic building block (**BB3**) was then alkylated onto the scaffold to yield **61**. It should be noted that after the removal of

Fmoc, the alkylation procedure with **BB3** required a total of 4.8 equivalents of the building block added as two separate portions to drive the reaction to full conversion. While the increased amount of building block used relative to that of **BB1** and **BB2** is not ideal, the preparation of **BB3** follows a much more simplified synthetic route and can be produced routinely in large quantities, giving it a degree of increased expendability.

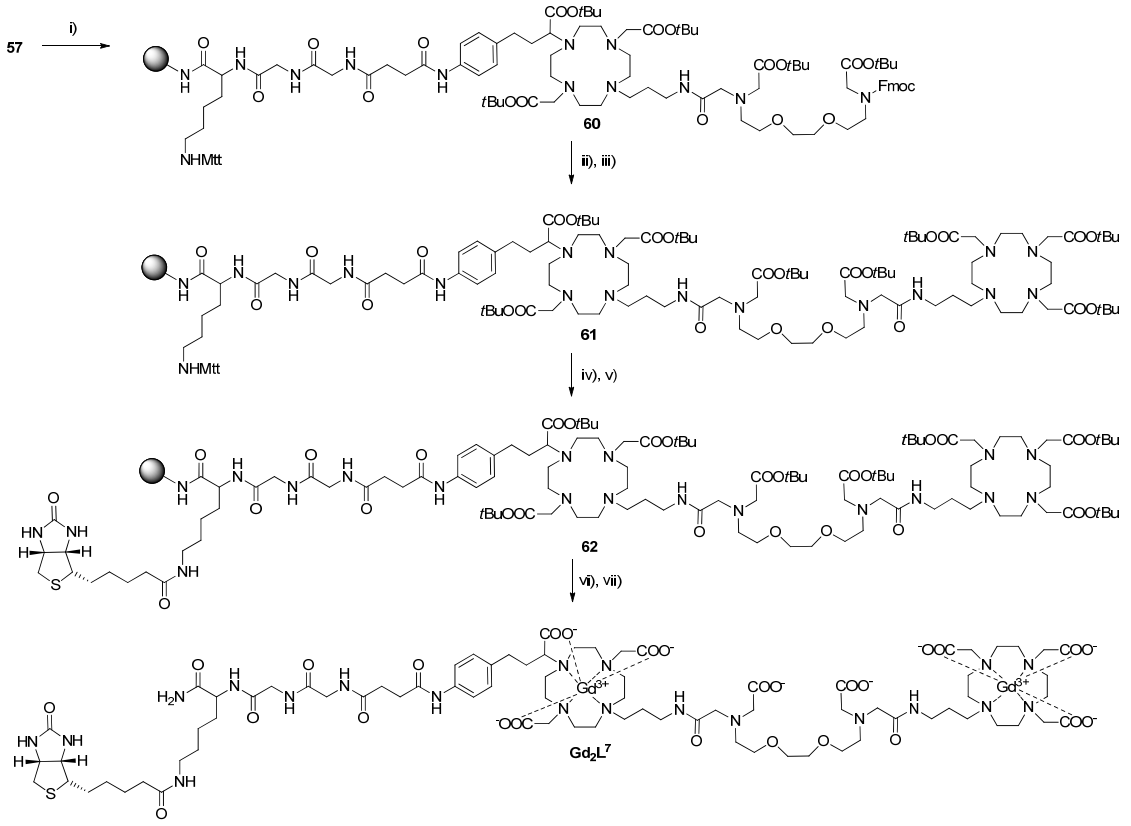

Scheme 19. Synthesis of $\mathbf{Gd_2L^7}$. Reagents and conditions: (i) **BB2**, HATU, DIPEA, DMF, RT. (ii) 40 % piperidine/DMF, RT. (iii) **BB3**, DIPEA, DMF, RT. (iv) TFA/triisopropylsilane/CH_2Cl_2 (3:3:94), 4x2 min, RT. (v) biotin, HATU, HOBt, DIPEA, DMF, RT. (vi) TFA/triisopropylsilane/H_2O (95:2.5:2.5). (vii) $GdCl_3.6H_2O$, H_2O, pH 7, RT.

Following the full assembly of the bismacrocyclic SCA onto the peptidyl resin, the introduction of a functional molecule was conducted by the removal of the Mtt protecting group of the lysine side chain followed by the coupling of the desired functional molecule. The purpose of this study was to demonstrate the principle of utilising SPPS methodologies to expand the scope of previously developed SCAs. To this end, as a proof of concept, biotin was incorporated as the functional molecule. Biotin was an ideal choice as its interactions with the protein avidin and related analogues have been thoroughly investigated and the strong non-covalent interactions exploited in many diagnostic, therapeutic, imaging and targeting systems.[323]

Treatment of **61** with multiple rounds of a solution of TFA/TIS/dichloromethane (3:3:96) removed the Mtt protecting group. The resulting free primary amine was exposed to a solution of biotin, HATU, HOBt and DIPEA in DMF for 24 hours followed by a second addition of identical mixture to afford **62**. Detachment of **62** from the rink amide resin was achieved with a cleavage cocktail of TFA/TIS/H_2O (95:2.5:2.5) over four hours and the solid crude product obtained via precipitation from the TFA mixture with cold diethyl ether. Purification of the crude material with reverse phase HPLC provided the final ligand $\mathbf{L^7}$. Complexation with gadolinium chloride in water at neutral pH followed by removal of excess gadolinium with Chelex® yielded the final biotinylated SCA ($\mathbf{Gd_2L^7}$) with an overall yield of 24 % across the whole SPS synthetic process.

5.3.5 Relaxometric characterisation

The relaxometric behaviour of the newly developed $\mathbf{Gd_2L^7}$ system was investigated through proton longitudinal and transverse relaxometric titrations with Ca^{2+}. The determined behaviour was greater than that of the original bismacrocycle SCA previously reported,[182] showing that the incorporation of the additional peptide linker and biotin moiety had no negative effect on the response of $\mathbf{Gd_2L^7}$. Both r_1 and r_2 exhibit increased upon the addition of Ca^{2+}. The longitudinal relaxivity increased by 118 % from 3.47 to 7.58 mM^{-1} s^{-1} while the transverse relaxivity rose by 150 % from 5.40 to 13.57 mM^{-1} s^{-1} (Figure 32). Naturally, the next phase was combine this biotinylated probe with avidin. This was performed both with the natural protein and with streptavidin coated beads. The assessment of available biotin binding sites available for $\mathbf{Gd_2L^7}$ was assessed by HABA assay, which revealed three sites (Figure S21.). The combination of both was carried out through incubation of both components in buffer (HEPES for avidin, PBS for streptavidin beads) for two hours, followed by washing procedures by centrifugation through 3 kDa cutoff filters to remove any excess unbound $\mathbf{Gd_2L^7}$. Subsequently, relaxometric titrations (avidin conjugate), T_1-weighted and T_2/T_1 ratiometric MR phantoms were recorded (Figure 32).

For the avidin conjugate, an increase in both r_1 (4.55 to 5.99 mM^{-1} s^{-1}) and r_2 (22.96 to 40.77 mM^{-1} s^{-1}) was observed in the relaxometric titrations upon Ca^{2+} addition saturating at 1.1 equivalents of Ca^{2+} (Figure S22). The overall enhancement in both r_1 (31 %) and r_2 (78 %) was less than that of $\mathbf{Gd_2L^7}$, although a decrease in r_1 is expected when conjugating a smaller SCA to a nanosized conjugate.[188] Subsequent, MR phantom recordings showed an increase in signal to noise ratio (SNR) for the T_1-weighted signal of about 7 % (Figure S23) and a change in SNR for the T_2/T_1 ratiometric protocol of 18 % (Figure 32). While these changes are small and expected from the observed changes in the relaxometric titration, the fundamental principles of this study were to demonstrate the application of SPS as a powerful synthetic tool for future Ca^{2+}-responsive SCA development. The choice of

biotin/avidin was clearly suboptimal and only served to demonstrate the principle. Specific interactions between the **Gd_2L^7** and avidin evidently impact the responsivity of the probe.

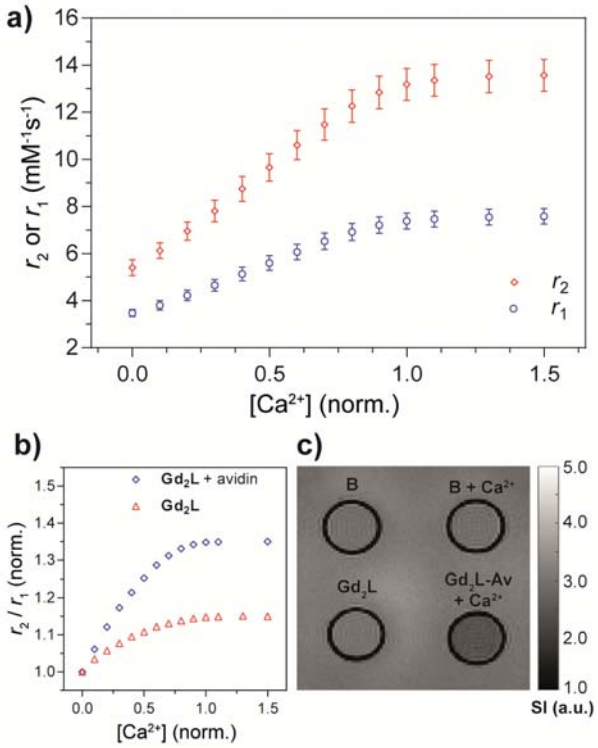

Figure 32. Relaxometric and MRI phantom experiments for **Gd_2L^7** and **Gd_2L^7** + avidin (**Gd_2L^7**-Av) with Ca^{2+} ([Gd^{3+}] = 1 mM, pH 7.4, 50 mM HEPES, 25 °C, 7 T). a) Relaxometric titration curves for **Gd_2L^7** with Ca^{2+}. b) Ratio of r_2 over r_1 from relaxometric titrations of **Gd_2L^7** and **Gd_2L^7**-Av with Ca^{2+}. c) T_2/T_1 ratiometric MR phantom images of the buffer (B (HEPES)) or **Gd_2L^7**-Av sample tubes in presence and absence of Ca^{2+} (1 equiv.). Reproduced with permission from Ref 312. Copyright 2019 American Chemical Society.

For the avidin coated beads, T_1-weighted MR phantom measurements revealed a change in SNR of 5 % upon Ca^{2+} addition (Figure S24).

5.4 Conclusion

In conclusion, a solid-phase protocol was employed for the development of a functionalized bismacrocyclic Ca^{2+} responsive SCA. Diverse SPS friendly building blocks were prepared including **BB1** with a pthalimide protecting group which was successfully removed using mild conditions. Combination of the building blocks with a peptide chain was achieved. The incorporation of an additional peptide scaffold and biotinylated group did not inhibit the responsiveness of **Gd_2L^7** to Ca^{2+}. Although the time-consuming synthesis of building blocks is still required, the process of combining them through SPS reduces the number of purification steps in comparison to solution

phase synthesis. Furthermore through the use of a peptide backbone, significantly high flexibility can be achieved in terms of designing a molecule which can be highly specific, biocompatible and possess a range of functional molecules. Although the results of this specific probe with avidin were suboptimal, the methods described here present an exciting range of possibilities for the design and synthesis of a host of future bifunctional bioresponsive probes. Utilising this powerful synthetic tool, multifunctional molecules or multimeric species can be developed, providing greater diversity and increased specificity of future molecular probes, and therefore further expanding the scope of use for future SCAs.

6 Solid-Phase Synthesis of a Targeted Bioresponsive MRI Probe.

6.1 Introduction

Clinically approved Gd^{3+}-based MRI CAs are of low molecular weight and interact in a non-specific manner with surrounding tissues, leading to faster clearance.[324] Additionally, their application for use in the early detection of disease imaging of specific biological events is limited. Developing CAs with high specificities to molecular targets enables prolonged lifetimes and can aid in the detection and treatment monitoring of diseases.[324] Challenges arise during the development process of such targeted MR CAs, in which two strategies have been employed.[61, 324] Namely, conjugation of a CA to an antibody, small organic molecule or peptide; or by developing a CA whose structure imitates that of a targeting vector. The development of such a CA must fulfill a number of requirements, specifically, that the CA must have an appropriate affinity and high specificity for the target of interest. The target itself should be one which is present in amounts relevant for MRI. Furthermore, any unbound probe should experience a rapid washout in comparison to the bound analogue and finally the relaxivity of the bound CA should be high.[61] Examples of targeted CAs include those containing hydrophobic moieties (Figure 5, Chapter 1) which can interact with serum albumin through non-covalent binding allowing for longer *in vivo* lifetimes. In order to further diversify and improve the specificity of CAs, various targeting vectors have been exploited to envisage specific events of interest.[61, 325] Frequently, these vectors are based on peptide sequences which specifically interact with a biological structure such as a protein. EP-2104R is a fibrin targeted CA which specifically differentiates fibrin from fibrinogen which circulates in the blood.[61] Composed of four Gd-DOTA units attached to a disulfide bridged cyclic peptide composed of six amino acids known to improve fibrin binding, this CA showed a much increased relaxivity when bound to fibrin.[61, 326-328] Specifically, the relaxivity of the unbound form was 11.1 mM^{-1} s^{-1} which increased to 24.9 mM^{-1} s^{-1} when bound (0.47 T, 37 °C). Additionally, the application of EP-2104R in human studies revealed a distribution similar to that of extracellular CAs which is cleared within 6 hours.[61, 329] Furthermore, EP-2104R proved effective in detecting thrombosis, making it the first targeted CA used to detect pathological biomarkers in humans.[329, 330]

Another vector which has been widely studied is that of the peptide RGD which is known to selectively bind to integrins. In the case of many synthesised molecular imaging probes, RGD or its cyclic derivative are used in cancer imaging where specific integrins are overexpressed.[331-337] As a target for neuroimaging, integrins are relevant cell surface receptors in the extracellular matrix that play important roles in many processes and diseases in the brain.[338] Due to the inherently low sensitivity of MRI, the inclusion of a targeting moiety and an increase the Gd^{3+} payload is desired and

can be achieved through the development of a multifunctional multimeric probe where the proportion of Gd^{3+} per particle is increased. As previously described (Chapter 5), SPPS provides an excellent platform for the development of peptide-based probes in which targeting units can be incorporated in a more straightforward manner compared to solution based chemistry. Additionally, with the flexibility afforded by the use of the peptide backbone, positions for the attachment of multiple SCAs can be exploited.

Following the development of a solid phase protocol for Ca-responsive SCAs (Chapter 5), the synthesis and characterisation of a multimeric MRI SCA with an RGD targeting vector was pursued. Specifically, the ability to incorporate a previously reported monomeric Ca^{2+}-responsive SCA onto a peptide-based unit through SPPS techniques is described and its responsivity to Ca^{2+} characterized. Furthermore, the synthetic protocol employed provides a degree of flexibility in which future SCAs can be developed for a range of targeted functions.

6.2 Synthetic design

Targeted imaging probes are generally based on similar template designs in which they possess both the imaging probe part and the targeting moiety joined together through a linker unit. The design approach described here followed this philosophy with a monomeric Ca^{2+}-responsive SCA coupled to an RGD targeting unit via a peptide backbone. The use of multiple lysine residues additionally allowed for the inclusion of three SCA per peptide (Figure 33).

In terms of synthetic approach, the method differs from that of the bismacrocyclic SCA previously described (Chapter 5). Specifically, the peptide backbone with targeting vector was assembled on the solid support prior to the attachment of the 'pre-prepared' monomeric Ca^{2+}-responsive SCA. For $\mathbf{Gd_2L^7}$, the probe was constructed step-wise on the peptidyl resin. Furthermore, for $\mathbf{Gd_2L^7}$ only one 'smart' unit was present per molecule; here we developed a multimeric species consisting of three SCA units per peptide scaffold, thus increasing the Gd^{3+} payload. The structure of the peptide unit was comprised of the RGD vector followed by a series of glycine and lysine amino acids which acted as spacer units and points of attachment respectively. The purpose of the glycine spacing units was to provide a reasonable distance between the lysine residues where the SCA units were attached, therefore reducing the potential synthetic complications due to any possible steric crowding that could be caused by the bulky macrocyclic units. Lysine residues were included to provide orthogonal amines which could be functionalised with the SCAs.

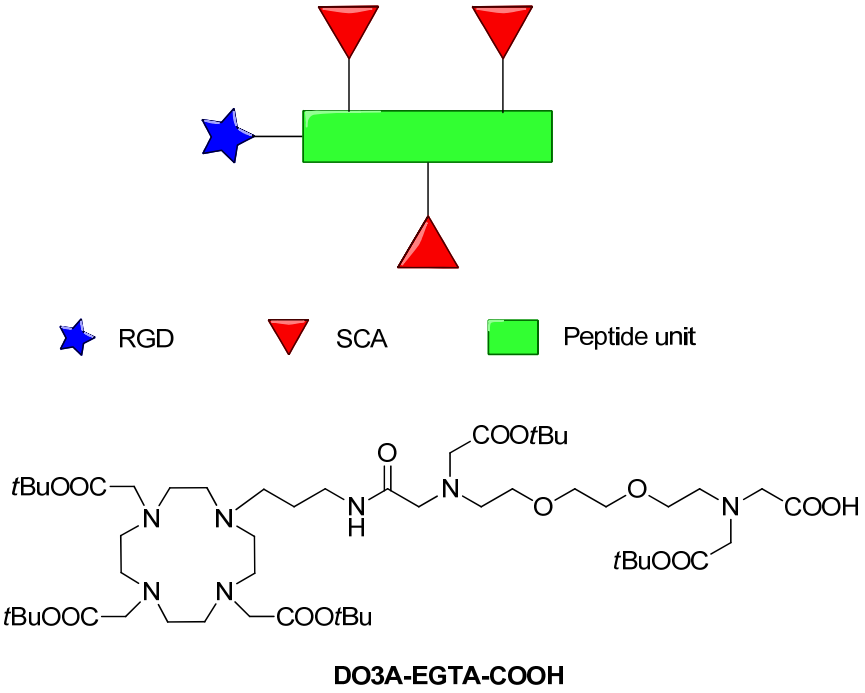

Figure 33. Representation of the molecular design of this RGD-targeted bioresponsive probe (top). Structure of the SCA (bottom).

6.3 Results and discussion

6.3.1 Synthesis of Gd_3L^8

Commencing from an Fmoc-protected Rink amide resin (loading 0.78 mmol/g), standard Fmoc SPPS protocols were employed to synthesise the peptide backbone. After the initial Fmoc-deprotection of the resin, a glycine residue was coupled as a spacer unit. Next, Fmoc-Arg(Pbf)-OH, Fmoc-Gly-OH and Fmoc-Asp(O*t*Bu)-OH were coupled sequentially to provide the linear RGD targeting vector. Subsequently, Fmoc-Gly-OH and Fmoc-Lys(Mtt)-OH residues were repeatedly coupled to form the final peptide unit, Resin-Gly-Arg(Pbf)-Gly-Asp(O*t*Bu)-Gly-Lys(Mtt)-Gly-Lys(Mtt)-Gly-Lys(Mtt)-Fmoc (**63**, Scheme 20). Removal of the acid labile Mtt protecting groups was achieved with a solution of 3% TFA in dichloromethane to yield amine **64**. Coupling of the **DO3A-EGTA-COOH** SCA units were then performed using HATU as the coupling agent, with HOBt and DIPEA as the base in DMF. It should be noted that attempts to perform this coupling reaction under conditions in which HOBt was omitted gave negative results due to incomplete coupling. To ensure as complete conversion as possible, a double coupling method was employed each with 24 hours of reaction time to afford **65**. Final cleavage from the resin and purification by RP-HPLC yielded the final multimeric targeted ligand $\mathbf{L^8}$, which was subsequently complexed with Gd^{3+} at pH 7 to give the final multimeric SCA,

Gd_3L^8. The ligand (**L^8**) was characterised by LC-MS, ^{1}H NMR and HRMS. Retention of the Fmoc protecting group simply provided a reference signal in the measured ^{1}H NMR which could assist in the analysis process. For future designs, this moiety could easily be removed and used as a point for further attachment of an additional SCA or functional molecule such a dye depending on the requirements for the compound.

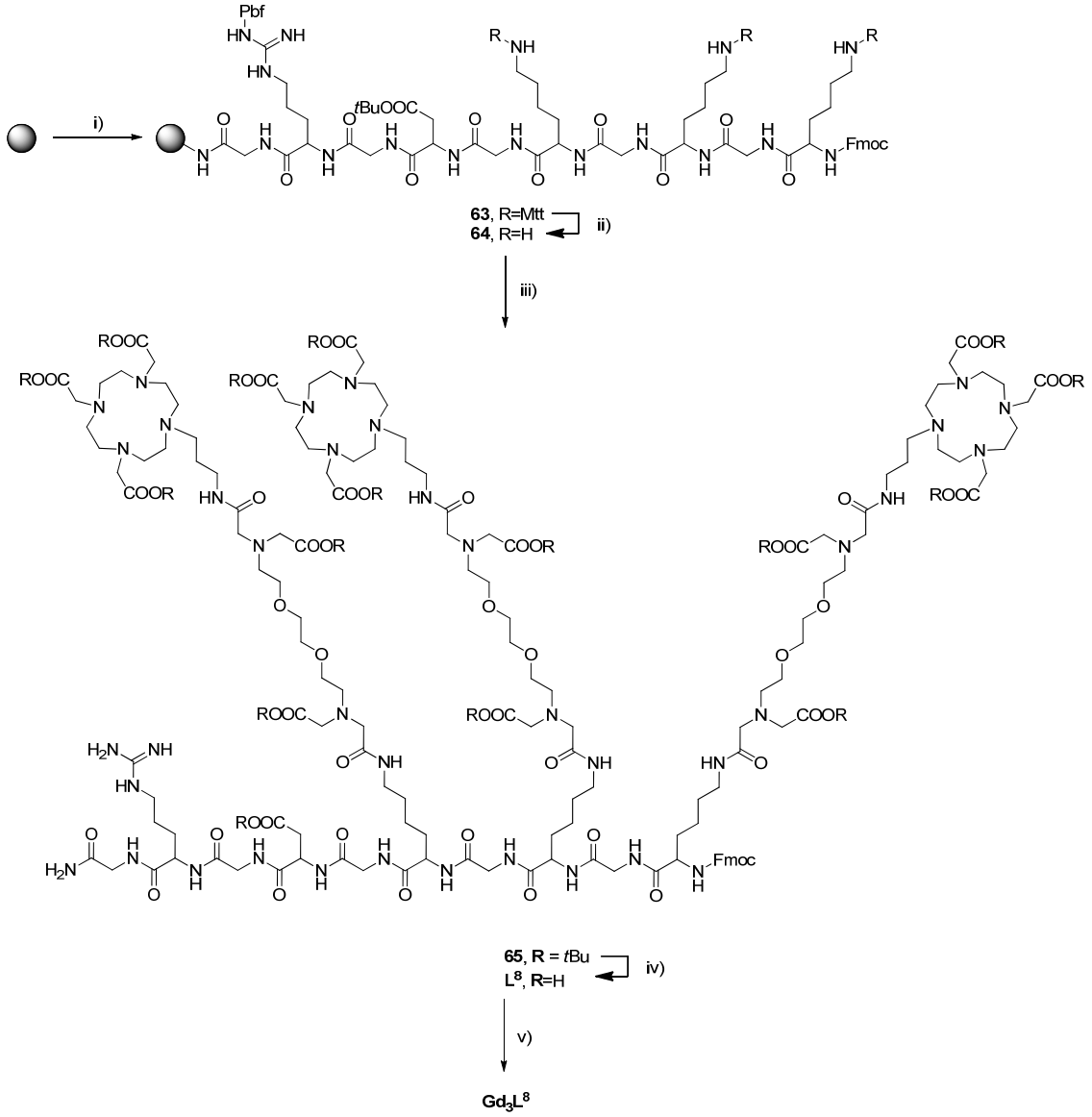

Scheme 20. Synthesis of **Gd_3L^8**. Reagents and conditions: (i) Fmoc-SPPS. (ii) TFA/TIS/CH_2Cl_2 (3:3:94), RT. (iii) **DO3A-EGTA-COOH**, HATU, HOBt, DIPEA, DMF, RT. (iv) TFA/TIS/H_2O, RT. (v) $GdCl_3.6H_2O$, H_2O, pH 7, RT.

6.3.2 Relaxometric characterisation

Proton longitudinal and transverse relaxometric titrations were performed with the addition of Ca^{2+} (Figure 34).

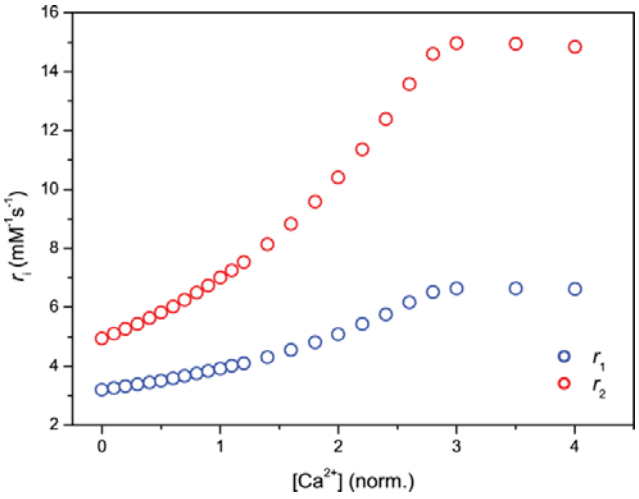

Figure 34. Relaxometric titration curves for **Gd_3L^8** ([Gd^{3+}] = 1 mM, pH = 7.4 (50 mM HEPES), 25 °C, 7 T).

The longitudinal relaxivity, r_1, displayed behaviour expected for such a system, specifically an increase in relaxivity from 3.20 to 6.64 mM^{-1} s^{-1} (107 %) was observed, saturating with 3 equivalents of Ca^{2+}.[137] The transverse relaxivity, r_2, also increased from 4.94 to 14.97 mM^{-1} s^{-1} (203 %). The difference in ratio of changes for r_1 and r_2 reflects on the multimeric nature of the system. The size of such a system is increased in comparison to the monomeric form which induces greater changes in r_2 in relation to r_1 resulting in an r_2/r_1 ratios of 1.46 and for the multimer, while remaining constant for the monomer. Although these changes in relaxivity are significant and in line with that expected of such a multimeric system, the span at which the changes take place is elongated and atypical with respect to previously investigated systems.[137] Possible explanations could arise from the lower affinity of the 'smart' units towards Ca^{2+}. Otherwise, the binding of Ca^{2+} to the peptide backbone could also be considered a possible explanation for this behaviour. Ultimately, this multimeric probe provides a significant enhancement in relaxometric behaviour and could be used as a potential candidate for *in vivo* T_1-weighted and r_2/r_1 ratiometric imaging applications.

6.4 Conclusion

The development and application of targeted probes is a widely investigated strategy to build platforms more suitable for the specific detection and monitoring of disease as well as biological events. Applying this strategy, a targeted Ca^{2+}-responsive multimeric probe was developed using more convenient solid phase synthesis protocols. The synthesis of the molecule was achieved

through building the peptide with a RGD targeting vector using standard Fmoc-SPPS techniques followed by coupling of the pre-made monomeric Ca^{2+}-responsive SCA to the ω-NH_2 moieties of the lysine residues. The behaviour of the newly developed multimer was assessed by proton longitudinal and transverse relaxometric titrations with Ca^{2+} revealing significant changes in line with that expected for such a multimeric unit. With the RGD targeting unit, an increase in specificity of this compound is expected due to the affinity of the moiety to integrins, making it an interesting candidate for future targeted *in vivo* applications. Furthermore, the approach undertaken here provides a template in which the targeting moiety can be exchanged to encompass alternate desired applications. Additionally, the number of SCAs appended can be altered through simple and convienient modifications of the peptide backbone, while the type of SCA can also be changed, providing extreme flexibility for any future SCA designs and further demonstrating the advantages of SPPS for this application.

7 Summary and outlook

To conclude, the aim of this PhD thesis was to explore and build upon knowledge regarding the development of Ca^{2+}-responsive MRI SCAs. With a shift towards functional imaging, the development of such bioresponsive CAs capable of reporting changes in their microenvironment is fundamental to visualising and understanding biological processes, and extracting vital information for the functioning of organs and tissue. Ca^{2+} is a robust target that is fundamentally important in a series of cellular processes and is widely touted as one of the main targets to track in the extracellular space whose deregulation is related to many neurodegenerative disease states. In this study, a series of projects were carried out demonstrating the development of highly responsive nano-sized, multimeric, and monomeric bioresponsive probes with either solution-based or solid phase synthetic techniques. Furthermore, the exploitation of alternate synthetic methods provided a basis for the development of functional probes with increased specificity and scope through the use of targeting moieties.

Chapter 3 describes a study aimed at characterising the favourable properties required to develop highly responsive nano-sized Ca^{2+}-responsive probes based on G4 PAMAM dendrimeric scaffolds for T_1-weighted and r_2/r_1 ratiometric imaging. Here, the dendrimeric scaffold played the role of SCA carrier enabling an increase in Gd^{3+} payload while also partaking in the responsive process through internal structural changes upon Ca^{2+} addition. Different types of cyclen-based macrocycle were utilised to assess the impact such changes can make. Namely, DO3A, DO3A-monoamide and DOTA macrocycles were used. These were linked to a bifunctional EGTA-derived chelator, which then was coupled to the dendrimeric surface to provide **DCAs$^{1\text{-}5}$**. Subsequent assessment of each DCA revealed that only the DO3A-based DCAs (**DCAs$^{1\text{-}2}$**) gave a significant relaxometric response to Ca^{2+}. Further investigations indicated a synergistic combination of properties led to these observed increases through the changing of q of the complex and the overall size and rigidity of the dendrimeric conjugate. Furthermore with the development of the highly responsive **DCA^{1}**, an improvement was made regarding the relaxometric response in comparison to the previously reported derivative,[191] making **DCA^{1}** a candidate for T_1-weighted and rapid r_2/r_1 ratiometric imaging *in vivo*. Finally, additional insights into the requirements for the development of highly responsive dendrimer Ca^{2+}-responsive SCAs were developed, providing a blueprint for future preparations. Overall, the responsive dendrimeric Ca-responsive SCAs reported here (**DCA$^{1\text{-}2}$**) offer beneficial properties of high Gd^{3+} loading and improved pharmacokinetic properties compared to monomeric analogues. Furthermore, with a significant relaxometric response to the coordination of Ca^{2+} and slow diffusion properties, this class of SCA offer significant advantages over monomeric derivatives.

Specifically, they allow for functional MRI studies to be performed over longer time periods while enabling the use of a rapid ratiometric imaging sequence which has advantages in terms of SNR per unit of time compared to conventional T_1- or T_2-weighted imaging sequences.

Chapter 4 focused on a deeper structural exploration of the monomeric units applied in the responsive dendrimers **DCAs**[1-2]. Through extension of the linker between the macrocyclic MR reporting and EGTA-derived Ca^{2+} chelator significant differences in the behaviour of the molecule in terms of relaxometric behaviour and *q* were observed. 1D and 2D NMR studies with a range of complexes (paramagnetic and diamagnetic) highlighted the structural changes undergone upon Ca^{2+} addition, which enable the responsive behaviour of such probes. DOSY experiments indicated species which did not change their diffusive behaviours significantly between the 'off' and 'on' states and thus do not change in terms of size or aggregation upon Ca^{2+} addition. Summarising the observations from this study, a clear correlation between minor structural changes of the SCA and responsive capabilities of the probes emerged, which further highlighted the need for specific and careful design of such CAs in order to achieve maximal relaxometric enhancements. **GdL**[6] produced similar relaxometric responses to that of the frequently applied propyl derivative while the shorter **GdL**[5] displayed smaller changes. As a result, **GdL**[6] is a potential candidate for future development and possible utilisation in functional studies *in vivo*. Furthermore, the results described highlight the significant importance of these types of systems as MRI SCAs for Ca^{2+} monitoring. Moreover, the evaluation of such systems provides a greater insight into the mechanism of response and the factors which influence such changes in relaxivity. With further knowledge of the systems, future probes can be developed which bring favourable properties, such as high relaxometric enhancement, to ultimately result in probes suitable for *in vivo* application.

Upon elaborating to more complicated designs, difficulties are often experienced in the synthetic process involving polyazapolycarboxylate scaffolds, limiting the scope of probe development using standard solution phase synthetic techniques. Chapters 5 and 6 focus on the utilisation of solid phase synthetic techniques as a viable alternative in the production of more complex SCA designs. Specifically, a functionalised derivative of the previously developed potent bismacrocyclic Ca^{2+}-responsive SCA was synthesised (Chapter 5). Additional functionalisation was achieved via the incorporation of biotin which was attached to a lysine residue of a small peptide. The synthesis of the bismacrocycle was performed in a step wise approach with various building blocks which were assembled on the solid support allowing for fast and efficient synthesis without the need for arduous intermediate purification steps. The biotinylated probe (**Gd_2L^7**) showed a slightly enhanced relaxivity to that of the non-functionalised derivative, indicating such changes did not affect the responsive

capabilities of the probe. However upon exposure to avidin, the relaxometric enhancement dropped possibly due to the specific interactions between this SCA and the protein or its arrangement in the binding pocket. While biotin is not the ideal functional molecule for this SCA, the methodology enables simple customisation in the development of future probes. For example, the inclusion of an alternate targeting moiety instead of biotin could be used. Otherwise, functional molecules of a different nature such as dyes or additional imaging probes could also be included. The number of functional moieties could also be expanded through a simple extension of the peptide backbone to provide numerous residues with additional points of attachment. Overall, this methodology enables the simple and convenient design of bioresponsive probes with increased functionality, thus expanding the scope of SCA application.

In chapter 6, a different approach was followed. Specifically, a targeted multimeric Ca^{2+}-responsive SCA was developed. Preparing targeted CAs are of extreme interest in the pursuit of monitoring specific disease states and biological processes. Again, by following simple SPPS protocols, a peptide backbone consisting of multiple lysine residues and the peptide sequence RGD was developed. RGD is a frequently explored targeting vector for binding to integrins, while the lysine residues fulfilled the role of anchor points for attaching the already 'pre-made' Ca^{2+}-responsive SCAs. The final multimer **Gd_3L^8** showed significant increases in relaxivity upon interaction with Ca^{2+}, which combined with its increased specificity though the introduction of the RGD targeting moiety, make it a prime candidate for further investigations *in vivo*.

Overall the studies conducted in Chapters 5 and 6 demonstrate the power of solid phase synthetic protocols in the development of imaging probes. The versatility of such a method enables the development of multimeric and multifunctional MRI probes which can be completely customised in a much simpler fashion when compared to standard solution phase chemistry. Additionally, the approach to incorporate the SCA can be altered with the coupling of a probe 'pre-made' in solution or the building of the probe in a stepwise approach on the resin itself being demonstrated here. The development of this approach opens the door for the convenient synthesis of bioresponsive probes with increased functionality and specificity. The resulting probes can then be applied to a wide range of applications, increasing the specificity of the future SCA probes.

To summarise the work conducted here describes multiple approaches in the development of Ca^{2+}-responsive SCAs. From this study, the design requirements for future dendrimeric probes have been identified. Additionally, the impacts of subtle structural changes have been highlighted in both small monomeric form or as a nano-sized conjugate. Alternative synthetic approaches have also been described adding to the toolbox for chemists involved in the design and development of more

elaborate and complicated derivatives to monitor a range of biological processes. Overall the knowledge gained here will assist in the future design of Ca^{2+}-responsive MRI SCAs and contribute towards the goal of monitoring Ca^{2+} fluctuations in the brain which is often associated with many neurodegenerative diseases or abnormalities.

8 Experimental

8.1 Materials and methods

Commercially available reagents and solvents were used without further purification. Purification of synthesised compounds was performed using silica gel 60 (0.03-0.2 mm) from Carl Roth (Germany). High resolution mass spectra were recorded on a Bruker Daltonics APEX II (FT-ICR-MS) with an electrospray ionization source. Low resolution mass spectra were recorded on an Agilent ion trap SL 1100 system with an electrospray ionization source. MALDI-TOF/MS analysis was performed by The Scripps Center for Mass Spectrometry, La Jolla, CA. All ^{1}H and ^{13}C NMR, diffusion and relaxometric experiments were performed on Bruker Avance III 300 MHz and Avance III 800 MHz spectrometers at 298 K. Processing was performed using TopSpin 2.1 (Bruker GmbH), ACD/SpecManager 9.0 (Advanced Chemistry Development, Inc.) or Sparky 3.115. The NMR spectra were obtained either in $CDCl_3$ or D_2O, using the deuterium lock frequency. The concentration of Gd^{3+}, Eu^{3+} or Yb^{3+} in analysed solutions was determined using the bulk magnetic susceptibility shift (BMS).[339] DLS and ζ potential measurements were done on a Malvern-Nano-ZS (Zetasizer, software ver. 6.2) instrument. The luminescence lifetime measurements were performed on a QuantaMasterTM 3 PH fluorescence spectrometer from Photon Technology International, Inc. (USA). Rink amide resin 100-200 mesh was purchased from Merck Millipore. Manual solid phase synthesis was performed with the synthesis 1 apparatus from Heidolph. LC-MS spectra were recorded on an Agilent 1100 series LC/MS system with a Polaris 5 C18-Ether column (250 x 4.6 mm). The LC-MS elution conditions are given in Table S1. Reversed-phase HPLC purification was performed on a Varian PrepStar Instrument (Austrailia) with PrepStar SD-1 pump heads. Analytical reversed-phase HPLC was performed with an Atlantis C18 column (4.6 x 150 mm, 5 µm particle size). Semipreparative reversed-phase HPLC was conducted with a Polaris 5 C18-A column (250 x 21.2 mm). Elution conditions are described in Table S2. G4 Starburst, a PAMAM dendrimer with a cystamine core, was purchased from Andrews ChemServices, USA. Dendrimers **D$^{1a–5a}$** were purified using lipophilic Sephadex LH-20 (bead size: 25− 100 µm) from Sigma-Aldrich (Germany). **DCAs$^{1–5}$** were purified using hydrophilic Sephadex G-15 (bead size: 40−120 µm) from GE Healthcare.

8.1.1 Dendrimer characterisation

Dendrimeric conjugate products were characterized by ^{1}H NMR and/or MALDI-TOF. Estimations of the number of monomeric units attached to the surface of the dendrimer unit were calculated using ^{1}H NMR on dendrimeric conjugates before (**D$^{1a–4a}$**) or after *t*Bu ester hydrolysis (**D$^{1b–4b}$**).[295] MALDI-TOF was carried out on the dendrimers **D$^{1b–4b}$** and the final **DCA$^{1–5}$**. The MALDI-TOF spectra exhibited

broad signals indicating the presence of species with high molecular masses. This prevented detailed quantitative analysis due to the presence of multiple species with different m/z values.

8.1.2 Relaxometric titrations

Proton longitudinal and transverse relaxometric titrations with Ca^{2+} were performed at 7.0 T, 25 °C, and pH 7.4 (50 mM HEPES buffer) using inversion recovery (T_1) and Car−Purcell−Meiboom−Gill (T_2) pulse sequences. A $CaCl_2$ solution of known concentration was added stepwise to **DCA**[1-5], **GdL**[5-6], **Gd_2L^7**, **Gd_2L^7** + avidin and **Gd_3L^8** solutions (starting concentration either 2.5 or 1 mM Gd^{3+}), and measurements of T_1 and T_2 were performed after each addition of the analyte. The longitudinal and transverse relaxivities, r_1 and r_2, were calculated from eq S1 where $T_{i,obs}$ is the measured T_1 (i = 1) or T_2 (i = 2), T_{id} is the diamagnetic contribution of the solvent, and [Gd] is the actual Gd^{3+} concentration at each point of the titration. All reported relaxivity values were the average of three independent measurements.

$$1/T_{i,obs} = T_{id} + r_i \text{ x } [\text{Gd}] \quad \text{(S1)}$$

8.1.3 DLS and ζ potential measurements

DLS and ζ potential measurements were carried out with filtered samples of **DCAs**[1–5] (0.3 mM Gd^{3+}, 25 mM HEPES, pH 7.4) with and without the addition of 2 equiv of Ca^{2+}. After the addition of Ca^{2+}, the samples were left to equilibrate for 5 min before measurement. Each DLS measurement included 5 repetitions of 15 scans (1 scan = 12 s, refractive index 1.345, absorption 1%), without delays in between the scans and with an equilibration time of 30 s prior to recording. The reported size was obtained from the values provided by a distribution analysis. Each ζ potential measurement included 5 repetitions (number of scans was determined by the device depending on the consistency of the data) after an initial calibration time (10 min).

8.1.4 High resolution NMR experiments.

All high resolution NMR spectra for **LnL**[5-6] (where Ln = Eu^{3+}, Yb^{3+}, or Y^{3+}) were acquired on a Bruker AVIII-800 spectrometer, processed with TopSpin 2.1 (Bruker GmbH), and analyzed with Sparky 3.115.[340] For every sample (20 mM [Ln^{3+}]), a ^{1}H - NMR spectra was measured, along with a DQF-COSY and a ^{13}C-HSQC. A standard DQF-COSY[341] was acquired with 4096 and 128 complex points in *t*2 and *t*1, respectively, performing 256 scans per increment.

The ^{13}C-HSQC was recorded at a resolution of 1024 (*t*2) × 128 (*t*1) complex points, using 64 scans per increment. All experiments were recorded at 298 K, using a relaxation delay of 1.5 s. Water

suppression was achieved via a pre-saturation for the ^{1}H -NMR and the COSY, while the ^{13}C-HSQC uses gradient selection (echo/ant-echo).

8.1.5 NMR diffusion measurements.

Diffusion coefficient determination was performed using 2D – Diffusion Ordered NMR Spectroscopy (DOSY). Samples of **EuL$^{5\text{-}6}$** with and without 2 equivalents of Ca^{2+} were dissolved in D_2O and the pD adjusted to 7.0. Measurements were performed at 298 K using 20, 10 and 5 mM [Eu^{3+}] samples (δt = 2 ms, ΔT = 250 ms). Data analysis was conducted with TopSpin 2.1 using 16 linear points with a 5-95 % gradient strength. The diffusion coefficients were calculated through the analysis of individual peaks in the aromatic region from three independent measurements. Each peak used in the determination of diffusion coefficient was within an error of 0.05 x 10^{-10} m^2 s^{-1}. The reported diffusion coefficients in Table 4 (section 4.2.4) are the averages of each of the peaks from the three independent measurements with their standard deviation.

8.1.6 Luminescence lifetime measurements.

Luminescence lifetime measurements were performed with **EuL$^{5\text{-}6}$** (5 mM [Eu^{3+}]) in D_2O and H_2O (298 K, pH 7.4, HEPES). The Eu^{3+} ion was directly excited and the emission intensity was recorded with a 10 µs resolution. The excitation and emission slits were set at 5 nm. In total, three independent measurements each with 25 scans were performed to obtain the data set. The obtained curves were fitted with a first order exponential decay with an r^2 = 0.99. The resulting q values were then calculated using eq S2.

$$q = 1.2 \text{ x } (\tau_{H2O}^{-1} - \tau_{D2O}^{-1} - 0.25) \quad \text{(S2)}$$

8.1.7 MRI phantom experiments

MRI measurements were performed on a Bruker BioSpec 70/30 USR magnet (software version Paravision 5.1) using a Bruker volume coil (RF RES 300 1H 075/040 QSN TR) and either a Fast Low Angle Single Shot (FLASH) or balanced steady state free precession (bSSFP) pulse sequence.[342]

8.1.7.1 MRI phantoms of Gd_2L^7 with avidin

MRI phantoms consisted of two pairs of 400 µl vials containing either 1 mM of **Gd_7L**-Av in HEPES buffer or HEPES buffer alone, both with and without Ca^{2+}. The Imaging parameters for the FLASH sequence were field-of-view (FOV)= 25 x 25 mm, matrix size (MTX) = 125 x 125, slice thickness 1 mm, flip angle (FA) = 90 ^{o}, repetition time (TR) = 155 ms, echo time (TE) = 2.75 ms, number of excitations (NEX) = 10, total acquisition time (TA)= 3 min 2 s 140 ms.

The imaging parameters for the bSSFP sequence were FOV= 25 x 25 mm, MTX 125 x 125, slice thickness 1 mm, FA = 65 ^{o}, TR = 2.2 ms, TE = 1.1 ms, NEX = 20, TA=23 s 222 ms.

8.1.7.2 MRI phantoms of Gd_2L^7 with avidin coated beads

MRI phantoms consisted of two pairs of 400 µl vials containing **Gd_2L^7**-avidin beads in HEPES buffer or HEPES buffer alone, both with and without Ca^{2+}. The imaging parameters for the FLASH sequence were FOV= 30 x 30 mm, MTX = 150 x 150, slice thickness 2 mm, FA = 90 ^{o}, TR = 164 ms, TE = 2.5 ms, NEX = 20, TA = 8 min 12 s 0 ms.

8.1.8 LC-MS

8.1.8.1 General procedure for producing LC-MS analytical data

After the reaction, a small portion of resin was taken and a deprotection solution (TFA/TIS/dichloromethane, 95:2.5:2.5) was added (2 mL) and allowed to shake for 4 h. Afterwards, the solution was collected and the resin washed a further two times with the deprotection solution (2 x 1 mL, 3 min each). The collected solutions were combined and the majority of TFA/TIS/dichloromethane removed under N_2 stream. The crude product was then precipitated from the remaining deprotection solution with cold diethyl ether and stored in the freezer overnight. The mixture was centrifuged at 3000g for 10 min and the solution was removed. The remaining solid was then subject to two further rounds of washing and centrifugation with cold diethyl ether before being dried and prepared for LC-MS analysis.

The conditions of elution are given below in table S1.

Table S1. Elution conditions for LC-MS analysis. A flow rate of 1 mL/min was used. Solvent A = 0.1 % CH_3COOH/H_2O. Solvent B = 0.1 % CH_3COOH/MeCN.

Time (min)	A %	B %
0	95	5
10	80	20
20	20	80
25	0	100
30	0	100
31	95	5
33	95	5

All LC-MS data was provided for the given compounds after removal from the resin and the deprotection of *t*Bu esters and where applicable, the Mtt protecting group.

8.1.9 HPLC

HPLC was performed on **Gd_2L^7** and **Gd_3L^8** after cleavage from the solid phase support. Both used the same conditions, which are detailed in table S2 below.

Table S2. Elution conditions for analytical and semi-preparative HPLC. Flow rates of 1 and 10 mL/min were used respectively. Solvent A = H_2O. Solvent B = MeCN.

Time (min)	A %	B %
0	95	5
5	95	5
20	0	100
39	0	100
40	95	5

8.2 Synthetic procedures

(4-Bromo-butyl)-carbamic acid benzyl ester (1).[291, 293]

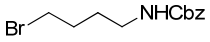

5-aminobutan-1-ol (5.00 g, 56.1 mmol) was dissolved in a solution of water (15 mL) and dioxane (15 mL). The solution was treated with dropwise additions of a solution of carbobenzoxy chloride (ZCl, 11.48 g, 67.3 mmol) in dioxane (25 mL) and of 3.5 M K_2CO_3 with vigorously stirring at room temperature. The pH was maintained at 6-7. After the addition of ZCl, the solution was stirred at pH 7-8 for 1 h. Excess ZCl was then hydrolyzed with 2M aqueous NaOH (1 mL) and stirred for a further 2 h. The mixture was extracted with ether. The combined ether was washed with 1M NaOH, water (x 2) and then dried over Na_2SO_4. The solvent was evaporated under vacuum and the product was recrystallised from toluene to yield benzyl (4-hydroxybutyl)carbamate as a white solid (8.99 g, 72 %).
^{1}H NMR (300 MHz, $CDCl_3$): δ (ppm) 1.56 (br. s., 4H) 2.42 (br. s., 1H) 3.19 (m, 2H) 3.62 (m, 2H) 5.08 (s, 3H) 7.26 - 7.38 (m, 5H). **^{13}C NMR** (75 MHz, $CDCl_3$): δ (ppm) 26.5, 29.6, 40.8, 62.2, 66.6 (-CH_2-), 128.1, 128.5, 136.6 (ArC), 156.7 (C=O).
Carbon tetrabromide (20.04 g, 60.4 mmol) and triphenylphosphine (15.85 g, 60.4 mmol) were added to a stirred solution of benzyl (4-hydroxybutyl)carbamate (8.99 g, 40.3 mmol) in dichloromethane (250 mL) at 0 °C. The solution was warmed to room temperature and stirred for a further 90 min, where water was added to the flask. Additional dichloromethane was added and the organic phase was washed with water (x 2), brine and dried over Na_2SO_4. The solvent was evaporated under vacuum and the crude product was purified by flash chromatography (silica gel, hexane/ethyl acetate, 80:20 v/v) to give the bromide **1** as transparent orange oil (8.88 g, 77 %).
^{1}H NMR (300 MHz, $CDCl_3$): δ (ppm) 1.65 (m, 2H), 1.86 (m, 2H) 3.20 (q, *J* = 6.5 Hz, 2H) 3.40 (t, *J* = 6.5 Hz, 2H) 4.90 (br. s., 1H) 5.09 (s, 2H), 7.34 (m, 5 H). **^{13}C NMR** (75 MHz, $CDCl_3$): δ (ppm) 28.7, 29.8, 33.2, 40.2, 66.7 (-CH_2-), 128.2, 128.6, 136.6 (ArC), 156.5 (C=O).

(5-Bromo-pentyl)-carbamic acid benzyl ester (2).[291, 292]

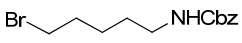

5-aminopentan-1-ol (10.00 g, 97.0 mmol) was dissolved in a solution of water (25 mL) and dioxane (25 mL). The solution was treated with dropwise additions of a solution of carbobenzoxy chloride (ZCl, 19.84 g, 116 mmol) in dioxane (25 mL) and of 3.5 M K_2CO_3 with vigorously stirring at room temperature. The pH was maintained at 6-7. After the addition of ZCl, the solution was stirred at pH 7-8 for 1 h. Excess ZCl was then hydrolyzed with 2M aqueous NaOH (1 mL) and stirred for a further 2 h. The mixture was extracted with ether. The combined ether was washed with 1M NaOH, water (x 2) and then dried over Na_2SO_4. The solvent was evaporated under vacuum and the crude product

was purified by column chromatography (silica gel, dichloromethane/methanol, 94:6 v/v) to yield benzyl (5-hydroxypentyl)carbamate (16.00 g, 70 %).

^{1}H NMR (300 MHz, $CDCl_3$): δ (ppm) 1.29 - 1.60 (m, 6H), 2.22 (br. s., 1H), 3.17 (q, *J*=6.4 Hz, 2H) 3.60 (t, *J*=6.3 Hz, 2H) 5.07 (m, 3H) 7.25 - 7.39 (m, 5H). **^{13}C NMR** (75 MHz, $CDCl_3$): δ (ppm) 22.9, 29.7, 32.2, 41.0, 62.5, 66.6 (-CH_2-), 128.1, 128, 136.7 (ArC), 156.6 (C=O).

Carbon tetrabromide (18.43 g, 55.6 mmol) and triphenylphosphine (14.57 g, 55.6 mmol) were added in portions to a stirred solution of benzyl (5-hydroxypentyl)carbamate (8.79 g, 37.0 mmol) in dichloromethane (250 mL) at 0 °C. The solution was warmed to room temperature and stirred for a further 4 h, where water was added to the flask. The organic phase was washed with water, brine and dried over Na_2SO_4. The solvent was evaporated under reduced pressure and the crude product was purified by flash chromatography (silica gel, hexane/ethyl acetate, 80:20 v/v) to give bromide **2** as an off-white low melting point solid (9.01 g, 81 %).

^{1}H NMR (300 MHz, $CDCl_3$): δ (ppm) 1.36 – 1.60 (m, 4H), 1.76 - 1.91 (m, 2H), 3.19 (q, *J* = 6.1 Hz, 2H), 3.38 (t, *J* = 6.70 Hz, 2H), 4.83 (br. s., 1H), 5.09 (s, 2H), 7.25 - 7.39 (m, 5H). **^{13}C NMR** (75 MHz, $CDCl_3$): δ (ppm) 25.3, 29.2, 32.3, 33.6, 40.8, 66.7 (-CH_2-), 128.1, 128.5, 136.6 (ArC), 156.44 (C=O).

[4-(4-Benzyloxycarbonylamino-butyl)-7,10-bis-*tert*-butoxycarbonylmethyl-1,4,7,10tetraaza-cyclododec-1-yl]-acetic acid *tert*-butyl ester (3).

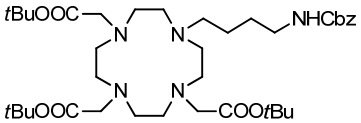

1,4,7,10-Tetraazacyclododecane-1,4,7-tris(t-butyl acetate) (DO3A, 5.58 g, 10.84 mmol) was dissolved in acetonitrile (200 mL) and potassium carbonate was added (4.49 g, 32.50 mmol). The reaction was stirred at room temperature for 30 min. Bromide **1** (3.72 g, 13.01 mmol) was then dissolved in acetonitrile (50 mL) and added to the solution. The mixture was heated at reflux for 16 h. Afterwards the mixture was allowed to cool to room temperature, filtered and the solvent evaporated under reduced pressure. The crude product was purified by column chromatography (silica gel, dichloromethane/methanol, 94:6 v/v) to yield **3** as a yellow/orange solid (7.32 g, 94 %).

^{1}H NMR (300 MHz, $CDCl_3$): δ (ppm) 1.24 – 1.90 (br, 31H), 2.05 – 3.72 (br, 26 H), 5.08 (br. s., 2 H) 7.14 - 7.41 (m, 5 H). **^{13}C NMR** (75 MHz, $CDCl_3$): δ (ppm) 23.1 (-CH_2-), 27.6, 27.7, 27.9 ($C(CH_3)_3$), 40.3, 49.9, 50.5, 53.6, 53.7, 55.5, 56.2, 65.9 (-CH_2-), 81.3, 81.4, 82.2, 82.5 ($C(CH_3)_3$), 127.6, 128.2, 136.8 (ArC), 156.4, 169.9, 170.3, 172.4, 173.3 (C=O). **ESI-HRMS**: (m/z) $[M+H]^+$ calcd. for $C_{38}H_{66}N_5O_8^+$, 720.4906, found: 720.4908.

[4-(5-Benzyloxycarbonylamino-pentyl)-7,10-bis-*tert*-butoxycarbonylmethyl-1,4,7,10tetraaza-cyclododec-1-yl]-acetic acid *tert*-butyl ester (4).

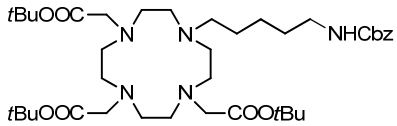

DO3A (7.14 g, 13.88 mmol) was dissolved in acetonitrile (300 mL) and potassium carbonate was added (5.75 g, 41.60 mmol). The reaction was stirred at room temperature for 30 min. Bromide **2** (5.00 g, 16.66 mmol) was then dissolved in acetonitrile (50 mL) and added to the solution. The mixture was heated at reflux for 16 h. Afterwards the mixture was allowed to cool to room temperature, filtered and the solvent evaporated under reduced pressure. The crude product was purified by column chromatography (silica gel, dichloromethane/methanol, 94:6 v/v) to yield **3** as an orange oil (8.57 g, 84 %).

^{1}H NMR (300 MHz, $CDCl_3$): δ (ppm) 0.99 – 1.87 (br, 33H), 1.97 – 3.77 (br, 26 H), 5.07 (br. s., 2 H), 5.54 (br. s., 1H), 7.17 - 7.45 (m, 5 H). **^{13}C NMR** (75 MHz, $CDCl_3$): δ (ppm) 24.5, 26.0 (-CH_2-), 27.6, 27.8, 27.9 ($C(CH_3)_3$), 40.6, 50.2, 52.7, 54.0, 55.5, 56.2, 66.0 (-CH_2-), 81.3, 81.4, 82.2, 82.5 ($C(CH_3)_3$), 127.6, 128.2, 136.7 (ArC), 156.4, 169.9, 170.3, 172.4, 173.3 (C=O). **ESI-HRMS**: (m/z) $[M+H]^+$ calcd. for $C_{39}H_{68}N_5O_8^+$, 734.5062, found: 734.5065.

[4-(4-Aminobutyl)-7,10-bis-*tert*-butoxycarbonylmethyl-1,4,7,10tetraaza-cyclododec-1-yl]-acetic acid *tert*-butyl ester (5).

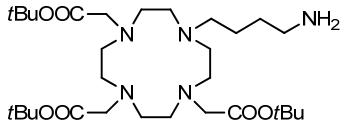

Macrocycle **3** (8.05 g, 11.18 mmol) was dissolved in ethanol (30 mL) and $Pd(OH)_2$/C catalyst (0.81 g) was added. A few drops of NH_3 in methanol (7 N) were then added to the heterogeneous mixture. The mixture was shaken for 5 h in a hydrogen atmosphere using a Parr hydrogenator (3 bar). The catalyst was removed by filtration through a plug of celite and the solvent evaporated under reduced pressure to give amine **5** as a black solid (6.38 g, 97 %). The resulting solid was used in subsequent reactions without further purification.

^{1}H NMR (300 MHz, $CDCl_3$): δ (ppm) 1.32 – 1.66 (br, 29H), 1.71 – 2.00 (m, 2H), 2.07-3.39 (br, 26H). **^{13}C NMR** (75 MHz, $CDCl_3$): δ (ppm) 23.4, 26.0, 26.8 (-CH_2-), 27.7, 27.9, 27.9 ($C(CH_3)_3$), 29.3, 39.3, 40.9, 50.1, 50.4, 50.6, 51.3, 53.9, 54.3, 55.6, 56.4, 56.8, 57.6 (-CH_2-), 81.6, 82.2, 82.4, 82.7 ($C(CH_3)_3$), 171.7, 171.7, 172.5, 173.4 (C=O). **ESI-HRMS**: (m/z) $[M+H]^+$ calcd. for $C_{30}H_{60}N_5O_6^+$, 586.4538, found: 586.4541.

[4-(5-Aminopentyl)-7,10-bis-*tert*-butoxycarbonylmethyl-1,4,7,10tetraaza-cyclododec-1-yl]-acetic acid *tert*-butyl ester (6).

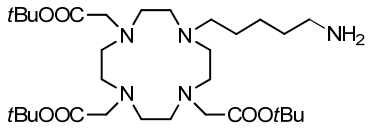

Macrocycle **4** (8.00 g, 10.90 mmol) was dissolved in ethanol (30 mL) and $Pd(OH)_2$/C catalyst (0.80 g) was added. A few drops of NH_3 in methanol (7 N) were then added to the heterogeneous mixture. The mixture was shaken for 5 h in a hydrogen atmosphere using a Parr hydrogenator (3 bar). The catalyst was removed by filtration through a plug of celite and the solvent evaporated under reduced pressure to give amine **6** as a black solid (6.31 g, 97 %). The resulting solid was used in subsequent reactions without further purification.

^{1}H NMR (300 MHz, $CDCl_3$): δ (ppm) 0.99 – 1.90 (br, 33H), 2.02 – 3.60 (br, 26H). **^{13}C NMR** (75 MHz, $CDCl_3$): δ (ppm) 22.7, 22.8, 24.7, 25.9 ($-CH_2-$), 27.7, 27.9, 28.0 ($C(CH_3)_3$), 30.6, 39.6, 40.8, 48.8, 50.2, 50.3, 51.7, 52.1, 52.9, 54.1, 55.6, 56.1, 56.4, 57.1, 57.6 ($-CH_2-$), 81.8, 81.8, 82.4, 82.7 ($C(CH_3)_3$), 170.4, 171.2, 172.4, 173.4 (C=O). **ESI-HRMS**: (m/z) $[M+H]^+$ calcd. for $C_{31}H_{62}N_5O_6^+$, 600.4695, found: 600.4700.

{4-[4-(2-Bromo-acetylamino)-butyl]-7,10-bis-*tert*-butoxycarbonylmethyl-1,4,7,10tetraaza-cyclododec-1-yl}-acetic acid *tert*-butyl ester (7).

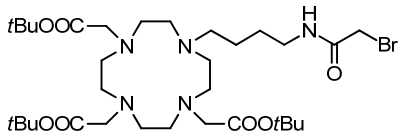

N,*N*'-methanediylidenedicyclohexanamine (1.779 g, 8.62 mmol) and 2-bromoacetic acid (1.198 g, 8.62 mmol) were dissolved in dichloromethane (40 mL). Amine **5** (4.210 g, 7.19 mmol) was dissolved in dichloromethane (30 mL) and added to the mixture. After 1.5 h of stirring at room temperature the mixture was filtered and the filtrate was evaporated under reduced pressure. The crude material was purified by column chromatography (silica gel, dichloromethane/methanol, 94:6 v/v) yielding bromide **7** as a white/yellow solid (2.686 g, 53 %).

^{1}H NMR (300 MHz, $CDCl_3$): δ (ppm) 0.95 – 1.83 (br, 31H), 1.86 – 3.70 (br, 26H), 4.08 (s, 2H). **^{13}C NMR** (75 MHz, $CDCl_3$): δ (ppm) 23.4, 26.9 ($-CH_2-$), 27.8, 28.0, 28.1 ($C(CH_3)_3$), 30.2, 39.5, 47.7, 50.2, 50.7, 52.5, 53.8, 55.6, 56.5, 56.8 ($-CH_2-$), 81.9, 82.6, 83.0 ($C(CH_3)_3$), 166.9, 167.4, 170.0, 170.5, 172.3, 173.4 (C=O). **ESI-HRMS**: (m/z) $[M+H]^+$ calcd. for $C_{32}H_{61}BrN_5O_7^+$, 706.3749, found: 706.3747.

{4-[5-(2-Bromo-acetylamino)-pentyl]-7,10-bis-*tert*-butoxycarbonylmethyl-1,4,7,10tetraaza-cyclododec-1-yl} acetic acid *tert*-butyl ester (8).

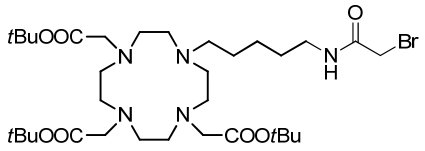

N,*N*'-methanediylidenedicyclohexanamine (2.105 g, 10.20 mmol) and 2-bromoacetic acid (1.418 g, 10.20 mmol) were dissolved in dichloromethane (40 mL). Amine **6** (5.100 g, 8.50 mmol) was dissolved in dichloromethane (30 mL) and added to the mixture. After 1.5 h of stirring at room temperature the mixture was filtered and the filtrate was evaporated under reduced pressure. The crude material was purified by column chromatography (silica gel, dichloromethane/methanol, 94:6 v/v) yielding bromide **8** as a white/yellow solid (4.241 g, 69 %).

^{1}H NMR (300 MHz, $CDCl_3$): δ (ppm) 1.04 – 1.94 (br, 33H), 2.06 – 3.90 (br, 26H), 4.05 (br. s., 2H). **^{13}C NMR** (75 MHz, $CDCl_3$): δ (ppm) 21.8, 23.5, 24.7, 25.8 (-CH_2-), 27.8, 27.9, 28.1 ($C(CH_3)_3$), 28.9, 30.1, 38.6, 39.5, 47.7, 50.2, 52.6, 53.0, 53.2, 54.2, 55.6, 56.3, 56.8 (-CH_2-), 81.7, 82.5, 82.9 ($C(CH_3)_3$), 166.6, 166.9, 169.9, 170.5, 172.3, 173.3 (C=O). **ESI-HRMS**: (m/z) $[M+H]^+$ calcd. for $C_{33}H_{63}BrN_5O_7^+$, 720.3905, found: 720.3903.

(2-{2-[2-(*tert*-Butoxycarbonylmethyl-amino)-ethoxy]-ethoxy}-ethylamino)-acetic acid *tert*-butyl ester (9).

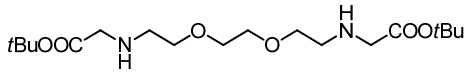

The synthesis of **9** was carried out using a previously published procedure.[182]

2-Bromo-*N*-[2-(4-nitro-phenyl)-ethyl]-acetamide (10).[343]

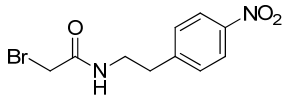

2-(4-nitrophenyl)ethylamine hydrochloride (10.00 g, 49.3 mmol) was suspended in dichloromethane (80 mL) and *N*,*N*-diisopropylethylamine (8.60 mL, 49.3 mmol). The solution was cooled to 0 °C and bromoacetic acid (6.86 g, 49.3 mmol) in dichloromethane (40 mL) was added. N^1-((ethylimino)methylene)-N^3,N^3-dimethylpropane-1,3-diamine hydrochloride (10.41 g, 54.3 mmol) and 1-hydroxybenzotriazole hydrate (7.34 g, 54.3 mmol) were then added and the mixture was stirred for 2 h at room temperature. The mixture was then cooled to 0 °C, filtered and washed with HCl (2 N) and brine. The organic layers were collected, dried over Na_2SO_4, filtered and concentrated *in vacuo* to yield a light brown solid (14.17 g, 79 %).[343]

^{1}H NMR (300 MHz, $CDCl_3$): δ (ppm) 2.99 (t, *J*=7.03, 2.17 Hz, 2H) 3.55 - 3.67 (q, *J*=6.66, Hz, 2H) 3.85 (s, 1H) 4.03 (s, 1H) 6.68 (br, 1 H) 7.39 (d, *J* = 8.50 Hz, 2H) 8.16 (d, *J* = 8.50 Hz, 2H). **^{13}C NMR** (75 MHz, $CDCl_3$): δ (ppm) 29.0, 35.4, 40.8 (-CH_2-), 123.9, 129.7, 146.4, 146.8 (ArC), 165.8 (C=O).

((2-{2-[2-(*tert*-Butoxycarbonylmethyl-amino)-ethoxy]-ethoxy}-ethyl)-{[2-(4-nitro-phenyl)-ethylcarbamoyl]-methyl}-amino)-acetic acid *tert*-butyl ester (11).

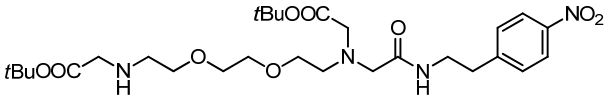

(2-{2-[2-(*tert*-Butoxycarbonylmethyl-amino)-ethoxy]-ethoxy}-ethylamino)-acetic acid *tert*-butyl ester (10.00 g, 26.6 mmol, prepared following a previously reported procedure) was dissolved in acetonitrile (500 mL) and potassium carbonate (2.94 g, 21.3 mmol) was added. After 30 min stirring, bromide **9** (6.10 g, 21.25 mmol) in acetonitrile (80 mL) was then added slowly to the mixture by dropwise addition and stirred overnight at room temperature. An additional amount of **10** (1.53 g, 5.3 mmol) and potassium carbonate (0.73 g, 5.3 mmol) were added and the reaction was allowed to stir for 4 days at room temperature. The resulting mixture was then filtered and the solvent evaporated under reduced pressure to yield the crude oil which was purified by column chromatography (silica gel, dichloromethane/methanol, 96:4 v/v) giving amine **11** (5.18 g, 34 %) as a dark orange/red oil.

^{1}H NMR (300 MHz, $CDCl_3$): δ (ppm) 1.46 (br, 18H), 2.69 – 2.88 (m, 4H), 2.98 (t, *J* = 7.08 Hz, 2H) 3.31 (m, 6H), 3.48 (t, *J* = 4.82 Hz, 2H), 3.57 (br. s., 8H), 7.42 (d, *J* = 8.31 Hz, 2H), 8.04 (br. s., 1H), 8.15 (d, *J* = 8.50 Hz, 2H). **^{13}C NMR** (75 MHz, $CDCl_3$): δ (ppm) 28.1 ($C(CH_3)_3$), 35.6, 39.6, 48.7, 51.6, 54.4, 56.8, 59.2, 68.9, 70.2, 70.7 (-CH_2-), 81.1 81.5 ($C(CH_3)_3$), 123.6, 129.7, 146.7, 147.2 (ArC), 170.6, 171.5, 171.6 (C=O). **ESI-HRMS**: (m/z) $[M+Na]^+$ calcd. for $C_{28}H_{46}N_4O_9Na^+$, 605.3157, found: 605.3161.

[*tert*-Butoxycarbonylmethyl-(2-{2-[2-(*tert*-butoxycarbonylmethyl-{[2-(4-nitro-phenyl)-ethylcarbamoyl]-methyl}-amino)-ethoxy]-ethoxy}-ethyl)-amino]-acetic acid allyl ester (11a)

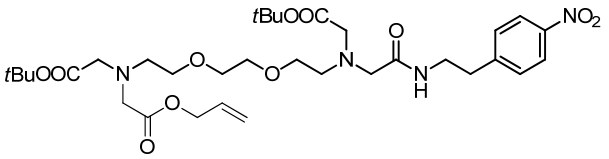

Secondary amine **11** (100.0 mg, 0.172 mmol) was dissolved in acetonitrile (2.5 mL) and potassium carbonate (56.9 mg, 0.412 mmol) was added. After stirring for 30 min, allyl chloroacetate (27.7 mg, 0.206 mmol) was added dropwise and stirred at 70 °C overnight. An additional portion of allyl chloroacetate (13.86 mg, 0.103 mmol) was then added and the reaction stirred for a further 2 days at 70 °C. The mixture was then cooled to room temperature, filtered and the solvent evaporated

under reduced pressure to give the crude oil which was then purified by column chromatography (silica gel, dichloromethane/methanol, 97:3 v/v) giving protected chelator **11a** (53.8 mg, 46 %).

^{1}H NMR (300 MHz, $CDCl_3$): δ (ppm) 1.45 (s, 18H), 2.82 (br s., 2H) 2.91 – 3.02 (br, 4H), 3.31 (br s., 4H), 3.43 – 3.69 (br, 14H), 4.57 – 4.72 (m, 2H), 5.21 – 5.37 (m, 2H), 5.91 (m, 1H), 7.42 (d, *J* = 8.31 Hz, 2H), 8.15 (d, *J* = 8.31 Hz, 2H). **^{13}C NMR** (75 MHz, $CDCl_3$): δ (ppm) 28.1 ($C(CH_3)_3$), 35.6, 39.7, 54.4, 55.7, 55.8, 56.7, 56.8, 59.1, 62.7, 65.1, 68.8, 70.2, 70.4 ($-CH_2-$), 81.1, 81.6 ($C(CH_3)_3$), 118.5 ($-CH_2=CH-$), 123.6, 129.7 (ArC), 132.0, 133.8 ($-CH_2=CH-$), 146.7, 147.2 (ArC), 165.3, 170.5, 171.1, 171.5 (C=O).

[*tert*-Butoxycarbonylmethyl-(2-{2-[2-(*tert*-butoxycarbonylmethyl-{[2-(4-nitro-phenyl) ethylcarbamoyl]-methyl}-amino)-ethoxy]-ethoxy}-ethyl)-amino]-acetic acid methyl ester (11b).

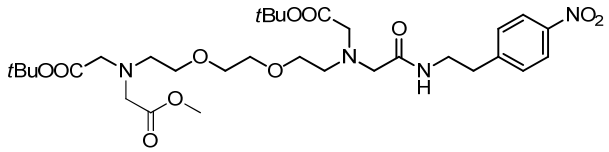

Secondary amine **11** (100.0 mg, 0.172 mmol) was dissolved in acetonitrile (2.5 mL) and potassium carbonate (56.9 mg, 0.412 mmol) was added. After stirring for 30 min, methyl bromoacetate (31.5 mg, 0.206 mmol) was added dropwise and the reaction mixture was stirred for 2 days at 70 °C. The solution was cooled to room temperature, filtered and the solvent removed under reduced pressure to yield a crude oil. Purification by column chromatography (silica gel, dichloromethane/methanol, 98:2 v/v) afforded to product **11b** (52.0 mg, 46 %).

^{1}H NMR (300 MHz, $CDCl_3$): δ (ppm) 1.45 (s, 18H), 2.81 (t, *J* = 4.82 Hz, 2H) 2.90 – 3.01 (m, 4H), 3.30 (br s., 4H), 3.43 – 3.63 (br, 14H), 3.69, (s, 3H), 7.42 (d, *J* = 8.50 Hz, 2H), 8.03 (br s., 1H), 8.15 (d, *J* = 8.50 Hz, 2H). **^{13}C NMR** (75 MHz, $CDCl_3$): δ (ppm) 28.1 ($C(CH_3)_3$), 35.7, 39.7, 51.6, 54.4, 55.7, 56.7, 56.9, 59.1, 68.9, 70.2, 70.3 ($-CH_2-$), 81.2, 81.6 ($C(CH_3)_3$), 123.7, 129.7, 146.7, 147.2 (ArC), 170.5, 170.7, 171.6, 171.9 (C=O).

[*tert*-Butoxycarbonylmethyl-(2-{2-[2-(*tert*-butoxycarbonylmethyl-{[2-(4-nitro-phenyl)-ethylcarbamoyl]-methyl}-amino)-ethoxy]-ethoxy}-ethyl)-amino]-acetic acid (11c).

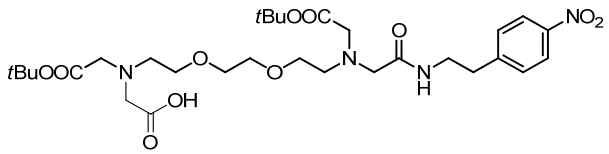

Route A: EGTA derivative **11a** (53.8 mg, 0.079 mmol) was dissolved in tetrahydrofuran (1 mL). To this, morpholine (68.8 mg, 0.790 mmol) and tetrakis(triphenylphosphine)palladium(0) (27.4 mg, 0.024 mmol) were added and the reaction was stirred overnight at room temperature. The solvent

was then removed under reduced pressure and the resulting crude material used without further purification.

Route B: EGTA derivative **11b** (57.7 mg, 0.088 mmol) was dissolved in a mixture of tetrahydrofuran/methanol/water (1.5:1:0.5, 3 mL) and lithium hydroxide (6.33 mg, 0.264 mmol) was added. The reaction was stirred for 3 h at room temperature after which the solvents were removed and the resulting crude material used without further purification.

((2-{2-[2-(*tert*-Butoxycarbonylmethyl-{[4-(4,7,10-tris-*tert*-butoxycarbonylmethyl-1,4,7,10tetraaza-cyclododec-1-yl)-butylcarbamoyl]-methyl}-amino)-ethoxy]-ethoxy}-ethyl)-{[2-(4-nitro-phenyl)-ethylcarbamoyl]-methyl}-amino)-acetic acid *tert*-butyl ester (12).

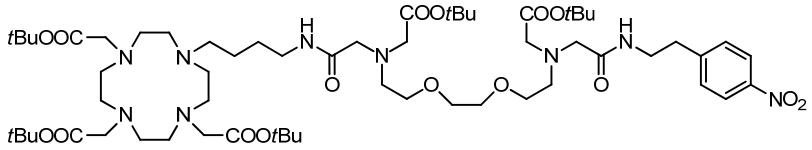

Amine **11** (1.50 g, 2.57 mmol) was dissolved in acetonitrile (100 mL) and potassium carbonate (0.854 g, 6.18 mmol) was added. After 30 min of stirring at room temperature, bromide **7** (2.18 g, 3.09 mmol) was added and the mixture was stirred at reflux overnight. An additional amount of bromide **7** (0.182 g, 0.26 mmol) was added and the reaction was left to stir at reflux for another 4 h. The mixture was allowed to cool to room temperature, filtered and the solvent removed under reduced pressure. The crude oil was purified by column chromatography (silica gel, dichloromethane/methanol, 94:6 v/v) to yield nitro **12** (1.80 g, 58 %) as an off-white solid.

^{1}H NMR (300 MHz, $CDCl_3$): δ (ppm) 1.31 – 1.73 (br, 49H), 2.14 – 3.67 (br, 50H), 7.47 (d, *J* = 8.31 Hz, 2H), 8.14 (d, *J* = 8.50 Hz, 2H). **^{13}C NMR** (75 MHz, $CDCl_3$): δ (ppm) 23.1 (-CH_2-), 27.8, 28.0, 28.1 ($C(CH_3)_3$), 35.6, 38.8, 39.7, 50.0, 50.9, 53.8, 54.5, 55.7, 56.5, 57.4, 59.0, 69.1, 70.1 (-CH_2-), 81.5, 81.5, 81.7, 82.5, 82.8 ($C(CH_3)_3$), 123.5, 129.9, 146.6, 147.5 (ArC), 170.0, 171.0, 171.3, 171.5, 172.5, 173.5 (C=O). **ESI-HRMS**: (m/z) $[M+H]^+$ calcd. for $C_{60}H_{106}N_9O_{16}^+$, 1208.7752, found: 1208.7745.

((2-{2-[2-(*tert*-Butoxycarbonylmethyl-{[4-(4,7,10-tris-*tert*-butoxycarbonylmethyl-1,4,7,10tetraaza-cyclododec-1-yl)-pentylcarbamoyl]-methyl}-amino)-ethoxy]-ethoxy}-ethyl)-{[2-(4-nitro-phenyl)-ethylcarbamoyl]-methyl}-amino)-acetic acid *tert*-butyl ester (13).

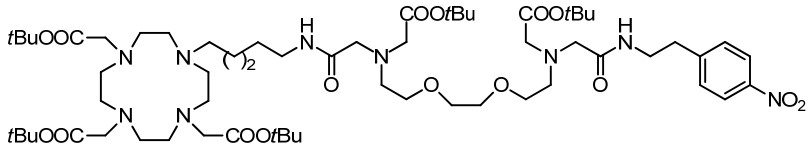

Amine **11** (1.50 g, 2.57 mmol) was dissolved in acetonitrile (100 mL) and potassium carbonate (0.854 g, 6.18 mmol) was added. After 30 min of stirring at room temperature, bromide **8** (2.227 g, 3.09

mmol) was added and the mixture was stirred at reflux overnight. An additional amount of bromide **8** (0.371 g, 0.52 mmol) and potassium carbonate (0.142 g, 1.03 mmol) was added and the reaction was left to stir at reflux for another 4 h. The mixture was allowed to cool to room temperature, filtered and the solvent removed under reduced pressure. The crude oil was purified by column chromatography (silica gel, dichloromethane/methanol, 94:6 v/v) to yield nitro **13** (1.706 g, 54 %) as an off-white solid.

^{1}H NMR (300 MHz, $CDCl_3$): δ (ppm) 1.09 – 1.83 (br, 51H), 2.15 – 3.65 (br, 50H), 7.46 (d, *J* = 8.50 Hz, 2H), 8.14 (d, *J* = 8.69 Hz, 2H). **^{13}C NMR** (75 MHz, $CDCl_3$): δ (ppm) 24.9, 25.7 ($-CH_2-$), 27.8, 28.0, 28.1 ($C(CH_3)_3$), 29.5, 35.6, 38.8, 39.7, 50.3, 54.3, 54.6, 55.7, 56.5, 57.3, 59.0, 69.0, 70.1 ($-CH_2-$), 81.5, 81.7, 82.5, 82.8 ($C(CH_3)_3$), 123.5, 129.9, 146.6, 147.5 (ArC), 170.0, 170.9, 171.3, 171.6, 172.5, 173.5 (C=O). **ESI-HRMS**: (m/z) $[M+H]^+$ calcd. for $C_{61}H_{108}N_9O_{16}^+$, 1222.7909, found: 1222.7902.

[{[2-(4-Amino-phenyl)-ethylcarbamoyl]-methyl}-(2-{2-[2-(*tert*-butoxycarbonylmethyl-{[4-(4,7,10-tris-*tert*-butoxycarbonylmethyl-1,4,7,10tetraazacyclododec-1-yl)-butylcarbamoyl]-methyl}-amino)-ethoxy]-ethoxy}-ethyl)-amino]-acetic acid *tert*-butyl ester (14).

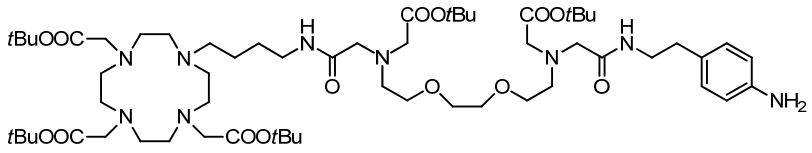

Pd/C (0.109 g) and a few drops of NH_3 in methanol (7 N) were added to a solution of nitro **12** (1.085 g, 0.898 mmol) in ethanol (20 mL). The heterogeneous mixture was shaken for 5 h in a hydrogen atmosphere using a Parr hydrogenator (3 bar). The catalyst was removed by filtration through a plug of celite and the solvent evaporated under reduced pressure to give amine **14** as an orange solid (1.052 g, 99 %). The resulting solid was used in subsequent reactions without any further purification.

^{1}H NMR (300 MHz, $CDCl_3$): δ (ppm) 1.16 – 1.79 (br, 49H), 2.02 – 3.66 (br, 50H), 6.63 (d, *J* = 8.31 Hz, 2H), 6.98 (d, *J* = 8.12 Hz, 2H). **^{13}C NMR** (75 MHz, $CDCl_3$): δ (ppm) 23.2 ($-CH_2-$), 27.8, 28.0, 28.1 ($C(CH_3)_3$), 29.6, 34.9, 38.8, 40.8, 50.1, 50.9, 53.8, 54.8, 55.7, 56.5, 57.6, 59.0, 68.8, 70.0 ($-CH_2-$), 81.4, 82.5, 82.8 ($C(CH_3)_3$), 115.2, 128.7, 129.5, 145.1 (ArC), 170.8, 171.1, 171.3, 172.5, 173.5 (C=O). **ESI-HRMS**: (m/z) $[M+H]^+$ calcd. for $C_{60}H_{108}N_9O_{14}^+$, 1178.8010, found: 1178.8007.

[{[2-(4-Amino-phenyl)-ethylcarbamoyl]-methyl}-(2-{2-[2-(*tert*-butoxycarbonylmethyl-{[4-(4,7,10-tris-*tert*-butoxycarbonylmethyl-1,4,7,10tetraazacyclododec-1-yl)-pentylcarbamoyl]-methyl}-amino)-ethoxy]-ethoxy}-ethyl)-amino]-acetic acid *tert*-butyl ester (15).

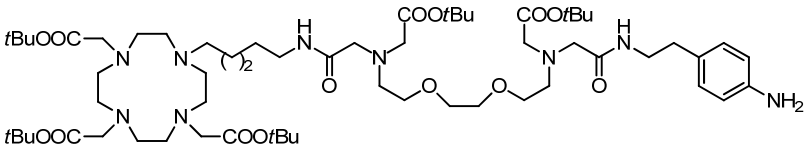

Pd/C (0.094 g) was added to a solution of nitro **13** (0.942 g, 0.771 mmol) in ethanol (30 mL). The heterogeneous mixture was shaken for 5 h in a hydrogen atmosphere using a Parr hydrogenator (3 bar). The catalyst was removed by filtration through a plug of celite and the solvent evaporated under reduced pressure to give amine **15** as a yellow/orange solid (0.850 g, 93 %). The resulting solid was used in subsequent reactions without any further purification.

^{1}H NMR (300 MHz, $CDCl_3$): δ (ppm) 1.09 – 1.83 (br, 51H), 2.05 – 3.65 (br, 50H), 6.63 (d, *J* = 8.12 Hz, 2H), 6.98 (d, *J* = 8.12 Hz, 2H). **^{13}C NMR** (75 MHz, $CDCl_3$): δ (ppm) 24.9, 25.7 ($-CH_2-$), 27.8, 27.9, 28.1 ($C(CH_3)_3$), 29.4, 34.8, 38.8, 40.6, 50.2, 50.9, 54.2, 54.6, 55.7, 56.4, 57.3, 59.0, 69.2, 70.0 ($-CH_2-$), 81.4, 81.6, 81.7, 82.4, 82.7 ($C(CH_3)_3$), 115.2, 128.5, 129.4, 145.1 (ArC), 169.9, 170.4, 170.7, 170.9, 171.2, 171.3, 172.5, 173.4 (C=O). **ESI-HRMS**: (m/z) $[M+H]^+$ calcd. for $C_{61}H_{110}N_9O_{14}^+$, 1192.8167, found: 1192.8160.

((2-{2-[2-(*tert*-Butoxycarbonylmethyl-{[4-(4,7,10-trimethyl-1,4,7,10tetraaza-cyclododec-1-yl)-butylcarbamoyl]-methyl}-amino)-ethoxy]-ethoxy}-ethyl)-{[2-(4-isothiocyanato-phenyl)-ethylcarbamoyl]-methyl}-amino)-acetic acid *tert*-butyl ester (L^{1}).

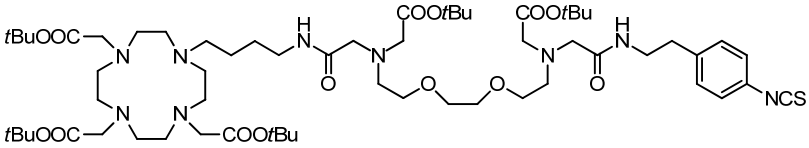

Amine **14** (0.986 g, 0.837 mmol) was dissolved in dichloromethane (10 mL) and solution of saturated sodium hydrogen carbonate (10 mL) was added. Thiophosgene (0.096 mL, 1.255 mmol) was added to the mixture and stirred for 1.5 h at room temperature. The organic layer was then separated; an additional portion of dichloromethane (100 mL) was added and washed with water (2 x 100 mL). The organic layers were combined, dried with sodium sulphate, filtered and the solvent was evaporated. The crude oil was then purified by column chromatography (silica gel, dichloromethane/methanol, 94:6 v/v) to yield isothiocyanate **L^{1}** as an orange oily solid (0.422 g, 41 %).

^{1}H NMR (300 MHz, $CDCl_3$): δ (ppm) 1.14 – 1.72 (br, 49H), 2.09 – 3.65 (br, 50H), 7.19 (dd, 4H), 7.87 (br. s., 2H). **^{13}C NMR** (75 MHz, $CDCl_3$): δ (ppm) 18.4, 23.2 ($-CH_2-$), 27.8, 28.0, 28.1 ($C(CH_3)_3$), 35.3, 38.8, 39.9, 50.0, 50.8, 53.8, 54.4, 55.7, 56.5, 56.7, 57.1, 57.3, 57.9, 59.2, 69.3, 70.2 ($-CH_2-$), 81.4, 81.5, 81.7,

82.5, 82.8 ($C(CH_3)_3$), 125.7, 129.2, 130.0 (ArC), 134.9 (NCS), 138.9 (ArC), 170.0, 170.6, 170.8, 171.2, 171.4, 172.5, 173.5 (C=O). **ESI-HRMS**: (m/z) $[M+H]^+$ calcd. for $C_{61}H_{106}N_9O_{14}S^+$, 1220.7575, found: 1220.7564.

((2-{2-[2-(*tert*-Butoxycarbonylmethyl-{[4-(4,7,10-trimethyl-1,4,7,10tetraaza-cyclododec-1-yl)-pentylcarbamoyl]-methyl}-amino)-ethoxy]-ethoxy}-ethyl)-{[2-(4-isothiocyanato-phenyl)-ethylcarbamoyl]-methyl}-amino)-acetic acid *tert*-butyl ester (L^2).

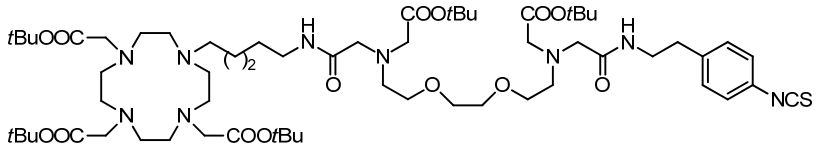

Amine **15** (0.761 g, 0.638 mmol) was dissolved in dichloromethane (10 mL) and solution of saturated sodium hydrogen carbonate (10 mL) was added. Thiophosgene (0.073 mL, 0.957 mmol) was added to the mixture and stirred for 1.5 h at room temperature. The organic layer was then separated; an additional portion of dichloromethane (100 mL) was added and washed with water (2 x 100 mL). The organic layers were combined, dried with sodium sulphate, filtered and the solvent was evaporated. The crude oil was then purified by column chromatography (silica gel, dichloromethane/methanol, 94:6 v/v) to yield isothiocyanate $\mathbf{L^2}$ as an orange oily solid (0.333 g, 42 %).

^{1}H NMR (300 MHz, $CDCl_3$): δ (ppm) 0.97 – 1.85 (br, 51H), 1.92 – 3.76 (br, 50H), 7.19 (dd, 4H), 7.59 – 8.09 (br, 2H). **^{13}C NMR** (75 MHz, $CDCl_3$): δ (ppm) 24.7, 25.6 ($-CH_2-$), 27.7, 27.8, 28.0 ($C(CH_3)_3$), 29.4, 35.2, 38.7, 39.8, 50.1, 50.6, 52.3, 53.0, 53.4, 54.1, 54.3, 55.6, 56.3, 56.7, 57.0, 57.1, 59.0, 69.1, 70.1 ($-CH_2-$), 81.3, 81.3, 81.5, 81.6, 82.3, 82.6 ($C(CH_3)_3$), 125.5, 129.1, 129.9 (ArC), 134.8 (NCS), 138.8 (ArC), 169.8, 170.3, 170.4, 170.5, 170.7, 171.1, 171.3, 172.3, 172.4, 173.3 (C=O). **ESI-HRMS**: (m/z) $[M+H]^+$ calcd. for $C_{62}H_{108}N_9O_{14}S^+$, 1234.7731, found: 1234.7715.

(4,7-Bis-*tert*-butoxycarbonylmethyl-10-{[2-(4-nitro-phenyl)-ethylcarbamoyl]-methyl}-1,4,7,10tetraaza-cyclododec-1-yl)-acetic acid *tert*-butyl ester (16).

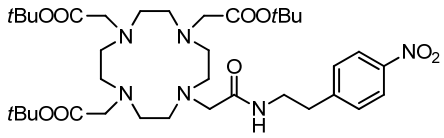

DO3A (14.98 g, 29.1 mmol) was dissolved in DMF (110 mL) and potassium carbonate was added (12.07 g, 87.0 mmol). The reaction was stirred at room temperature for 30 min. Bromide **10** (10.87 g, 37.8 mmol) was then dissolved in DMF (80 mL) and slowly added into the solution. The mixture was stirred at room temperature overnight. The mixture was then filtered and the solvent evaporated

under reduced pressure. The crude product was purified by column chromatography (silica gel, dichloromethane/methanol, 94:6 v/v) to yield **16** as an orange oil (14.11 g, 67 %).

^{1}H NMR (300 MHz, $CDCl_3$): δ (ppm) 1.32 – 1.59 (br, 27H), 1.89 – 3.67 (br, 28 H), 7.53 (d, *J* = 8.50 Hz, 2H), 8.09 (d, *J* = 8.69 Hz, 2H), 8.86 (t, 1H). **^{13}C NMR** (75 MHz, $CDCl_3$): δ (ppm) 28.9, 29.0 ($C(CH_3)_3$), 56.5, 56.6, 57.2 (-CH_2-), 82.7, 82.8 ($C(CH_3)_3$), 124.3, 131.1, 147.3, 149.5 (ArC), 172.5, 173.3 (C=O). **ESI-HRMS**: (m/z) $[M+H]^+$ calcd. for $C_{36}H_{61}N_6O_9^+$, 721.4495, found: 721.4495.

(4-{[2-(4-Amino-phenyl)-ethylcarbamoyl]-methyl}-7,10-bis-*tert*-butoxycarbonylmethyl-1,4,7,10tetraaza-cyclododec-1-yl)-acetic acid *tert*-butyl ester (17).

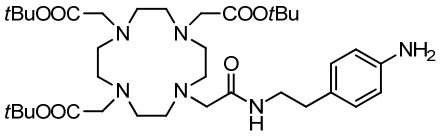

Pd/C (1.410 g) was added to a solution of nitro **16** (14.106 g, 19.57 mmol) in ethanol (30 mL). The heterogeneous mixture was shaken for 16 h in a hydrogen atmosphere using a Parr hydrogenator (3 bar). The catalyst was removed by filtration through a plug of celite and the solvent evaporated under reduced pressure to give amine **17** as a brown solid (12.195 g, 90 %). The resulting solid was used in subsequent reactions without any further purification.

^{1}H NMR (300 MHz, $CDCl_3$): δ (ppm) 1.46 (s, 27H), 1.83 – 3.58 (br, 28H), 6.43 – 6.71 (m, 2H), 6.91 – 7.17 (m, 2H). **^{13}C NMR** (75 MHz, $CDCl_3$): δ (ppm) 27.9, 28.0 ($C(CH_3)_3$), 34.9, 40.8, 55.7, 56.4 (-CH_2-), 81.7, 81.8 ($C(CH_3)_3$), 115.1, 129.8, 129.9, 144.4 (ArC), 171.4, 172.4 (C=O). **ESI-HRMS**: (m/z) $[M+H]^+$ calcd. for $C_{36}H_{63}N_6O_7^+$, 691.4753, found: 691.4749.

[4-({2-[4-(2-Bromo-acetylamino)-phenyl]-ethylcarbamoyl}-methyl)-7,10-bis-*tert*-butoxycarbonylmethyl-1,4,7,10tetraaza-cyclododec-1-yl]-acetic acid *tert*-butyl ester (18).

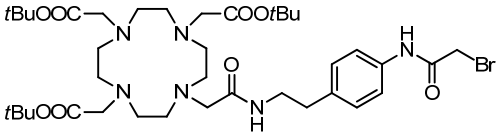

N,*N*'-methanediylidenedicyclohexanamine (2.240 g, 10.86 mmol) and 2-bromoacetic acid (1.508 g, 10.86 mmol) were dissolved in dichloromethane (10 mL). Amine **17** (5.000 g, 7.24 mmol) was dissolved in dichloromethane (20 mL) and added to the mixture. The reaction mixture was stirred overnight. The mixture was then filtered and the filtrate was evaporated under reduced pressure. The crude material was purified by column chromatography (silica gel, dichloromethane/methanol, 92:8 v/v) yielding bromide **18** as a yellow oil (2.612 g, 45 %).

^{1}H NMR (300 MHz, $CDCl_3$): δ (ppm) 1.44 (s, 27H), 1.75 – 3.66 (br, 28H), 4.32 (s, 2H), 7.16 (d, *J* = 8.31 Hz, 2H), 7.75 (d, *J* = 8.31 Hz, 2H), 7.95 (br. s., 1H), 10.37 (s, 1H). **^{13}C NMR** (75 MHz, $CDCl_3$): δ (ppm)

27.9, 28.0 ($C(CH_3)_3$), 31.0, 35.1, 40.4, 55.5, 55.7, 56.4 ($-CH_2-$), 81.6, 81.8 ($C(CH_3)_3$), 120.3, 129.3, 135.4, 136.8 (ArC), 165.3, 171.2, 172.4 (C=O). **ESI-HRMS**: (m/z) $[M+H]^+$ calcd. for $C_{38}H_{64}BrN_6O_8^+$, 833.3783, found: 833.3773.

({2-[2-(2-{*tert*-butoxycarbonylmethyl-[(4-{2-[2-(4,7,10-tris-*tert*-butoxycarbonylmethyl-1,4,7,10tetraaza-cyclododec-1-yl)-acetylamino]-ethyl}-phenylcarbamoyl)-methyl]-amino}-ethoxy)-ethoxy]-ethyl}-{[2-(4-nitro-phenyl)-ethylcarbamoyl]-methyl}-amino)-acetic acid *tert*-butyl ester (19).

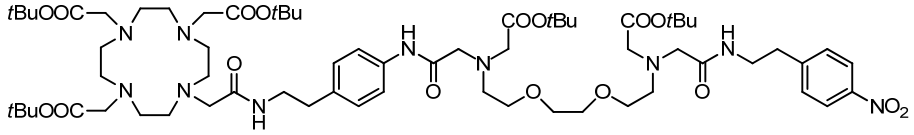

Amine **11** (1.500 g, 2.57 mmol) was dissolved in acetonitrile (50 mL) and potassium carbonate (1.067 g, 7.72 mmol) was added. After 30 min of stirring at room temperature, bromide **18** (2.508 g, 3.09 mmol) was added and the mixture was stirred at reflux overnight. The mixture was allowed to cool to room temperature, filtered and the solvent removed under reduced pressure. The crude oil was purified by column chromatography (silica gel, dichloromethane/methanol, 95:5 v/v) to yield nitro **19** (2.010 g, 59 %) as a yellow solid.

^{1}H NMR (300 MHz, $CDCl_3$): δ (ppm) 1.35 – 1.53 (br, 45H), 1.90 – 3.66 (br, 52H), 7.21 (d, *J* = 7.74 Hz, 2H), 7.42 (d, *J* = 8.31 Hz, 2H), 7.53 (d, *J* = 7.37 Hz, 2H), 8.01 (br. s., 1H), 8.13 (d, *J* = 8.50 Hz, 2H), 8.35 (br. s., 1H), 9.75 (br. s., 1H). **^{13}C NMR** (75 MHz, $CDCl_3$): δ (ppm) 27.9, 28.0, 28.1 ($C(CH_3)_3$), 35.1, 35.5, 39.6, 40.5, 54.3, 54.8, 55.6, 55.6, 56.2, 57.0, 57.5, 59.1, 59.9, 69.1, 70.1, 70.3 ($-CH_2-$), 81.4, 81.7, 81.8 ($C(CH_3)_3$), 119.5, 123.5, 129.3, 129.8, 135.4, 136.1, 146.5, 147.2 (ArC), 169.5, 170.7, 171.4, 171.6, 172.1, 172.4 (C=O). **ESI-HRMS**: (m/z) $[M+Na]^+$ calcd. for $C_{66}H_{108}N_{10}O_{17}Na^+$, 1335.7786, found: 1335.7771.

({[2-(4-Amino-phenyl)-ethylcarbamoyl]-methyl}-{2-[2-(2-{*tert*-butoxycarbonylmethyl-[(4-{2-[2-(4,7,10-tris-*tert*-butoxycarbonylmethyl-1,4,7,10tetraaza-cyclododec-1-yl)-acetylamino]-ethyl}-phenylcarbamoyl)-methyl]-amino}-ethoxy)-ethoxy]-ethyl}-amino)-acetic acid *tert*-butyl ester (20).

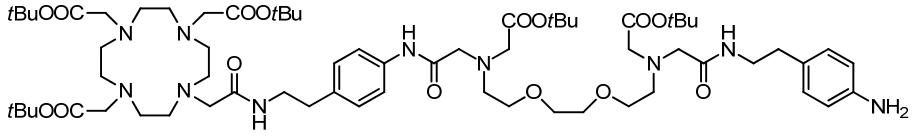

Pd/C (0.20 g) was added to a solution of nitro **19** (2.01 g, 1.53 mmol) in ethanol (10 mL). The heterogeneous mixture was shaken for 5 h in a hydrogen atmosphere using a Parr hydrogenator (3 bar). The catalyst was removed by filtration through a plug of celite and the solvent evaporated

under reduced pressure to give amine **20** as a yellow solid (1.49 g, 76 %). The resulting solid was used in subsequent reactions without any further purification.

^{1}H NMR (300 MHz, $CDCl_3$): δ (ppm) 1.3 – 1.62 (br, 45H), 1.86 – 3.69 (br, 52H), 6.61 (d, *J* = 8.12 Hz, 2H), 7.96 (d, *J* = 8.12 Hz, 2H), 7.19 (d, *J* = 8.12 Hz, 2H), 7.53 (d, *J* = 7.74 Hz, 2H). **^{13}C NMR** (75 MHz, $CDCl_3$): δ (ppm) 27.8, 27.9, 28.0 ($C(CH_3)_3$), 31.7, 33.6, 34.7, 35.0, 40.4, 54.2, 54.7, 55.5, 55.5, 56.1, 56.9, 57.3, 59.0, 59.8, 69.0, 69.2, 70.1, 70.2 ($-CH_2-$), 81.3, 81.6, 81.7 ($C(CH_3)_3$), 113.9, 115.1, 119.3, 119.8, 126.8, 127.2, 128.3, 128.5, 129.2, 129.3, 135.4, 135.9, 139.1, 141.1, 144.9 (ArC), 169.4, 170.4, 170.6, 171.1, 171.4, 172.2 (C=O). **ESI-HRMS**: (m/z) $[M+Na]^+$ calcd. for $C_{66}H_{110}N_{10}O_{15}Na^+$, 1305.8044, found: 1305.8041.

({2-[2-(2-{*tert*-butoxycarbonylmethyl-[(4-{2-[2-(4,7,10-tris-*tert*-butoxycarbonylmethyl-1,4,7,10tetraaza-cyclododec-1-yl)-acetylamino]-ethyl}-phenylcarbamoyl)-methyl]-amino}-ethoxy)-ethoxy]-ethyl}-{[2-(4-isothiocyanato-phenyl)-ethylcarbamoyl]-methyl}-amino)-acetic acid *tert*-butyl ester (L^3).

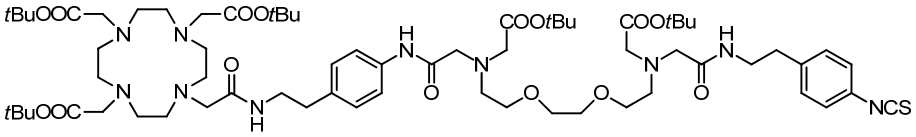

Amine **20** (1.220 g, 0.950 mmol) was dissolved in dichloromethane (20 mL) and solution of saturated sodium hydrogen carbonate (20 mL) was added. Thiophosgene (0.109 mL, 1.426 mmol) was added to the mixture and stirred for 3 h at room temperature. The organic layer was then separated; an additional portion of dichloromethane (100 mL) was added and the organic phase was washed with water (2 x 100 mL). The organic layers were then combined, dried with sodium sulphate, filtered and the solvent was evaporated. The crude oil was then purified by column chromatography (silica gel, dichloromethane/methanol, 94:6 v/v) to yield isothiocyanate **L^3** as a yellow solid (0.690 g, 55 %).

^{1}H NMR (300 MHz, $CDCl_3$): δ (ppm) 1.35 – 1.61 (br, 45H), 1.96 – 3.73 (br, 52H), 7.04 – 7.31 (m, 6H), 7.45 – 7.72 (m, 2H). **^{13}C NMR** (75 MHz, $CDCl_3$): δ (ppm) 27.9, 28.0, 28.1 ($C(CH_3)_3$), 31.9, 33.8, 35.2, 35.3, 40.0, 40.6, 54.3, 54.8, 55.7, 56.2, 57.0, 57.5, 59.2, 60.0, 69.2, 69.3, 70.2, 70.4 ($-CH_2-$), 81.5, 81.7, 81.8 ($C(CH_3)_3$), 119.4, 119.9, 125.7, 129.2, 129.4, 130.0 (ArC), 134.9 (NCS), 135.7, 136.0, 138.9, 139.2 (ArC), 169.5, 170.7, 170.8, 171.5, 172.3 (C=O). **ESI-HRMS**: (m/z) $[M+Na]^+$ calcd. for $C_{67}H_{108}N_{10}O_{15}SNa^+$, 1347.7609, found: 1347.7594.

6-Benzyloxycarbonylamino-2-bromo-hexanoic acid *tert*-butyl ester (21).

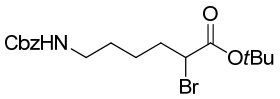

Synthesis was performed following a previously published method. The analytical data matched that which was previously reported.[294]

6-Benzyloxycarbonylamino-2-(4,7,10-tris-*tert*-butoxycarbonylmethyl-1,4,7,10tetraaza-cyclododec-1-yl)-hexanoic acid *tert*-butyl ester (22).

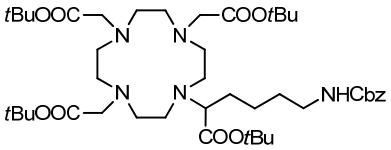

DO3A (3.00 g, 5.8 mmol) was dissolved in DMF (15 mL) and potassium carbonate (4.03 g, 29.1 mmol) was added. The mixture was left to stir at room temperature for 30 min. Bromide **21** (3.50 g, 8.7 mmol) was dissolved in DMF (5 mL) and added to the mixture dropwise. The reaction mixture was heated to 45 °C and was stirred for 1 day. The insoluble salts were removed by filtration and the filtrate was concentrated under reduced pressure to yield the crude product which was then purified by column chromatography (silica gel, dichloromethane/methanol, 90:10 v/v) to yield **22** (3.83 g, 79 %).

^{1}H NMR (300 MHz, $CDCl_3$): δ (ppm) 0.97 – 1.75 (br, 42H), 1.77 – 3.50 (br, 25H), 5.08 (s, 2H), 7.02 – 7.44 (m, 5H). **^{13}C NMR** (75 MHz, $CDCl_3$): δ (ppm) 24.4, 26.6 (-CH_2), 27.8, 27.9 (C(CH_3)$_3$), 30.0, 40.6, 44.7, 47.3, 48.2, 48.6, 52.5, 55.6, 55.9, 61.3 (-CH_2-), 66.4 (-CH-), 81.9, 81.9, 82.0 (C(CH_3)$_3$), 127.9, 128.4, 136.8 (ArC), 156.5, 172.8, 172.9, 175.1 (C=O).

6-Amino-2-(4,7,10-tris-*tert*-butoxycarbonylmethyl-1,4,7,10tetraaza-cyclododec-1-yl)-hexanoic acid *tert*-butyl ester (23).

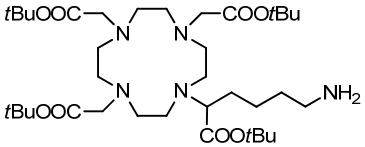

Macrocycle **22** (2.00 g, 2.398 mmol) was dissolved in ethanol (20 mL) and $Pd(OH)_2$/C catalyst (0.20 g) was added. The mixture was shaken overnight in a hydrogen atmosphere using a Parr hydrogenator (3 bar). The catalyst was removed by filtration through a plug of celite and the solvent evaporated under reduced pressure to give amine **23** as brown oil (1.66 g, 99 %). The resulting solid was used in subsequent reactions without further purification.

^{1}H NMR (300 MHz, $CDCl_3$): δ (ppm) 1.12 – 1.75 (br, 42H), 1.71 – 2.00 (m, 2H), 1.89 – 3.50 (br, 25H). **^{13}C NMR** (75 MHz, $CDCl_3$): δ (ppm) 24.9, 26.7 (-CH_2-), 27.9 ($C(CH_3)_3$), 29.7, 40.4, 44.8, 47.3, 48.2, 48.6, 48.6, 52.6, 52.7, 55.6, 55.8, 55.9 (-CH_2-), 61.4 (-CH-), 81.8, 81.9, 82.0 ($C(CH_3)_3$), 172.7, 172.9, 175.3 (C=O).

6-(2-Bromo-acetylamino)-2-(4,7,10-tris-*tert*-butoxycarbonylmethyl-1,4,7,10tetraaza-cyclododec-1-yl)-hexanoic acid *tert*-butyl ester (24).

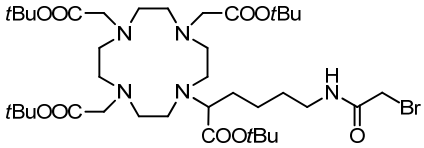

N,*N*'-methanediylidenedicyclohexanamine (0.739 g, 3.58 mmol) and 2-bromoacetic acid (0.498 g, 3.58 mmol) were dissolved in dichloromethane (40 mL). Amine **23** (2.090 g, 2.99 mmol) was dissolved in dichloromethane (20 mL) and added to the mixture. The reaction mixture was stirred overnight. The mixture was then filtered and the filtrate was evaporated under reduced pressure. The crude material was purified by column chromatography (silica gel, dichloromethane/methanol, 90:10 v/v) yielding bromide **24** (1.250 g, 51 %).

^{1}H NMR (300 MHz, $CDCl_3$): δ (ppm) 1.32-1.82 (br, 42H), 1.99 – 3.55 (br, 25H), 4.01 – 4.14 (m, 2H. **^{13}C NMR** (75 MHz, $CDCl_3$): δ (ppm) 24.9, 26.6 (-CH_2-), 27.8 ($C(CH_3)_3$), 29.0, 30.2, 39.3, 44.6, 47.2, 48.1, 48.4, 48.5, 52.5, 52.6, 55.5, 55.7, 55.8, (-CH_2-), 61.3 (-CH-), 81.9, 82.0, 82.1 ($C(CH_3)_3$), 120.3, 129.3, 135.4, 136.8 (ArC), 166.8, 172.6, 172.8, 175.2 (C=O). **ESI-HRMS**: (m/z) $[M+Na]^+$ calcd. for $C_{38}H_{70}BrN_5O_9Na^+$, 842.4249, found: 842.4245.

6-{2-[*tert*-butoxycarbonylmethyl-(2-{2-[2-(*tert*-butoxycarbonylmethyl-{[2-(4-nitro-phenyl)-ethylcarbamoyl]-methyl}-amino)-ethoxy]-ethoxy}-ethyl)-amino]-acetylamino}-2-(4,7,10-tris-*tert*-butoxycarbonylmethyl-1,4,7,10tetraaza-cyclododec-1-yl)-hexanoic acid *tert*-butyl ester (25).

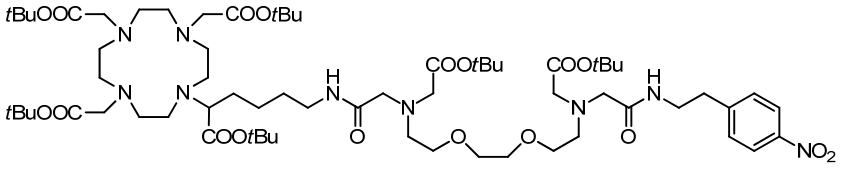

Amine **11** (0.865 g, 1.485 mmol) was dissolved in acetonitrile (60 mL) and potassium carbonate (0.492 g, 3.560 mmol) was added. After 30 min of stirring at room temperature, bromide **24** (1.462 g, 1.781 mmol) was added and the mixture was stirred at reflux overnight. An additional portion of **24** was then added (0.244 g, 0.297 mmol) and the reaction was allowed to react further at reflux for an additional 6 hours. The mixture was then allowed to cool to room temperature, filtered and the solvent removed under reduced pressure. The crude oil was purified by column chromatography

(silica gel, dichloromethane/methanol, 94:6 v/v) to yield nitro **25** (1.502 g, 76 %) as an off white solid.

^{1}H NMR (300 MHz, $CDCl_3$): δ (ppm) 1.18 – 1.79 (br, 60H), 1.97 – 3.85 (br, 49H), 7.38 – 7.56 (m, 2H), 7.97 – 8.22 (m, 2H). **^{13}C NMR** (75 MHz, $CDCl_3$): δ (ppm) 22.7, 25.2 ($-CH_2-$), 26.0, 26.1, 26.4 ($C(CH_3)_3$), 28.2, 30.1, 32.0, 33.8, 36.9, 37.9, 43.0, 45.6, 46.4, 46.8, 50.7, 50.8, 50.9, 51.9, 52.6, 53.8, 54.0, 54.1, 55.2, 55.4, 57.4 ($-CH_2-$), 59.6 (-CH-), 67.5, 68.4 ($-CH_2-$) 79.6, 80.2, 80.2, 80.3 ($C(CH_3)_3$), 121.7, 128.1, 144.8, 145.6 (ArC), 168.9, 169.5, 169.8, 169.8, 171.0, 171.1, 173.3 (C=O). **ESI-HRMS**: (m/z) $[M+Na]^+$ calcd. for $C_{66}H_{115}N_9O_{18}Na^+$, 1344.8252, found: 1344.8245.

6-{2-[(2-{2-[2-({[2-(4-Amino-phenyl)-ethylcarbamoyl]-methyl}-*tert*-butoxycarbonylmethyl-amino)-ethoxy]-ethoxy}-ethyl)-*tert*-butoxycarbonylmethyl-amino]-acetylamino}-2-(4,7,10-tris-*tert*-butoxycarbonylmethyl-1,4,7,10tetraaza-cyclododec-1-yl)-hexanoic acid *tert*-butyl ester (26).

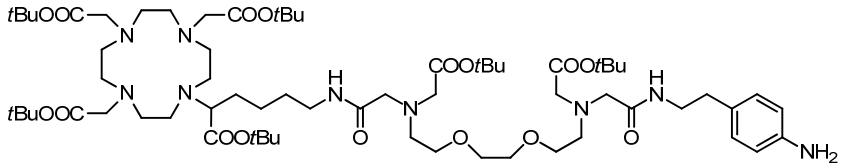

Pd/C (0.067 g) was added to a solution of nitro **25** (0.445 g, 0.336 mmol) in ethanol (15 mL). The heterogeneous mixture was shaken for 5 h in a hydrogen atmosphere using a Parr hydrogenator (3 bar). The catalyst was removed by filtration through a plug of celite and the solvent evaporated under reduced pressure to give amine **26** as a brown solid (0.435 g, 100 %). The resulting solid was used in subsequent reactions without any further purification.

^{1}H NMR (300 MHz, $CDCl_3$): δ (ppm) 0.61 – 1.54 (br, 60H), 1.55 – 4.09 (br, 49H), 5.96 – 8.32 (m, 4H). **^{13}C NMR** (75 MHz, $CDCl_3$): δ (ppm) 22.3, 24.2, 26.6 ($-CH_2-$), 27.6, 27.8 ($C(CH_3)_3$), 28.9, 29.3, 31.5, 34.6, 35.0, 35.3, 38.4, 39.4, 39.8, 40.5, 44.4, 47.1, 47.8, 48.2, 52.3, 54.4, 55.2, 55.5, 57.0, 58.6 ($-CH_2-$), 61.0 (-CH-), 68.4, 69.6 ($-CH_2-$), 81.0, 81.6 ($C(CH_3)_3$), 114.8, 121.8, 125.4, 127.8, 129.1, 145.3 (ArC), 170.6, 171.0, 172.5, 172.6, 174.8 (C=O). **ESI-HRMS**: (m/z) $[M+Na]^+$ calcd. for $C_{66}H_{117}N_9O_{16}Na^+$, 1314.8511, found: 1314.8488.

6-{2-[*tert*-butoxycarbonylmethyl-(2-{2-[2-(*tert*-butoxycarbonylmethyl-{[2-(4-isothiocyanato-phenyl)-ethylcarbamoyl]-methyl}-amino)-ethoxy]-ethoxy}-ethyl)-amino]-acetylamino}-2-(4,7,10-tris-*tert*-butoxycarbonylmethyl-1,4,7,10tetraaza-cyclododec-1-yl)-hexanoic acid *tert*-butyl ester (L^4).

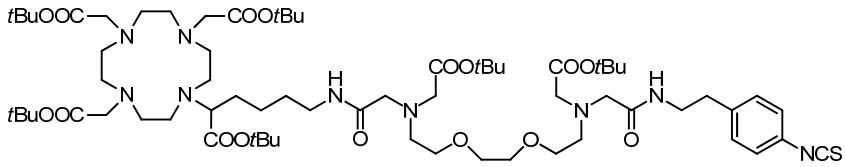

Amine **26** (0.460 g, 0.356 mmol) was dissolved in dichloromethane (5 mL) and solution of saturated sodium hydrogen carbonate (5 mL) was added. Thiophosgene (0.041 mL, 0.534 mmol) was added to the mixture and stirred for 1.5 h at room temperature. The organic layer was then separated; an additional portion of dichloromethane (100 mL) was added and the organic phase was washed with water (2 x 100 mL). The organic layers were then combined, dried with sodium sulphate, filtered and the solvent was evaporated. The crude oil was then purified by column chromatography (silica gel, dichloromethane/methanol, 94:6 v/v) to yield isothiocyanate **L^4** as a yellow solid (0.200 g, 42 %).
^{1}H NMR (300 MHz, $CDCl_3$): δ (ppm) 0.73 – 1.53 (br, 60H), 1.62 – 3.48 (br, 49H), 6.73 – 7.13 (m, 2H), 7.46 – 7.94 (m, 2H). **^{13}C NMR** (75 MHz, $CDCl_3$): δ (ppm) 24.4, 26.8 (-CH_2-), 27.8, 27.8, 28.1 ($C(CH_3)_3$), 29.8, 31.2, 35.3, 38.6, 39.9, 44.6, 47.3, 48.0, 48.4, 52.5, 52.6, 53.7, 54.3, 55.5, 55.7, 55.8, 57.0, 57.2, 57.6, 59.0, 59.1 (-CH_2-), 61.3 (-CH-), 69.1, 70.1 (-CH_2-), 81.4, 81.9, 82.0, 82.1 ($C(CH_3)_3$), 125.6, 129.0, 130.1 (ArC), 134.8 (NCS), 139.0 (ArC), 170.7, 170.8, 171.3, 171.5, 172.7, 172.8, 175.0 (C=O). **LRMS**: (m/z) $[M+Na]^+$ calcd. for $C_{67}H_{115}N_9O_{16}SNa^+$, 1356.8, found 1356.5.

(2-{2-[2-(Benzyl-*tert*-butoxycarbonylmethyl-amino)-ethoxy]-ethoxy}-ethylamino)-acetic acid *tert*-butyl ester (27).

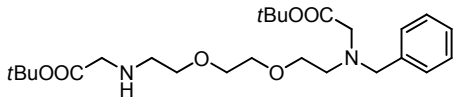

Compound **27** was synthesised in accordance with a previously reported literature procedure.[188]

6-{2-[(2-{2-[2-(Benzyl-*tert*-butoxycarbonylmethyl-amino)-ethoxy]-ethoxy}-ethyl)-*tert*-butoxycarbonylmethyl-amino]-acetylamino}-2-(4,7,10-tris-*tert*-butoxycarbonylmethyl-1,4,7,10-tetraaza-cyclododec-1-yl)-hexanoic acid *tert*-butyl ester (28).

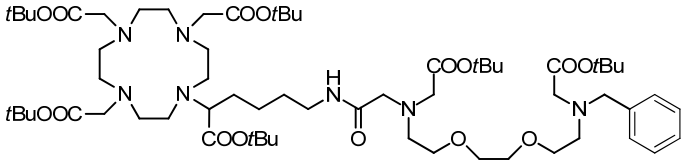

Amine **27** (0.508 g, 1.088 mmol) was dissolved in DMF (6 mL) and potassium carbonate (0.451 g, 3.26 mmol) was added. The resulting mixture was stirred for 30 min before a solution of bromide **24** (1.25 g, 1.523 mmol) in DMF (4 mL) was added dropwise. The reaction mixture was allowed to stir at room temperature for 4 days. The reaction mixture was filtered and the solvent was then removed under reduced pressure to yield a crude oil which was purified by column chromatography (silica gel, dichloromethane/methanol, 94:6 v/v) to yield the final product (0.467 g, 36 %).

^{1}H NMR (300 MHz, $CDCl_3$): δ (ppm) 1.23 – 1.69 (br, 60H), 1.91 – 3.88 (br, 45H), 7.17 – 7.39 (m, 5H). **^{13}C NMR** (75 MHz, $CDCl_3$): δ (ppm) 24.4, 26.9 (-CH_2-), 27.7, 27.8, 28.0, 28.1 ($C(CH_3)_3$), 29.9, 38.6, 44.7, 47.2, 48.2, 48.5, 52.4, 52.6, 54.3, 55.5, 55.7, 55.8, 56.9, 58.5, 59.1 (-CH_2-), 61.3 (-CH-), 68.9, 70.1 (-CH_2-), 77.2, 81.7, 81.8, 81.8, 81.8 ($C(CH_3)_3$), 127.0, 128.1, 128.8, 139.1 (ArC), 170.8, 171.2, 172.7, 172.8, 175.0 (C=O).

6-{2-[*tert*-Butoxycarbonylmethyl-(2-{2-[2-(*tert*-butoxycarbonylmethyl-amino)-ethoxy]-ethoxy}-ethyl)-amino]-acetylamino}-2-(4,7,10-tris-*tert*-butoxycarbonylmethyl-1,4,7,10-tetraaza-cyclododec-1-yl)-hexanoic acid *tert*-butyl ester (29).

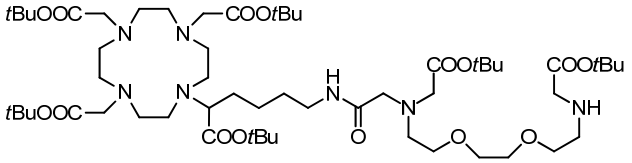

Compound **28** (0.422 g, 0.350 mmol) was dissolved in ethanol (15 mL). $Pd(OH)_2$/C (130 mg) and NH_3 in MeOH (50 µL) was added. The heterogeneous mixture was shaken for 16 h in a hydrogen atmosphere using a Parr hydrogenator (3 bar). The catalyst was then removed by filtration through a plug of celite and the solvent evaporated under reduced pressure to give amine **29** (0.353 g, 90 %). The resulting solid was used in subsequent reactions without any further purification.

^{1}H NMR (300 MHz, $CDCl_3$): δ (ppm) 1.17 – 1.80 (br, 60H), 2.03 – 3.74 (br, 43H). **^{13}C NMR** (75 MHz, $CDCl_3$): δ (ppm) 24.3, 26.8 (-CH_2-), 27.7, 27.7, 27.9, 28.0 ($C(CH_3)_3$), 29.5, 29.7, 38.6, 44.6, 47.2, 48.1, 48.5, 51.1, 52.4, 52.4, 52.6, 54.5, 55.4, 55.7, 55.7, 57.1, 59.0 (-CH_2-), 61.2 (-CH-), 68.8, 70.0 (-CH_2-), 81.2, 81.4, 81.7, 81.8, 81.8, 81.8 ($C(CH_3)_3$), 170.8, 171.0, 171.3, 172.7, 172.8, 175.0 (C=O).

General procedure for the preparation of DCAs$^{1-5}$.[289]

DCAs$^{1-5}$ were each prepared following the same general procedure.[295] Specifically, G4 PAMAM dendrimer (1 equiv with 64 amino surface groups, 10% dendrimer solution in methanol) was dried under reduced pressure. The residue was dissolved in DMF, triethylamine (160 equiv) was added to the reaction, and the mixture was stirred at 45 °C for 45 min. Macrocyclic isothiocyanate (**L$^{1-4}$**, 1.5 equiv per amino surface group of the dendrimer) was dissolved in DMF and added in four portions (one portion every 12 h) while the temperature of the mixture was maintained at 45 °C. After the final addition of isothiocyanate, the mixture was stirred for an additional 12 h at 45 °C. The solvent was then removed by bulb-to-bulb vacuum distillation at 50 °C. The resulting residue was redissolved in methanol and purified by size exclusion chromatography using lipophilic Sephadex with methanol as the eluent. The solvent was then evaporated under reduced pressure yielding the tert-butyl protected dendrimer **D^{1a-4a}**. For the preparation of **DCA^{5}**, the dendrimer **D^{4a}** underwent an additional capping reaction with methyl isothiocyanate (62 equiv) and triethylamine (103 equiv) in DMF and was purified using the procedure described for the macrocyclic isothiocyanates **L$^{1-4}$** to result in the dendrimer **D^{5a}**. The tert-butyl protected dendrimers **D^{1a-5a}** were then dissolved in formic acid, and the mixture was stirred at 60 °C for 24 h. The solvent was removed under reduced pressure. The residue was redissolved in water and lyophilized to give the dendrimers **D^{1b-5b}**. The resulting solids were then dissolved in water, and the pH was adjusted to 7 by the addition of sodium hydroxide (0.1 M). A solution of gadolinium chloride hexahydrate (1.1 equiv relative to the number of amino surface groups of the dendrimer) in water was then added to the mixture portionwise over 1 h while the pH was maintained at 7 with the addition of a solution of sodium hydroxide (0.05 M). The resulting solution was stirred for 24 h at room temperature. EDTA (1.5 equiv relative to the number of amino surface groups of the dendrimer) was added to the solution over a period of 1 h while the pH was maintained at 7. The mixture was further stirred for 2 h at room temperature, and the solvent was evaporated. This was redissolved in a small volume of water and purified by size-exclusion chromatography with hydrophilic Sephadex using water as the eluent. The fractions were collected and centrifuged using a 3 kDa centrifugal filter for 40 min at 2000g. This process was repeated until the filtrate showed an absence of GdEDTA and EDTA (checked by low resolution ESI-MS). The product was then lyophilized to obtain the final **DCAs$^{1-5}$** as off white/yellow solids.

General procedure for ligands L^5 and L^6.

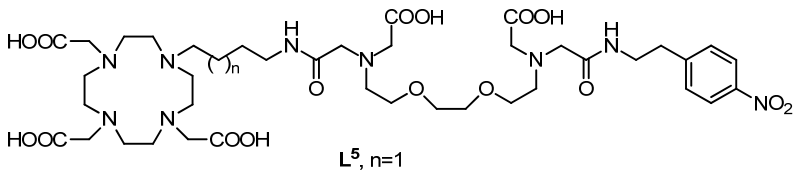

L^5, n=1
L^6, n=2

Protected compounds **12** or **13** were dissolved in formic acid and the mixture was stirred at 60 °C overnight. The solvent was then removed under reduced pressure and the resulting residue was redissolved in water and lyophilized to give ligands L^{5-6} which were used without further purification.

[4,7-Bis-carboxymethyl-10-(4-{2-[carboxymethyl-(2-{2-[2-(carboxymethyl-{[2-(4-nitro-phenyl)-ethylcarbamoyl]-methyl}-amino)-ethoxy]-ethoxy}-ethyl)-amino]-acetylamino}-butyl)-1,4,7,10-tetraaza-cyclododec-1-yl]-acetic acid (L^5).

^{1}H NMR (300 MHz, D_2O) δ (ppm): 1.45 – 1.81 (m, 4H), 2.92 (t, *J*=6.2 Hz, 2H), 2.98 – 3.94 (br, 44H), 4.02 (s, 2H), 4.12 (s, 2H), 7.43 (d, *J*=8.3 Hz), 8.10 (d, *J*=8.3 Hz). **^{13}C NMR** (75 MHz, D_2O) δ (ppm): 20.7, 25.5, 34.6, 38.9, 40.1, 48.7, 49.8, 51.1, 53.6, 54.0, 54.9, 55.2, 55.8, 56.1, 57.0, 57.2, 64.4, 64.6, 69.8 (-CH_2-), 123.7, 130.1, 146.3, 147.6 (ArC), 165.0, 165.3, 169.5, 169.7, 170.3, 174.3 (C=O). **ESI-HRMS**: (m/z) $[M+Ca-H]^+$ calcd. for $C_{40}H_{64}CaN_9O_{16}^+$, 966.40914, found: 966.40732.

[4,7-Bis-carboxymethyl-10-(5-{2-[carboxymethyl-(2-{2-[2-(carboxymethyl-{[2-(4-nitro-phenyl)-ethylcarbamoyl]-methyl}-amino)-ethoxy]-ethoxy}-ethyl)-amino]-acetylamino}-pentyl)-1,4,7,10-tetraaza-cyclododec-1-yl]-acetic acid (L^6).

^{1}H NMR (300 MHz, $CDCl_3$) δ (ppm): 1.22 – 1.82 (m, 6H) 2.62 – 4.20 (br, 50H), 7.44 (d, *J*=7.9 Hz, 2H), 8.12 (d, *J*=7.9 Hz, 2H). **^{13}C NMR** (75 MHz, D_2O) δ (ppm): 22.6, 23.2, 27.7, 34.6, 39.2, 40.1, 48.5, 49.9, 51.3, 53.8, 54.0, 54.9, 55.2, 55.8, 56.0, 56.2, 57.0, 57.2, 64.4, 64.6, 69.8 (-CH_2-), 123.7, 130.1, 146.3, 147.6 (ArC), 165.0, 165.1, 169.4, 169.7, 170.1, 174.5 (C=O). **ESI-HRMS**: (m/z) $[M-3H+Ca]^-$ calcd. for $C_{41}H_{64}CaN_9O_{16}^-$, 978.41024, found: 978.4113.

General procedure for the synthesis of LnL^{5-6} complexes.

Ligands L^1 or L^2 were dissolved in water and the pH adjusted to 7 by addition of a 0.1 M NaOH solution. A slight excess of lanthanide hydrate was then added portionwise while maintaining the pH at 7 with 0.1 M NaOH. After the final addition of lanthanide, the reaction was stirred at room temperature overnight. The removal of excess lanthanide was achieved by repeated treatments with Chelex®, before filtering and lyophilising to yield the final complex. Each complex was then checked by ESI-LRMS.

ESI-LRMS: GdL[5] (m/z) $[M-H]^-$ calcd. for $C_{40}H_{61}GdN_9O_{16}^-$, 1081.3, found: 1081.3. **EuL[5]** (m/z) $[M-H]^-$ calcd. for $C_{40}H_{61}EuN_9O_{16}^-$, 1076.3, found: 1076.3. **YbL[5]** (m/z) $[M-H]^-$ calcd. for $C_{40}H_{61}YbN_9O_{16}^-$, 1097.4, found: 1097.3. **YL[5]** (m/z) $[M-H]^-$ calcd. for $C_{40}H_{61}YN_9O_{16}^-$, 1012.3, found: 1012.4. **GdL[6]** (m/z) $[M-H]^-$ calcd. for $C_{41}H_{63}GdN_9O_{16}^-$, 1095.4, found: 1095.4. **EuL[6]** (m/z) $[M-H]^-$ calcd. for $C_{41}H_{63}EuN_9O_{16}^-$, 1090.4, found: 1090.4. **YbL[6]** (m/z) $[M-H]^-$ calcd. for $C_{41}H_{63}YbN_9O_{16}^-$, 1111.4, found: 1111.4. **YL[6]** (m/z) $[M-H]^-$ calcd. for $C_{41}H_{63}YN_9O_{16}^-$, 1026.3, found: 1026.3.

2-(4,10-Bis-*tert*-butoxycarbonylmethyl-1,4,7,10tetraaza-cyclododec-1-yl)-4-(4-nitro-phenyl)-butyric acid *tert*-butyl ester (30).

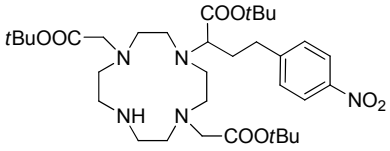

The synthesis of **30** was carried out according to a previously reported procedure.[294]

2-{4,10-Bis-*tert*-butoxycarbonylmethyl-7-[3-(1,3-dioxo-1,3-dihydro-isoindol-2-yl)-propyl]-1,4,7,10tetraaza-cyclododec-1-yl}-4-(4-nitro-phenyl)-butyric acid *tert*-butyl ester (31).

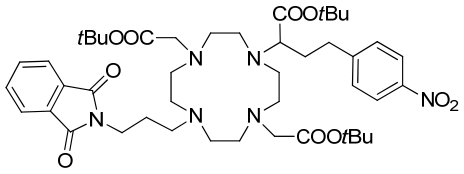

The synthesis of **31** was carried out according to a previously reported procedure.[344]

4-(4-Amino-phenyl)-2-{4,10-bis-*tert*-butoxycarbonylmethyl-7-[3-(1,3-dioxo-1,3-dihydroisoindol-2-yl)-propyl]-1,4,7,10tetraaza-cyclododec-1-yl}-butyric acid *tert*-butyl ester (BB1).

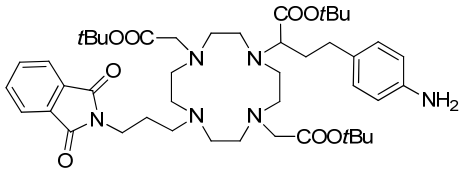

The synthesis of **BB1** was carried out according to a previously reported procedure.[344]

2-phenylpropan-2-yl 2-bromoacetate (32).

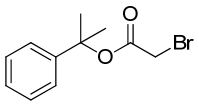

The synthesis of 2-phenylpropan-2-yl 2-bromoacetate was performed with a previously published procedure.[317]

[2-(2-{2-[*tert*-Butoxycarbonylmethyl-(1-methyl-1-phenyl-ethoxycarbonylmethyl)-amino]-ethoxy}-ethoxy)-ethylamino]-acetic acid *tert*-butyl ester (33).

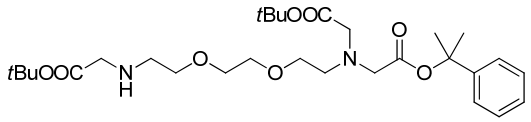

Compound **9** (0.80 g, 2.125 mmol) was dissolved in acetonitrile (50 mL) and potassium carbonate (0.29 g, 2.125 mmol) was added. After stirring for 30 min, 2-phenylpropan-2-yl 2-bromoacetate (0.55 g, 2.125 mmol) was dissolved in acetonitrile (5 mL) and slowly added to the mixture by dropwise addition. The reaction mixture was then stirred at room temperature for 2 days. The resulting mixture was then filtered and the solvent evaporated under reduced pressure to yield a crude oil which was purified by column chromatography (silica gel, dichloromethane/methanol, 97:3 v/v) giving amine **33** (0.52 g, 44 %) as a yellow oil.

^{1}H NMR (300 MHz, $CDCl_3$): δ (ppm) 1.46 (m, 18H), 1.77 (s, 6H), 2.78 (t, J=5.19 Hz, 2H), 2.91 (t, J=5.67, 2H), 3.24 – 3.35 (m, 2H), 3.46 (s, 2H), 3.50 – 3.65 (m, 10H), 7.14 – 7.39 (m, 5H). **^{13}C NMR** (75 MHz, $CDCl_3$): δ (ppm) 28.0, 28.1 ($C(CH_3)_3$), 28.6 ($C(CH_3)_2$), 48.7, 51.5, 53.6, 56.6, 70.0, 70.4 (-CH_2-), 80.9, 80.9 ($C(CH_3)_3$), 82.0 ($C(CH_3)_2$), 124.2, 126.9, 128.2, 145.6 (ArC), 170.2, 170.8, 171.6 (C=O). **ESI-HRMS**: (m/z) $[M+H]^+$ calcd. for $C_{29}H_{48}N_2O_8^+$, 553.3483, found: 553.3481.

[[2-(2-{2-[*tert*-Butoxycarbonylmethyl-(1-methyl-1-phenylethoxycarbonylmethyl)-amino]-ethoxy}-ethoxy)-ethyl]-(9H-fluoren-9-ylmethoxycarbonyl)-amino]-acetic acid *tert*-butyl ester (34).

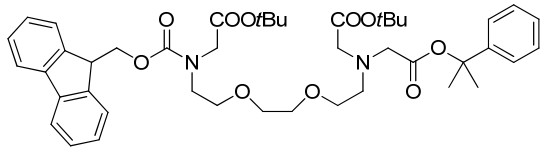

Compound **34** was synthesized following a slightly modified acylation procedure with FmocCl.[284] Amine **33** (1.735 g, 3.14 mmol) was dissolved in dioxane (24 mL) and a solution of Na_2CO_3 (0.998 g, 9.42 mmol) in H_2O (24 mL) was added. The reaction mixture was cooled to 0 °C and a solution of 9-fluorenylmethylchloroformate (0.975 g, 3.77 mmol) in dioxane (15 mL) was added dropwise to the mixture. The reaction mixture was then allowed to warm to room temperature and stirred overnight. The solvents were evaporated under reduced pressure and the residue was purified by column chromatography (silica gel, dichloromethane/ethyl acetate, 80:20 v/v) to yield **6** (1.70 g, 70 %).

^{1}H NMR (300 MHz, $CDCl_3$): δ (ppm) 1.45 (br. s., 18H), 1.77 (br. s., 6H), 2.86 – 3.01 (m, 2H), 3.28 – 3.72 (m, 14H), 3.93 – 4.09 (m, 2H), 4.17 – 4.30 (m, 2H), 4.36 (d, *J*=7.18 Hz, 1H), 4.48 (d, *J*=6.23 Hz, 1H) 7.20 – 7.44 (m, 9H), 7.58 (d, *J*=7.37 Hz, 2H), 7.75 (d, *J*=7.55 Hz, 2H). **^{13}C NMR** (75 MHz, $CDCl_3$): δ (ppm) 28.0, 28.1 ($C(CH_3)_3$), 28.6 ($C(CH_3)_2$), 47.3 (-CH-), 47.8, 48.4, 50.7, 53.3, 56.4, 67.3, 67.8, 69.8, 70.1,

70.4 (-CH_2-), 80.8, 81.5, 81.6 ($C(CH_3)_3$), 82.0 ($C(CH_3)_2$), 119.9, 124.2, 124.8, 125.1, 126.9, 127.0, 127.6, 128.2, 141.2, 141.3, 143.9, 145.6 (ArC), 156.0, 156.1, 168.9, 169.0, 170.0, 170.7 (C=O). **ESI-HRMS**: (m/z) $[M+H]^+$ calcd. for $C_{44}H_{58}N_2O_{10}^+$, 775.4164, found: 775.4172.

{*tert*-Butoxycarbonylmethyl-[2-(2-{2-[*tert*-butoxycarbonylmethyl-(9*H*-fluoren-9 ylmethoxycarbonyl)-amino]-ethoxy}-ethoxy)-ethyl]-amino}-acetic acid (BB2).

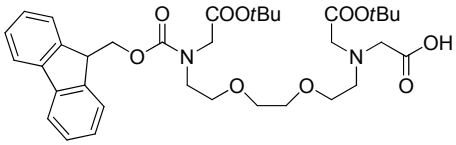

Compound **34** (0.3 g, 0.387 mmol) was dissolved in a solution of 3 % TFA/dichloromethane and stirred for 1 h. The solvent was evaporated under reduced pressure giving a yellow oil which was used in subsequent reactions without further purification.

Analytical data was obtained from a portion of the product after purification with column chromatography (silica gel, dichloromethane/methanol, 97:3 v/v).

^{1}H NMR (300 MHz, $CDCl_3$) δ (ppm): 1.46 (s, 18H), 3.01-3.19 (m, 2H), 3.36 (s, 2H), 3.41 – 3.70 (m, 12H), 4.00 (d, 2H), 4.15 – 4.30 (m, 1H), 4.37 (d, 1H), 4.49 (d, 1H), 7.30 (t, *J* = 7.18 Hz, 2H), 7.39 (t, *J* = 7.37 Hz, 2H), 7.58 (d, *J* = 7.37 Hz, 2H), 7.75 (d, *J* = 7.37 Hz, 2H). **^{13}C NMR** (75 MHz, $CDCl_3$) δ (ppm): 27.9, 27.9, 28.0 ($C(CH_3)_3$), 47.1, 47.2 (-CH-), 47.8, 48.3, 50.5, 50.7, 53.3, 53.4, 53.4, 54.7, 56.6, 57.1, 57.2, 67.9, 68.0, 69.7, 70.1, 70.2 (-CH_2-), 81.5, 81.7, 82.7, 82.8 ($C(CH_3)_3$), 119.8, 119.9, 124.7, 124.8, 125.0, 125.0, 127.0, 127.6, 141.1, 141.2, 143.8, 143.9 (ArC), 156.1, 168.9, 169.0, 171.4, 171.4 (C=O). **ESI-HRMS**: (m/z) $[M+H]^+$ calcd. for $C_{35}H_{49}N_2O_{10}^+$, 657.33817, found: 657.33832.

[*tert*-Butoxycarbonylmethyl-(2-{2-[2-(*tert*-butoxycarbonylmethyl-amino)-ethoxy]-ethoxy}-ethyl)-amino]-acetic acid allyl ester (35).

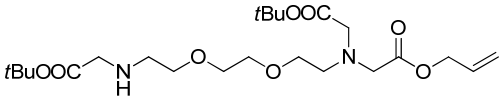

Diamine **9** (3.44 g, 9.14 mmol) was dissolved in acetonitrile (175 mL) and potassium carbonate was added (1.26 g, 9.14 mmol). After stirring at room temperature for 30 min, a solution of allyl 2-chloroacetate (1.23 g, 9.14 mmol) in acetonitrile (20 mL) was added dropwise over 1 h. The resulting mixture was left to stir at room temperature for 4 days. The solution was filtered and the solvent was then removed *in vacuo* and the resulting crude oil was purified by column chromatography (silica gel, dichloromethane/methanol, 94:4 v/v) to yield **35** as a yellow oil (1.50 g, 35 %).

^{1}H NMR (300 MHz, $CDCl_3$) δ: 1.40 – 1.51 (br, 18H), 2.79 (t, *J*=5.19 Hz, 2H), 2.96 (t, *J*=5.57, 2H), 3.32 (s, 2H), 3.38 – 3.74 (br, 14H), 4.52 – 4.69 (br, 2H), 5.16 – 5.38 (m, 2H), 5.79 – 6.00 (m, 1H). **^{13}C NMR** (75

MHz, $CDCl_3$) δ: 28.0, 28.1 ($C(CH_3)_3$), 48.6, 51.6, 53.5, 55.7, 56.6, 65.0, 70.2, 70.3, 70.6 (-CH_2-), 80.9, 80.9 ($C(CH_3)_3$), 118.3 (**CH_2**=CH), 132.0 (-**CH**=CH_2), 170.6, 171.1, 171.4 (C=O).

{Allyloxycarbonylmethyl-[2-(2-{2-[*tert*-butoxycarbonylmethyl-(9*H*-fluoren-9-ylmethoxycarbonyl)-amino]-ethoxy}-ethoxy)-ethyl]-amino}-acetic acid *tert*-butyl ester (36).

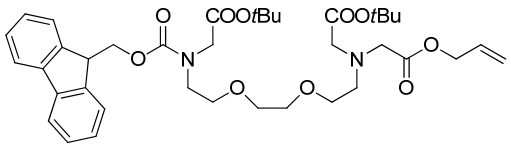

Compound **35** (0.86 g, 1.821 mmol) was dissolved in dioxane (8 mL) and an aqueous solution of Na_2CO_3 (0.58 g, 5.463 mmol, 3 equiv in 8 mL of water) was added. The reaction mixture was immersed in an ice bath for 20 minutes and then a solution of 9-fluorenylmethylchloroformate (0.42 g, 1.639 mmol) in dioxane (5 mL) was added dropwise. The solution was allowed to warm to room temperature and stirred overnight. The solvents were then evaporated under reduced pressure. The residue was dissolved in dichloromethane and washed with water and brine. The solvent was evaporated again and the crude residue was purified by column chromatography (silica gel, dichloromethane/ethyl acetate, 70:30 v/v) to yield **36** (0.80 g, 63%).

^{1}H NMR (300 MHz, $CDCl_3$) δ: 1.45 (s, 18H), 2.85 – 3.01 (br, 2H), 3.30 – 3.69 (br, 14H), 3.98 (s, 1H), 4.05 (s, 1H), 4.36 (d, *J*=6.99 Hz, 1H), 4.49 (d, *J*=6.23 Hz, 1H), 4.60 (d, *J*=5.67 Hz, 1H), 4.59 (d, 2H), 5.16 – 5.37 (m, 2H), 5.81 – 6.00 (m, 1H), 7.24 – 7.43 (m, 4H), 7.58 (d, *J*=7.37 Hz, 2H), 7.75 (d, *J*=7.55 Hz, 2H). **^{13}C NMR** (75 MHz, $CDCl_3$) δ: 28.0, 28.1 ($C(CH_3)_3$), 47.2, 47.3, 47.8, 48.4, 50.7, 53.4, 53.5, 55.7, 56.6, 65.0, 67.3, 67.8, 69.9, 70.1, 70.3, 70.4 (-CH_2-), 80.9, 81.5, 81.6 ($C(CH_3)_3$), 118.4 (**CH_2**=CH), 119.7, 119.9, 120.9, 124.7, 124.8, 125.1, 127.0, 127.6 (-CH- fluorenyl ring), 132.0 (-**CH**=CH_2), 141.2, 141.3, 143.9 (-C- fluorenyl ring), 156.0, 156.1, 168.9, 169.0, 170.6, 171.1 (C=O).

[Benzyloxycarbonylmethyl-(2-{2-[2-(*tert*-butoxycarbonylmethyl-amino)-ethoxy]-ethoxy}-ethyl)-amino]-acetic acid *tert*-butyl ester (37).

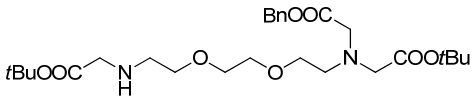

Compound **37** was synthesised according to a previously reported literature procedure.[190]

2-oxopropyl 2-bromoacetate (38).

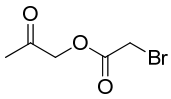

Bromide **38** was synthesised following a slightly modified literature procedure.[318] 1-hydroxypropan-2-one (1.00 g, 13.50 mmol) was dissolved in dichloromethane (15 mL) and potassium carbonate (3.73 g, 27.0 mmol) was added. The mixture was cooled to 0 °C and bromoacetyl bromide (4.09 g, 20.25 mmol) was added. The mixture was stirred for 2 h after which water (1 mL) was added. The mixture was extracted with chloroform, dried (Na_2CO_3), filtered and the solvent evaporated to yield **38** (1.24 g, 47 %). The compound was used in the next step without further purification.

^{1}H NMR (300 MHz, $CDCl_3$) δ: 2.14 – 2.22 (br, 3H), 3.92 – 3.98 (br, 2H), 4.70 – 4.77 (br, 2H). **^{13}C NMR** (75 MHz, $CDCl_3$) δ: 25.0 (-CH_2-), 26.0 (CH_3), 69.3 (-CH_2-), 166.5, 200.4 (C=O).

[(2-{2-[2-(Benzyloxycarbonylmethyl-*tert*-butoxycarbonylmethyl-amino)-ethoxy]-ethoxy}-ethyl)-*tert*-butoxycarbonylmethyl-amino]-acetic acid 2-oxo-propyl ester (39).

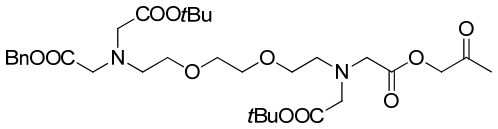

Amine **37** (345 mg, 0.658 mmol) was dissolved in acetonitrile (5 mL) and potassium carbonate (218 mg, 1.578 mmol) was added to the solution. After stirring for 30 min at room temperature, bromide **38** (154 mg, 0.789 mmol) was dissolved in acetonitrile (5 mL) and added to the mixture. The mixture was then stirred overnight at reflux. After cooling to room temperature, the mixture was filtered and the solvent evaporated. The crude oil was then purified by column chromatography (silica gel, dichloromethane/methanol, 97:3 v/v) to yield **39** as an orange/brown oil (153 mg, 36 %).

^{1}H NMR (300 MHz, $CDCl_3$) δ: 1.45 (s, 18H), 2.10 – 2.22 (br, 2H), 2.85 – 3.02 (br, 4H), 3.21 – 3.82 (br, 17H), 4.66 – 4.85 (br, 2H), 5.15 (s, 2H), 7.27 – 7.43 (br, 5H). **^{13}C NMR** (75 MHz, $CDCl_3$) δ: 25.8 (CH_3) 27.7 ($C(CH_3)_3$), 54.6, 55.9, 56.2, 57.0, 66.3, 68.4, 69.4 (-CH_2-), 81.3 ($C(CH_3)_3$), 127.8, 127.9, 128.0, 128.2, 135.2 (ArC), 170.9, 171.1, 171.7, 200.7 (C=O).

{*tert*-Butoxycarbonylmethyl-[2-(2-{2-[*tert*-butoxycarbonylmethyl-(2-oxo-propoxycarbonylmethyl)-amino]-ethoxy}-ethoxy)-ethyl]-amino}-acetic acid (40).

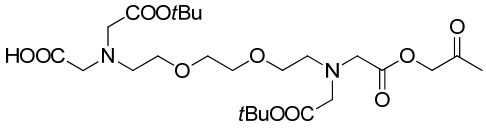

Compound **39** (153 mg, 0.240 mmol) was dissolved in ethanol (5 mL) and Pd/C (15 mg) was added to the solution. The heterogeneous mixture was shaken for 16 h in a hydrogen atmosphere using a Parr

hydrogenator (3 bar). The catalyst was then removed by filtration through a plug of celite and the solvent evaporated under reduced pressure to give carboxylic acid **40** (131 mg, 88 %). The resulting oil was used in subsequent reactions without any further purification.

^{1}H NMR (300 MHz, $CDCl_3$) δ: 1.46 (s, 18H), 2.01 – 2.45 (br, 3H), 2.68 – 3.08 (br, 4H), 3.13 – 3.93 (br, 17H), 4.61 – 5.00 (br, 2H). **^{13}C NMR** (75 MHz, $CDCl_3$) δ: 25.9 (CH_3) 27.8 ($C(CH_3)_3$), 29.4, 55.7, 56.1, 56.6, 57.7, 58.2, 58.4, 66.9, 67.1, 68.7, 68.9 (-CH_2-), 81.7, 81.8 ($C(CH_3)_3$), 171.4, 171.5, 171.7, 174.6 201.0 (C=O).

Solid phase peptide synthesis

The synthesis of the peptide sequences was carried out using the standard Fmoc chemistry strategy on a manual peptide synthesizer. A Rink Amide MBHA resin (substitution 0.78 mmol g^{-1}) was used as the solid support. Before the first amino acid was coupled, the resin was allowed to swell in DMF for 1 h. Fmoc deprotection of the resin was carried out using a solution of 20 % piperidine in DMF (3 x 15 min). Prior to each reaction, the resin was allowed to swell in DMF for 1 h. After the coupling of the first amino acid, a capping procedure using an acetic anhydride/pyridine solution (3:2, 4 mL) was performed for 30 min. The resin was then washed with DMF (5 x 3 mL). Each relevant coupling and deprotection procedure was checked by the Kaiser test for completeness. All reactions on solid phase were performed at room temperature.

General amino acid coupling procedure

Fmoc-protected amino acids (3 equiv. relative to the resin substitution) were dissolved in DMF (4 mL) and activated in situ with HBTU (2.9 equiv) and DIPEA (6 equiv). After 10 min of pre-activation, the mixture was added to the pre-swelled resin and agitated for 2 h. After, the solution was removed and the procedure was repeated with half the initial amount of amino acid, HBTU and DIPEA for 1 h. After coupling, the resin was washed with DMF (5 x 3 mL) and dichloromethane (3 x 3 mL) to remove excess reagents.

General Fmoc deprotection procedure

Fmoc deprotections of the resin and amino acids were carried out with 3 treatments (15 min each) of a 20 % piperidine in DMF solution. After deprotection, the resin was washed with DMF (5 x 3 mL) and prepared for the next procedure.

Compound 41.

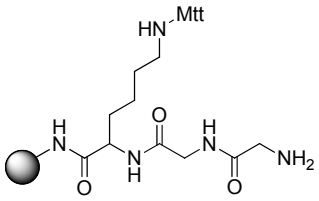

Compound **41** was synthesised following the standard Fmoc SPPS protocols previously described.

Compound 42.

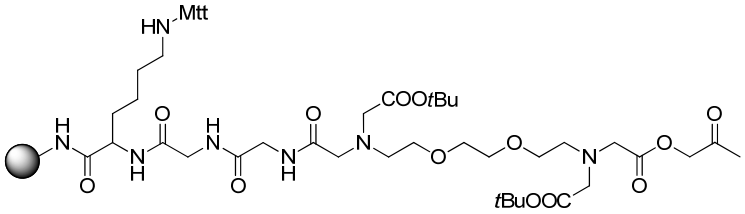

Peptidyl resin **41** was allowed to swell in DMF (2 mL) for 1 h, after which a solution of **40** (0.115g, 0.210 mmol), DIPEA (0.073 mL, 0.419 mmol) and HATU (0.074 g, 0.194 mmol) was added. The mixture was allowed to shake for 16 h before being washed with DMF (5 x 3 mL) and dichloromethane (5 x 3 mL). The coupling was checked by the Kaiser test.

Compound 42-x (Compound 42 after micro cleavage from resin).

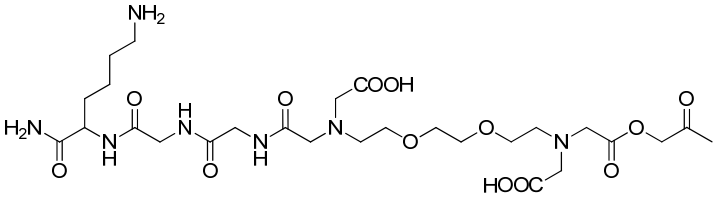

A small portion of **42** was then subject to a micro cleavage using the standard procedure described previously and analysed by LC-MS.

LC-MS: (m/z) $[M+H]^+$ calcd. for $C_{27}H_{48}N_7O_{13}^+$, 678.3, found: 678.4. $[M+2H]^+$ calcd. for $C_{27}H_{49}N_7O_{13}^{2+}$, 339.7, found: 339.6.

Compound 43.

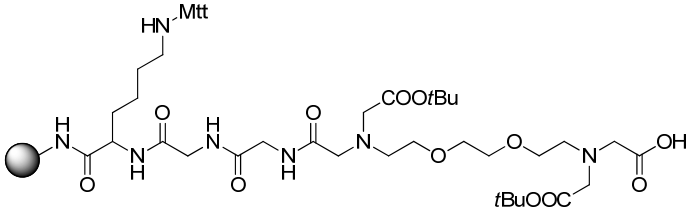

Resin **42** was swelled in DMF for 1 h, after which the solvent was drained and a solution of TBAF.$3H_2O$ (0.365 g, 1.156 mmol) in THF was added. The resulting mixture was shaken overnight at room temperature. The resin was then drained and washed with THF (3 x 3 mL), DMF (3 x 3 mL) and dichloromethane (3 x 3 mL). The reaction was checked by the malachite green resin test for carboxylic acids.[320]

Compound 43-x (compound 43 after micro cleavage from resin).

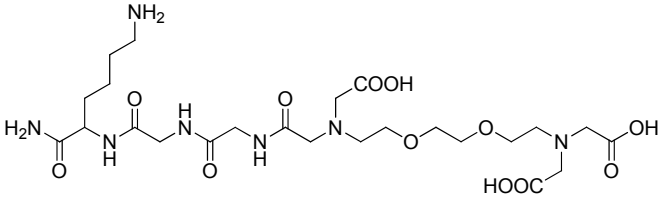

A small amount of **43** was then subject to a micro cleavage using the standard procedure described previously and analysed by LC-MS.

LC-MS: (m/z) $[M+H]^+$ calcd. for $C_{24}H_{44}N_7O_{12}^+$, 622.3, found: 622.4.

[*tert*-Butoxycarbonylmethyl-(2-{2-[2-(*tert*-butoxycarbonylmethyl-amino)-ethoxy]-ethoxy}-ethyl)-amino]-acetic acid methyl ester (45).

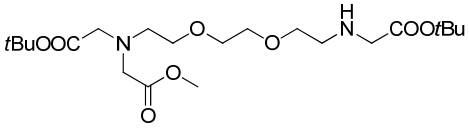

Diamine **9** (0.50 g, 1.328 mmol) was dissolved in acetonitrile (25 mL) and potassium carbonate (0.147 g, 1.062 mmol) was added to the solution. After stirring at room temperature for 30 min, a solution of methyl-2-bromoacetate (0.165 g, 1.076 mmol) in acetonitrile (2.5 mL) was added and the reaction stirred overnight at room temperature. The solution was then filtered and the solvent evaporated under reduced pressure. The crude oil was then purified via column chromatography (silica gel, dichloromethane/methanol, 97:3 v/v) to yield **45** (0.20 g, 34 %).

^{1}H NMR (300 MHz, $CDCl_3$) δ: 1.41-1.51 (overlapping s, 18H), 2.82 (t, *J*=5.10 Hz, 2H), 2.96 (t, *J*=5.57 Hz 2H), 3.35 (s, 2H), 3.49 (s, 2H), 3.53 – 3.66 (br, 10H), 3.70 (s, 3H). **^{13}C NMR** (75 MHz, $CDCl_3$) δ: 27.9, 28.0 ($C(CH_3)_3$), 48.5 ($-CH_2-$), 51.3 (CH_3), 53.4, 55.5, 56.5, 69.9, 70.0, 70.0, 70.2 ($-CH_2-$), 80.8, 80.9, 81.0 ($C(CH_3)_3$), 170.4, 170.5, 171.0, 171.8, 171.9 (C=O).

[(2-{2-[2-(Benzyl-*tert*-butoxycarbonylmethyl-amino)-ethoxy]-ethoxy}-ethyl) benzyloxycarbonylmethyl-amino]-acetic acid *tert*-butyl ester (48).

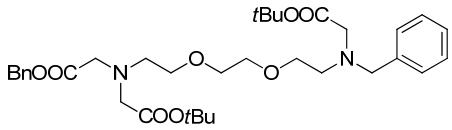

Amine **27** (1.020 g, 2.186 mmol) was dissolved in DMF (5 mL) and potassium carbonate (0.604 g, 4.37 mmol) was added to the solution. After 30 min stirring at room temperature, benzyl-2-bromoacetate (0.701 g, 3.06 mmol) was added and the reaction stirred overnight at room temperature. The reaction mixture was filtered and the solvent was then removed under reduced pressure. The resulting crude oil was purified by column chromatography (silica gel, dichloromethane/ethyl acetate, 70:30 v/v) to yield **48** (0.180 g, 13 %).

^{1}H NMR (300 MHz, $CDCl_3$) δ: 1.34 – 1.50 (br, 18H), 2.78 – 3.01 (br, 4H), 3.29 (s, 2H), 3.38 – 3.73 (br, 12H), 3.83 (s, 2H), 5.05 – 5.20 (br, 2H), 7.13 – 7.45 (br, 10H). **^{13}C NMR** (75 MHz, $CDCl_3$) δ: 28.1, 28.2 ($C(CH_3)_3$), 52.9, 53.5, 55.6, 55.8, 56.7, 58.5, 66.1, 70.0, 70.2, 70.2, 70.4 ($-CH_2-$), 80.6, 80.9 ($C(CH_3)_3$), 126.9, 128.2, 128.2, 128.5, 128.9, 135.8, 139.2 (ArC), 170.6, 170.9, 171.3 (C=O).

[*tert*-Butoxycarbonylmethyl-(2-{2-[2-(*tert*-butoxycarbonylmethyl-amino)-ethoxy]-ethoxy}-ethyl)-amino]-acetic acid (49).

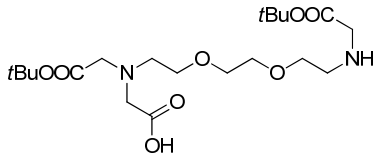

Compound **48** (251 mg, 0.408 mmol) was dissolved in ethanol (5 mL) and $Pd(OH)_2/C$ (25.0 mg) was added to the solution along with 3 drops of NH_3/methanol (7N). The heterogeneous mixture was shaken for 16 h in a hydrogen atmosphere using a Parr hydrogenator (3 bar). The catalyst was then removed by filtration through a plug of celite and the solvent evaporated under reduced pressure to give compound **49** (170 mg, 96 %). The resulting oil was used in subsequent reactions without any further purification.

^{1}H NMR (300 MHz, $CDCl_3$) δ: 1.36 – 1.57 (br, 18H), 2.98 (br s., 2H), 3.21 (br s., 2H), 3.37 – 3.96 (br, 14H). **^{13}C NMR** (75 MHz, $CDCl_3$) δ: 27.9, 28.0 ($C(CH_3)_3$), 47.5, 48.7, 54.4, 57.1, 57.8, 67.3, 68.7, 69.9, 69.9 ($-CH_2-$), 81.6, 82.8 ($C(CH_3)_3$), 167.3, 170.3, 174.1 (C=O).

[(2-{2-[2-(Allyloxycarbonylmethyl-*tert*-butoxycarbonylmethyl-amino)-ethoxy]-ethoxy}-ethyl)-*tert*-butoxycarbonylmethyl-amino]-acetic acid (50).

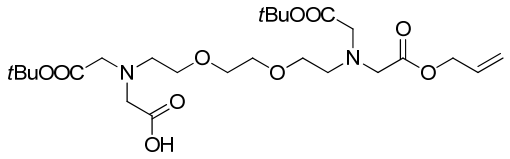

Compound **49** (170 mg, 0.391 mmol) was dissolved in acetonitrile (10 mL) and potassium carbonate (151 mg, 1.095 mmol) was added to the solution. After stirring for 30 min at room temperature, potassium iodide (91 mg, 0.548 mmol) and allyl 2-chloroacetate (73.7 mg, 0.548 mmol) were added to the mixture. The reaction mixture was stirred for 16 h at room temperature before being filtered and the solvent removed under reduced pressure. The resulting crude product was used without further purification.

Crude ^{1}H NMR (300 MHz, $CDCl_3$) δ: 1.38 – 1.52 (br, 18H), 2.79 – 3.01 (br, 4H), 3.38 – 3.79 (br, 16H), 4.56 – 4.82 (br), 5.19 – 5.44 (m), 5.82 – 6.02 (m). **Crude ^{13}C NMR** (75 MHz, $CDCl_3$) δ: 28.0 ($C(CH_3)_3$), 54.9, 56.4, 57.3, 57.4, 60.4, 61.0, 65.6, 65.9, 66.4, 67.7, 69.9 (-CH_2-), 81.8 ($C(CH_3)_3$), 118.7, 118.8, 119.0 (**CH_2**=CH), 131.2, 131.3, 131.6 (-**CH**=CH_2), 167.3, 168.4, 171.0, 171.6, 172.9 (C=O).

{4-[3-(2-Bromo-acetylamino)propyl]-7,10-bis-tert-butoxycarbonylmethyl-1,4,7,10-tetraaza-cyclododec-1-yl}acetic acid tert-butyl ester (DO3A-propyl amine, BB3).

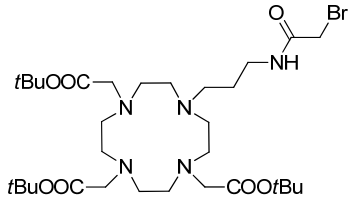

The synthesis of **BB3** was carried out in accordance with a previously reported literature procedure.[182]

Compound 55.

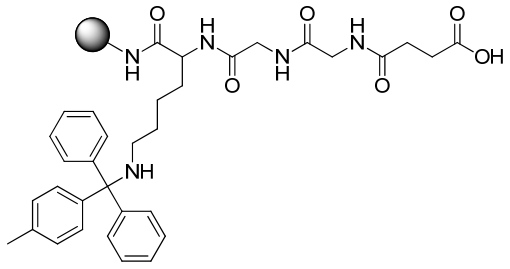

The peptide sequence (Lys(Mtt)-Gly-Gly-NH_2) was synthesised following the general procedures previously described. The resin was then treated with a solution of succinic anhydride (78 mg, 0.78

mmol, 10 equiv) and DIPEA (0.272 mL, 1.56 mmol, 20 equiv) in DMF (4 mL) for 5 h. The peptidyl resin was then washed with DMF (5 x 3 mL) and dichloromethane (3 x 3 mL).

Compound 55-x (Compound 55 after micro cleavage from resin).

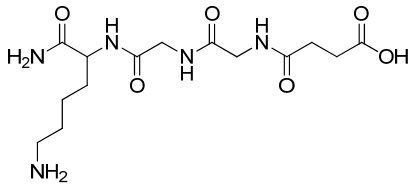

A small portion of **55** was then subject to a micro cleavage using the standard procedure described previously and analysed by LC-MS.

LC-MS: (m/z) $[M+H]^+$ calcd. for $C_{14}H_{26}N_5O_6^+$, 360.2, found: 360.0.

Compound 56.

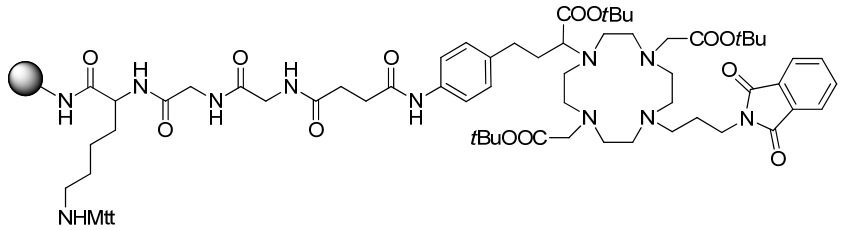

BB1 (128 mg, 0.156 mmol, 2 equiv), HATU (56 mg, 0.148 mmol, 1.9 equiv) and DIPEA (68 µL, 0.390 mmol, 5 equiv) were dissolved in DMF (4 mL) and added to the pre-swollen resin with compound **55**. This was allowed to agitate for 18 h. Excess reagents were removed by extensive washing with DMF (5 x 3 mL) and dichloromethane (3 x 3 mL).

Compound 56-x (compound 56 after cleavage from resin).

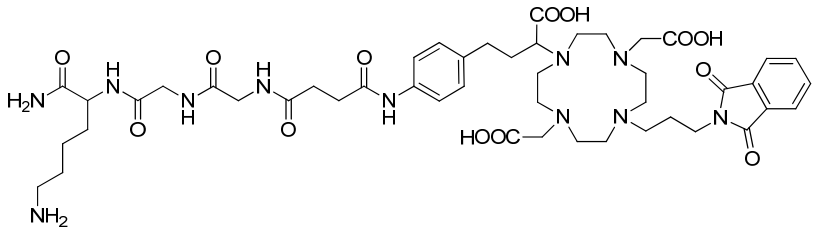

A small portion of **56** was then subject to a micro cleavage using the standard procedure described previously and analysed by LC-MS.

LC-MS: (m/z) $[M-H]^-$ calcd. for $C_{47}H_{66}N_{11}O_{13}^-$, 992.5, found: 992.5.

Compound 57.

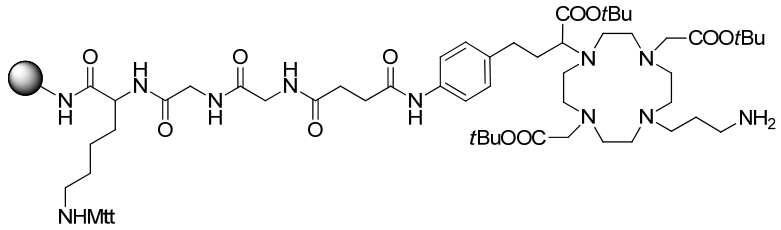

Resin with pthalimide **56** was suspended in isopropanol (4 mL) and ethylene diamine (47 mg, 0.78 mmol, 10 equiv) was added. The mixture was agitated for 24 h. The resin was then washed with isopropanol (3 x 3 mL), DMF (3 x 3 mL) and dichloromethane (3 x 3 mL) and the reaction progress checked by the Kaiser test.

Compound 57-x (compound 57 after micro cleavage from resin).

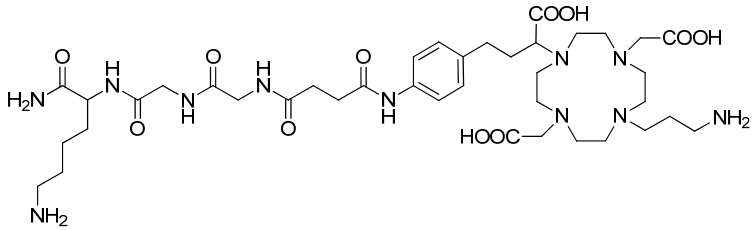

A small portion of **57** was then subject to a micro cleavage using the standard procedure described previously and analysed by LC-MS.

LC-MS: (m/z) $[M-H]^-$ calcd. for $C_{39}H_{64}N_{11}O_{11}^-$, 862.5, found: 862.6.

Compound 58.

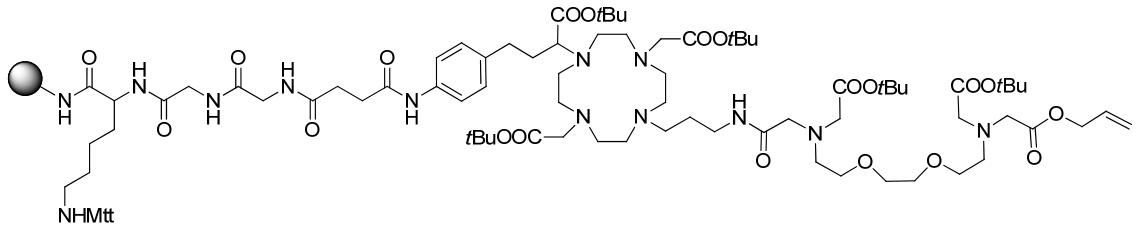

Resin with amine **57** was treated with a solution of **50** (80.8 mg, 0.152 mmol, 2 equiv), HATU (54.8 mg, 0.144 mmol, 1.9 equiv) and DIPEA (66 µL, 0.379 mmol, 5 equiv) in DMF (3 mL). The mixture was agitated for 24 h. The resin was washed with DMF (5 x 3 mL) and dichloromethane (3 x 3 mL) and the reaction progress checked by the Kaiser test, giving **58**.

Compound 60.

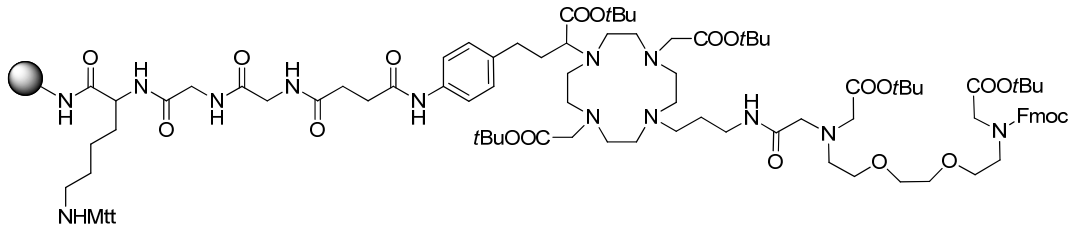

Resin with amine **57** was treated with a solution of **BB2** (102 mg, 0.156 mmol, 2 equiv), HATU (56 mg, 0.148 mmol, 1.9 equiv) and DIPEA (68 µL, 0.390 mmol, 5 equiv) in DMF (3 mL). The mixture was agitated for 24 h. The resin was washed with DMF (5 x 3 mL) and dichloromethane (3 x 3 mL) to give **60**.

Compound 60-x (compound 60 after micro cleavage from the resin).

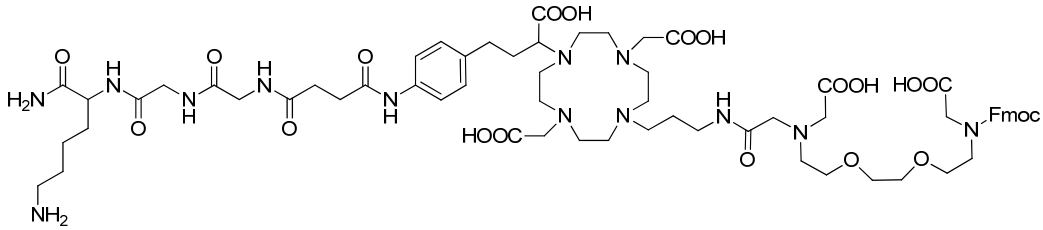

A small portion of **60** was then subject to a micro cleavage using the standard procedure described previously and analysed by LC-MS.

LC-MS: (m/z) $[M-H]^-$ calcd. for $C_{66}H_{94}N_{13}O_{20}^-$, 1388.7, found: 1388.6.

Compound 61.

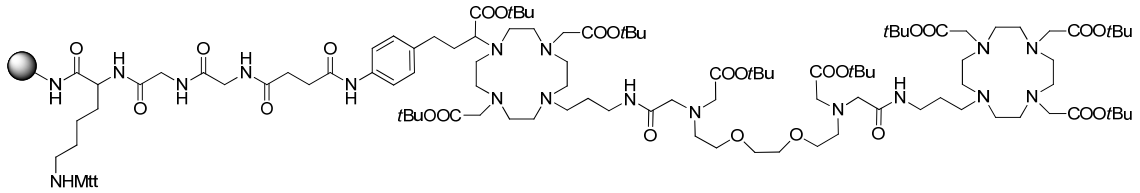

Resin with compound **60** was exposed to a solution of 40 % piperidine in DMF (3 mL) for 15 min. This was repeated a further two times to remove the Fmoc protecting group. The resin was then washed with DMF (5 x 3 mL). A mixture of **BB3** (130 mg, 0.187 mmol, 2.4 equiv) and DIPEA (68 µL, 0.390 mmol, 5 equiv) in DMF (3 mL) was then added and agitated for 24 h. The solution was then removed and a further portion of **BB3** (2.4 equiv) and DIPEA (5 equiv) in DMF (3 mL) was added and allowed to shake for a further 24 h. The resin was then washed with DMF (5 x 3 mL) and dichloromethane (3 x 3 mL).

Compound 61-x (compound 61 after micro cleavage from the resin).

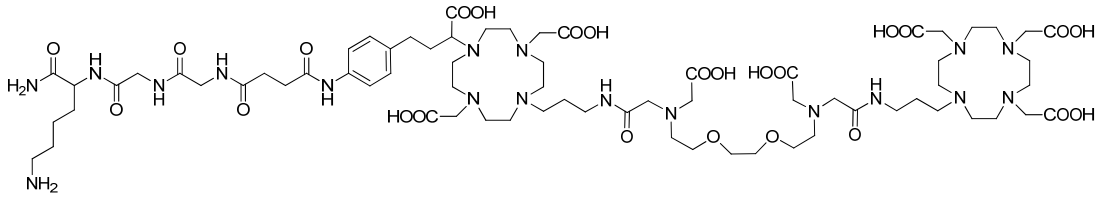

A small portion of **60** was then subject to a micro cleavage using the standard procedure described previously and analysed by LC-MS.

LC-MS: (m/z) $[M+H]^+$ calcd. for $C_{70}H_{119}N_{18}O_{25}^+$, 1611.9, found 1611.8. (m/z) $[M+2H]^{2+}$ calcd. for $C_{70}H_{120}N_{18}O_{25}^{2+}$, 806.4, found 806.5. (m/z) $[M+3H]^{3+}$ calcd. for $C_{70}H_{121}N_{18}O_{25}^{3+}$, 538.0, found 538.1.

Compound 62.

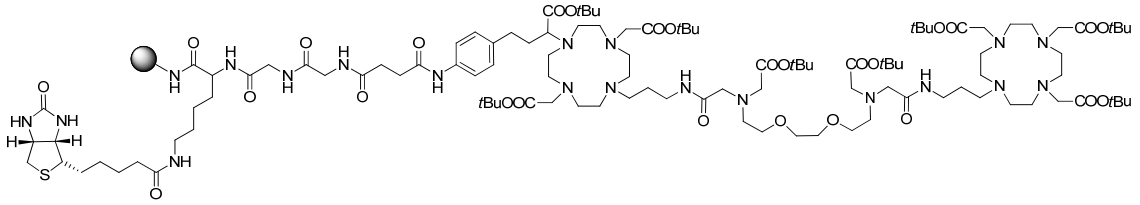

Resin with compound **61** was washed with dichloromethane (5 x 3 mL). A solution of TFA/ TIS/dichloromethane (3:3:94, 3 mL) was then added to the resin and agitated for 2 min. The solution was then removed and the repeated a further 4 times. After 5 treatments, the resin was washed with dichloromethane (5 x 3 mL) and used further. The resin was then allowed to swell in DMF for 1 h. Biotin (95 mg, 0.390 mmol, 5 equiv), HATU (145 mg, 0.382 mmol, 4.9 equiv), HOBt (52 mg, 0.382 mmol, 4.9 equiv) and DIPEA (136 µL, 0.780 mmol, 10 equiv) were dissolved in DMF (3 mL) and added to the resin. The mixture was shaken for 24 h. The solution was then removed and the resin treated again with a second portion of biotin (5 equiv), HATU (4.9 equiv), HOBt (4.9 equiv) and DIPEA (10 equiv) in DMF (3 mL) for a further 24 h. The solution was then removed and the resin washed with DMF (5 x 3 mL) and dichloromethane (3 x 3 mL).

Compound L[7]

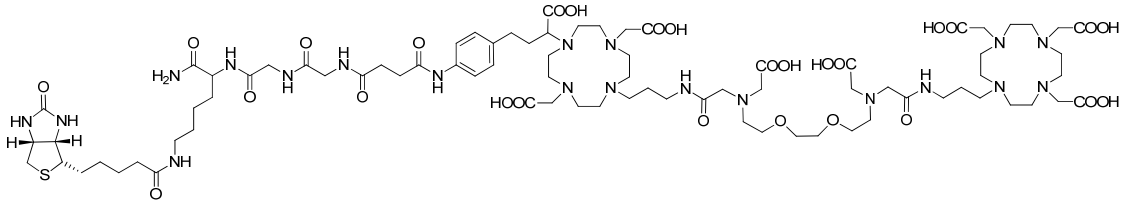

Resin with compound **62** was treated with a deprotection solution of TFA/TIS/dichloromethane (95:2.5:2.5, 3 mL) for 4 h. The solution was collected and the resin was washed twice with the deprotection solution (2 x 3 mL) which was also collected. The deprotection solutions were

combined and the majority of the solvent was evaporated. The crude product was precipitated from the remaining deprotection solution with cold diethyl ether and stored in the freezer overnight. The mixture was centrifuged at 3000g for 10 min and the solution was removed. The remaining solid was then subject to two further rounds of washing with cold diethyl ether. The crude solid was dried, purified by reverse phase HPLC and lyophilized to yield biotinylated **L^7** (35 mg, 24 % (overall yield across all steps)) as a white solid.

^{1}H NMR: (300 MHz, D_2O): δ (ppm): 1.17 – 4.38 (br, 109H), 7.29 (dd, 4H). **ESI-HRMS**: (m/z) $[M-2H]^{2-}$ calcd. for $C_{80}H_{130}N_{20}O_{27}S^{2-}$, 917.4573, found: 917.4577.

Complex Gd_2L^7

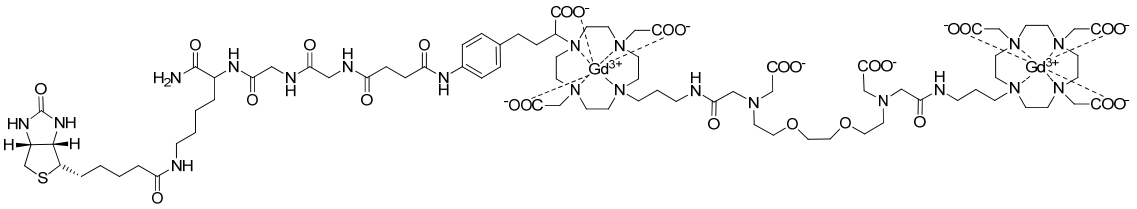

Compound **L^7** (35 mg, 0.019 mmol) was dissolved in water (5 mL) and the pH adjusted to 7. A solution of $GdCl_3.6H_2O$ (15.57 mg, 0.042 mmol) in water (1 mL) was added and left to stir at room temperature for 24 h while maintaining the pH at 7. Excess Gd^{3+} was removed by treating with Chelex for 24 h. The mixture was filtered and lyophilized to obtain **Gd_2L** as a white solid.

ESI-HRMS: (m/z) $[M-2H]^{2-}$ calcd. for $C_{80}H_{124}Gd_2N_{20}O_{27}S^{2-}$, 1072.3579, found: 1072.3590.

Compound 63.

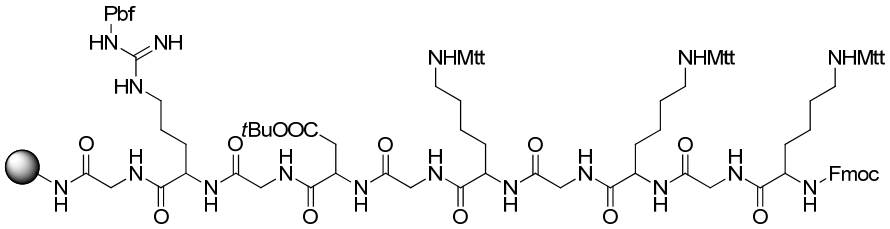

Compound **63** was synthesised following standard Fmoc SPPS protocols as described previously. The reactions were monitored by the Kaiser test.

Compound 63-x (compound 63 after micro cleavage from the resin).

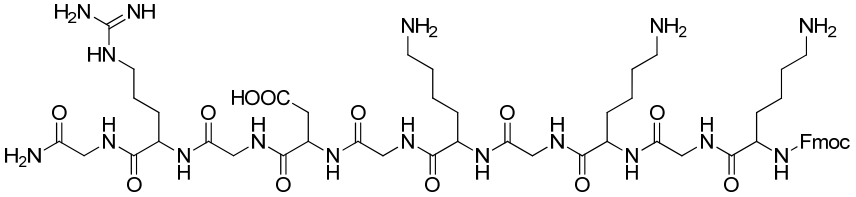

A small portion of **63** was then subject to a micro cleavage using the standard procedure described previously and analysed by LC-MS.

LC-MS: (m/z) $[M+H]^+$ calcd. for $C_{53}H_{82}N_{17}O_{14}^+$, 1180.6, found 1180.7. (m/z) $[M+2H]^{2+}$ calcd. for $C_{53}H_{83}N_{17}O_{14}^{2+}$, 590.8, found 590.9. (m/z) $[M+3H]^{3+}$ calcd. for $C_{53}H_{84}N_{17}O_{14}^{3+}$, 394.2, found 394.3. (m/z) $[M-H]^-$ calcd. for $C_{53}H_{80}N_{17}O_{14}^+$, 1178.6, found 1178.8.

Compound 64.

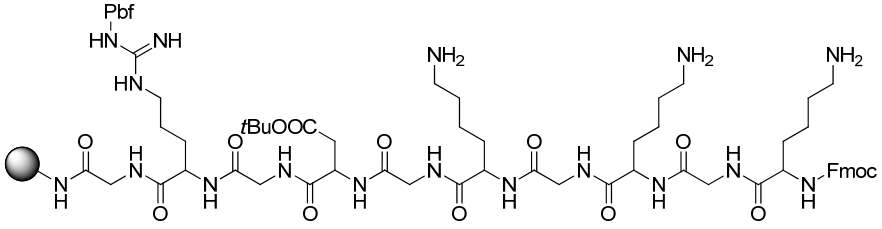

Resin with compound **63** was washed with dichloromethane (5 x 3 mL). A solution of TFA/dichloromethane (3:94, 3 mL) was then added to the resin and agitated for 2 min. The solution was then removed and the repeated a further 5 times. After 6 treatments, the resin was washed with dichloromethane (5 x 3 mL). The resin was then checked by sampling a few beads and adding a solution of 50 % TFA/dichloromethane solution. A resulting colourless solution indicated the reaction was complete (yellow solution is a negative result). The Kaiser test was also to confirm deprotection.

Compound 65.

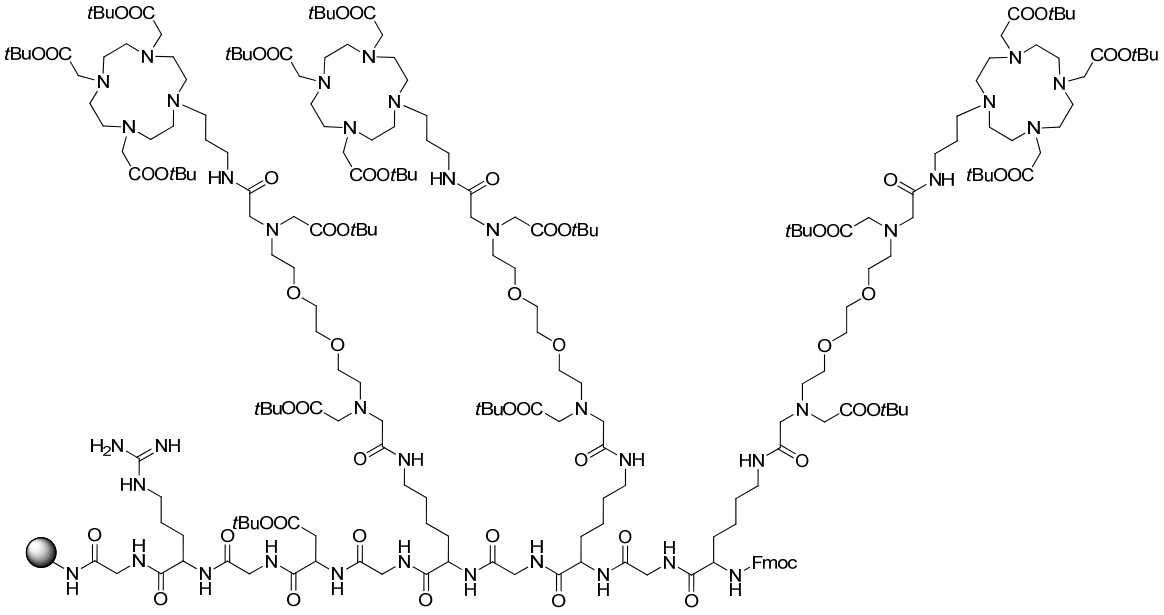

A solution of **DO3A-EGTA-COOH** (233.0 mg, 0.222 mmol, 3 equiv), HATU (82.0 mg, 0.215 mmol, 2.9 equiv), HOBt (29.0 mg, 0.215 mmol, 2.9 equiv) and DIPEA (33 µL, 0.187 mmol, 12 equiv) in DMF (2

mL) was added to the pre-swollen resin with compound **64**. The resin was agitated for 16 h at room temperature and then washed with DMF (5 x 3 mL) and dichloromethane (5 x 3 mL).

Compound L^8.

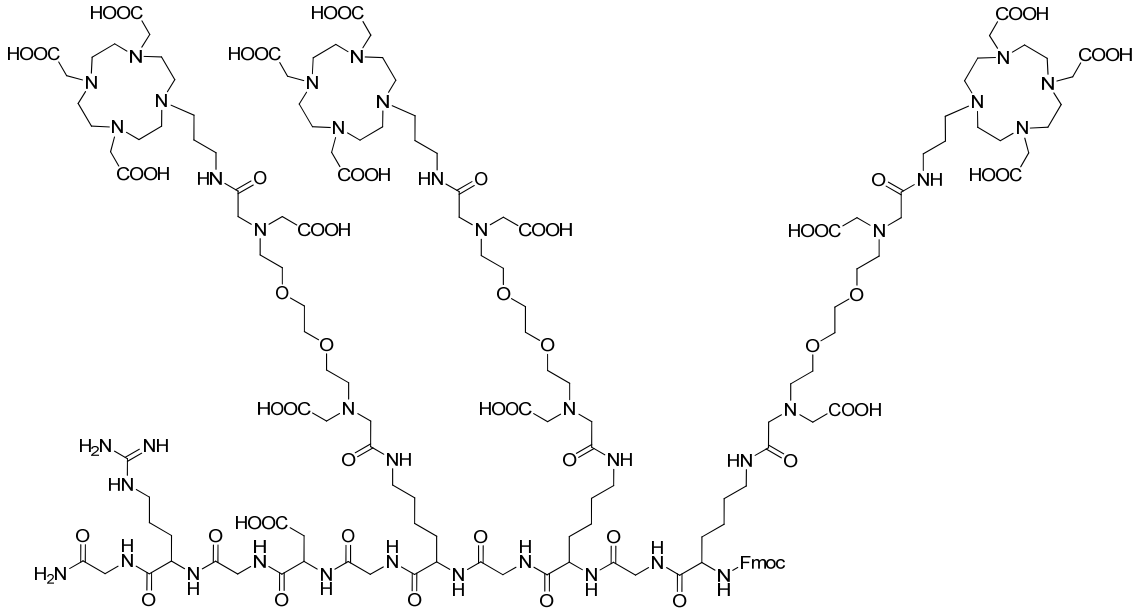

Resin with compound **65** was treated with a deprotection solution of TFA/TIS/dichloromethane (95:2.5:2.5, 3 mL) for 4 h. The solution was collected and the resin was washed twice with the deprotection solution (2 x 3 mL) which was also collected. The deprotection solutions were combined and the majority of the solvent was evaporated. The crude product was precipitated from the remaining deprotection solution with cold diethyl ether and stored in the freezer overnight. The mixture was centrifuged at 3000g for 10 min and the solution was removed. The remaining solid was then subject to two further rounds of washing with cold diethyl ether. The crude solid was dried, purified by reverse phase HPLC and lyophilized to yield **L^8** (24 mg) as a white solid.

^{1}H NMR: (300 MHz, D_2O): δ (ppm): 0.82 – 4.56 (br, 194H), 7.13 – 7.96 (m, 8H). **ESI-HRMS**: (m/z) $[M-4H]^{4-}$ calcd. for $C_{146}H_{236}N_{38}O_{56}^{4-}$, 854.42023, found: 854.42103. (m/z) $[M-3H]^{3-}$ calcd. for $C_{146}H_{237}N_{38}O_{56}^{3-}$, 1139.56274, found: 1139.56319.

Complex Gd_3L^8.

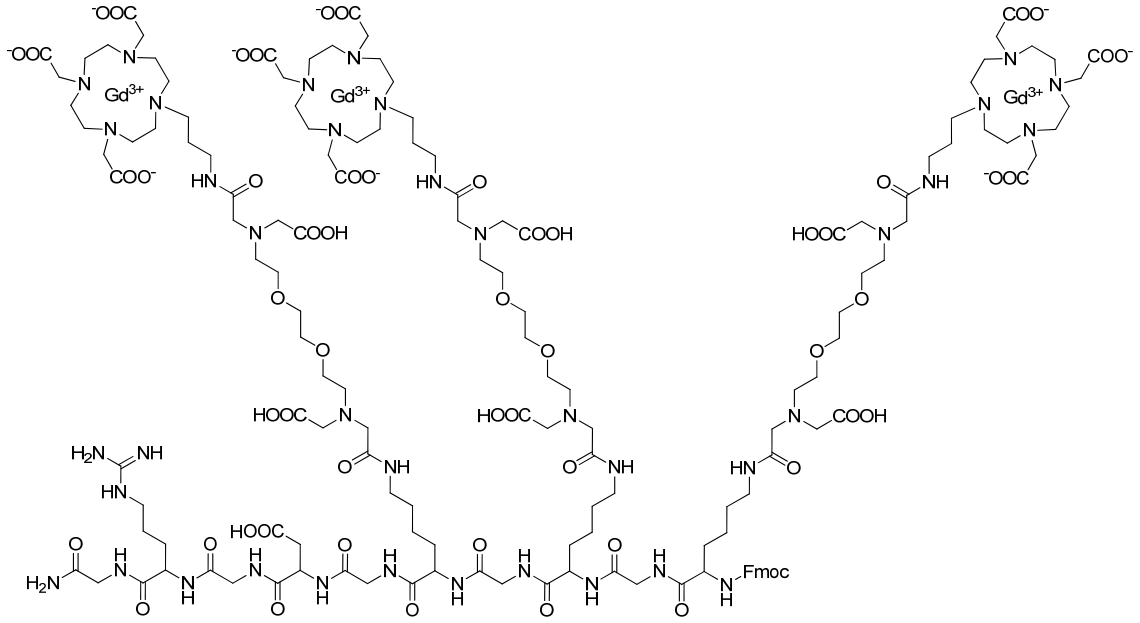

Compound $\mathbf{L^8}$ (22 mg, 6.43 µmol) was dissolved in water (2 mL) and the pH was adjusted to 7. A solution of $GdCl_3.6H_2O$ (7.88 mg, 0.021 mmol) in water (1 mL) was added and left to stir at room temperature for 24 h while maintaining the pH at 7. Excess Gd^{3+} was removed by three successive treatments with Chelex for 45 min each. The mixture was then filtered and lyophilized to obtain $\mathbf{Gd_3L^8}$ as a white solid.

8.3 NMR spectra for ligands L^{1-8}, D^{1a-5a} and D^{1b-5b}.

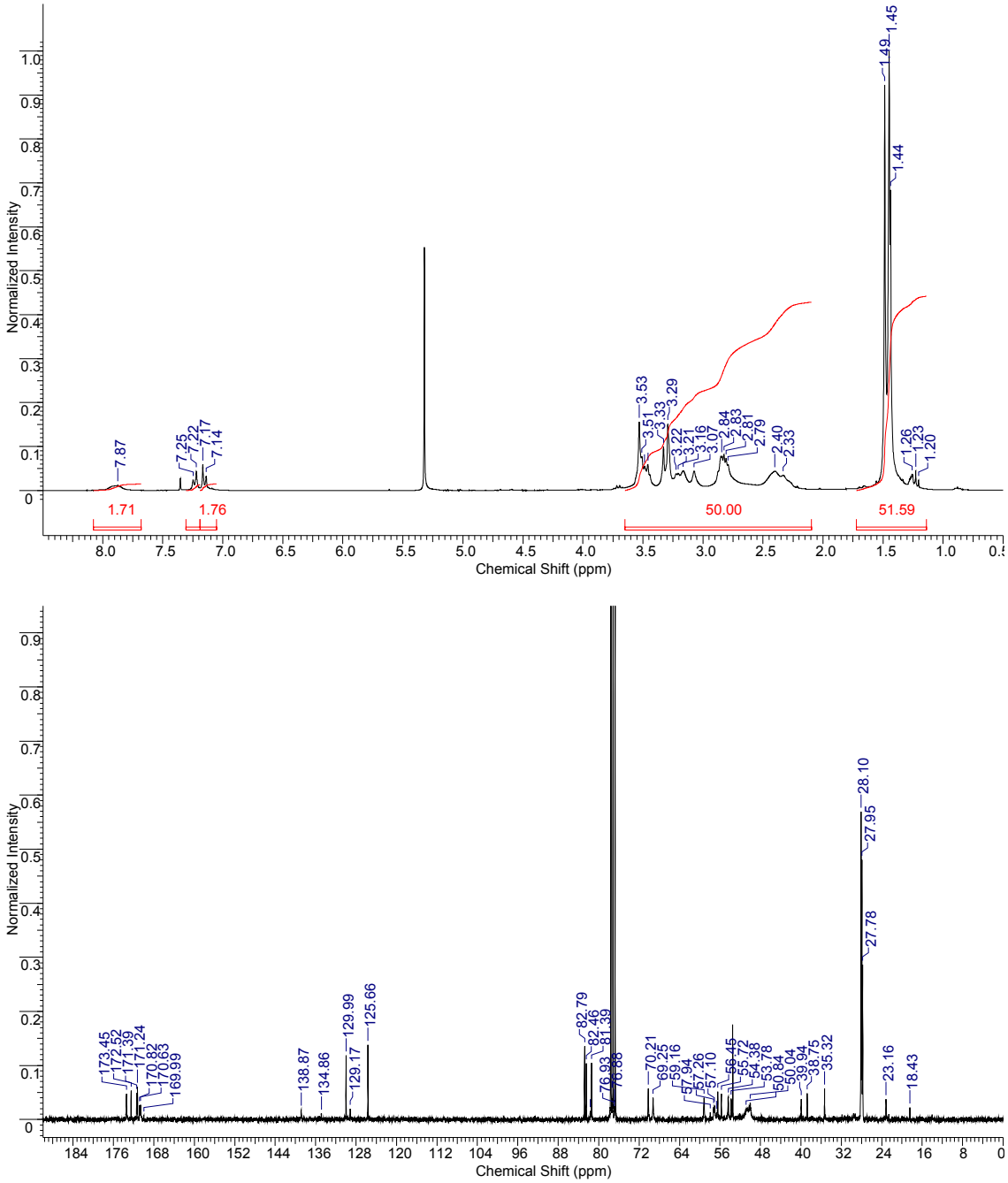

Figure S1. ^{1}H (top) and ^{13}C (bottom) NMR of $\mathbf{L^1}$ (300 MHz, $CDCl_3$).

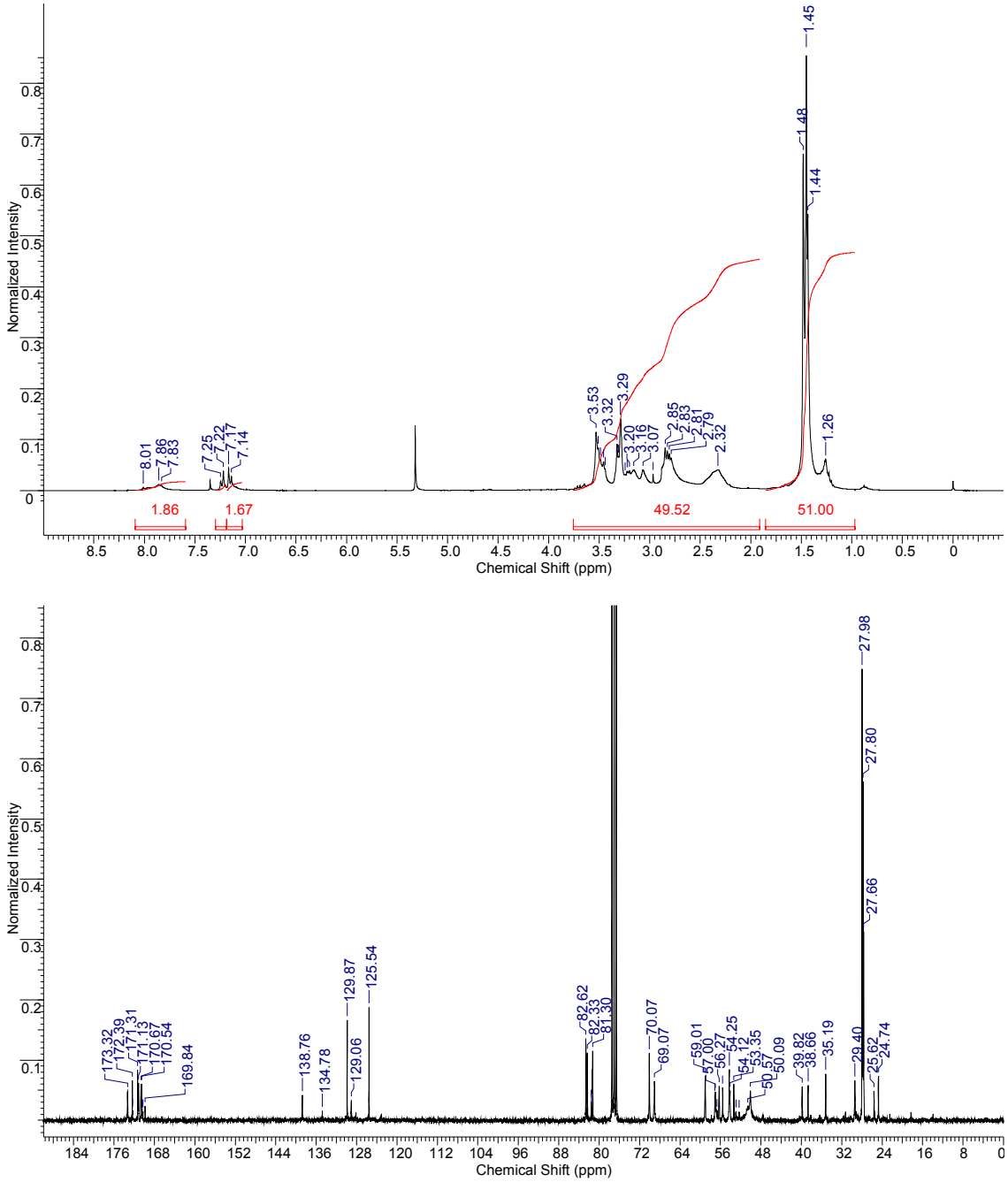

Figure S2. ^{1}H (top) and ^{13}C (bottom) NMR of **L²** (300 MHz, $CDCl_3$).

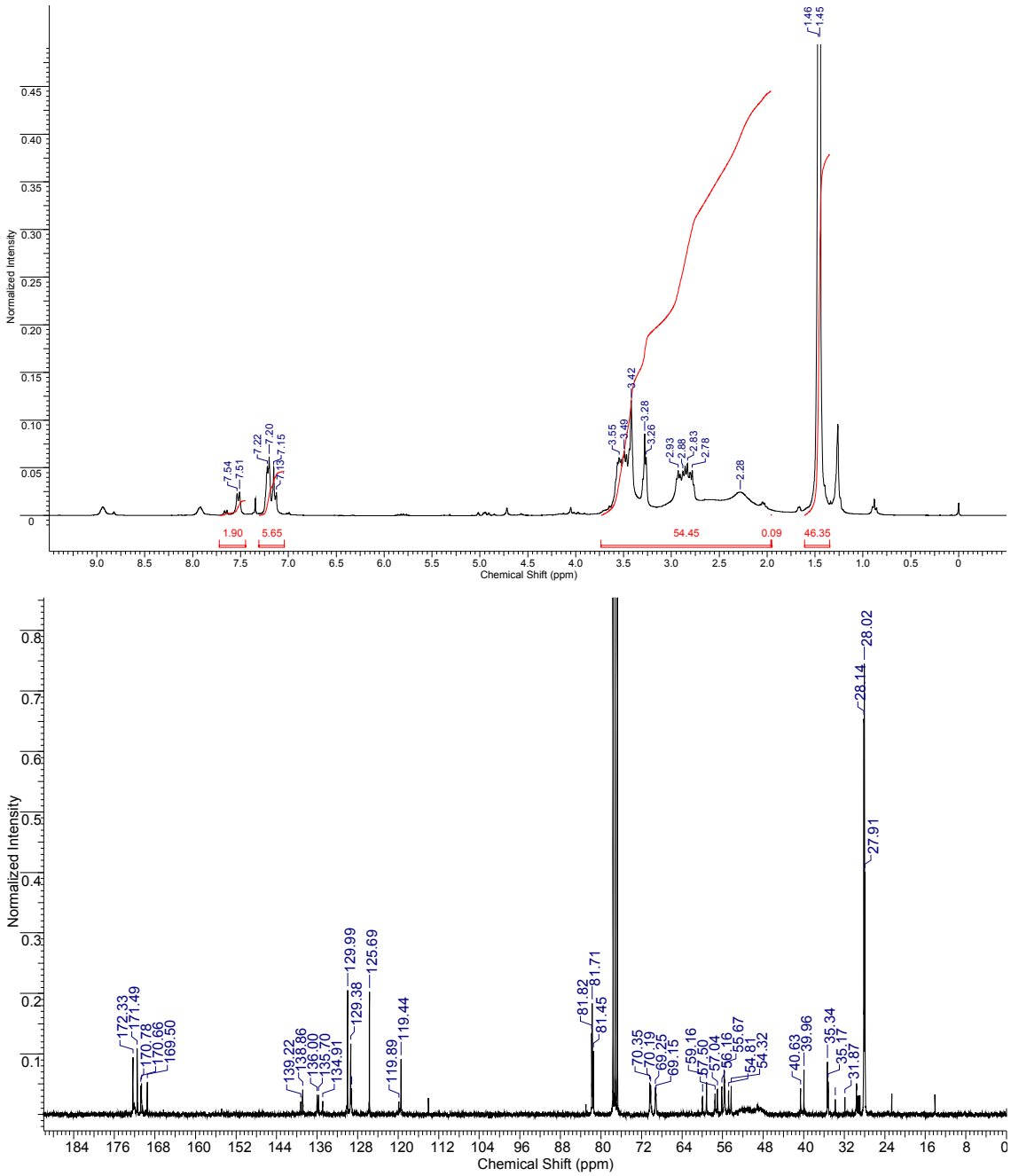

Figure S3. ^{1}H (top) and ^{13}C (bottom) NMR of $\mathbf{L^3}$ (300 MHz, $CDCl_3$).

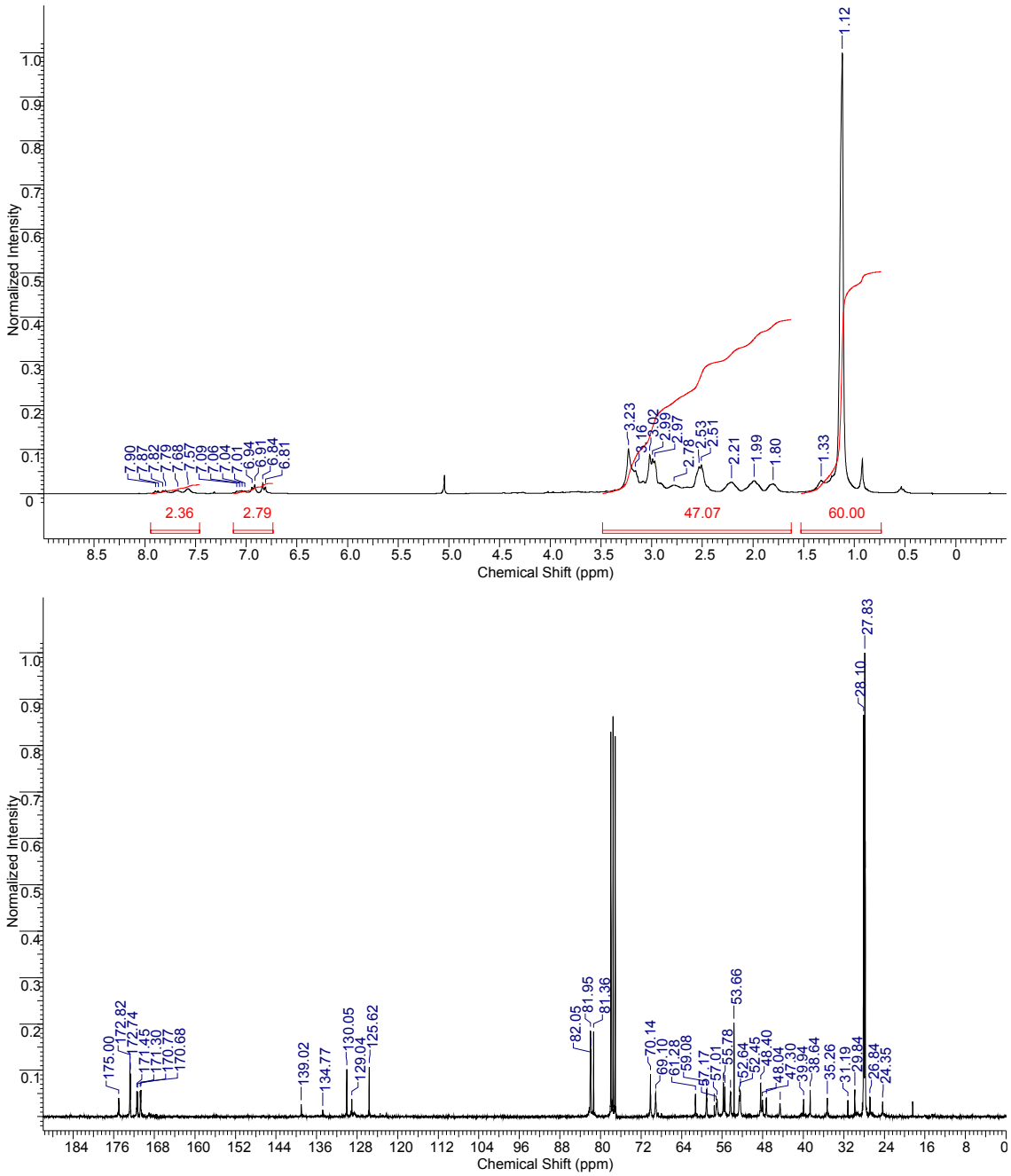

Figure S4. ^{1}H (top) and ^{13}C (bottom) NMR of **L**^{4} (300 MHz, $CDCl_3$).

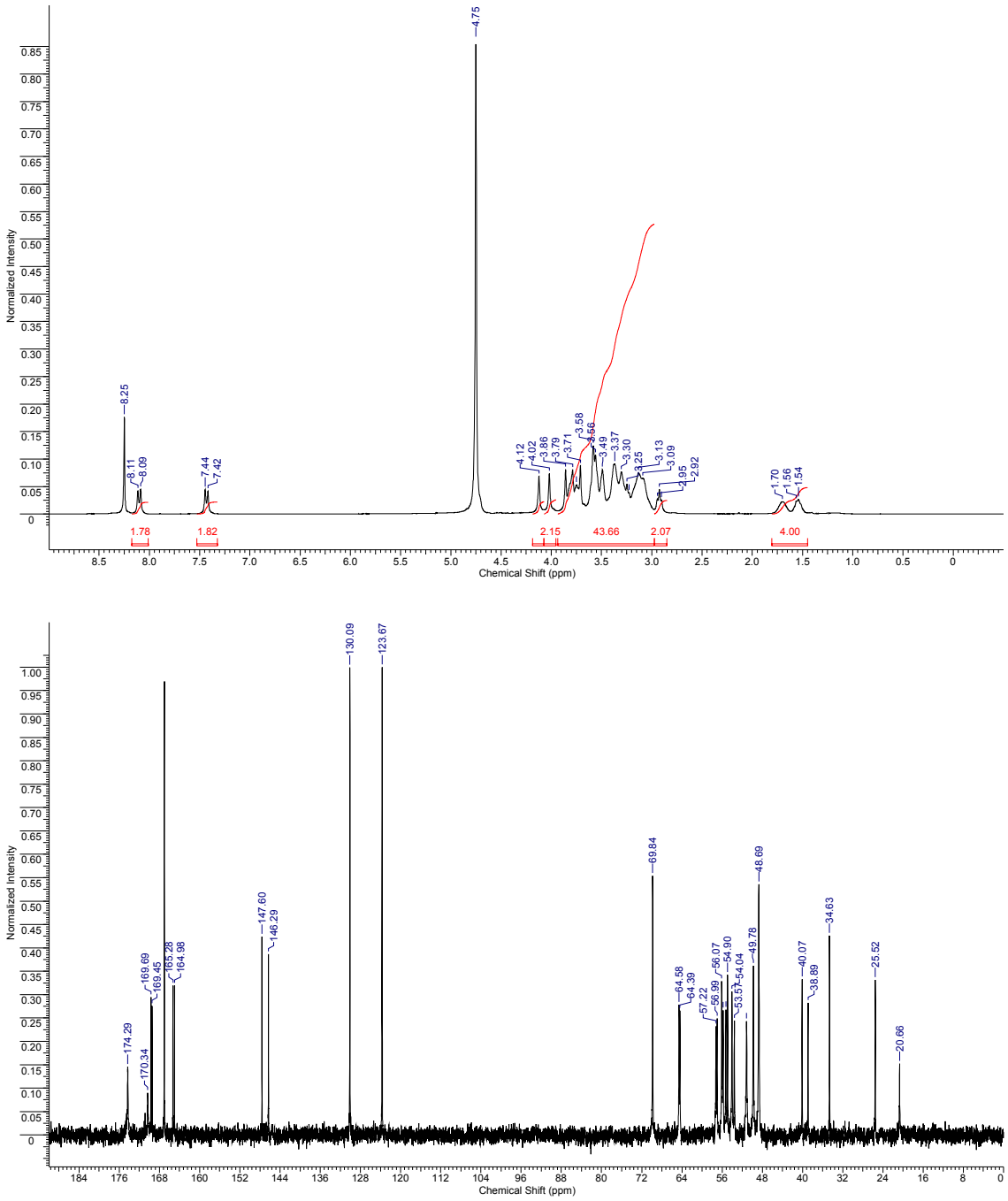

Figure S5. ^{1}H (top) and ^{13}C (bottom) NMR of **L^{5}** (300 MHz, D_2O).

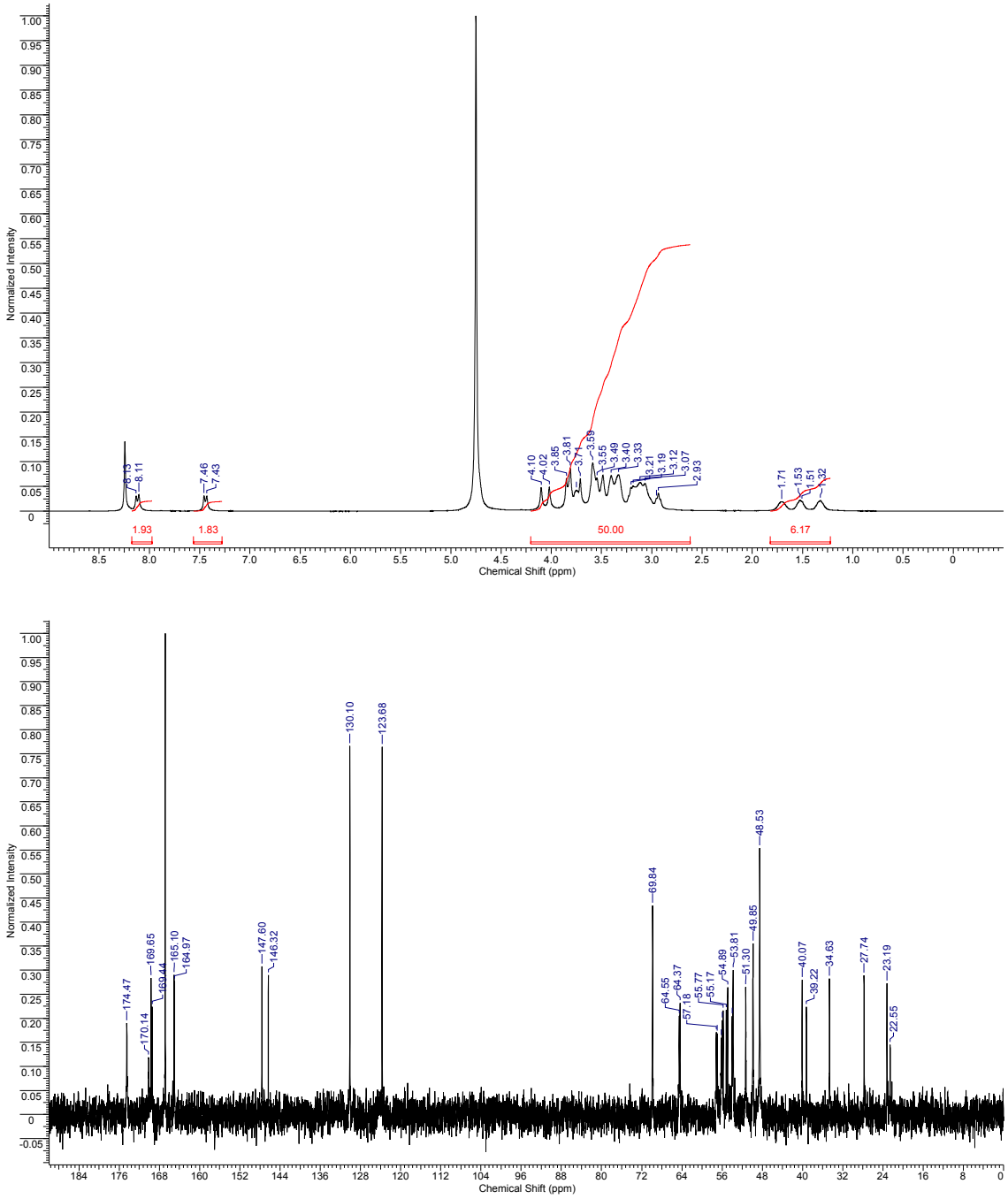

Figure S6. ^{1}H (top) and ^{13}C (bottom) NMR of **L^{6}** (300 MHz, D_2O).

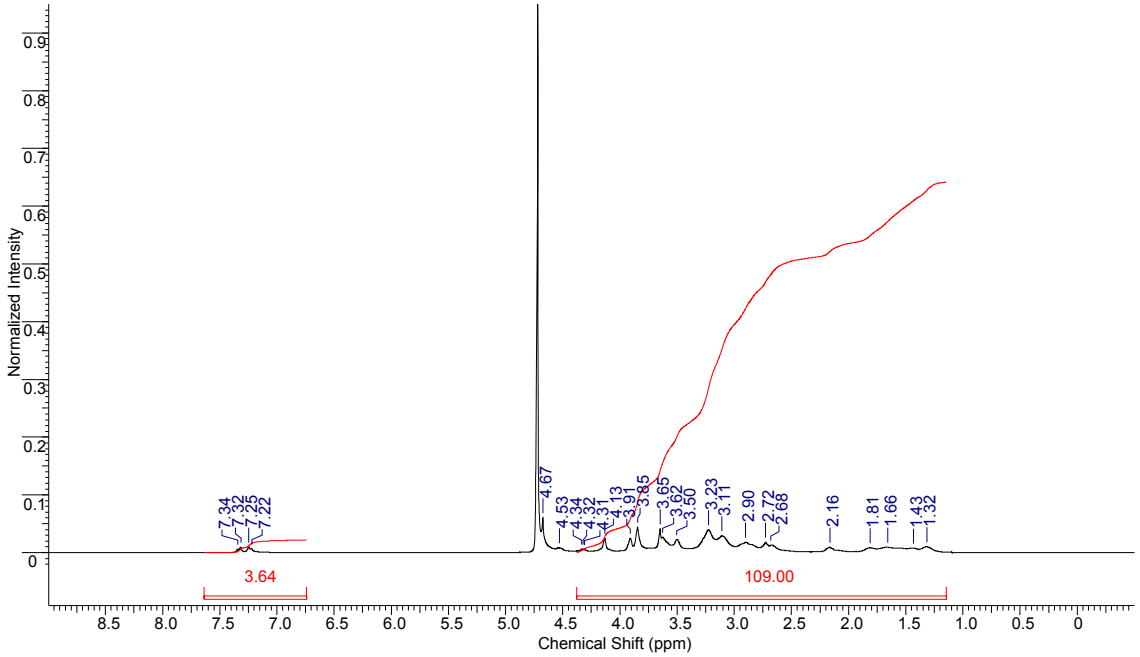

Figure S7. ^{1}H NMR of **L^{7}** (300 MHz, D_2O).

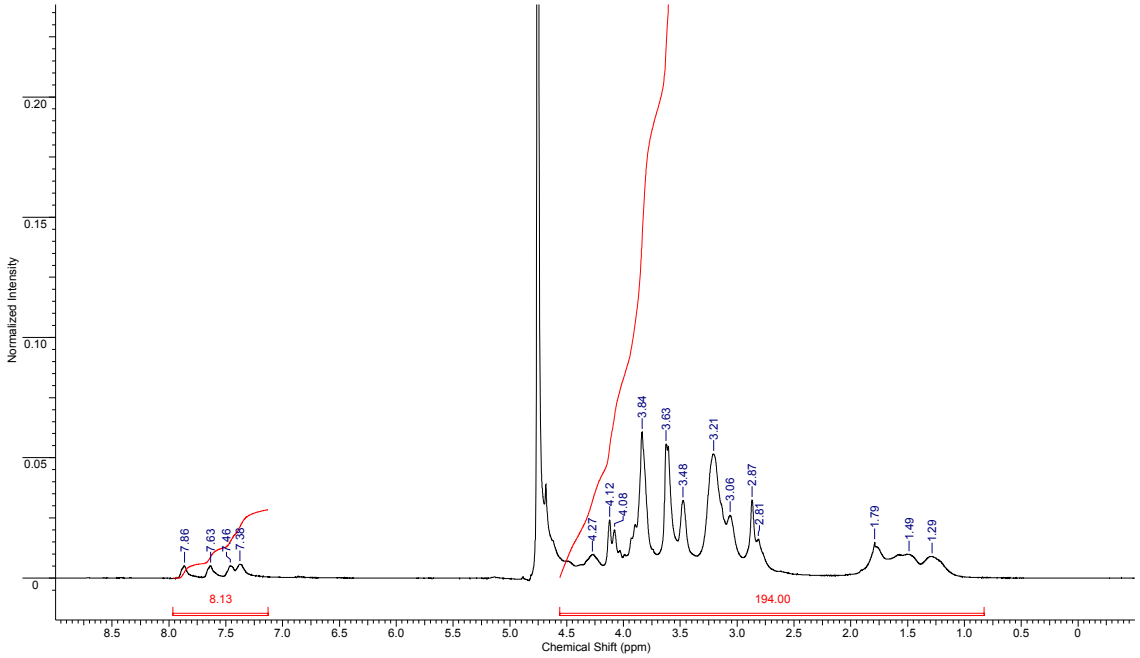

Figure S8. ^{1}H NMR of **L^{8}** (300 MHz, D_2O).

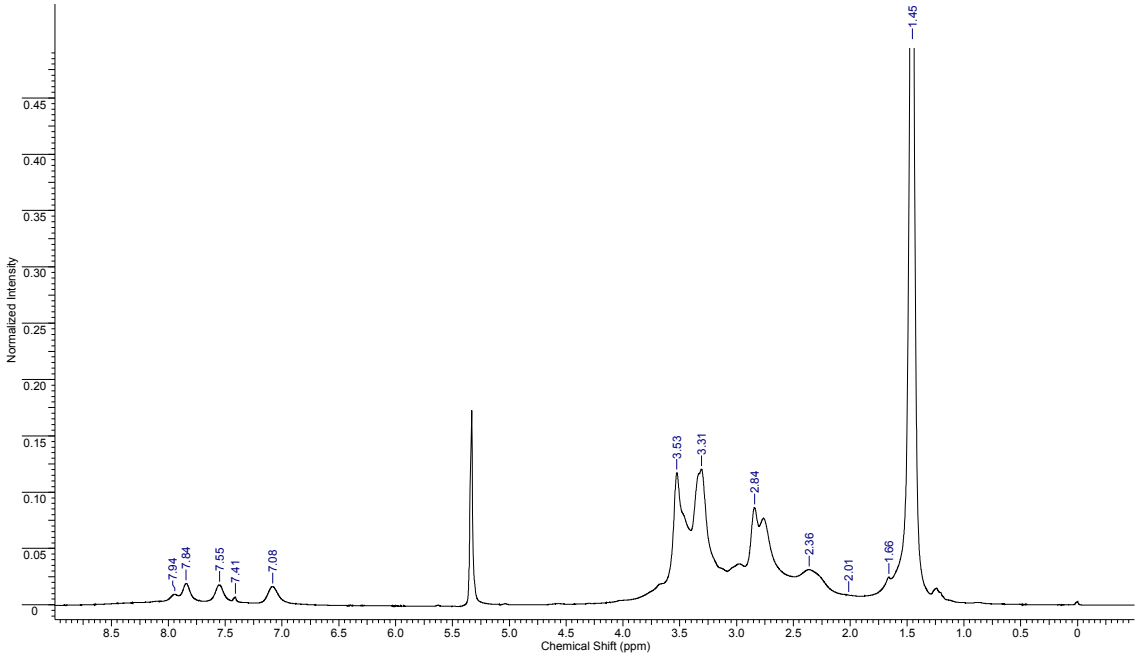

Figure S9. ^{1}H NMR of **D^{1a}** (300 MHz, $CDCl_3$).

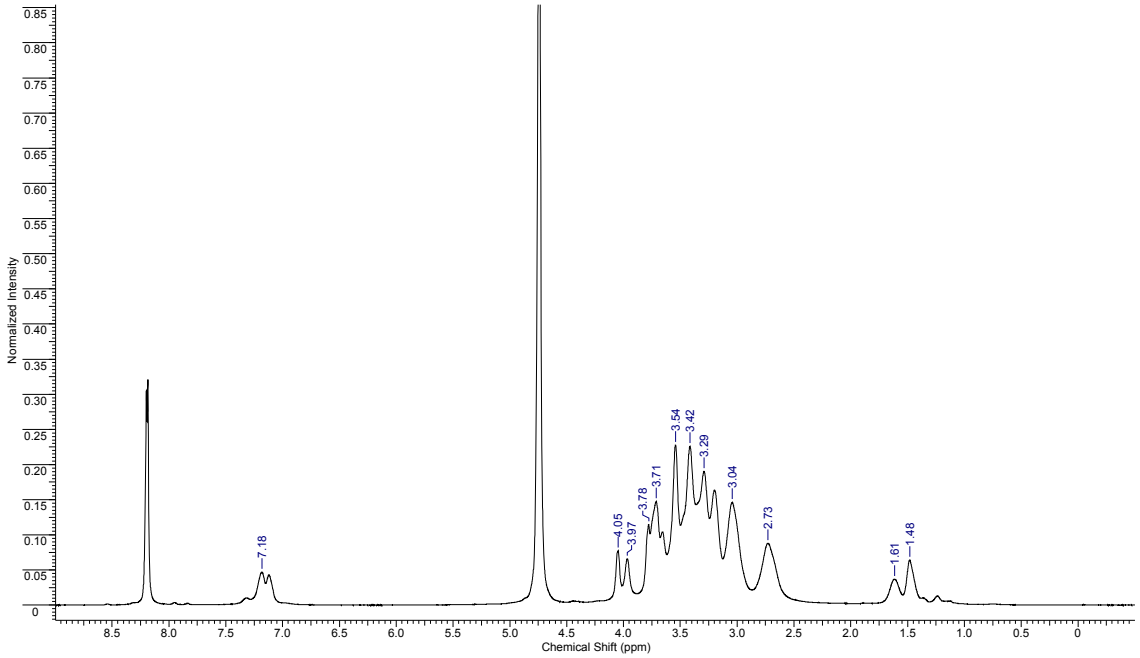

Figure S10. ^{1}H NMR of **D^{1b}** (300 MHz, D_2O).

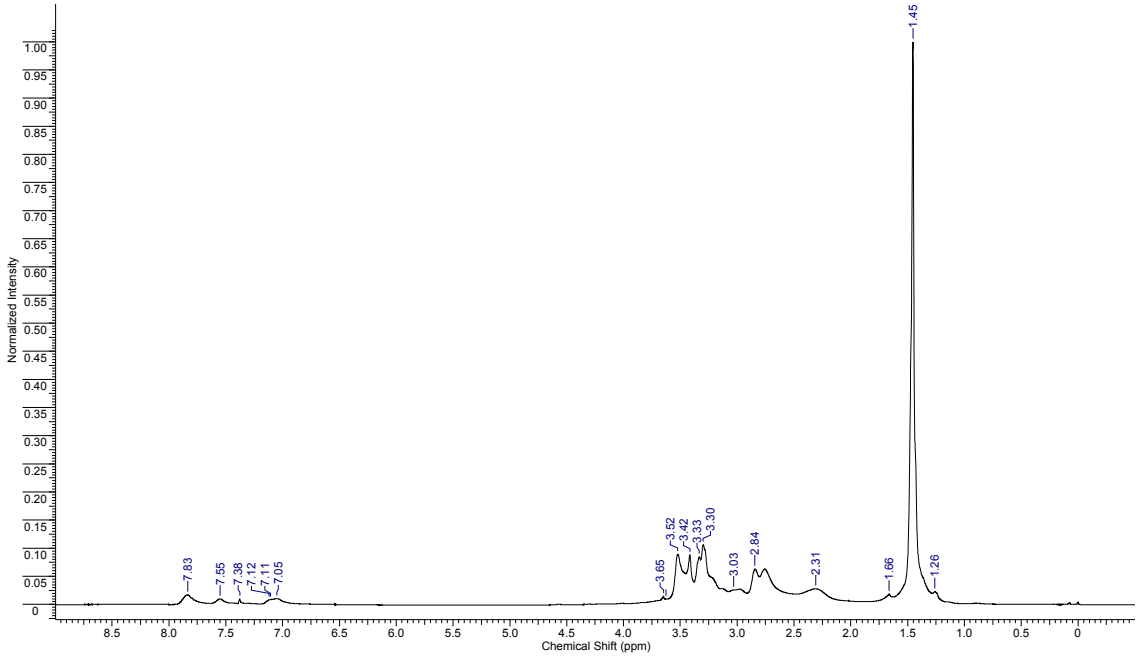

Figure S11. ^{1}H NMR of **D^{2a}** (300 MHz, $CDCl_3$).

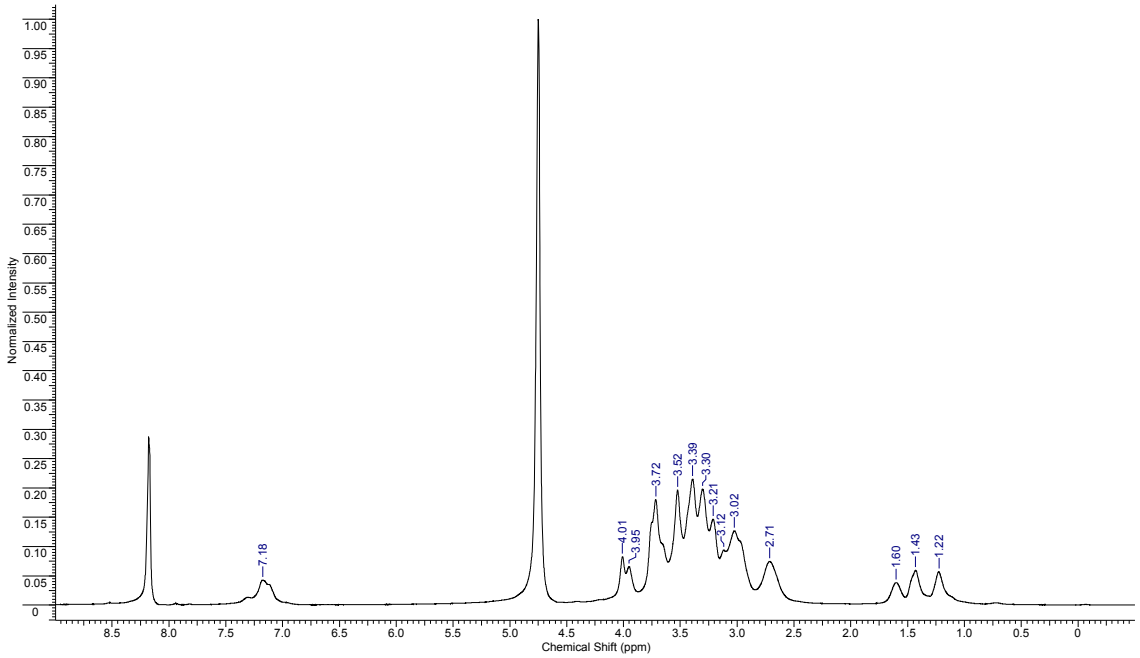

Figure S12. ^{1}H NMR of **D^{2b}** (300 MHz, D_2O).

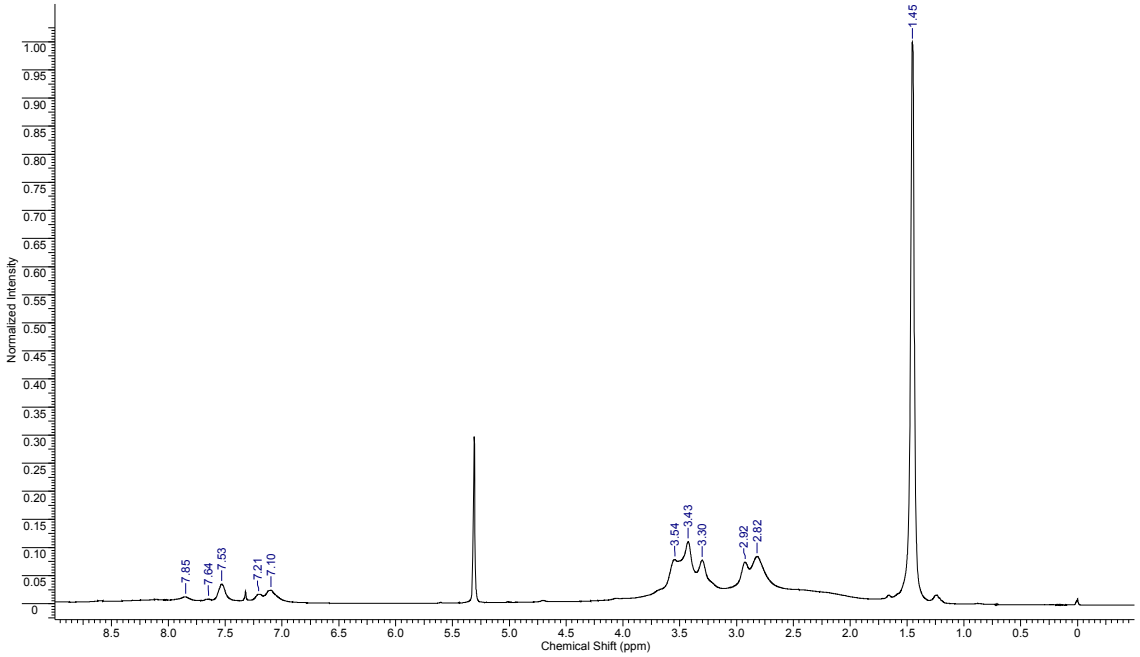

Figure S13. ^{1}H NMR of **D^{3a}** (300 MHz, $CDCl_3$).

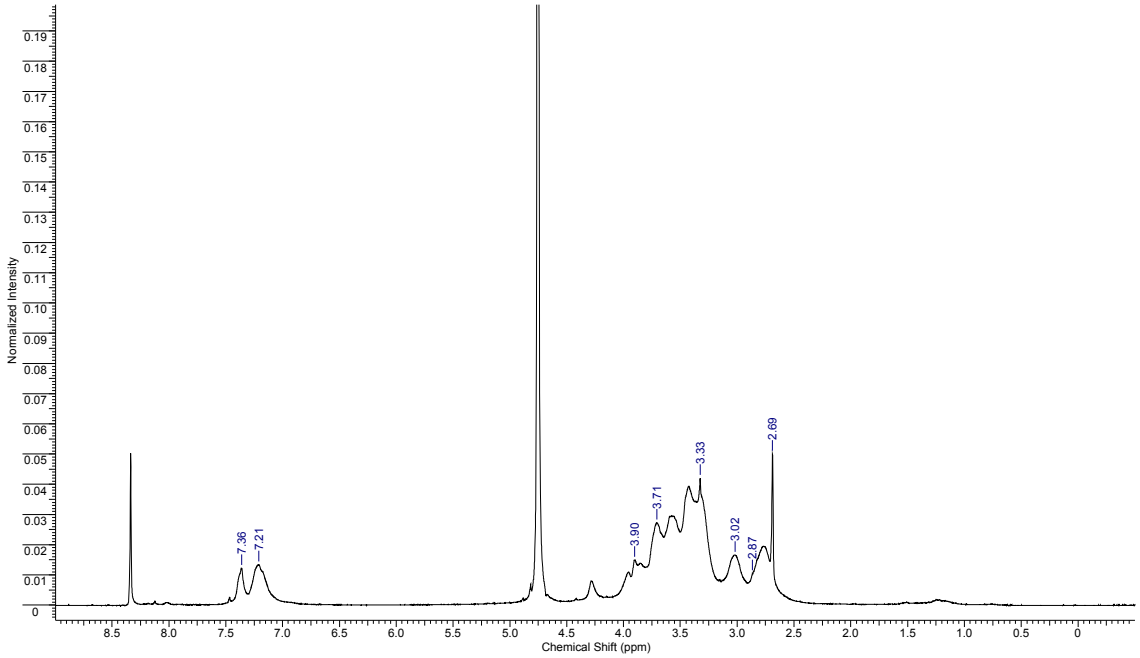

Figure S14. ^{1}H NMR of **D^{3b}** (300 MHz, D_2O).

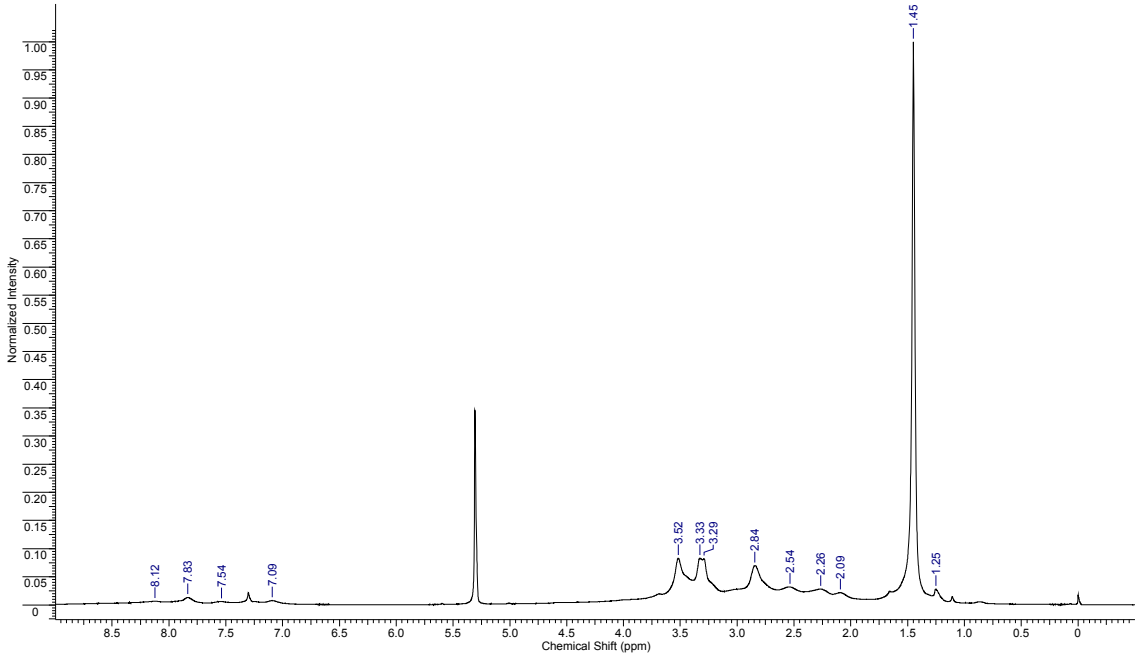

Figure S15. ^{1}H NMR of **D^{4a}** (300 MHz, $CDCl_3$).

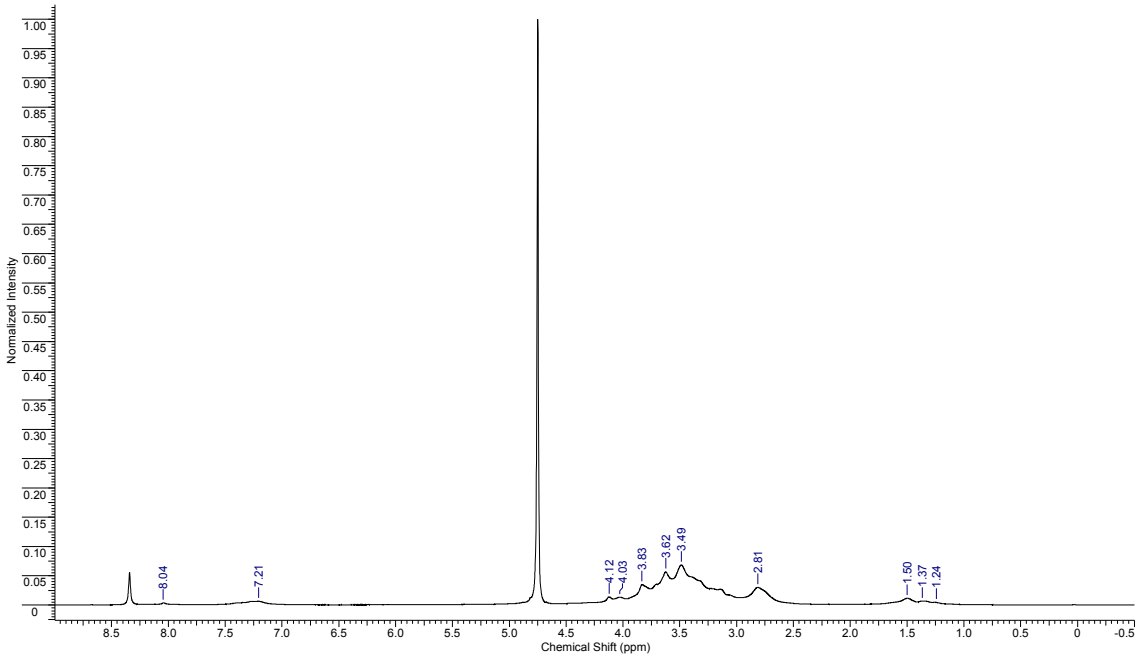

Figure S16. ^{1}H NMR of **D^{4b}** (300 MHz, D_2O).

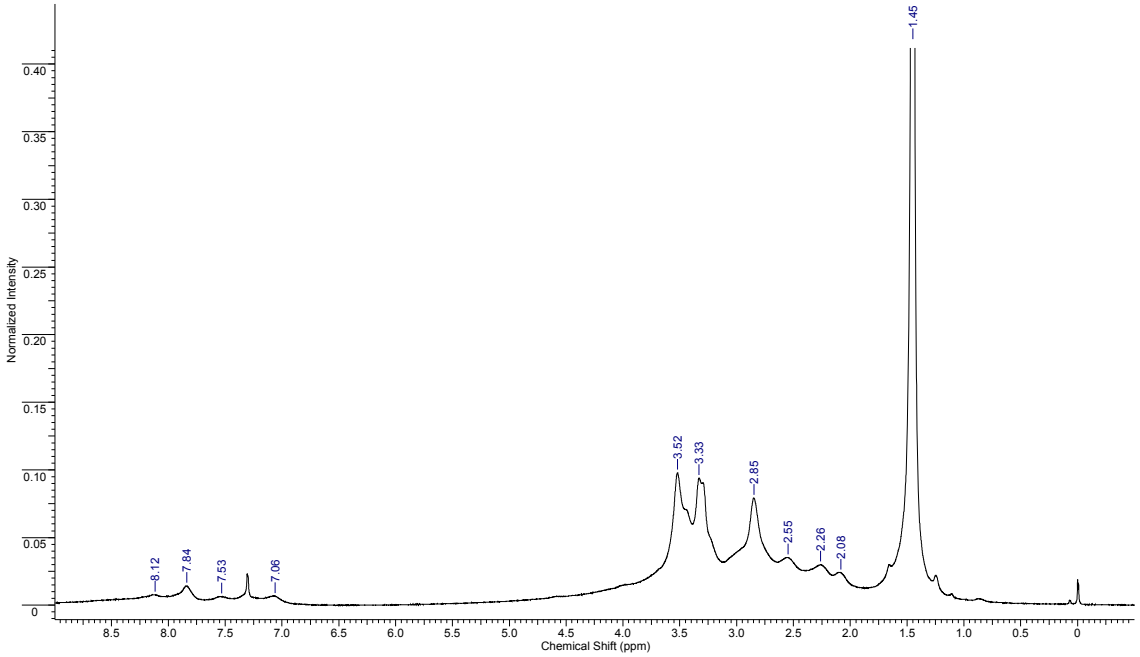

Figure S17. ^{1}H NMR of **D^{5a}** (300 MHz, $CDCl_3$).

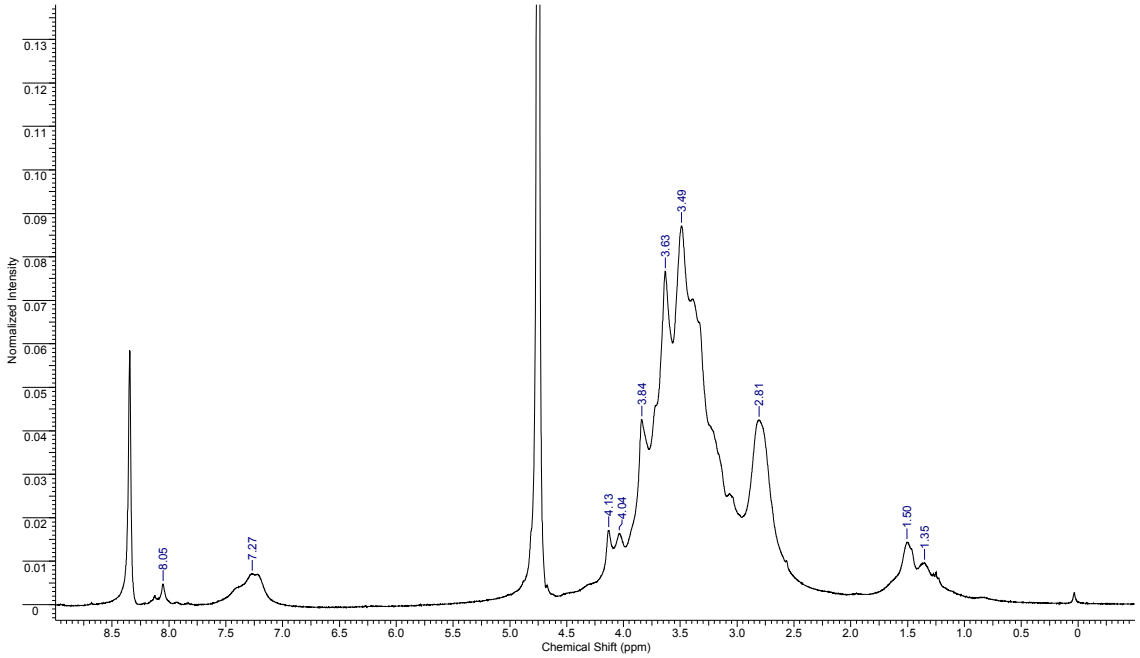

Figure S18. ^{1}H NMR of **D^{5b}** (300 MHz, D_2O).

8.4 LC-MS data

Compound 42-x

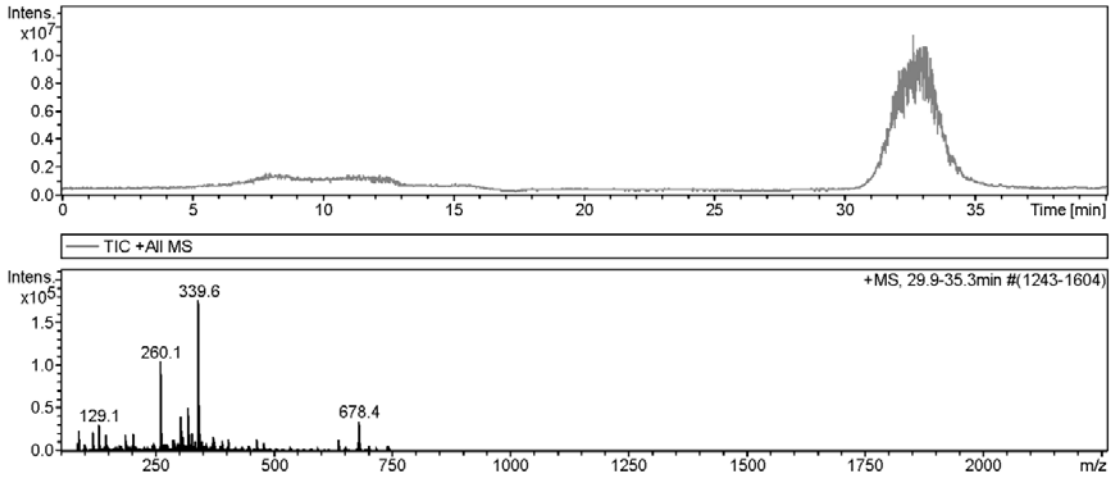

Compound 43-x

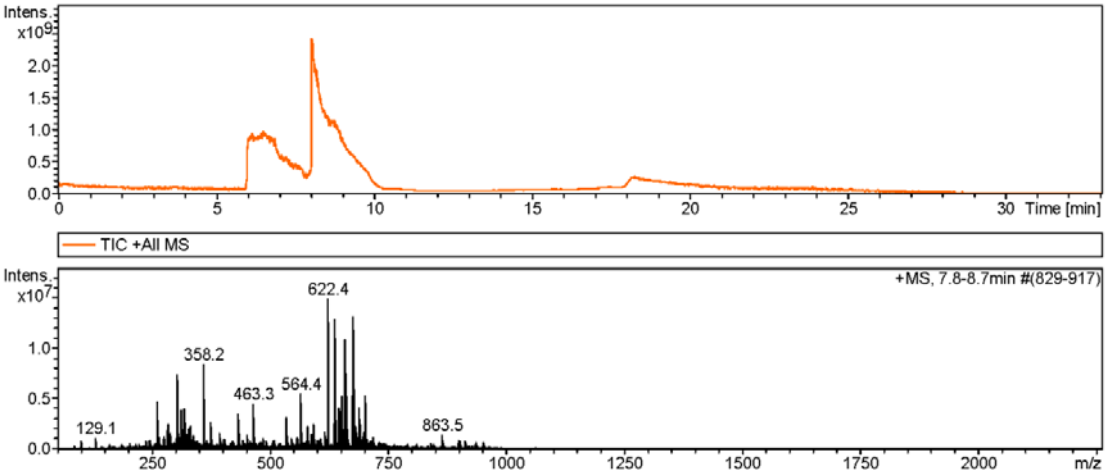

Compound 55-x

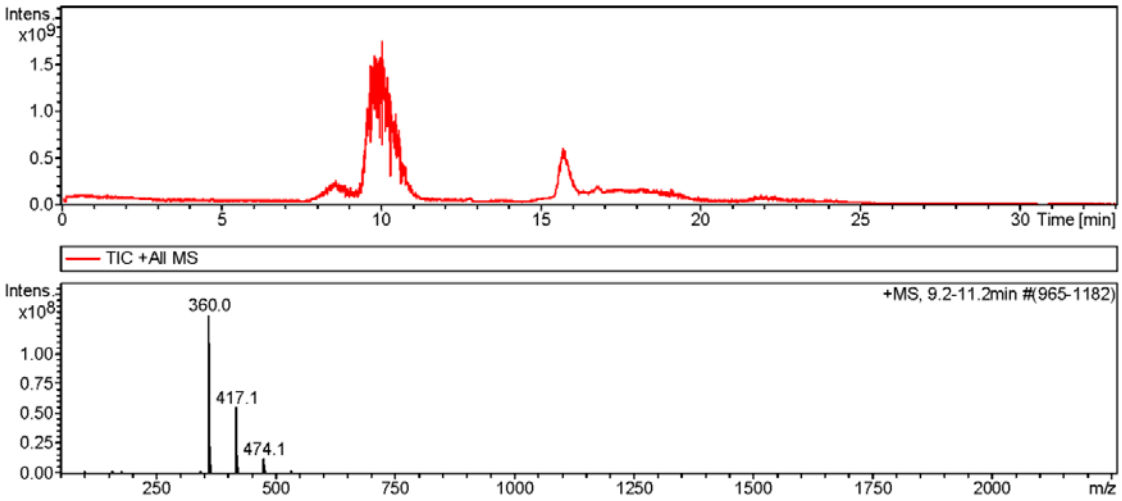

Compound 56-x

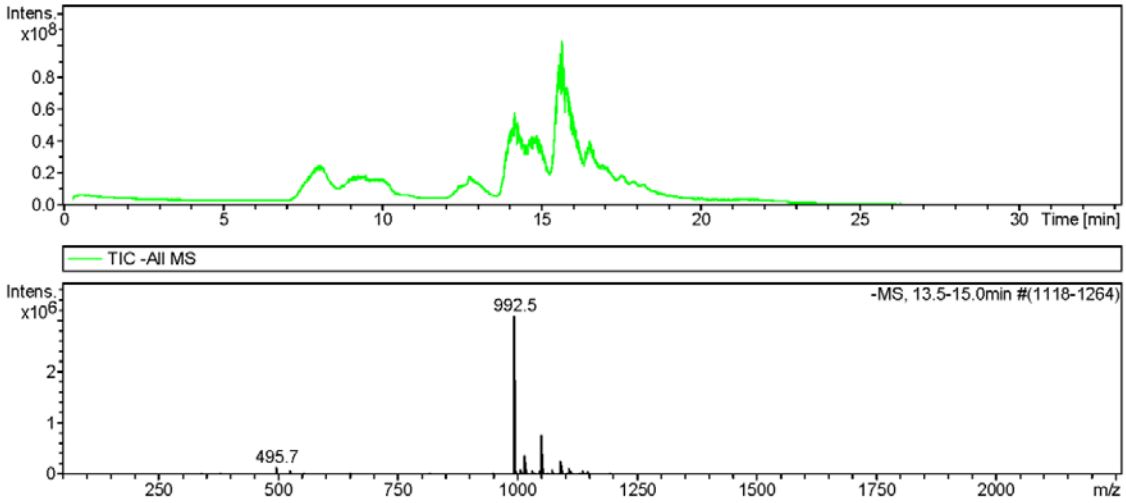

Compound 57-x

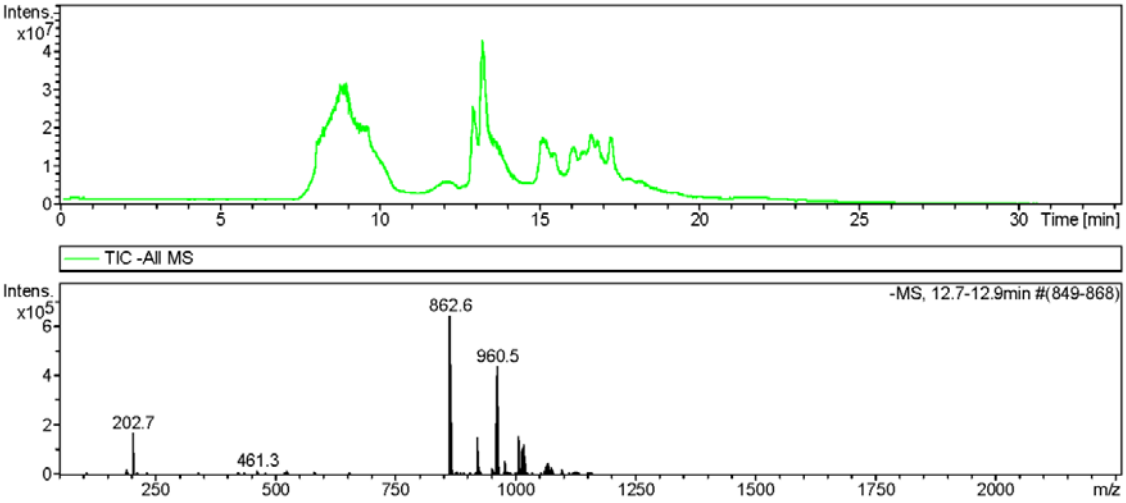

Compound 60-x

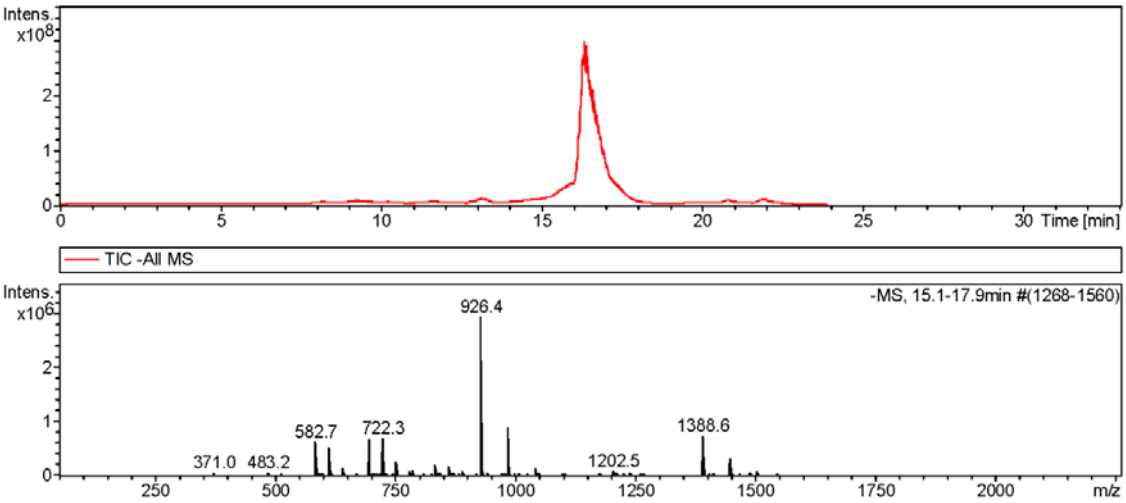

Compound 61-x

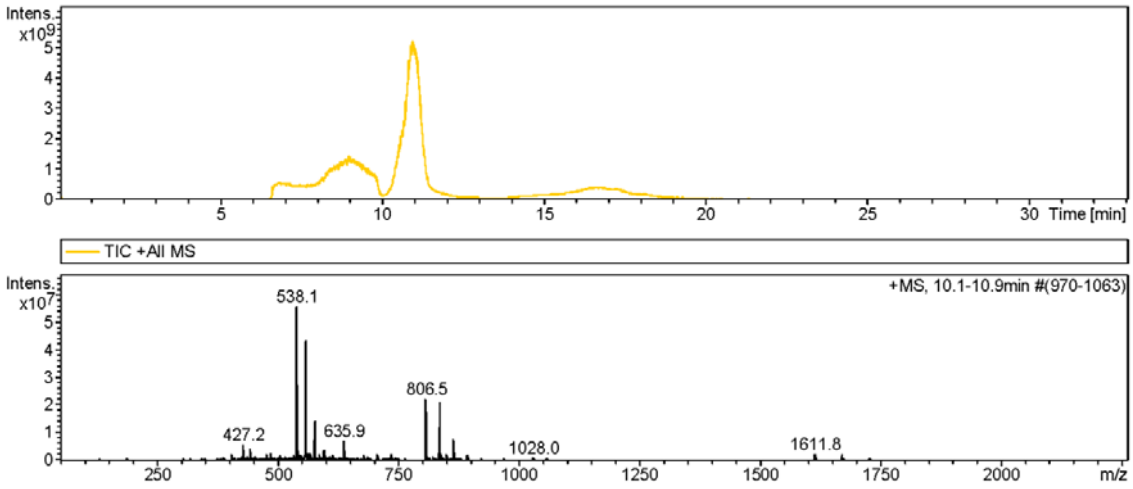

Compound 63-x

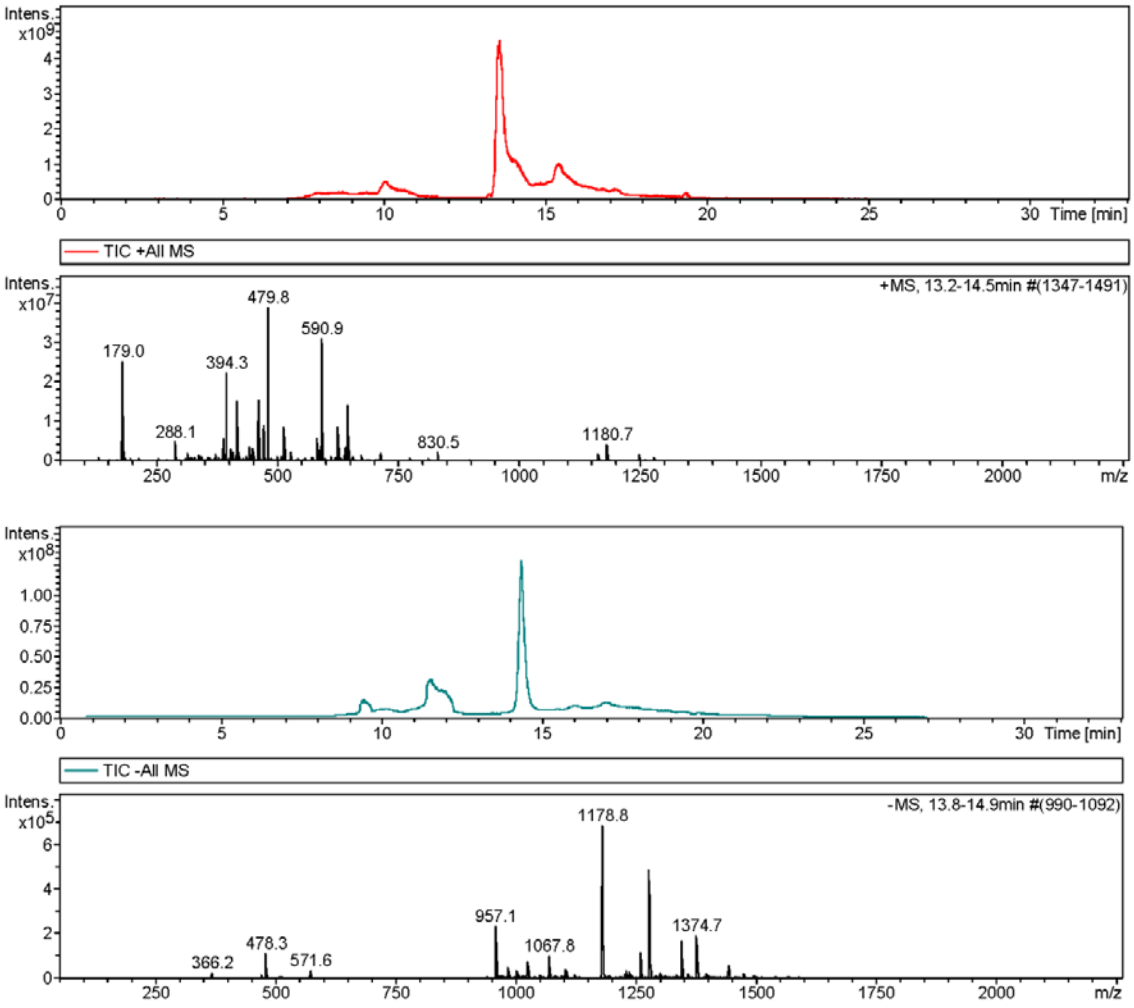

8.5 DLS graphs

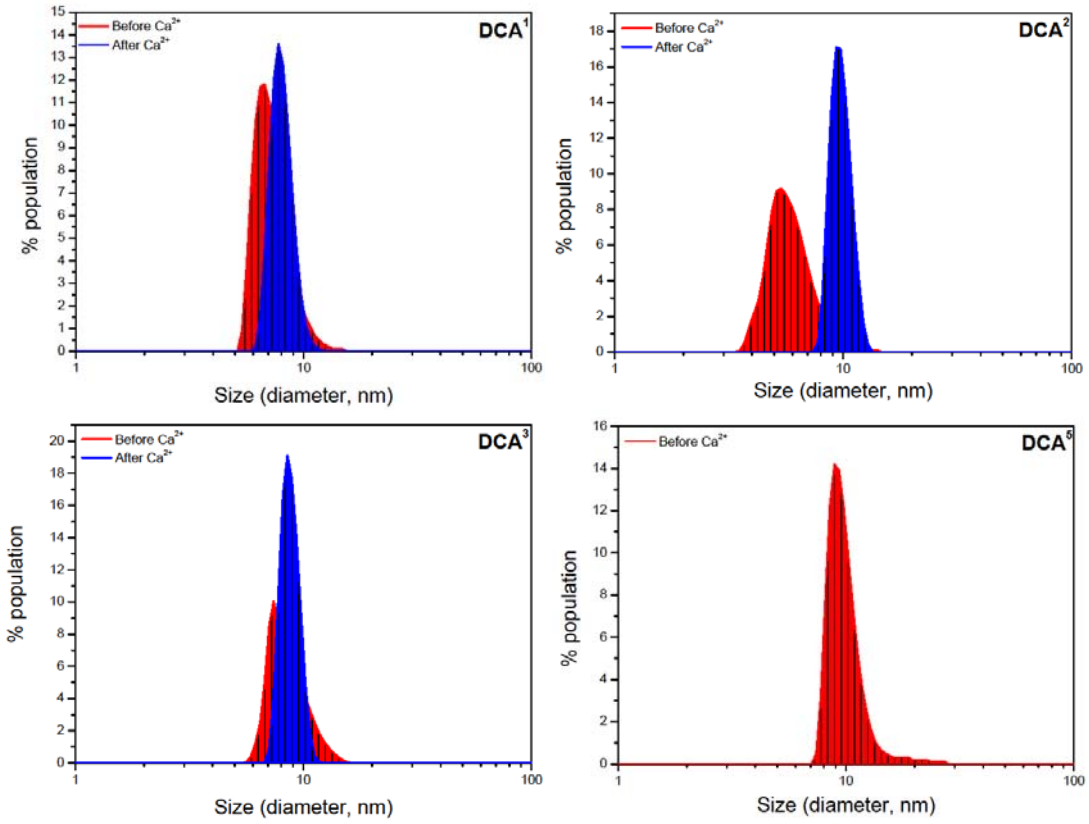

Figure S19. DLS graphs of **DCA**$^{1\text{-}3}$ before and after the addition of Ca^{2+}, and **DCA**^{5} prior to Ca^{2+} addition**.** Reproduced with permission from Ref 289. Copyright 2018 American Chemical Society.

8.6 HSQC spectra of paramagnetic L^5 + L^6 complexes

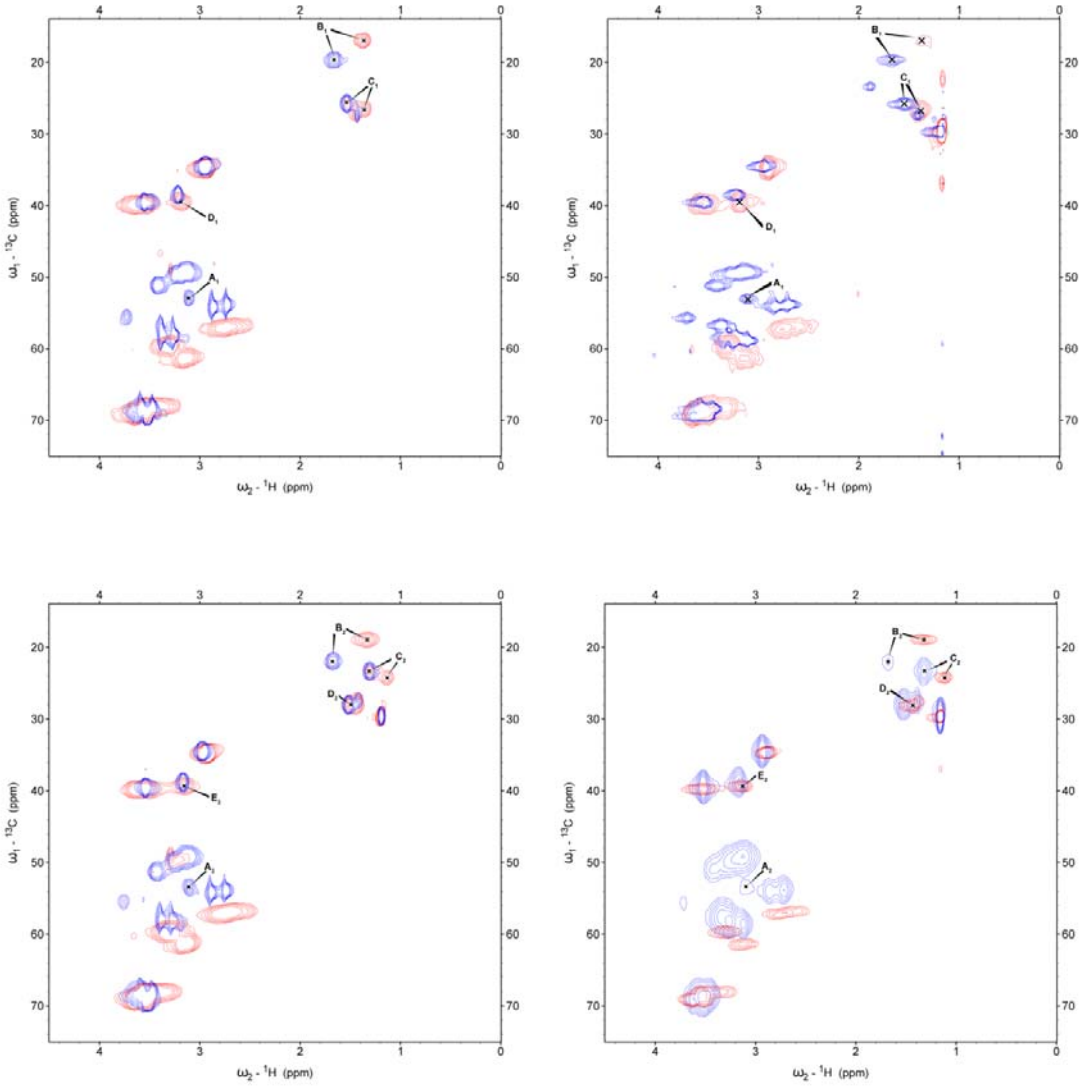

Figure S20. HSQC spectra of Eu^{3+} (left) and Yb^{3+} (right) complexes of **L^5** (top) and **L^6** (bottom) with the signals of interest assigned pre-(blue) and post-Ca^{2+} (red) addition. Chemical structures of studied complexes are presented in Figures 26 and 27. Reproduced with permission from Ref 309. Copyright 2019.

8.7 HABA assay

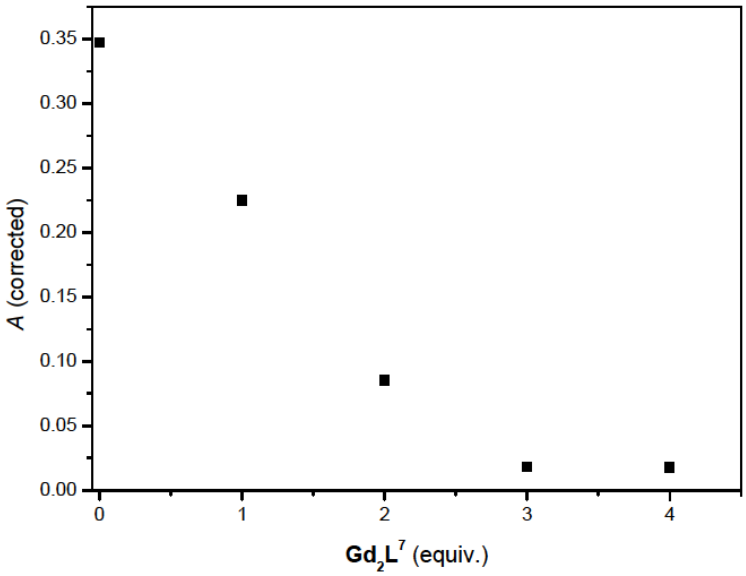

Figure S21. HABA assay of $\mathbf{Gd_2L^7}$ with avidin.[345] A plot of corrected UV/Vis absorbance at 500 nm versus the equivalents of $\mathbf{Gd_2L^7}$ added (25 mM HEPES, pH 7.4, 25 °C). Reproduced with permission from Ref 312. Copyright 2019 American Chemical Society.

8.8 Relaxometric titrations and MRI phantoms for Gd_2L^7 with avidin/avidin coated beads

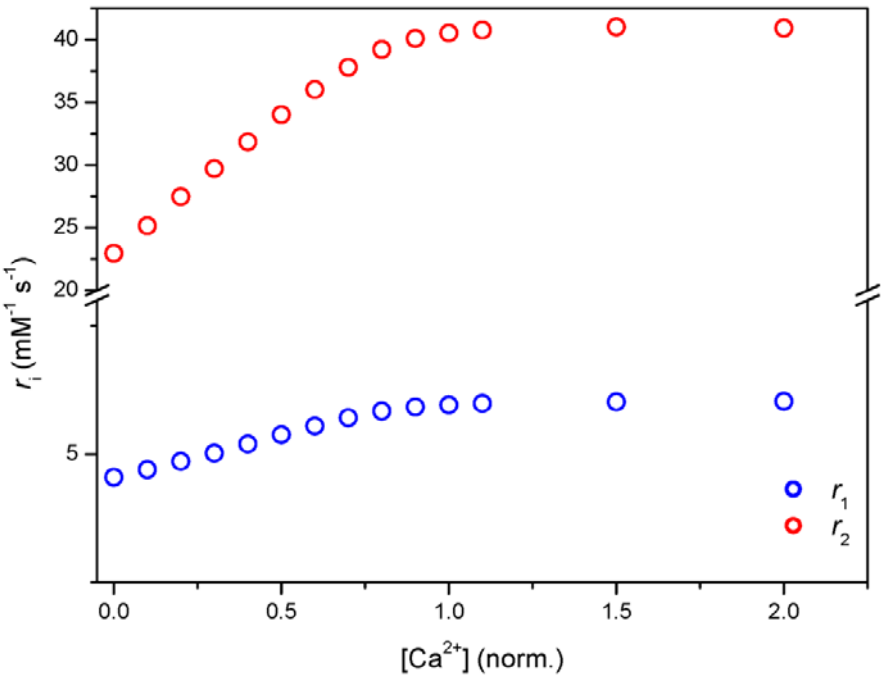

Figure S22. Relaxometric titration curves of the **Gd_2L^7**-avidin conjugate with Ca^{2+} ([Gd^{3+}] = 1 mM, pH 7.4, 50 mM HEPES, 25 °C, 7 T). Reproduced with permission from Ref 312. Copyright 2019 American Chemical Society.

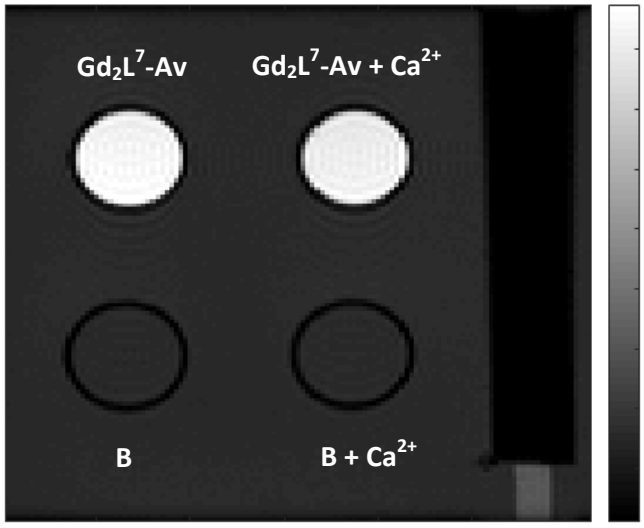

Figure S23. T_1-weighted MR phantom images of the buffer (B (HEPES)) or **Gd_2L^7**-Av sample tubes in presence and absence of Ca^{2+} (1 equiv.) ([Gd^{3+}] = 1 mM, pH 7.4, 50 mM HEPES, 25 °C, 7 T).

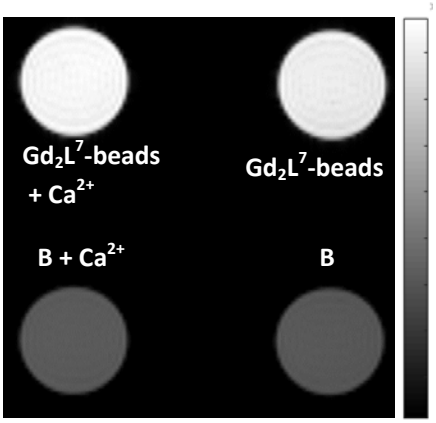

Figure S24. T_1-weighted MR phantom images of the buffer (B (HEPES)) or **Gd_2L^7**-conjugated to avidin beads in the presence and absence of Ca^{2+} (1 equiv.).

9. References

1. M. L. James and S. S. Gambhir, *Physiol. Rev.*, 2012, **92**, 897-965.
2. G.-L. Davies, I. Kramberger and J. J. Davis, *Chem. Commun.*, 2013, **49**, 9704-9721.
3. P. Caravan, *Chem. Soc. Rev.*, 2006, **35**, 512-523.
4. C. F. G. C. Geraldes and S. Laurent, *Contrast Media Mol. Imaging*, 2009, **4**, 1-23.
5. M. M. J. Modo and J. W. M. Bulte, *Molecular and cellular MR imaging*, CRC Press, Boca Raton, FL, 2007.
6. P. Caravan, J. J. Ellison, T. J. McMurry and R. B. Lauffer, *Chem. Rev.*, 1999, **99**, 2293-2352.
7. A. E. Merbach and É. Tóth, *The Chemistry of Contrast Agents in Medical Magnetic Resonance Imaging*, Wiley, Chichester, 2001.
8. R. W. Brown, Y.-C. N. Cheng, E. M. Haacke, M. R. Thompson and R. Venkatesan, *Magnetic resonance imaging : physical principles and sequence design*, John Wiley & Sons, Inc, Hoboken, New Jersey, 2014.
9. R. E. Hendrick and E. Mark Haacke, *J. Magn. Reson. Imaging*, 1993, **3**, 137-148.
10. A. Ericsson, T. Bach-Gansmo, F. Niklasson and A. Hemmingsson, *Acta Radiol.*, 1995, **36**, 41-46.
11. S. Aime, S. G. Crich, E. Gianolio, G. B. Giovenzana, L. Tei and E. Terreno, *Coord. Chem. Rev.*, 2006, **250**, 1562-1579.
12. E. J. Rummeny and G. Marchal, *Acta Radiol.*, 1997, **38**, 626-630.
13. M. Rogosnitzky and S. Branch, *Biometals*, 2016, **29**, 365-376.
14. A. D. Sherry, P. Caravan and R. E. Lenkinski, *J. Magn. Reson. Imaging*, 2009, **30**, 1240-1248.
15. R. B. Lauffer, *Chem. Rev.*, 1987, **87**, 901-927.
16. S. Aime and P. Caravan, *J. Magn. Reson. Imaging*, 2009, **30**, 1259-1267.
17. V. C. Pierre, M. J. Allen and P. Caravan, *J. Biol. Inorg. Chem.*, 2014, **19**, 127-131.
18. E. M. Gale, I. P. Atanasova, F. Blasi, I. Ay and P. Caravan, *J. Am. Chem. Soc.*, 2015, **137**, 15548-15557.
19. S. M. Abozeid, E. M. Snyder, T. Y. Tittiris, C. M. Steuerwald, A. Y. Nazarenko and J. R. Morrow, *Inorg. Chem.*, 2018, **57**, 2085-2095.
20. P. B. Tsitovich, F. Gendron, A. Y. Nazarenko, B. N. Livesay, A. P. Lopez, M. P. Shores, J. Autschbach and J. R. Morrow, *Inorg. Chem.*, 2018, **57**, 8364-8374.
21. C. Corot and D. Warlin, *Wiley Interdiscip. Rev. Nanomed. Nanobiotechnol.*, 2013, **5**, 411-422.
22. Y.-X. J. Wang, *Quant. Imaging. Med. Surg.*, 2011, **1**, 35-40.
23. C. Corot, P. Robert, J.-M. Idée and M. Port, *Adv. Drug Delivery Rev.*, 2006, **58**, 1471-1504.
24. S. Laurent, D. Forge, M. Port, A. Roch, C. Robic, L. Vander Elst and R. N. Muller, *Chem. Rev.*, 2008, **108**, 2064-2110.
25. J. Wan, X. Chen, Z. Wang, X. Yang and Y. Qian, *J. Cryst. Growth*, 2005, **276**, 571-576.
26. M. Kimata, D. Nakagawa and M. Hasegawa, *Powder Technol.*, 2003, **132**, 112-118.
27. G. Salazar-Alvarez, M. Muhammed and A. A. Zagorodni, *Chem. Eng. Sci.*, 2006, **61**, 4625-4633.
28. S. Basak, D.-R. Chen and P. Biswas, *Chem. Eng. Sci.*, 2007, **62**, 1263-1268.
29. A. B. Chin and I. I. Yaacob, *J. Mater. Process. Technol.*, 2007, **191**, 235-237.
30. C. Albornoz and S. E. Jacobo, *J. Magn. Magn. Mater.*, 2006, **305**, 12-15.
31. E. Hee Kim, H. Sook Lee, B. Kook Kwak and B.-K. Kim, *J. Magn. Magn. Mater.*, 2005, **289**, 328-330.
32. S.-J. Lee, J.-R. Jeong, S.-C. Shin, J.-C. Kim and J.-D. Kim, *J. Magn. Magn. Mater.*, 2004, **282**, 147-150.
33. I. Martínez-Mera, M. E. Espinosa-Pesqueira, R. Pérez-Hernández and J. Arenas-Alatorre, *Mater. Lett.*, 2007, **61**, 4447-4451.
34. Y.-k. Sun, M. Ma, Y. Zhang and N. Gu, *Colloids Surf., A*, 2004, **245**, 15-19.
35. J. Qiu, R. Yang, M. Li and N. Jiang, *Mater. Res. Bull.*, 2005, **40**, 1968-1975.

36. B. Bonnemain, *J. Drug Targeting*, 1998, **6**, 167-174.
37. A. Roch, R. N. Muller and P. Gillis, *J. Chem. Phys.*, 1999, **110**, 5403-5411.
38. R. N. Muller, P. Gillis, F. Moiny and A. Roch, *Magn. Reson. Med.*, 1991, **22**, 178-182.
39. R. N. Muller, L. Vander Elst, A. Roch, J. A. Peters, E. Csajbok, P. Gillis and Y. Gossuin, in *Adv. Inorg. Chem.*, Academic Press, 2005, vol. 57, pp. 239-292.
40. C. Chambon, O. Clement, A. Le Blanche, E. Schouman-Claeys and G. Frija, *Magn. Reson. Imaging*, 1993, **11**, 509-519.
41. E. Canet, D. Revel, R. Forrat, C. Baldy-Porcher, M. de Lorgeril, L. Sebbag, J.-P. Vallee, D. Didier and M. Amiel, *Magn. Reson. Imaging*, 1993, **11**, 1139-1145.
42. M. Gueron, *J. Magn. Reson.*, 1975, **19**, 58-66.
43. P. Gillis and S. H. Koenig, *Magn. Reson. Med.*, 1987, **5**, 323-345.
44. S. H. Koenig and K. E. Kellar, *Magn. Reson. Med.*, 1995, **34**, 227-233.
45. W. Krause, *Contrast Agents I : Magnetic Resonance Imaging*, Springer, Berlin, Germany, 2002.
46. X. Yin, S. E. Russek, G. Zabow, F. Sun, J. Mohapatra, K. E. Keenan, M. A. Boss, H. Zeng, J. P. Liu, A. Viert, S.-H. Liou and J. Moreland, *Sci. Rep.*, 2018, **8**, 11863.
47. E. Taboada, E. Rodríguez, A. Roig, J. Oró, A. Roch and R. N. Muller, *Langmuir*, 2007, **23**, 4583-4588.
48. Z. Zhou, L. Wang, X. Chi, J. Bao, L. Yang, W. Zhao, Z. Chen, X. Wang, X. Chen and J. Gao, *ACS Nano*, 2013, **7**, 3287-3296.
49. B. H. Kim, N. Lee, H. Kim, K. An, Y. I. Park, Y. Choi, K. Shin, Y. Lee, S. G. Kwon, H. B. Na, J.-G. Park, T.-Y. Ahn, Y.-W. Kim, W. K. Moon, S. H. Choi and T. Hyeon, *J. Am. Chem. Soc.*, 2011, **133**, 12624-12631.
50. Z. Zhou, Z. Zhao, H. Zhang, Z. Wang, X. Chen, R. Wang, Z. Chen and J. Gao, *ACS Nano*, 2014, **8**, 7976-7985.
51. L. Li, W. Jiang, K. Luo, H. Song, F. Lan, Y. Wu and Z. Gu, *Theranostics*, 2013, **3**, 595-615.
52. G. Jarockyte, E. Daugelaite, M. Stasys, U. Statkute, V. Poderys, T.-C. Tseng, S.-H. Hsu, V. Karabanovas and R. Rotomskis, *Int. J. Mol. Sci.*, 2016, **17**, 1193.
53. A. C. Anselmo and S. Mitragotri, *Bioeng. Transl. Med.*, 2016, **1**, 10-29.
54. P. Caravan, C. T. Farrar, L. Frullano and R. Uppal, *Contrast Media Mol. Imaging*, 2009, **4**, 89-100.
55. M. Holz, *Magn. Reson. Chem.*, 1993, **31**, S154-S154.
56. M. Botta, *Eur. J. Inorg. Chem.*, 2000, **2000**, 399-407.
57. E. J. Werner, A. Datta, C. J. Jocher and K. N. Raymond, *Angew. Chem. Int. Ed.*, 2008, **47**, 8568-8580.
58. I. Solomon, *Phys. Rev.*, 1955, **99**, 559-565.
59. N. Bloembergen, E. M. Purcell and R. V. Pound, *Phys. Rev.*, 1948, **73**, 679-712.
60. L. P. Hwang and J. H. Freed, *J. Chem. Phys.*, 1975, **63**, 4017-4025.
61. J. Wahsner, E. M. Gale, A. Rodríguez-Rodríguez and P. Caravan, *Chem. Rev.*, 2019, **119**, 957-1057.
62. M. Rohrer, H. Bauer, J. Mintorovitch, M. Requardt and H.-J. Weinmann, *Investig. Radiol.*, 2005, **40**, 715-724.
63. M. Norek and J. A. Peters, *Prog. Nucl. Magn. Reson. Spectrosc.*, 2011, **59**, 64-82.
64. N. Bloembergen and L. O. Morgan, *J. Chem. Phys.*, 1961, **34**, 842-850.
65. L. M. De León-Rodríguez, A. F. Martins, M. Pinho, N. Rofsky and A. D. Sherry, *J. Magn. Reson. Imaging*, 2015, **42**, 545-565.
66. S. Aime, E. Gianolio, E. Terreno, G. B. Giovenzana, R. Pagliarin, M. Sisti, G. Palmisano, M. Botta, M. P. Lowe and D. Parker, *J. Biol. Inorg. Chem.*, 2000, **5**, 488-497.
67. R. M. Supkowski and W. D. Horrocks, *Inorg. Chem.*, 1999, **38**, 5616-5619.
68. K. Kumar, C. A. Chang, L. C. Francesconi, D. D. Dischino, M. F. Malley, J. Z. Gougoutas and M. F. Tweedle, *Inorg. Chem.*, 1994, **33**, 3567-3575.

69. K. N. Raymond and V. C. Pierre, *Bioconjugate Chem.*, 2005, **16**, 3-8.
70. C. J. Jocher, M. Botta, S. Avedano, E. G. Moore, J. Xu, S. Aime and K. N. Raymond, *Inorg. Chem.*, 2007, **46**, 4796-4798.
71. E. J. Werner, S. Avedano, M. Botta, B. P. Hay, E. G. Moore, S. Aime and K. N. Raymond, *J. Am. Chem. Soc.*, 2007, **129**, 1870-1871.
72. J. Xu, S. J. Franklin, D. W. Whisenhunt and K. N. Raymond, *J. Am. Chem. Soc.*, 1995, **117**, 7245-7246.
73. S. Hajela, M. Botta, S. Giraudo, J. Xu, K. N. Raymond and S. Aime, *J. Am. Chem. Soc.*, 2000, **122**, 11228-11229.
74. S. M. Cohen, J. Xu, E. Radkov, K. N. Raymond, M. Botta, A. Barge and S. Aime, *Inorg. Chem.*, 2000, **39**, 5747-5756.
75. A. R. Johnson, B. O'Sulliva and K. N. Raymond, *Inorg. Chem.*, 2000, **39**, 2652-2660.
76. M. K. Thompson, D. M. J. Doble, L. S. Tso, S. Barra, M. Botta, S. Aime and K. N. Raymond, *Inorg. Chem.*, 2004, **43**, 8577-8586.
77. D. M. J. Doble, M. Botta, J. Wang, S. Aime, A. Barge and K. N. Raymond, *J. Am. Chem. Soc.*, 2001, **123**, 10758-10759.
78. S. Aime, M. Botta, L. Frullano, S. Geninatti Crich, G. Giovenzana, R. Pagliarin, G. Palmisano, F. R. Sirtori and M. Sisti, *J. Med. Chem.*, 2000, **43**, 4017-4024.
79. S. Aime, M. Botta, S. Geninatti Crich, G. B. Giovenzana, G. Jommi, R. Pagliarin and M. Sisti, *Inorg. Chem.*, 1997, **36**, 2992-3000.
80. S. Aime, L. Calabi, C. Cavallotti, E. Gianolio, G. B. Giovenzana, P. Losi, A. Maiocchi, G. Palmisano and M. Sisti, *Inorg. Chem.*, 2004, **43**, 7588-7590.
81. M. Tripepi, F. Capuana, E. Gianolio, F. Kock, A. Pagoto, R. Stefania, G. Digilio and S. Aime, *Bioconjugate Chem.*, 2018, **29**, 1428-1437.
82. W. D. Horrocks, G. F. Schmidt, D. R. Sudnick, C. Kittrell and R. A. Bernheim, *J. Am. Chem. Soc.*, 1977, **99**, 2378-2380.
83. W. D. Horrocks and D. R. Sudnick, *J. Am. Chem. Soc.*, 1979, **101**, 334-340.
84. M. C. Alpoim, A. M. Urbano, C. F. G. C. Geraldes and J. A. Peters, *J. Chem. Soc., Dalton Trans.*, 1992, **0**, 463-467.
85. A. M. Raitsimring, A. V. Astashkin, D. Baute, D. Goldfarb, O. G. Poluektov, M. P. Lowe, S. G. Zech and P. Caravan, *ChemPhysChem*, 2006, **7**, 1590-1597.
86. P. Caravan, *Acc. Chem. Res.*, 2009, **42**, 851-862.
87. A. D. Sherry and Y. Wu, *Curr. Opin. Chem. Biol.*, 2013, **17**, 167-174.
88. P. Caravan and Z. Zhang, *Eur. J. Inorg. Chem.*, 2012, **2012**, 1916-1923.
89. K. Micskei, L. Helm, E. Brucher and A. E. Merbach, *Inorg. Chem.*, 1993, **32**, 3844-3850.
90. K. Micskei, D. H. Powell, L. Helm, E. Brücher and A. E. Merbach, *Magn. Reson. Chem.*, 1993, **31**, 1011-1020.
91. C. F. G. C. Geraldes, A. D. Sherry, W. P. Cacheris, K.-T. Kuan, R. D. Brown, S. H. Koenic and M. Spillers, *Magn. Reson. Med.*, 1988, **8**, 191-199.
92. S. Aime, M. Botta, M. Fasano and E. Terreno, *Chem. Soc. Rev.*, 1998, **27**, 19-29.
93. J. Kotek, P. Lebdušková, P. Hermann, L. V. Elst, R. N. Muller, C. F. G. C. Geraldes, T. Maschmeyer, I. Lukeš and J. A. Peters, *Chem. - Eur. J.*, 2003, **9**, 5899-5915.
94. S. Aime, M. Botta, S. G. Crich, G. Giovenzana, R. Pagliarin, M. Sisti and E. Terreno, *Magn. Reson. Chem.*, 1998, **36**, S200-S208.
95. M. K. Thompson, M. Botta, G. Nicolle, L. Helm, S. Aime, A. E. Merbach and K. N. Raymond, *J. Am. Chem. Soc.*, 2003, **125**, 14274-14275.
96. E. J. Werner, J. Kozhukh, M. Botta, E. G. Moore, S. Avedano, S. Aime and K. N. Raymond, *Inorg. Chem.*, 2009, **48**, 277-286.
97. J. Xu, D. G. Churchill, M. Botta and K. N. Raymond, *Inorg. Chem.*, 2004, **43**, 5492-5494.
98. S. Aime, A. Barge, M. Botta, D. Parker and A. S. De Sousa, *J. Am. Chem. Soc.*, 1997, **119**, 4767-4768.

99. S. Aime, M. Botta, M. Fasano, S. Paoletti and E. Terreno, *Chem. - Eur. J.*, 1997, **3**, 1499-1504.
100. P. Hermann, J. Kotek, V. Kubíček and I. Lukeš, *Dalton Trans.*, 2008, **0**, 3027-3047.
101. S. Laus, A. Sour, R. Ruloff, É. Tóth and A. E. Merbach, *Chem. - Eur. J.*, 2006, **11**, 3064-3076.
102. S. L. Fossheim, A. K. Fahlvik, J. Klaveness and R. N. Muller, *Magn. Reson. Imaging*, 1999, **17**, 83-89.
103. Y. Li, M. Beija, S. Laurent, L. v. Elst, R. N. Muller, H. T. T. Duong, A. B. Lowe, T. P. Davis and C. Boyer, *Macromolecules*, 2012, **45**, 4196-4204.
104. P. Mi, H. Cabral, D. Kokuryo, M. Rafi, Y. Terada, I. Aoki, T. Saga, I. Takehiko, N. Nishiyama and K. Kataoka, *Biomaterials*, 2013, **34**, 492-500.
105. P. Caravan, G. Parigi, J. M. Chasse, N. J. Cloutier, J. J. Ellison, R. B. Lauffer, C. Luchinat, S. A. McDermid, M. Spiller and T. J. McMurry, *Inorg. Chem.*, 2007, **46**, 6632-6639.
106. J. A. Peters and K. Djanashvili, *Eur. J. Inorg. Chem.*, 2012, **2012**, 1961-1974.
107. C. Casali, M. Janier, E. Canet, J. F. Obadia, S. Benderbous, C. Corot and D. Revel, *Acad. Radiol.*, 1998, **5**, S214-S218.
108. S. Aime, M. Botta and E. Terreno, in *Adv. Inorg. Chem.*, Academic Press, 2005, vol. 57, pp. 173-237.
109. K. W.-Y. Chan and W.-T. Wong, *Coord. Chem. Rev.*, 2007, **251**, 2428-2451.
110. M. Bottrill, L. Kwok and N. J. Long, *Chem. Soc. Rev.*, 2006, **35**, 557-571.
111. P. Lebdušková, J. Kotek, P. Hermann, L. Vander Elst, R. N. Muller, I. Lukeš and J. A. Peters, *Bioconjugate Chem.*, 2004, **15**, 881-889.
112. D. M. Corsi, L. Vander Elst, R. N. Muller, H. van Bekkum and J. A. Peters, *Chem. - Eur. J.*, 2001, **7**, 64-71.
113. G. M. Nicolle, É. Tóth, H. Schmitt-Willich, B. Radüchel and A. E. Merbach, *Chem. - Eur. J.*, 2002, **8**, 1040-1048.
114. L. M. Z. Jászberényi, P. Schmidt, C. Weidensteiner, R. Kneuer, A. E. Merbach, L. Helm and É. Tóth, *J. Biol. Inorg. Chem.*, 2007, **12**, 406-420.
115. J. Rudovský, M. Botta, P. Hermann, K. I. Hardcastle, I. Lukeš and S. Aime, *Bioconjugate Chem.*, 2006, **17**, 975-987.
116. P. Lebdušková, A. Sour, L. Helm, É. Tóth, J. Kotek, I. Lukeš and A. E. Merbach, *Dalton Trans.*, 2006, **0**, 3399-3406.
117. J. Paris, C. Gameiro, V. Humblet, P. K. Mohapatra, V. Jacques and J. F. Desreux, *Inorg. Chem.*, 2006, **45**, 5092-5102.
118. V. Comblin, D. Gilsoul, M. Hermann, V. Humblet, V. Jacques, M. Mesbahi, C. Sauvage and J. F. Desreux, *Coord. Chem. Rev.*, 1999, **185-186**, 451-470.
119. J. Costa, R. Ruloff, L. Burai, L. Helm and A. E. Merbach, *J. Am. Chem. Soc.*, 2005, **127**, 5147-5157.
120. J. B. Livramento, É. Tóth, A. Sour, A. Borel, A. E. Merbach and R. Ruloff, *Angew. Chem. Int. Ed.*, 2005, **44**, 1480-1484.
121. V. C. Pierre, M. Botta, S. Aime and K. N. Raymond, *J. Am. Chem. Soc.*, 2006, **128**, 9272-9273.
122. S. Flacke, S. Fischer, M. J. Scott, R. J. Fuhrhop, J. S. Allen, M. McLean, P. Winter, G. A. Sicard, P. J. Gaffney, S. A. Wickline and G. M. Lanza, *Circulation*, 2001, **104**, 1280-1285.
123. W. J. M. Mulder, G. J. Strijkers, G. A. F. v. Tilborg, A. W. Griffioen and K. Nicolay, *NMR Biomed.*, 2006, **19**, 142-164.
124. E. Spuentrup, A. Buecker, M. Katoh, A. J. Wiethoff, E. C. Parsons, Jr., R. M. Botnar, R. M. Weisskoff, P. B. Graham, W. J. Manning and R. W. Gunther, *Circulation*, 2005, **111**, 1377-1382.
125. Z. Zhang, M. T. Greenfield, M. Spiller, T. J. McMurry, R. B. Lauffer and P. Caravan, *Angew. Chem. Int. Ed.*, 2005, **44**, 6766-6769.
126. M. Port, C. Corot, I. Raynal, J.-M. Idee, A. Dencausse, E. Lancelot, D. Meyer, B. Bonnemain and J. Lautrou, *Investig. Radiol.*, 2001, **36**, 445-454.

127. D. A. Fulton, M. O'Halloran, D. Parker, K. Senanayake, M. Botta and S. Aime, *Chem. Commun.*, 2005, **0**, 474-476.
128. B. G. Jenkins, E. Armstrong and R. B. Lauffer, *Magn. Reson. Med.*, 1991, **17**, 164-178.
129. R. B. Lauffer, *Magn. Reson. Med.*, 1991, **22**, 339-342.
130. S. Aime, Botta, M., Fasano, M. et al., *J. Biol. Inorg. Chem.*, 1996, **1**, 312-319.
131. S. Aime, M. Botta, L. Frullano, S. G. Crich, G. B. Giovenzana, R. Pagliarin, G. Palmisano and M. Sisti, *Chem. - Eur. J.*, 1999, **5**, 1253-1260.
132. S. Aime, M. Botta, F. Fedeli, E. Gianolio, E. Terreno and P. Anelli, *Chem. - Eur. J.*, 2001, **7**, 5261-5269.
133. S. Aime, E. Gianolio, E. Terreno, I. Menegotto, C. Bracco, L. Milone and G. Cravotto, *Magn. Reson. Chem.*, 2003, **41**, 800-805.
134. S. Aime, E. Gianolio, F. Uggeri, S. Tagliapietra, A. Barge and G. Cravotto, *J. Inorg. Biochem.*, 2006, **100**, 931-938.
135. P. Caravan, N. J. Cloutier, M. T. Greenfield, S. A. McDermid, S. U. Dunham, J. W. M. Bulte, J. C. Amedio, R. J. Looby, R. M. Supkowski, W. D. Horrocks, T. J. McMurry and R. B. Lauffer, *J. Am. Chem. Soc.*, 2002, **124**, 3152-3162.
136. E. Gianolio, G. B. Giovenzana, D. Longo, I. Longo, I. Menegotto and S. Aime, *Chem. - Eur. J.*, 2007, **13**, 5785-5797.
137. G. Angelovski, *Acc. Chem. Res.*, 2017, **50**, 2215-2224.
138. C. S. Bonnet and É. Tóth, *AJNR Am. J. Neuroradiol.*, 2010, **31**, 401-409.
139. M. C. Heffern, L. M. Matosziuk and T. J. Meade, *Chem. Rev.*, 2014, **114**, 4496-4539.
140. R. A. Moats, S. E. Fraser and T. J. Meade, *Angew. Chem. Int. Ed.*, 1997, **36**, 726-728.
141. E. L. Que and C. J. Chang, *Chem. Soc. Rev.*, 2010, **39**, 51-60.
142. J. L. Major and T. J. Meade, *Acc. Chem. Res.*, 2009, **42**, 893-903.
143. B. Yoo and M. D. Pagel, *Front. Biosci.*, 2008, **13**, 1733-1752.
144. C.-T. Yang and K.-H. Chuang, *MedChemComm*, 2012, **3**, 552-565.
145. C. S. Bonnet and E. Toth, *Chimia*, 2016, **70**, 102-108.
146. D. V. Hingorani, A. S. Bernstein and M. D. Pagel, *Contrast Media Mol. Imaging*, 2015, **10**, 245-265.
147. W. Xu and Y. Lu, *Chem. Commun.*, 2011, **47**, 4998-5000.
148. S. Zhang, R. Trokowski and A. D. Sherry, *J. Am. Chem. Soc.*, 2003, **125**, 15288-15289.
149. S. Aime, D. Delli Castelli, F. Fedeli and E. Terreno, *J. Am. Chem. Soc.*, 2002, **124**, 9364-9365.
150. A. X. Li, F. Wojciechowski, M. Suchy, C. K. Jones, R. H. E. Hudson, R. S. Menon and R. Bartha, *Magn. Reson. Med.*, 2008, **59**, 374-381.
151. D. Delli Castelli, E. Terreno and S. Aime, *Angew. Chem. Int. Ed.*, 2011, **50**, 1798-1800.
152. S. Zhang, C. R. Malloy and A. D. Sherry, *J. Am. Chem. Soc.*, 2005, **127**, 17572-17573.
153. S. Aime, M. Botta, E. Gianolio and E. Terreno, *Angew. Chem. Int. Ed.*, 2000, **39**, 747-750.
154. P. Z. Sun, Z. B. Schoening and A. Jasanoff, *Magn. Reson. Med.*, 2003, **49**, 609-614.
155. B. Song, Y. Wu, M. Yu, P. Zhao, C. Zhou, G. E. Kiefer and A. D. Sherry, *Dalton Trans.*, 2013, **42**, 8066-8069.
156. F. A. Rojas-Quijano, G. Tircsó, E. Tircsóné Benyó, Z. Baranyai, H. Tran Hoang, F. K. Kálmán, P. K. Gulaka, V. D. Kodibagkar, S. Aime, Z. Kovács and A. D. Sherry, *Chem. - Eur. J.*, 2012, **18**, 9669-9676.
157. C. Tu and A. Y. Louie, *Chem. Commun.*, 2007, **0**, 1331-1333.
158. C. Tu, E. A. Osborne and A. Y. Louie, *Tetrahedron*, 2009, **65**, 1241.
159. G. Angelovski, *Angew. Chem. Int. Ed.*, 2016, **55**, 7038-7046.
160. V. C. Pierre, S. M. Harris and S. L. Pailloux, *Acc. Chem. Res.*, 2018, **51**, 342-351.
161. K. L. Haas and K. J. Franz, *Chem. Rev.*, 2009, **109**, 4921-4960.
162. M. J. Berridge, *Neuron*, 1998, **21**, 13-26.
163. G. W. Zamponi, *ACS Chem. Neurosci.*, 2017, **8**, 2583-2585.

164. G. G. Somjen, *Ions in the Brain: Normal Function, Seizures, and Stroke*, Oxford University Press, USA, 2004.
165. W. C. Koller, *Exp. Neurol.*, 1997, **144**, 24-28.
166. A. V. Panov, J. R. Burke, W. J. Strittmatter and J. T. Greenamyre, *Arch. Biochem. Biophys.*, 2003, **410**, 1-6.
167. D. C. Jimerson, R. M. Post, J. S. Carman, D. P. van Kammen, J. H. Wood, F. K. Goodwin and W. E. Bunney, Jr., *Biol. Psychiatry*, 1979, **14**, 37-51.
168. A. Yarlagadda, *Med. Hypotheses*, 2002, **58**, 182-186.
169. A. P. de Silva, H. Q. N. Gunaratne, T. Gunnlaugsson, A. J. M. Huxley, C. P. McCoy, J. T. Rademacher and T. E. Rice, *Chem. Rev.*, 1997, **97**, 1515-1566.
170. C. Grienberger and A. Konnerth, *Neuron*, 2012, **73**, 862-885.
171. Y.-J. Lin and A. P. Koretsky, *Magn. Reson. Med.*, 1997, **38**, 378-388.
172. A. P. Koretsky and A. C. Silva, *NMR Biomed.*, 2004, **17**, 527-531.
173. K. W. MacRenaris, Z. Ma, R. L. Krueger, C. E. Carney and T. J. Meade, *Bioconjugate Chem.*, 2016, **27**, 465-473.
174. N. K. Logothetis and B. A. Wandell, *Annu. Rev. Physiol.*, 2004, **66**, 735-769.
175. D. J. Heeger and D. Ress, *Nat. Rev. Neurosci.*, 2002, **3**, 142.
176. N. K. Logothetis, *Nature*, 2008, **453**, 869.
177. W.-h. Li, S. E. Fraser and T. J. Meade, *J. Am. Chem. Soc.*, 1999, **121**, 1413-1414.
178. W.-h. Li, G. Parigi, M. Fragai, C. Luchinat and T. J. Meade, *Inorg. Chem.*, 2002, **41**, 4018-4024.
179. A. Barandov, B. B. Bartelle, C. G. Williamson, E. S. Loucks, S. J. Lippard and A. Jasanoff, *Nature Communications*, 2019, **10**, 897.
180. K. Dhingra, Fousková, P., Angelovski, G. et al., *J. Biol. Inorg. Chem.*, 2008, **13**, 35.
181. A. Mishra, P. Fousková, G. Angelovski, E. Balogh, A. K. Mishra, N. K. Logothetis and É. Tóth, *Inorg. Chem.*, 2008, **47**, 1370-1381.
182. G. Angelovski, P. Fouskova, I. Mamedov, S. Canals, E. Toth and N. K. Logothetis, *ChemBioChem*, 2008, **9**, 1729-1734.
183. J. Henig, I. Mamedov, P. Fouskova, É. Tóth, N. K. Logothetis, G. Angelovski and H. A. Mayer, *Inorg. Chem.*, 2011, **50**, 6472-6481.
184. G. Angelovski, S. Gottschalk, M. Milošević, J. Engelmann, G. E. Hagberg, P. Kadjane, P. Andjus and N. K. Logothetis, *ACS Chem. Neurosci.*, 2014, **5**, 360-369.
185. I. Mamedov, S. Canals, J. Henig, M. Beyerlein, Y. Murayama, H. A. Mayer, N. K. Logothetis and G. Angelovski, *ACS Chem. Neurosci.*, 2010, **1**, 819-828.
186. G. E. Hagberg, I. Mamedov, A. Power, M. Beyerlein, H. Merkle, V. G. Kiselev, K. Dhingra, V. Kubìček, G. Angelovski and N. K. Logothetis, *Contrast Media Mol. Imaging*, 2014, **9**, 71-82.
187. T. L. Doane and C. Burda, *Chem. Soc. Rev.*, 2012, **41**, 2885-2911.
188. S. Gunduz, N. Nitta, S. Vibhute, S. Shibata, M. E. Mayer, N. K. Logothetis, I. Aoki and G. Angelovski, *Chem. Commun.*, 2015, **51**, 2782-2785.
189. A. Moussaron, S. Vibhute, A. Bianchi, S. Gündüz, S. Kotb, L. Sancey, V. Motto-Ros, S. Rizzitelli, Y. Crémillieux, F. Lux, N. K. Logothetis, O. Tillement and G. Angelovski, *Small*, 2015, **11**, 4900-4909.
190. F. Garello, S. Vibhute, S. Gündüz, N. K. Logothetis, E. Terreno and G. Angelovski, *Biomacromolecules*, 2016, **17**, 1303-1311.
191. S. Gündüz, T. Savić, R. Pohmann, N. K. Logothetis, K. Scheffler and G. Angelovski, *ACS Sensors*, 2016, **1**, 483-487.
192. A. Jasanoff, *Curr. Opin. Neurobiol.*, 2007, **17**, 593-600.
193. T. Atanasijevic, M. Shusteff, P. Fam and A. Jasanoff, *Proc. Natl. Acad. Sci. U.S.A.*, 2006, **103**, 14707.
194. M. G. Shapiro, T. Atanasijevic, H. Faas, G. G. Westmeyer and A. Jasanoff, *Magn. Reson. Imaging*, 2006, **24**, 449-462.

195. E. Rodriguez, V. S. Lelyveld, T. Atanasijevic, S. Okada and A. Jasanoff, *Chem. Commun.*, 2014, **50**, 3595-3598.
196. S. Okada, B. B. Bartelle, N. Li, V. Breton-Provencher, J. J. Lee, E. Rodriguez, J. Melican, M. Sur and A. Jasanoff, *Nat. Nanotechnol.*, 2018, **13**, 473-477.
197. S. Ghosh, P. Harvey, J. C. Simon and A. Jasanoff, *Curr. Opin. Neurobiol.*, 2018, **50**, 201-210.
198. M. Stefanidou, Maravelias, C., Dona, A. et al., *Arch. Toxicol.*, (2006), **80**, 1.
199. C. J. Frederickson, S. W. Suh, D. Silva, C. J. Frederickson and R. B. Thompson, *J. Nutr.*, 2000, **130**, 1471S-1483S.
200. K. Hanaoka, K. Kikuchi, Y. Urano and T. Nagano, *J. Chem. Soc., Perkin Trans. 2*, 2001, **0**, 1840-1843.
201. K. Hanaoka, K. Kikuchi, Y. Urano, M. Narazaki, T. Yokawa, S. Sakamoto, K. Yamaguchi and T. Nagano, *Chem. Biol.*, 2002, **9**, 1027-1032.
202. J. L. Major, G. Parigi, C. Luchinat and T. J. Meade, *Proc. Natl. Acad. Sci. U.S.A.*, 2007, **104**, 13881-13886.
203. J. L. Major, R. M. Boiteau and T. J. Meade, *Inorg. Chem.*, 2008, **47**, 10788-10795.
204. L. M. Matosziuk, J. H. Leibowitz, M. C. Heffern, K. W. MacRenaris, M. A. Ratner and T. J. Meade, *Inorg. Chem.*, 2013, **52**, 12250-12261.
205. M. Regueiro-Figueroa, S. Gündüz, V. Patinec, N. K. Logothetis, D. Esteban-Gómez, R. Tripier, G. Angelovski and C. Platas-Iglesias, *Inorg. Chem.*, 2015, **54**, 10342-10350.
206. A. C. Esqueda, J. A. López, G. Andreu-de-Riquer, J. C. Alvarado-Monzón, J. Ratnakar, A. J. M. Lubag, A. D. Sherry and L. M. De León-Rodríguez, *J. Am. Chem. Soc.*, 2009, **131**, 11387-11391.
207. L. M. De León-Rodríguez, A. J. M. Lubag, J. A. López, G. Andreu-de-Riquer, J. C. Alvarado-Monzón and A. D. Sherry, *MedChemComm*, 2012, **3**, 480-483.
208. R. Trokowski, J. Ren, F. K. Kálmán and A. D. Sherry, *Angew. Chem. Int. Ed.*, 2005, **44**, 6920-6923.
209. X.-a. Zhang, K. S. Lovejoy, A. Jasanoff and S. J. Lippard, *Proc. Natl. Acad. Sci. U.S.A.*, 2007, **104**, 10780.
210. T. N. Parac-Vogt, L. Vander Elst, K. Kimpe, S. Laurent, C. Burtéa, F. Chen, R. Van Deun, Y. Ni, R. N. Muller and K. Binnemans, *Contrast Media Mol. Imaging*, 2006, **1**, 267-278.
211. R. Ruloff, G. v. Koten and A. E. Merbach, *Chem. Commun.*, 2004, **0**, 842-843.
212. S. Aime, M. Botta, M. Fasano and E. Terreno, *Spectrochim. Acta A*, 1993, **49**, 1315-1322.
213. T. N. Parac-Vogt, K. Kimpe and K. Binnemans, *J. Alloys Compd.*, 2004, **374**, 325-329.
214. E. Abbasi, S. F. Aval, A. Akbarzadeh, M. Milani, H. T. Nasrabadi, S. W. Joo, Y. Hanifehpour, K. Nejati-Koshki and R. Pashaei-Asl, *Nanoscale Res. Lett.*, 2014, **9**, 247-247.
215. A. P. Sherje, M. Jadhav, B. R. Dravyakar and D. Kadam, *Int. J. Pharm.*, 2018, **548**, 707-720.
216. B. K. Nanjwade, H. M. Bechra, G. K. Derkar, F. V. Manvi and V. K. Nanjwade, *Eur. J. Pharm. Sci.*, 2009, **38**, 185-196.
217. E. Buhleier, W. Wehner and F. Vögtle, *Synthesis*, 1978, **1978**, 155-158.
218. R. G. Denkewalter, J. Kolc and W. J. Lukasavage, *Macromolecular highly branched homogeneous compound based on lysine units,* 1981.
219. D. A. Tomalia, H. Baker, J. Dewald, M. Hall, G. Kallos, S. Martin, J. Roeck, J. Ryder and P. Smith, *Polym. J.*, 1985, **17**, 117.
220. G. R. Newkome, Z. Yao, G. R. Baker and V. K. Gupta, *J. Org. Chem.*, 1985, **50**, 2003-2004.
221. D. A. Tomalia, *Macromol. Symp.*, 1996, **101**, 243-255.
222. C. J. Hawker and J. M. J. Frechet, *J. Am. Chem. Soc.*, 1990, **112**, 7638-7647.
223. K. L. Wooley, C. J. Hawker and J. M. J. Frechet, *J. Am. Chem. Soc.*, 1991, **113**, 4252-4261.
224. K. L. Wooley, C. J. Hawker and J. M. J. Fréchet, *Angew. Chem. Int. Ed.*, 1994, **33**, 82-85.
225. G. L'Abbé, B. Forier and W. Dehaen, *Chem. Commun.*, 1996, **0**, 2143-2144.
226. T. Kawaguchi, K. L. Walker, C. L. Wilkins and J. S. Moore, *J. Am. Chem. Soc.*, 1995, **117**, 2159-2165.

227. V. Maraval, A. M. Caminade, J. P. Majoral and J. C. Blais, *Angew. Chem. Int. Ed.*, 2003, **42**, 1822-1826.
228. V. Maraval, J. Pyzowski, A.-M. Caminade and J.-P. Majoral, *J. Org. Chem.*, 2003, **68**, 6043-6046.
229. P. Wu, A. K. Feldman, A. K. Nugent, C. J. Hawker, A. Scheel, B. Voit, J. Pyun, J. M. J. Fréchet, K. B. Sharpless and V. V. Fokin, *Angew. Chem. Int. Ed.*, 2004, **43**, 3928-3932.
230. U. Boas, J. B. Christensen and P. M. H. Heegaard, *J. Mater. Chem.*, 2006, **16**, 3785-3798.
231. O. A. Matthews, A. N. Shipway and J. F. Stoddart, *Prog. Polym. Sci.*, 1998, **23**, 1-56.
232. S. Svenson and D. A. Tomalia, *Adv. Drug Delivery Rev.*, 2005, **57**, 2106-2129.
233. K. Lorenz, D. Hölter, B. Stühn, R. Mülhaupt and H. Frey, *Adv. Mater.*, 1996, **8**, 414-416.
234. H. Frey, K. Lorenz, R. Mülhaupt, U. Rapp and F. J. Mayer-Posner, *Macromol. Symp.*, 1996, **102**, 19-26.
235. V. Percec, P. Chu, G. Ungar and J. Zhou, *J. Am. Chem. Soc.*, 1995, **117**, 11441-11454.
236. N. Boiko, X. Zhu, A. Bobrovsky and V. Shibaev, *Chem. Mater.*, 2001, **13**, 1447-1452.
237. C. Hawker and J. M. J. Fréchet, *J. Chem. Soc., Chem. Commun.*, 1990, **0**, 1010-1013.
238. C. J. Hawker, K. L. Wooley and J. M. J. Fréchet, *J. Chem. Soc., Perkin Trans. 1*, 1993, **0**, 1287-1297.
239. T. A. Betley, J. A. Hessler, A. Mecke, M. M. Banaszak Holl, B. G. Orr, S. Uppuluri, D. A. Tomalia and J. R. Baker, *Langmuir*, 2002, **18**, 3127-3133.
240. D. Seebach, P. B. Rheiner, G. Greiveldinger, T. Butz and H. Sellner, *Chiral Dendrimers. In: Dendrimers.*, Springer, Berlin, 1998.
241. J. P. Tam, *Proc. Natl. Acad. Sci. U.S.A.*, 1988, **85**, 5409-5413.
242. J. d. A. Twibanire and T. B. Grindley, *Polymers*, 2014, **6**, 179.
243. P. R. Dvornic, A. M. de Leuze-Jallouli, M. J. Owen and S. V. Perz, *Macromolecules*, 2000, **33**, 5366-5378.
244. R. Roy, D. Zanini, S. J. Meunier and A. Romanowska, *J. Chem. Soc., Chem. Commun.*, 1993, **0**, 1869-1872.
245. A. Pushechnikov, S. S. Jalisatgi and M. F. Hawthorne, *Chem. Commun.*, 2013, **49**, 3579-3581.
246. M. J. Cloninger, *Curr. Opin. Chem. Biol.*, 2002, **6**, 742-748.
247. L. Crespo, G. Sanclimens, M. Pons, E. Giralt, M. Royo and F. Albericio, *Chem. Rev.*, 2005, **105**, 1663-1682.
248. W. B. Turnbull and J. F. Stoddart, *Rev. Mol. Biotechnol.*, 2002, **90**, 231-255.
249. J. J. Khandare, S. Jayant, A. Singh, P. Chandna, Y. Wang, N. Vorsa and T. Minko, *Bioconjugate Chem.*, 2006, **17**, 1464-1472.
250. H. J. Hsu, J. Bugno, S. r. Lee and S. Hong, *Wiley Interdiscip. Rev. Nanomed. Nanobiotechnol.*, 2017, **9**.
251. J. P. Tam, Y. A. Lu and J. L. Yang, *Eur. J. Biochem.*, 2002, **269**, 923-932.
252. B. V. Worley, D. L. Slomberg and M. H. Schoenfisch, *Bioconjugate Chem.*, 2014, **25**, 918-927.
253. S. Battah, S. O'Neill, C. Edwards, S. Balaratnam, P. Dobbin and A. J. MacRobert, *Int. J. Biochem. Cell Biol.*, 2006, **38**, 1382-1392.
254. G. Wu, R. F. Barth, W. Yang, M. Chatterjee, W. Tjarks, M. J. Ciesielski and R. A. Fenstermaker, *Bioconjugate Chem.*, 2004, **15**, 185-194.
255. S. Kasai, H. Nagasawa, M. Shimamura, Y. Uto and H. Hori, *Bioorg. Med. Chem. Lett.*, 2002, **12**, 951-954.
256. A. Lakshminarayanan, V. K. Ravi, R. Tatineni, Y. B. R. D. Rajesh, V. Maingi, K. S. Vasu, N. Madhusudhan, P. K. Maiti, A. K. Sood, S. Das and N. Jayaraman, *Bioconjugate Chem.*, 2013, **24**, 1612-1623.
257. M. Longmire, P. L. Choyke and H. Kobayashi, *Curr. Top. Med. Chem.*, 2008, **8**, 1180-1186.
258. M. T. McMahon and J. W. M. Bulte, *Wiley Interdiscip. Rev. Nanomed. Nanobiotechnol.*, 2018, **10**, e1496.

259. J. Lim, B. Turkbey, M. Bernardo, L. H. Bryant, M. Garzoni, G. M. Pavan, T. Nakajima, P. L. Choyke, E. E. Simanek and H. Kobayashi, *Bioconjugate Chem.*, 2012, **23**, 2291-2299.
260. L. H. Bryant, M. W. Brechbiel, C. Wu, J. W. M. Bulte, V. Herynek and J. A. Frank, *J. Magn. Reson. Imaging*, 1999, **9**, 348-352.
261. M. R. Longmire, M. Ogawa, P. L. Choyke and H. Kobayashi, *Wiley Interdiscip. Rev. Nanomed. Nanobiotechnol.*, 2014, **6**, 155-162.
262. E. Wiener, M. W. Brechbiel, H. Brothers, R. L. Magin, O. A. Gansow, D. A. Tomalia and P. C. Lauterbur, *Magn. Reson. Med.*, 1994, **31**, 1-8.
263. K. Nwe, L. H. Bryant and M. W. Brechbiel, *Bioconjugate Chem.*, 2010, **21**, 1014-1017.
264. M. Ogawa, C. A. S. Regino, B. Marcelino, M. Williams, N. Kosaka, L. H. Bryant, P. L. Choyke and H. Kobayashi, *Bioconjugate Chem.*, 2010, **21**, 955-960.
265. H. Kobayashi and M. W. Brechbiel, *Mol. Imaging*, 2003, **2**, 1-10.
266. H. Kobayashi, S. Kawamoto, S.-K. Jo, H. L. Bryant, M. W. Brechbiel and R. A. Star, *Bioconjugate Chem.*, 2003, **14**, 388-394.
267. K. Hisataka and W. B. Martin, *Curr. Pharm. Biotechnol.*, 2004, **5**, 539-549.
268. H. Kobayashi and M. W. Brechbiel, *Adv. Drug Delivery Rev.*, 2005, **57**, 2271-2286.
269. J. K. Young, G. R. Baker, G. R. Newkome, K. F. Morris and C. S. Johnson, *Macromolecules*, 1994, **27**, 3464-3471.
270. L. D. Margerum, B. K. Campion, M. Koo, N. Shargill, J.-J. Lai, A. Marumoto and P. Christian Sontum, *J. Alloys Compd.*, 1997, **249**, 185-190.
271. R. B. Merrifield, *J. Am. Chem. Soc.*, 1963, **85**, 2149-2154.
272. R. B. Merrifield, *Angew. Chem. Int. Ed.*, 1985, **24**, 799-810.
273. D. M. M. Jaradat, *Amino Acids*, 2018, **50**.
274. M. Stawikowski and G. B. Fields, *Curr. Protoc. Protein. Sci.*, 2002, **18**, 18.
275. J. M. Palomo, *RSC Advances*, 2014, **4**, 32658-32672.
276. W. Chan and P. D. White, *Fmoc Solid Phase Peptide Synthesis*, Oxford University Press, 2000.
277. F. Gaggini, A. Porcheddu, G. Reginato, M. Rodriquez and M. Taddei, *J. Comb. Chem.*, 2004, **6**, 805-810.
278. N. Thieriet, F. Guibé and F. Albericio, *Org. Lett.*, 2000, **2**, 1815-1817.
279. R. Sasubilli and W. G. Gutheil, *J. Comb. Chem.*, 2004, **6**, 911-915.
280. L. M. De León-Rodríguez and Z. Kovacs, *Bioconjugate Chem.*, 2008, **19**, 391-402.
281. X. Wang, M. Milne, F. Martinez, T. J. Scholl and R. H. E. Hudson, *RSC Advances*, 2017, **7**, 45222-45226.
282. B. Yoo and M. D. Pagel, *Bioconjugate Chem.*, 2007, **18**, 903-911.
283. B. Yoo, V. R. Sheth and M. D. Pagel, *Tetrahedron Lett.*, 2009, **50**, 4459-4462.
284. L. M. De León-Rodriguez, Z. Kovacs, G. R. Dieckmann and A. D. Sherry, *Chem. - Eur. J.*, 2004, **10**, 1149-1155.
285. W. Su, R. Mishra, J. Pfeuffer, K. H. Wiesmüller, K. Ugurbil and J. Engelmann, *Contrast Media Mol. Imaging*, 2007, **2**, 42-49.
286. R. Napolitano, T. C. Soesbe, L. M. De León-Rodríguez, A. D. Sherry and D. G. Udugamasooriya, *J. Am. Chem. Soc.*, 2011, **133**, 13023-13030.
287. J. Singh, V. Rustagi, S. Zhang, A. D. Sherry and D. G. Udugamasooriya, *Magn. Reson. Chem.*, 2017, **55**, 747-753.
288. J. Jayapaul and L. Schröder, *Bioconjugate Chem.*, 2018.
289. L. Connah and G. Angelovski, *Biomacromolecules*, 2018, **19**, 4668-4676.
290. N. Cakic, T. Z. Verbic, R. M. Jelic, C. Platas-Iglesias and G. Angelovski, *Dalton Trans.*, 2016, **45**, 6555-6565.
291. W.-h. Wei, T. Tomohiro, M. Kodaka and H. Okuno, *J. Org. Chem.*, 2000, **65**, 8979-8987.
292. M. N. Chatterjee, E. R. Kay and D. A. Leigh, *J. Am. Chem. Soc.*, 2006, **128**, 4058-4073.
293. E. Boseggia, M. Gatos, L. Lucatello, F. Mancin, S. Moro, M. Palumbo, C. Sissi, P. Tecilla, U. Tonellato and G. Zagotto, *J. Am. Chem. Soc.*, 2004, **126**, 4543-4549.

294. S. M. Vibhute, J. Engelmann, T. Verbić, M. E. Maier, N. K. Logothetis and G. Angelovski, *Org. Biomol. Chem.*, 2013, **11**, 1294-1305.
295. S. Gündüz, T. Savić, Đ. Toljić and G. Angelovski, *JoVE*, 2016, **118**, e54776.
296. S. Gündüz, A. Power, M. E. Maier, N. K. Logothetis and G. Angelovski, *ChemPlusChem*, 2015, **80**, 612-622.
297. J. D. Clogston and A. K. Patri, in *Characterization of Nanoparticles Intended for Drug Delivery*, ed. S. E. McNeil, Humana Press, Totowa, NJ, 2011, vol. 697, pp. 63-70.
298. T. M. Isailović, M. N. Todosijević, S. M. Đorđević and S. D. Savić, in *Microsized and Nanosized Carriers for Nonsteroidal Anti-Inflammatory Drugs*, ed. B. Čalija, Academic Press, Boston, 2017, pp. 179-217.
299. G. W. Lu and P. Gao, in *Handbook of Non-Invasive Drug Delivery Systems*, William Andrew Publishing, Boston, 2010, pp. 59-94.
300. M. Carril, *J. Mater. Chem. B*, 2017, **5**, 4332-4347.
301. P. Kadjane, C. Platas-Iglesias, P. Boehm-Sturm, V. Truffault, G. E. Hagberg, M. Hoehn, N. K. Logothetis and G. Angelovski, *Chem. - Eur. J.*, 2014, **20**, 7351-7362.
302. S. Gündüz, S. Vibhute, R. Botár, F. K. Kálmán, I. Tóth, G. Tircsó, M. Regueiro-Figueroa, D. Esteban-Gómez, C. Platas-Iglesias and G. Angelovski, *Inorg. Chem.*, 2018, **57**, 5973-5986.
303. S. Hoeft and K. Roth, *Chem. Ber.*, 1993, **126**, 869-873.
304. S. Aime, M. Botta and G. Ermondi, *Inorg. Chem.*, 1992, **31**, 4291-4299.
305. V. Jacques and J. F. Desreux, *Inorg. Chem.*, 1994, **33**, 4048-4053.
306. S. Aime, M. Botta, G. Ermondi, E. Terreno, P. L. Anelli, F. Fedeli and F. Uggeri, *Inorg. Chem.*, 1996, **35**, 2726-2736.
307. S. Aime, A. Barge, M. Botta, A. S. De Sousa and D. Parker, *Angew. Chem. Int. Ed.*, 1998, **37**, 2673-2675.
308. S. Aime, A. Barge, J. I. Bruce, M. Botta, J. A. K. Howard, J. M. Moloney, D. Parker, A. S. de Sousa and M. Woods, *J. Am. Chem. Soc.*, 1999, **121**, 5762-5771.
309. L. Connah, V. Truffault and G. Angelovski, 2019, DOI: 10.26434/chemrxiv.8158013.v1.
310. A. Beeby, I. M. Clarkson, R. S. Dickins, S. Faulkner, D. Parker, L. Royle, A. S. de Sousa, J. A. Gareth Williams and M. Woods, *J. Chem. Soc., Perkin Trans. 2*, 1999, **0**, 493-504.
311. L. Lattuada, A. Barge, G. Cravotto, G. B. Giovenzana and L. Tei, *Chem. Soc. Rev.*, 2011, **40**, 3019-3049.
312. L. Connah, R. Joshi, S. Vibhute, G. Gambino, J. D. G. Correia and G. Angelovski, *Org. Lett.*, 2019, **21**, 5378-5382.
313. E. Cros, M. Planas, G. Barany and E. Bardají, *Eur. J. Org. Chem.*, 2004, **2004**, 3633-3642.
314. N. Murai, M. Miyano, M. Yonaga and K. Tanaka, *Org. Lett.*, 2012, **14**, 2818-2821.
315. O. Kanie, S. C. Crawley, M. M. Palcic and O. Hindsgaul, *Carbohydr. Res.*, 1993, **243**, 139-164.
316. Z. Kovacs and A. D. Sherry, *Synthesis*, 1997, **1997**, 759-763.
317. P. Demay-Drouhard, H. Y. V. Ching, D. Akhmetzyanov, R. Guillot, L. C. Tabares, H. C. Bertrand and C. Policar, *ChemPhysChem*, 2016, **17**, 2066-2078.
318. S. Chanthamath, S. Takaki, K. Shibatomi and S. Iwasa, *Angew. Chem. Int. Ed.*, 2013, **52**, 5818-5821.
319. B. Kundu, *Tetrahedron Lett.*, 1992, **33**, 3193-3196.
320. M. E. Attardi, G. Porcu and M. Taddei, *Tetrahedron Lett.*, 2000, **41**, 7391-7394.
321. M. Oliver, M. R. Jorgensen and A. D. Miller, *Synlett*, 2004, **2004**, 453-456.
322. A. Isidro-Llobet, M. Álvarez and F. Albericio, *Chem. Rev.*, 2009, **109**, 2455-2504.
323. W. X. Ren, J. Han, S. Uhm, Y. J. Jang, C. Kang, J.-H. Kim and J. S. Kim, *Chem. Commun.*, 2015, **51**, 10403-10418.
324. S. M. Vithanarachchi and M. J. Allen, *Curr. Mol. Imaging*, 2012, **1**, 12-25.
325. S. Lee, J. Xie and X. Chen, *Biochemistry*, 2010, **49**, 1364-1376.
326. A. F. Kolodziej, S. A. Nair, P. Graham, T. J. McMurry, R. C. Ladner, C. Wescott, D. J. Sexton and P. Caravan, *Bioconjugate Chem.*, 2012, **23**, 548-556.

327. K. Overoye-Chan, S. Koerner, R. J. Looby, A. F. Kolodziej, S. G. Zech, Q. Deng, J. M. Chasse, T. J. McMurry and P. Caravan, *J. Am. Chem. Soc.*, 2008, **130**, 6025-6039.
328. S. A. Nair, A. F. Kolodziej, G. Bhole, M. T. Greenfield, T. J. McMurry and P. Caravan, *Angew. Chem. Int. Ed.*, 2008, **47**, 4918-4921.
329. J. Vymazal, E. Spuentrup, G. Cardenas-Molina, A. J. Wiethoff, M. G. Hartmann, P. Caravan and E. C. J. Parsons, *Investig. Radiol.*, 2009, **44**, 697-704.
330. E. Spuentrup, R. M. Botnar and A. J. Wiethoff, *Eur. Radiol.*, 2008, **18**, 1995-2005.
331. J. S. Desgrosellier and D. A. Cheresh, *Nat. Rev. Cancer*, 2010, **10**, 9.
332. X. Sun, Y. Li, T. Liu, Z. Li, X. Zhang and X. Chen, *Adv. Drug Delivery Rev.*, 2017, **110-111**, 38-51.
333. F. Wang and Z. Liu, in *Advanced Topics in Science and Technology in China*, Springer, Berlin, Heidelberg, 2013, DOI: 10.1007/978-3-642-34303-2_15, pp. 513-538.
334. J.-A. Park, Y. J. Lee, I. O. Ko, T.-J. Kim, Y. Chang, S. M. Lim, K. M. Kim and J. Y. Kim, *Biochem. Biophys. Res. Commun.*, 2014, **455**, 246-250.
335. J. Gallo, I. S. Alam, I. Lavdas, M. Wylezinska-Arridge, E. O. Aboagye and N. J. Long, *J. Mater. Chem. B*, 2014, **2**, 868-876.
336. J.-A. Park, J.-J. Lee, J.-C. Jung, D.-Y. Yu, C. Oh, S. Ha, T.-J. Kim and Y. Chang, *ChemBioChem*, 2008, **9**, 2811-2813.
337. G. Hao, X. Sun, Q. N. Do, B. Ocampo-García, A. Vilchis-Juárez, G. Ferro-Flores and L. M. De León-Rodríguez, *Dalton Trans.*, 2012, **41**, 14051-14054.
338. X. Wu and D. S. Reddy, *Pharmacol. Ther.*, 2012, **134**, 68-81.
339. D. M. Corsi, C. Platas-Iglesias, H. v. Bekkum and J. A. Peters, *Magn. Reson. Chem.*, 2001, **39**, 723-726.
340. T. D. Goddard and D. G. Kneller, SPARKY 3, University of California, San Francisco.
341. A. E. Derome and M. P. Williamson, *J. Magn. Reson.*, 1990, **88**, 177-185.
342. K. Scheffler and S. Lehnhardt, *Eur. Radiol.*, 2003, **13**, 2409-2418.
343. B. Moreno, P. Villoslada, J. Messeguer, G. Navarro and A. Messeguer, *Preparation of 3-oxopiperazinium derivatives as nerve growth factor agonists,* WO2011024078A1, 2011.
344. S. M. Vibhute, PhD thesis, Eberhard Karls University Tübingen, 2013.
345. N. M. Green, in *Methods Enzymol.*, Academic Press, 1970, vol. 18, pp. 418-424.